

The Geology and Geochemistry of the Sakatti Cu-Ni-PGE Deposit, N. Finland

William Brownscombe

Earth Science and Engineering Department

Imperial College London

CID 00427654

Supervisors: Andrew Berry, Jim Coppard, Richard Herrington, Christian Ihlenfeld and Jamie Wilkinson

Project fully funded by Anglo American plc.

The work contained comprises of the author's work, assisted by the supervisors listed, and all else included is appropriately referenced. Figures and text from a chapter, published by the author, in the book *Mineral Deposits of Finland* are reproduced with permission.

The copyright of this thesis rests with the author and is made available under a Creative Commons Attribution Non-Commercial No Derivatives licence. Researchers are free to copy, distribute or transmit the thesis on the condition that they attribute it, that they do not use it for commercial purposes and that they do not alter, transform or build upon it. For any reuse or redistribution, researchers must make clear to others the licence terms of this work.

Abstract

The Sakatti Cu-Ni-PGE (platinum group elements) deposit is a newly discovered mineral deposit in northern Finland. The deposit is a magmatic sulphide hosted in an ultramafic intrusion in the Central Lapland Greenstone Belt. The major lithologies and styles of mineralisation of the deposit are characterised and defined in this project and their origin investigated.

The host rock is composed primarily of olivine with forsterite content between 0.85 and 0.91 and a Ni content between 3000-3700 ppm. This suggests that the olivine is undepleted with respect to Ni and has not been derived from a sulphide-saturated melt. The intrusion sits in a plagioclase-picrite and the locus of the deposit occurs at a change in gradient that occurs when the intrusion transgresses to a stratigraphically higher lithology.

Sulphur isotope analysis shows that the Sakatti deposit has consistent $\delta^{34}\text{S}$ values 2.6 ± 2.4 ‰. This is not consistent with the regional Matarakoski schists contributing S to the deposit. The deposit has unusually low Ni/Cu values, particularly the shallower portions. Magnetite trace element analysis, PPGE/IPGE values and Ni isotope analysis presented suggest that this is due to sulphide fractionation and loss of early fractionating Ni-rich sulphide cumulates.

The PGE mineralogy in the Sakatti deposit is exclusively PGE tellurides, derived from sulphide melt. The dominance of tellurides leads to a wide array of moncheite-merenskyite-melonite compositions that is not seen elsewhere globally.

A model is presented for the formation of the deposit where earlier Ni-rich cumulates are lost at an earlier stage in the conduit-like intrusion and remobilised by later silicate melt that does not re-equilibrate with the sulphides.

Acknowledgements

Thanks are due to Andrew Berry, Jim Coppard, Christian Ihlenfeld, Richard Herrington and Jamie Wilkinson for their supervision, in particular Christian who has provided scientific engagement throughout and Jim and Richard who conceived the project. Julie Prytulak and Jens Andersen are thanked for their fair and thorough examination of the project and for their numerous well-thought through comments.

Sincere and heartfelt thanks to the former geological team of Anglo American Exploration in Finland including, but not limited to, Klara Collis, Peter Dodds, Craig Hartshorne, Janne Kaukolinna, Steffi Klatt, Ryan Preece, Cat Reynolds, Janne Siikalouma, Sebastian Stelter and Louise Wright. Thanks also to the non-geological staff for the warmth and hospitality including, but not limited to, Peter, Jani, Risto, Jurgen, Kirsti, Bo, Pauli and Paivi.

Thanks to Tracey Kerr and Stuart MacCracken for their enthusiasm and support in the latter stages of the project and thanks also to Jukka Jokola and Tapio Halkoaho for robust and healthy geological discussion around the project.

Thanks to Robin Armstrong, Alla Dolgoplova, Chris Halls, Reimar Seltmann, Baruch Spiro and the rest of the LODE group for their scientific support.

Thanks to Chris Hunter and Kate Jillings for the cooperative undertaking of MSci projects both of which were done excellently and fed into this overall project.

Thanks for analytical assistance to: Anton Kearsley and John Spratt for both SEM and EPMA; Chris Stanley for reflected light microscopy; Adrian Boyce and Alison MacDonald for S isotope analysis; Matthew Cooper, Agnieszka Michelik and Rex Taylor for Sm/Nd analysis; Martina Bertini, Teresa Jeffries, Anna Morris and Clara Wilkinson for silicate and oxide LA-ICP-MS; Iain McDonald for sulphide LA-ICP-MS; Russell Garwood and Lauren Howard for HRXCT; and Stanislav Strekopytov and Emma Humphreys-Williams for whole-rock geochemistry.

Thanks to Louise Gall for undertaking Ni isotope analysis on Sakatti samples using techniques that she has developed and for allowing me to use the results.

Eileen Cox, Anna Hutson and Julie Gray are thanked for their logistical support at the NHM.

This study is dedicated to the Anglo American Exploration Finland team that was active during the majority of this project, for their enthusiasm, the thrill of shared geological discovery and for allowing me to be a small part of that team.

Contents

1	Introduction.....	10
1.1	Project conception.....	10
1.2	Project outline.....	10
1.3	Discovery History.....	11
1.4	Genetic models of Ni-Cu-PGE deposits.....	12
1.4.1	Magma source.....	13
1.4.2	Sulphide saturation.....	14
1.4.3	Formation of a deposit.....	17
1.5	General characteristics of Ni-Cu-PGE deposits.....	20
1.5.1	Mineralogy.....	20
1.5.2	Host rocks.....	20
1.5.3	Structure.....	21
1.5.4	Settings.....	21
1.6	Stable isotope geochemistry applied to ore deposits.....	22
1.6.1	Overview.....	22
1.6.2	S isotopes.....	23
1.6.3	Ni isotopes.....	24
1.7	Discussion.....	25
2	The Geology of Northern Finland.....	26
2.1	Tectonic History of the Fennoscandian Shield.....	26
2.1.1	Archaean.....	26
2.1.2	Palaeoproterozoic.....	27
2.1.3	Post-Palaeoproterozoic.....	28
2.2	The Karelian craton.....	30
2.3	The Central Lapland Greenstone Belt.....	31

2.4	Local Geology – The Sodankylä area	32
2.4.1	The Lapponi supergroup	32
2.4.2	Higher stratigraphy	35
2.4.3	Metamorphism of the CLGB	35
2.4.4	The Koitelainen Layered Igneous Intrusion	36
2.4.5	The Kevitsa-Satosvaara Intrusion	38
2.4.6	Gabbro-Wehrlite 2.2 Ga associations	40
2.5	Discussion	41
3	Silicate geology and geochemistry.....	43
3.1	Introduction	43
3.1.1	Key questions	43
3.1.2	Geological Setting	44
3.1.3	Deposit overview	44
3.2	Sampling	53
3.3	Petrography.....	54
3.3.1	Volcano-sedimentary Unit.....	54
3.3.2	Breccia Unit.....	56
3.3.3	Mafic suite.....	58
3.3.4	Host Olivine Cumulate or Peridotite Unit.....	59
3.3.5	Aphanitic Unit	69
3.3.6	Contact between the Olivine Cumulate Unit and the Aphanitic Unit	72
3.3.7	Petrographic interpretations.....	76
3.4	Mineral chemistry.....	80
3.4.1	Olivine	81
3.4.2	Chromite.....	91
3.4.3	Pyroxene.....	92
3.4.4	Plagioclase	96
3.4.5	Amphibole	96
3.5	Whole-rock geochemistry	100

The Sakatti Cu-Ni-PGE deposit

3.5.1	Summary	100
3.5.2	Parental melt	100
3.5.3	Layering or Serpentinisation	101
3.5.4	Aphanitic Unit	106
3.5.5	Classification of the Aphanitic Unit.....	107
3.6	Isotopic studies	108
3.6.1	Sm/Nd	108
3.7	Discussion	112
3.7.1	Intrusive vs. extrusive	112
3.7.2	Crustal contamination	112
3.7.3	Comparison with regional geology	116
3.7.4	Multiple pulses within the intrusion	118
3.7.5	Base of the intrusion	119
3.7.6	Nature of contact with the Aphanitic Unit.....	119
3.7.7	Pegmatoidal Gabbro Sub-Unit.....	121
3.7.8	Serpentinisation.....	121
3.7.9	Dissociation of olivine chemistry with mineralisation	122
3.8	Conclusions.....	123
3.9	Implications for exploration and further work	123
4	Sulphide mineralisation.....	124
4.1	Introduction	124
4.1.1	Deposit overview.....	124
4.1.2	Key questions	129
4.2	Sampling	131
4.3	Results.....	132
4.3.1	Petrography	132
4.3.2	Mineral chemistry	143
4.3.3	Bulk sulphide chemistry.....	155
4.3.4	Isotopic studies.....	158

The Sakatti Cu-Ni-PGE deposit

4.4	Discussion	170
4.4.1	Overview	170
4.4.2	Effect of alteration.....	170
4.4.3	Formation of sulphides	170
4.4.4	Evidence in favour of an evolved sulphide melt.....	172
4.4.5	Pyrite.....	176
4.5	Conclusions.....	179
4.6	Implications for exploration and further work	179
4.6.1	Implications for exploration	179
4.6.2	Further work.....	180
5	PGE mineralisation at the Sakatti Deposit.....	181
5.1	Introduction	181
5.1.1	PGE mineralogy in Ni-Cu-PGE deposits.....	181
5.1.2	PGE mineralogy at the Kevitsa deposit.....	183
5.1.3	Experimental studies	183
5.2	Sampling	184
5.2.1	Petrology and mineral chemistry	184
5.2.2	CT Scanning.....	184
5.3	Results.....	185
5.3.1	Mineralogy.....	185
5.3.2	Chemistry.....	186
5.3.3	Morphology.....	192
5.3.4	Host mineralogy.....	196
5.3.5	PGE mineral locations.....	197
5.3.6	Whole-rock PGE data	198
5.4	Discussion	200
5.4.1	Origin of PGE mineralisation	200
5.4.2	Disseminated vs. massive mineralisation.....	200
5.4.3	Comparison with other PGE deposits	200

The Sakatti Cu-Ni-PGE deposit

5.4.4	Controls on PGE mineralogy	202
5.5	Conclusions.....	208
5.6	Further work and implications for exploration.....	208
6	Discussion	210
6.1	Overview of discussion.....	210
6.1.1	Summary of silicate discussion.....	210
6.1.2	Summary of sulphide discussion.....	210
6.1.3	Summary of PGE discussion.....	211
6.2	Model constraints from the geology.....	211
6.2.1	Origins of ultramafic magmatism	213
6.2.2	The origin of sulphide mineralisation.....	214
6.2.3	Disequilibrium between silicate and sulphide	215
6.2.4	Cu-rich nature of mineralisation.....	216
6.2.5	Genetic model.....	217
7	Conclusions.....	221
7.1	Conclusions.....	221
7.2	Implications for exploration.....	222
7.3	Further work.....	223
8	References.....	225
9	Appendix.....	234
9.1	Analytical parameters	234
9.1.1	SEM and EPMA.....	234
9.1.2	Silicate LA-ICP-MS.....	234
9.1.3	Whole Rock geochemistry	238
9.1.4	Sulphide LA-ICP-MS.....	239
9.1.5	Sm/Nd analysis.....	240
9.1.6	S isotope analysis.....	242
9.1.7	Ni isotope analysis	243
9.1.8	High Resolution X-Ray Computed Tomography (HRXCT).....	244

The Sakatti Cu-Ni-PGE deposit

9.1.9	Analytical References.....	245
9.2	Glossary of mineral abbreviations	246
9.3	LA-ICP-MS Data.....	247
9.4	EPMA Data.....	247

1 Introduction

1.1 Project conception

This PhD project has arisen out of a desire for greater geological understanding by the Anglo American Exploration Finland team concerning their new discovery, the Sakatti deposit. The project was initiated by Jim Coppard a year after the discovery drill hole was recovered and has run concurrently with a greatly expanding exploration programme on the deposit. A PhD associated with such an early stage exploration project is unusual and has presented numerous opportunities and challenges.

The author spent a total of 5 months in Finland at the Anglo American Exploration offices and core shed and the project is fundamentally based on the geological skill and understanding of the Anglo American Finland team. The project was wholly funded by Anglo American plc. and supported throughout by their staff.

1.2 Project outline

The project has a very broad remit in part due to the fact that it is the first academic study on a new deposit. Aside from the increasing knowledge around the processes that formed the Sakatti deposit, very few specific goals were outlined prior to the project's inception; instead the important questions arose out of the first year of study.

A traditional petrographic approach forms the backbone of the project progressing from core logging to transmitted and reflected light microscopy to scanning electron microscopy and electron microprobe analysis. This is supported by mineral trace element analysis, whole-rock geochemistry and X-ray diffraction. Where it was necessary to address the key questions below isotopic analysis was used, both stable and radiogenic.

The project is split into silicate, sulphide and PGE mineral sections. Although all these topics are interdependent, the analysis types split along these lines and so a chapter is presented on each of the three groups of minerals. The principal questions addressed in the project are listed below and the approach taken to resolve these questions is given in the introduction of the relevant chapter.

Silicate questions

- What is the nature of the parent melt from which the mineralisation formed?
- How does the deposit fit with the regional stratigraphy?
- Is there any layering of different pulses of magmatism coherent with mineralisation?
- Is there any alteration that affects mineralisation?
- What is the relevance of the Aphanitic Unit?

Sulphide questions

- What is the cause of S saturation?
- Why is the deposit Cu-rich?
- What is the origin of the pyrite mineralisation?
- To what extent do hydrothermal processes effect the mineralisation?

Platinum Group Element (PGE) mineralisation questions

- What is the nature of PGE mineralisation at Sakatti?
- How does that compare to other Ni-Cu-PGE deposits?
- What are the controls on PGE mineralisation and what is its origin?
- Is there a hydrothermal component to the PGE distribution?
- Is there a mineralogical control on the Pt:Pd distribution at Sakatti and can the spatial variation in Pt:Pd ratio be explained?

1.3 Discovery History

The Sakatti deposit was discovered in 2009 by the Anglo American Exploration Finland Team, led by Jim Coppard. Ni sulphide exploration in Fennoscandia had been initiated in 2002 focusing on mafic/ultramafic sills in the Central Lapland Greenstone Belt (CLGB). Targets were identified using publicly available Aeromagnetic Frequency Electromagnetic data provided by the Geological Survey of Finland. These targets were followed up by ground geophysical methods and base-of-till (BOT) geochemistry, which proved more effective than soil geochemistry (Fig. 1.1).

Drilling began in 2006 with three drill holes, one of which returned significant Cu-PGE-Au mineralisation. The deposit was downgraded as Cu-rich mineralisation was deemed unprospective by Ni commodity experts. In 2007 infill BOT geochemistry revealed a significant anomaly which was followed with further drilling that intersected disseminated and minor

vein-related mineralisation and the official discovery drill hole (M8013) was drilled in 2009 with 110.00 m at 1.3 wt% Cu, 0.2 wt% Ni, 0.5 g/t Pt, 0.3 g/t Pd, and 0.4 g/t Au.

When this study commenced in 2010, 30 drill holes had been drilled in the shallow NW part of the deposit. While the project continued numerous drill holes were drilled bringing the total to more than 150 at present producing over 100 km of core and changing the shape and understanding of the deposit considerably. In the latter half of the project fresh drilling on the main body of the deposit has been curtailed by permitting issues.

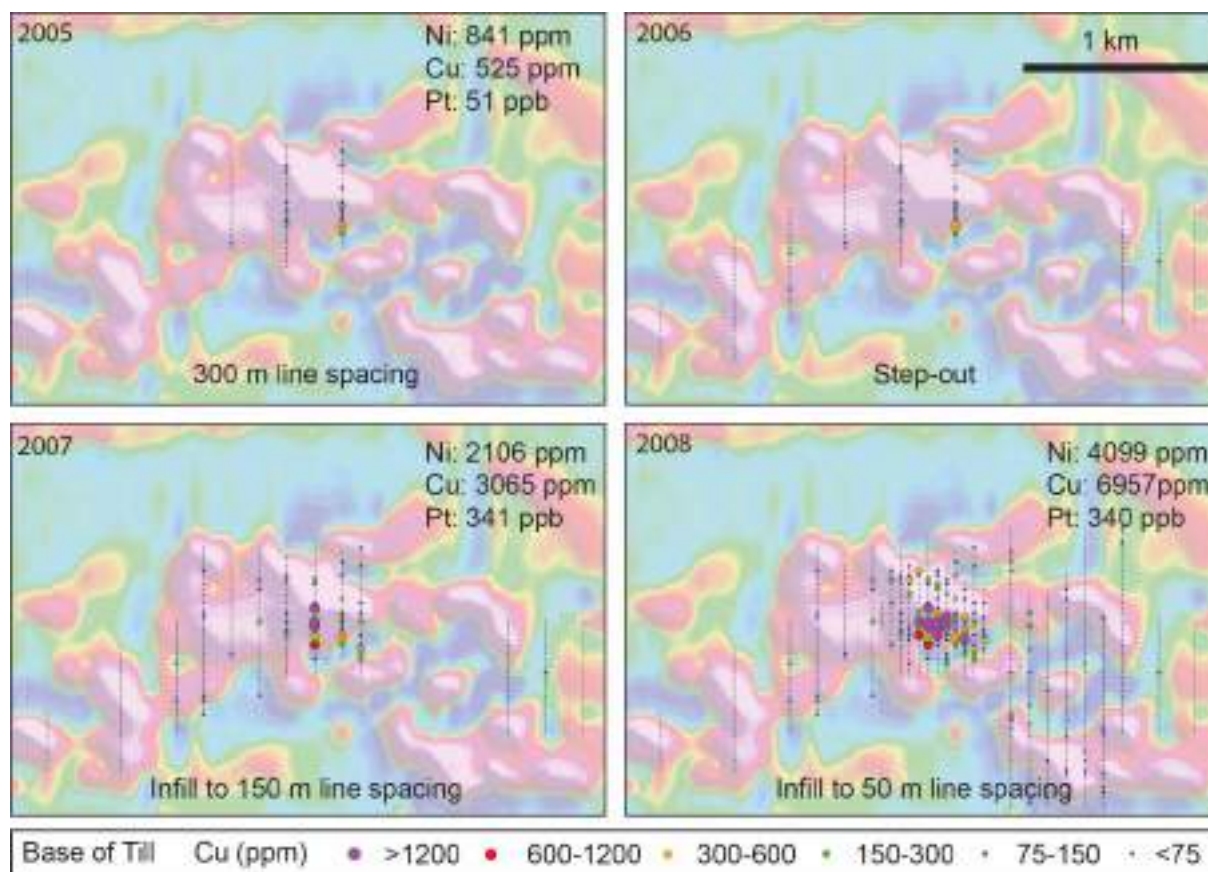


Figure 1.1 - Base-of-till geochemistry undertaken over the Sakatti deposit prior to discovery, overlain on an airborne magnetic map (reduced to pole). The base-of-till anomaly was well defined by 2008 and was approximately 150 m by 150 m (Brownscombe et al., 2015).

1.4 Genetic models of Ni-Cu-PGE deposits

Magmatic Ni-Cu-PGE deposits occur throughout the world (Fig. 1.2) associated with a variety of mafic and ultramafic hosts. This review aims to briefly cover the principal characteristics and the features of the genetic model that has a broad consensus in the literature. The theoretical elements that are necessary considerations of the genetic model are discussed. The regional and local geology of Finland is covered in the next chapter.



Figure 1.2 – Global sketch map of major Ni-Cu sulphide deposits, showing the approximate area of the Sakatti exploration project (Barnes and Lightfoot, 2005).

The genesis of magmatic Ni-Cu-PGE deposits is defined in a general model that has a consensus across the literature (Barnes and Lightfoot, 2005; Naldrett, 2004). An ultramafic or mafic melt is required, carrying PGE, Cu and Ni. This is emplaced into the crust and is brought to a point of S saturation after which immiscible liquid sulphide is formed. This immiscible sulphide liquid must then collect or be pooled either under gravity or by flow dynamics in order to form a deposit. The most important points of the genetic model for each individual deposit is the mechanism by which sulphide saturation is induced and the mechanism by which immiscible sulphide liquid is concentrated to form the deposit.

1.4.1 Magma source

Ultramafic melts derive from a high degree of partial melting of the mantle. The metal content of a melt will also depend on the degree of partial melting (Arndt et al., 2008).

Within the mantle, Cu and PGE are chalcophile meaning they reside predominantly in a sulphide phase. This is because of the high partition coefficient ($D^{\text{sulphide-silicate}}$) of Cu and the exceedingly high partition coefficient of PGE (Mungall and Brenan, 2014). In order to liberate the PGE the entire sulphide phase must be incorporated into the melt, which typically occurs at 15-25% partial melting (Arndt et al., 2005). Additional partial melting will only dilute the Cu and PGE contents of the melt. Ni behaves differently as it resides in olivine and so an increased degree of partial melting will result in increasing Ni concentration in the melt.

Earlier literature focused on the degree of partial melting of the mantle host and consequently the concentrations of metals in the melt prior to sulphide saturation. Later ideas progressed towards magma dynamics and the ability of a melt to assimilate country rock being a much more important factor (Arndt et al., 2005). Therefore, though the magma source is important, the focus of this study shall be on the subsequent processes that resulted in the formation of the mineral deposit.

1.4.2 Sulphide saturation

To form a deposit a melt must be pushed to sulphide saturation. Above sulphide saturation a melt will form an immiscible liquid sulphide phase into which PGE and Cu will readily partition.

1.4.2.1 Conditions for sulphide saturation

The S content of individual magmas at the time of sulphide saturation can be described by an empirically-derived equation (Li and Ripley, 2005).

$$\ln X_S = 1.229 - 0.74 \left(\frac{10^4}{T} \right) - 0.021P - 0.311 \ln X_{FeO} - 6.166X_{SiO_2} - 9.153X_{Na_2O+K_2O} \\ - 1.914X_{MgO} + 6.594X_{FeO}$$

Equation 1.1 – Empirical equation for S content of magma at sulphide saturation. Where T = degrees in Kelvin; X = mole fraction and P = pressure in kBar. fs₂ is not included in the equation as it is controlled by fo₂, which is defined by FeO and temperature (Li and Ripley, 2005).

If sulphide over-saturation is reached, immiscible liquid sulphide will separate from the silicate melt until the system is returned to sulphide saturation.

1.4.2.2 Controls on S solubility

i. Temperature

Decreasing temperature will decrease the solubility of S. Maximum dissolved S can be expected to decrease three to five times between 1450°C and 1200°C in a natural system (Naldrett, 2004).

ii. Pressure

Decreasing pressure will increase the solubility of S. This will counteract the effect of decreasing temperature as magma rises. It has been concluded that in natural systems S solubility will most likely never decrease during ascent (Mavrogenes and O'Neill, 1999).

In other words, the effect of pressure will always outweigh the effect of temperature, though this does not take into account any contamination.

iii. *Oxygen fugacity/FeO content*

Oxygen fugacity (f_{O_2}) is an important control on the solubility of S. Sulphur dissolves by displacing oxygen associated with Fe^{2+} in the melt. Increased f_{O_2} will favour Fe^{3+} , decreasing the amount of available Fe^{2+} and therefore decreasing the solubility of S (Maclean, 1969). At high levels of f_{O_2} S will dissolve as sulphate (SO_4^{2-}) which will not result in the formation of sulphide deposits.

1.4.2.3 Mechanisms for sulphide saturation

As stated above, during ascent magma will become less saturated with S. Therefore a mechanism is required to induce oversaturation of the S and subsequent immiscible separation of a sulphide liquid phase.

i. *Fractional crystallisation*

Decreasing the temperature will decrease S solubility and also change the composition of the magma as crystallisation occurs. Figure 1.3 shows the changing solubility of S with increasing degrees of crystallisation. Crystallisation of olivine will decrease the overall Fe content of the melt, decreasing S solubility. Plagioclase crystallisation, by contrast, will increase the Fe content as a percentage of the melt, therefore increasing S solubility (Mathez, 1976). The tempering effect of plagioclase crystallisation can be seen in (Fig. 1.3).

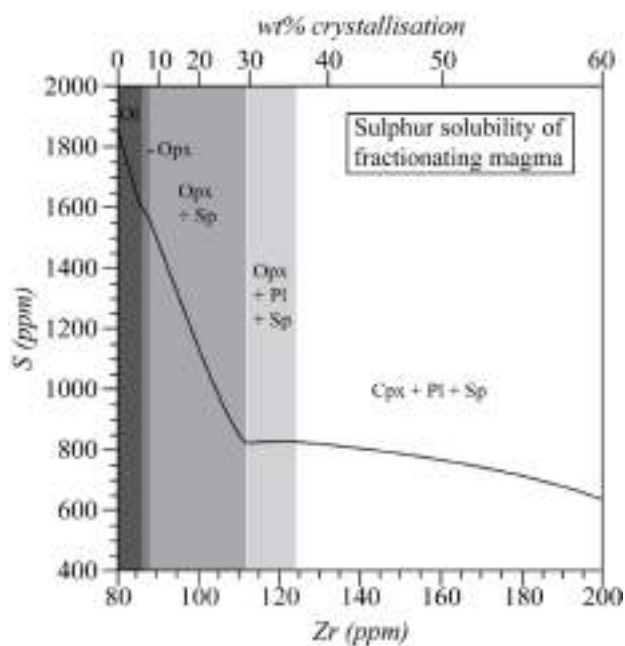


Figure 1.3 – Plot of S solubility in a silicate melt with increasing degree of crystallisation, with Zr used as an index of crystallisation. Crystallising phases of olivine (Ox), orthopyroxene (Opx), spinel (Sp), plagioclase (Pl) and clinopyroxene (Cpx) are shown. (after Harmer and Sharpe, 1985; Li et al., 2001b; Naldrett, 2004).

The principal problem with fractional crystallisation as a model is that it does not allow the formation of a massive sulphide (type I) deposit. It requires simultaneous silicate crystallisation, which would settle and interfere with the formation of the massive sulphide ore body, leading to a disseminated deposit (Mungall and Su, 2005).

ii. *Magma mixing/granitic contamination*

The addition of a granitic or more evolved mafic melt would change the chemistry of a silicate melt. An increase in fO_2 will decrease the solubility of S, and therefore the addition of a felsic melt could trigger sulphide immiscibility (Li and Naldrett, 1993). However, in order for this path to be successful the melt already has to be close to sulphide saturation (Naldrett, 2004).

iii. *Sulphur addition*

The addition of S-rich sediments is the most obvious way to induce S immiscibility. A number of deposits pass through sulphide-rich sediments (Eg. Noril'sk Talnakh). This is thought to be the principal way in which sulphide immiscibility can be triggered in melts that are particularly S under-saturated (Naldrett, 2004).

1.4.2.4 Collection of PGE

The formation of an immiscible sulphide phase will scavenge PGE from a silicate melt due to the extremely high partition coefficient ($D^{sulphide-silicate}$). It will also scavenge Ni and Cu but at a slower rate (Fig. 1.4).

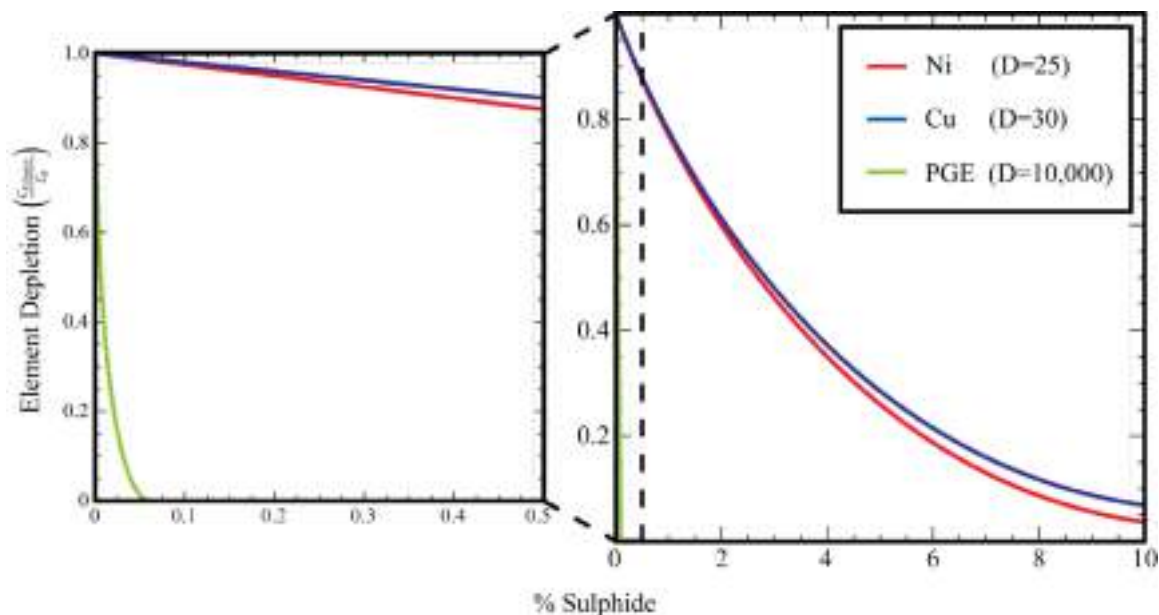


Figure 1.4 – Depletion of Cu, Ni and PGE in a silicate melt to a sulphide melt, with increasing sulphide (as a percentage of total silicate+sulphide). Based on assumed partition coefficients of 25 for Ni, 30 for Cu and 10,000 for PGE (Mungall and Brenan, 2014; Rajamani and Naldrett, 1978). The lithophile behaviour of Ni has not been taken into account.

This difference in partition coefficients has a dramatic influence on behaviour of the metals. Before the immiscible sulphide phase has become 0.1% of the total melt, 99% of the PGE have

been removed to the sulphide. Nickel and Cu by contrast only reach >90% removal by 10% of the melt being the sulphide phase. This assumes sufficient mixing for the sulphide droplets to scavenge all the PGE. The majority of models for certain deposits include a degree of transport of the sulphide droplets within the silicate melt, allowing for thorough scavenging from both the host and usually additional magma that has not been preserved (Barnes and Lightfoot, 2005).

This separate behaviour explains the initial classification in the scheme put forward by Naldrett (2004). Deposits with a very small amount of sulphide can have exceedingly high concentrations of PGE. By contrast, deposits with a large amount of sulphide will be richer in Ni and Cu but with a dramatically reduced, diluted, PGE grade.

1.4.3 Formation of a deposit

1.4.3.1 Assimilation of country rock

The ability of a melt to assimilate country rock is critical if contamination is the primary method for inducing S saturation. The main factors governing the ability of a melt to assimilate country rock will be (Arndt et al., 2005; Arndt et al., 2008; Lesher and Keays, 2002):

i. Density

A fluid which is too dense will not ascend through the crust and the density of ultramafic melts can exceed that of solid crustal rocks. If a fluid is not dense enough (too buoyant) it will ascend quickly and vertically, resulting in minimal assimilation of country rock.

ii. Viscosity

Turbulent flow dramatically increases the thermal erosion of the country rock. If a melt is too viscous the flow will be laminar and assimilation will be minimal.

iii. Temperature

Temperature has a significant influence on viscosity. Higher temperatures also increase the ability of the magma to melt country rock.

iv. Flux

Insufficiently low flux and the flow will be laminar instead of turbulent. If the flux is too high then the contamination will be diluted by the larger amount of original melt.

v. Nature of the wall rock and mode of emplacement

These will also be important factors although these are not directly related to the properties of the melt.

These factors are more important for the formation of a deposit than the PGE concentration of the original melt, meaning that studies focusing on partial melting in the mantle are as not as

influential as once thought (Arndt et al., 2005). For example, komatiite magmas are common hosts not because of high initial PGE contents but because they have very high temperatures and low viscosities and can therefore easily become contaminated (Williams et al., 2001).

1.4.3.2 Trapping of sulphide melt

Sulphide droplets need to accumulate in significant concentrations in order to produce an economic deposit. Sulphides are typically found at the base of intrusions and flows or as veins extending into the country rock. Embayments or depressions in the base of a conduit are likely to accumulate sulphides due to density and also a drop in flow energy. A feeder conduit entering a magma chamber is also a possible location of sulphide deposits, as the flow speed will decrease and sulphide droplets could accumulate (Eg. Eastern Deeps; Barnes and Lightfoot, 2005).

The level of interaction of the sulphide droplets with the melt will directly control the metal content of the sulphide. In many cases the sulphide droplets have been exposed to a greater amount of parent magma than is apparent, for example in a conduit where large volumes pass through. This leads to unlikely levels of enrichment that can only be explained by exposure to additional melt (Arndt et al., 2005).

1.4.3.3 Enrichment of sulphide melt

The overloading of PGE in these deposits is a cause of contention. Often considerably more PGE is held in the sulphide phase than could have been in the silicate host, meaning that the sulphide phase probably has a more complex history including transport through larger quantities of melt (Kerr and Leitch, 2005). This further magma flow results in upgrading the deposit beyond the PGE content of the original silicate melt. The dynamics of PGE transfer from a large silicate melt into a relatively small sulphide phase are not well understood. A certain amount of mixing is usually invoked in order to achieve a high degree of PGE transfer into the sulphide phase. Subsequent dissolution of the sulphide liquid phase by a silicate melt that has been lowered below sulphide saturation will also upgrade the deposit, provided it is not complete, as the remaining sulphide will be relatively richer in PGE and Cu (Kerr and Leitch, 2005).

1.4.3.4 Solid solution and crystallisation of sulphide melt

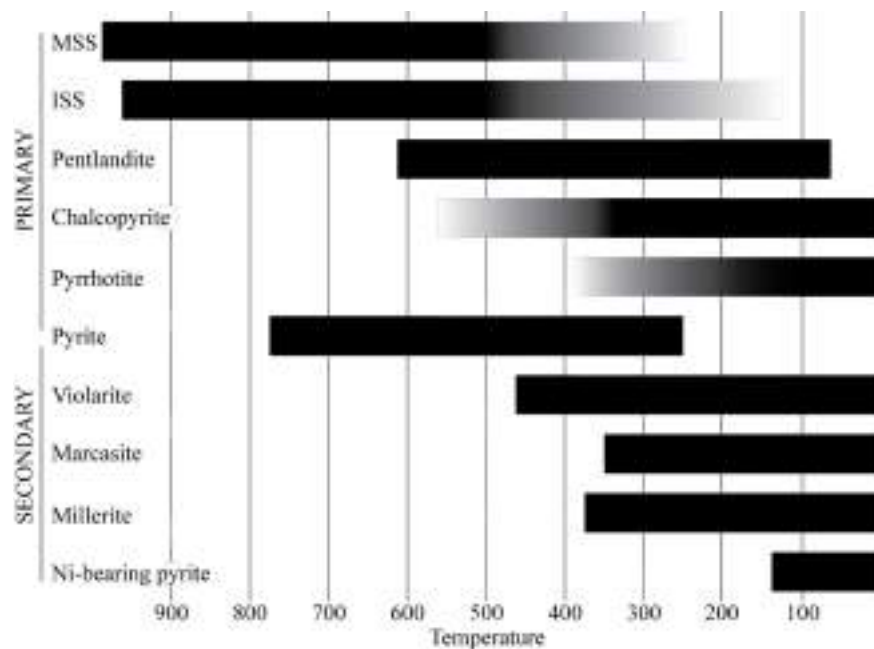


Figure 1.5 – Approximate temperature ranges over which principal Ni-Cu sulphide deposit minerals are stable.

Based on the paragenetic evolution of the Kilvenjärvi deposit (Andersen et al., 2006).

The approximate temperature stabilities of the main minerals that form in magmatic Ni-Cu sulphide deposits are shown in (Fig. 1.5) monosulphide solid solution (MSS) is a Fe-Ni mineral that forms at high temperature and alters to pentlandite and pyrrhotite at lower temperatures. Intermediate solid solution (ISS) is a Cu sulphide mineral that alters to chalcopyrite at lower temperatures. MSS will crystallise first leaving a Cu-rich sulphide liquid which will crystallise to form ISS. This segregation of Ni and Cu will be preserved and can be observed in many deposits (Fig. 1.6). Typically Fe remaining in the Cu melt will form magnetite as well as pyrrhotite.

The temperature of crystallisation of the host mafic-ultramafic melts will usually be higher than the formation temperature of ISS, meaning that a liquid sulphide phase may remain underneath solidified silicate melt. In combination with the weakness of the sulphide minerals, this gives rise to the unusual and distorted structures often seen in these deposits and the type 1b and 1c structures discussed in 1.5.3 (Arndt et al., 2005). By a temperature of 1000°C the MSS phase will be solid, while the Cu phase would still be molten (Holwell and McDonald, 2010). If the Cu-rich phase was mobilised at this stage then dykes and sills overwhelmingly dominated by chalcopyrite can result.

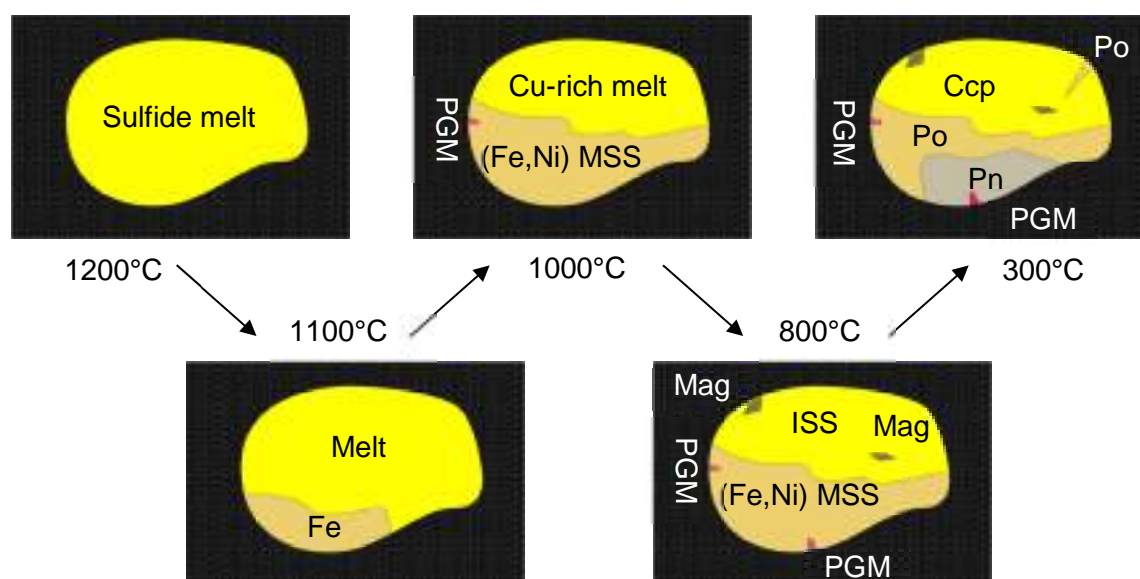


Figure 1.6 – Diagrammatic representation of the sequence of mineral formation in an idealised bleb of sulphide melt (after Holwell and McDonald, 2010). Mineral phases are monosulphide solid solution (MSS), platinum group metals (PGM), intermediate solid solution (ISS), magnetite (Mag), chalcopyrite (Ccp), pentlandite (Pn) and pyrrhotite (Po).

1.5 General characteristics of Ni-Cu-PGE deposits

1.5.1 Mineralogy

The mineralogy of Ni-Cu sulphide deposits usually consists of intergrown pyrrhotite, pentlandite and chalcopyrite, typically associated with 1-15% magnetite. Cobalt, gold and PGE are usually economically significant by-products of the deposits. Cobalt substitutes into pentlandite while PGE usually form small grains of separate varied minerals, with the exception of Pd which often exists in solid solution within pentlandite (Barnes and Lightfoot, 2005).

1.5.2 Host rocks

Ni-Cu deposits are found associated with a range of mantle-derived rocks, including principally komatiites, tholeiitic picrites, ferropicrites and high Al basalts. The Naldrett scheme for classification of Ni-Cu sulphide deposits is based on their host rock and geological setting (Naldrett, 2004). The initial separation is between those which consist of small quantities of sulphides that are PGE-rich and those that consist of much larger quantities of sulphides with economic Ni and Cu tonnages but much lower PGE grades. This is an economic separation as these two end-members generally represent the economic deposits. The genetic reason for the separation of these styles is discussed in 1.4.2.4. The degree of partial melting that formed a

host rock is also a factor in determining whether it could host a Ni-Cu deposit, this is discussed in 1.4.1. The host rocks can be both intrusive and extrusive, with continental flood basalts and komatiite flows hosting some deposits (Arndt et al., 2008).

1.5.3 Structure

The Arndt scheme for the classification of Ni-Cu sulphide deposits (Arndt et al., 2005; Arndt et al., 2008) uses morphology to distinguish deposit types (Fig. 1.7). ‘Type I’ structures are basal units which occur below an intrusion or flow, typically in depressions. These include ‘Type Ia’, which are layers of massive sulphide at the base of the intrusion, whereas ‘Type Ib’ and ‘Type Ic’ are veins and sills intruded into country rock and igneous host rock respectively.

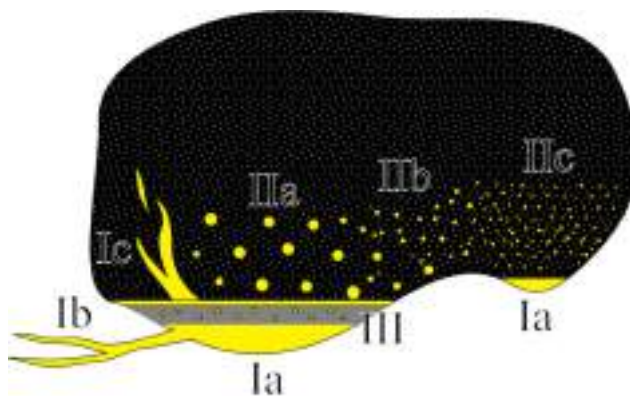


Figure 1.7 – Diagrammatic cartoon representing the principal deposit structural classes of Arndt et al. (2005).

‘Type II’ structures are disseminated ore minerals throughout the host, with IIa being coarse-medium disseminations, IIb being fine disseminations and IIc being very fine disseminations. ‘Type III’ structures are layers or disseminations within specific layers in a layered igneous intrusion, particularly those associated with chromite layers. It is debated whether the PGE minerals found in chromite layers, such as those in the Bushveld complex, are associated with magmatic sulphides but recent findings strongly suggest that they are and therefore have a valid place in this classification (Godel et al., 2010).

Although these structures are presented in an intrusive style they can also be extrusive, with a common deposit style being basal layers forming in depressions and channels cut by komatiite flows.

1.5.4 Settings

Typically Ni-Cu-PGE hosts arise from mafic/ultramafic melts found in continental settings, where the depth of melting was sufficient to produce a large degree of partial melting (1.4.1). Continental rifts or failed rifts along with Archaean/Proterozoic greenstone belts are typical settings. The Sudbury deposits of Canada are an exception and were formed by flash melting following a bolide impact and are therefore independent of tectonic setting (Naldrett, 2004).

1.6 Stable isotope geochemistry applied to ore deposits

A brief summary of the principal aspects of isotope geochemistry that are relevant to this project is provided below.

1.6.1 Overview

There are several effects that fractionate stable isotopes including: equilibrium fractionation, kinetic fractionation, diffusion and mass independent fractionation (Hoefs, 2008). Of these equilibrium fractionation and kinetic fractionation are the most important. The field of stable isotope geochemistry was established as a method of determining temperature of formation of carbonates (Urey, 1947).

1.6.1.1 Equilibrium fractionation

Equilibrium fractionation of isotopes is the process of separation of isotopes during chemical equilibrium between phases. In most cases pertinent to geology this is due to differences in vibrational energy between heavier isotopes and lighter ones. The bond strength within a molecule will vary with lower energy bonds between heavier isotopes being more easily broken. The heavy isotope will generally be concentrated in the phase in which it is most strongly bound. An equilibrium constant can be calculated for various systems (Bigeleisen and Mayer, 1947) and in geological cases this usually has a strong dependence on temperature. As bond strengths generally converge at higher temperatures, this effect is more pronounced at lower temperatures.

When an equilibrium reaction involves a change of state such as evaporation or condensation then it is possible for the two phases to become separated immediately. This means that the reaction progresses and both the generated phase and the residual evolve as a function of the amount of residual phase remaining. This is Rayleigh fractionation and an example is the change in $\delta^{18}\text{O}$ isotopes in rainfall with distance from the vapour source. Rayleigh effects have to be considered as well as temperature effects.

1.6.1.2 Kinetic fractionation

Kinetic fractionation occurs in fast, uni-directional, incomplete reactions, typically many biologically mediated reactions. It occurs when a reaction rate is sensitive to the mass of the reactants, for a non-biological example light isotopes will generally preferentially evaporate into a gas as the velocity of lighter isotopes is higher. At higher temperatures the velocities of isotopes is higher and therefore the relative difference between isotopes is larger, hence this

fractionation has a greater effect at higher temperatures. Biologically mediated reactions usually generate large kinetic fractionations.

1.6.1.3 Mass-independent fractionation

Mass independent fractionation is not considered in this project, however it is suggested for further work. Mass independent fractionation is any isotopic fractionation where the amount of separation of isotopes is not in proportion with the mass of those isotopes. In geology these fractionations occur in photochemical reactions within the atmosphere and can be used to study the behaviour of S prior to the oxygenation of the atmosphere and the beginning of biologically controlled S isotope fractionation.

1.6.1.4 Notation

Stable isotope systems are generally expressed using delta notation.

$$\delta_A = \left(\frac{R_A}{R_{St}} - 1 \right) \cdot 10^3 (\text{‰})$$

Equation 1.2 – Delta notation where R_A is the ratio of two isotopes in phase A and R_{St} is a defined ratio of the two isotopes in a known standard. The resulting value is per mille deviations from the known standard.

1.6.2 S isotopes

Sulphur has four stable isotopes ^{32}S , ^{33}S , ^{34}S and ^{36}S . Analysis of these isotopes has long been used to resolve questions about the S cycle, historically focusing on ^{32}S and ^{34}S as they are the most abundant, and therefore relatively easy to measure. These S isotopes are heavily kinetically fractionated by biologically-mediated sulphate reduction.

$$\delta^{34}\text{S} = \left(\frac{\left(\frac{^{34}\text{S}/^{32}\text{S}}{\right)_{\text{Sample}}}{\left(\frac{^{34}\text{S}/^{32}\text{S}}{\right)_{\text{VCDT}}} - 1 \right) \cdot 10^3 (\text{‰})$$

Equation 1.3 – Where VCDT is the Vienna Canyon Diabole Troilite in which $^{34}\text{S}/^{32}\text{S} = 0.450$

Biologically mediated sulphate reduction occurs in anoxic environments where sulphate is reduced by organisms in place of O_2 . The resultant sulphide will be heavily depleted by 45 ‰ to 70 ‰. In closed systems, Raleigh fractionation will occur meaning with time sulphide forming will become heavier as the residual sulphate source becomes heavier.

Thermochemical (non-biological) sulphate reduction also occurs at higher temperatures, this can be used as a thermometer where pairs of minerals can be used to determine the temperature at which they coprecipitated, however the starting $\delta^{34}\text{S}$ must be known.

1.6.3 Ni isotopes

Ni has five stable isotopes, ^{58}Ni , ^{60}Ni , ^{61}Ni , ^{62}Ni and ^{64}Ni , with the respective abundances of 68.08 %, 26.22 %, 1.14 %, 3.63 % and 0.93 % (Gramlich et al., 1989). Four of these isotopes can be used for stable isotope analysis to trace processes (physical/chemical/biological) that fractionate Ni isotopes mass-dependently.

Stable Ni isotope analysis is a relatively novel technique but it has been used to examine marine systems, organic-rich sediments and hydrocarbon formation (Cameron and Vance, 2014; Fujii et al., 2014; Gall et al., 2013; Porter et al., 2014; Ventura et al., 2015). The technique has also been used to look at weathering of ultramafic systems to form lateritic deposits (Ratie et al., 2015) and in banded Fe formations (Wasylenki et al., 2015) and meteorites (Cook et al., 2007; Moynier et al., 2007).

Observed Ni isotope fraction occurs in the formation of sulphide from silicate magma. This fractionation is evidently mass-dependent and abiotic (Gueguen et al., 2013) occurring either at the segregation of a sulphide liquid from a silicate liquid or at the crystallisation of solid sulphide from liquid sulphide or in both situations.

1.7 Discussion

The purpose of this project is to establish a genetic model for the Sakatti deposit.

In order to create a deposit, sulphide saturation has to be reached. Therefore assuming this was the case at Sakatti, the mechanism by which sulphide saturation was achieved needs to be established. The main mechanisms for this are either contamination by crustal material or direct contamination with a sulphide-rich rock (1.4.2.3). Therefore assessing the degree of crustal contamination of the ultramafic host is fundamental. Isotopic S values in the sulphides are compared with those found in potential sulphide-rich contaminants to investigate whether direct sulphide contamination has been important. This is discussed further in 4.3.4.1.

Immiscible sulphide has to be trapped and pooled in order to form a deposit. Assessing this process will mainly rely on structural interpretation. However the structure of the deposit is poorly understood, so the use of petrology to provide insights, such as potential layering, is another principal aim of this project.

The Sakatti deposit has both disseminated mineralisation and massive mineralisation. While the disseminated ore is confined to the cumulate unit, the massive sulphides are found irrespective of the unit. The origin of the massive sulphides has been proposed to be hydrothermal veins with remobilised sulphide from the magmatic deposit, however, they could also be interpreted as 'dykes' of a pure sulphide melt such as deposit style Ib and Ic in 1.5.3. Therefore the determination of the magmatic or hydrothermal nature of the massive sulphides is a third principal aim of this project.

2 The Geology of Northern Finland

An understanding of the regional geology of the Sakatti deposit informs what processes can be expected in the genesis and subsequent alteration of the Sakatti deposit. The deposit is located in Lapland in Finland in the centre of the Fennoscandian Shield. It is in the Palaeoproterozoic Central Lapland Greenstone Belt (CLGB) within the, mostly Archaean, Karelian craton.

2.1 Tectonic History of the Fennoscandian Shield

2.1.1 Archaean

The main Archaean terranes of the Fennoscandian shield are the large Karelian craton, the Norbotten craton and the accreted terranes of the Lapland-Kola orogen, also referred to as the Kola craton (Lahtinen et al., 2005). The Karelian craton is divided into three complexes: the central Karelian, Iisalmi and Pudasjärvi (Weihed et al., 2005). A large part of the Archaean geology of the Karelian craton is granitoid and gneisses, the oldest being 3.5 Ga in the Pudasjärvi complex (Mutanen and Huhma, 2003), with the majority forming between 2.75-2.6 Ga (Sorjonen-Ward and Luukkonen, 2005). Four generations of greenstone belts suggest a complex Archaean history particularly the Oijarvi, Suomussalmi-Kuhmo-Tipasjärvi, Nunnanlahti and Hattu-Kovero belts in the Finnish part of the Karelian craton (Sorjonen-Ward and Luukkonen, 2005) and the Vedlozero-Segozero, South Vygozero, Sumozero-Kenozero in the Russian part of the Karelian craton (Bogdanov, 1987; Slabunov et al., 2006). The earliest crustal nucleus is the 3.5-3.1 Ga Vodlozero terrane in the Russian part of the Karelian craton around which new crust accreted in the form of the Vedlozero-Segozero greenstone belt (Slabunov et al., 2006). By 2.75 Ga much of the Archaean Karelian craton had formed. The fragmentary nature of the remaining Archaean crust means that a coherent model for the accretion of these terranes has not been produced (Rämö et al., 2005; Sorjonen-Ward and Luukkonen, 2005).

The Suomussalmi-Kuhmo-Tipasjärvi greenstone belt is the most studied of these Archaean belts (Halkoaho et al., 2000; Papunen et al., 1998; Piirainen, 1988; Weihed et al., 2005). It consists of a basal sequence of 2.81-2.79 Ga felsic to intermediate volcanics, overlain by tholeiites, Al-depleted komatiites including olivine cumulate bodies interpreted as channel facies, basalts and finally volcanoclastic deposits (Weihed et al., 2005). The sequence is cut by granodiorites and tonalities varying from 2.75 Ga to 2.69 Ga in age (Luukkonen, 1992).

2.1.2 Palaeoproterozoic

The Palaeoproterozoic tectonic history of the Fennoscandian Shield is split into a period of rifting and continental break-up (~2.5-2.1 Ga) followed by a succession of collisions and micro-continent accretion (~2.1-1.7 Ga) generally referred to as the Svecofennian or Svecokarelian orogeny (Lahtinen et al., 2005).

2.1.2.1 Rifting of a supercontinent

Around 2.7 Ga large amounts of new continental crust were formed and accreted into a supercontinent (Rämö et al., 2005). This mass began extensive rifting at ~2.44 Ga, possibly initiated by a mantle plume, which is marked by the intrusion of over 20 coeval layered mafic intrusions, including the Koitelainen intrusion (2.4.4), the Portimo complex (Iljina and Hanski, 2005), the Penikat intrusion (Alapieti and Lahtinen, 1986) and the Koillismaa-Narankavaara complex (Karinen, 2010). This rifting continued until ~1.98 Ga and resulted in considerable mafic volcanism and the formation of Palaeoproterozoic greenstone belts (Rämö et al., 2005), including the Central Lapland Greenstone Belt (CLGB). The CLGB is in the Karelian craton, between the Pudasjärvi complex and the central Karelian craton. The sediments and volcanics of the CLGB, which formed during this ~2.44-1.98 Ga rifting, are interpreted as basinal rather than a large-scale oceanic setting (Hanski and Huhma, 2005). This basin was closed during the subsequent Svecofennian orogeny.

2.1.2.2 Svecofennian/Svecokarelian orogeny

The Svecofennian orogeny is split into separate events (the Lapland-Kola, Lapland-Savo, Fennian, Svecobaltic and Nordic orogenies; see figure and table 2.1) that represent the suturing of each of the micro-continent collisions following a tectonic model outlined by Lahtinen et al. (2005). This interpretation is controversial with some disputing that conventional plate tectonics can be applied to the Svecofennian orogeny (Weihed et al., 2005), however it seems to be the most satisfactory explanation of the different terranes found in the Fennoscandian shield.

The first phase is the Lapland-Kola orogeny. This is an amalgamation of rifted Neo-Archaean fragments and accreted Palaeoproterozoic terranes (Daly et al., 2006) on the north side of the Karelian craton. The following Lapland-Savo orogeny is the collision of the Archaean Norbotton and Bothnia microcontinents and the Palaeoproterozoic Keitele microcontinent with the south and west of the Karelian craton (Fig. 2.1). The Norbotton craton carried accreted Palaeoproterozoic arcs such as Knaften arc. It also emplaced the Kittilä allochthon onto the Karelian craton (2.4.2). The subsequent orogenies (Fennian, Svecobaltic and Nordic, see table

ocean terranes, on the western margin of the Fennoscandian shield as Laurentia collided with Baltica.

Age (Ga)	Orogeny/Event	Sub-orogeny	Principal microcontinents accreted onto Karelian craton	Direction of collision	Effect on Karelian craton
0.4	Caledonian orogeny			From north and west	Deformation and magmatism on the northern and western side of the Karelian craton.
1.15-0.9	Sveconorwegian orogeny	Multiple		From south and west	Reworking of the Gothian terranes, limited effect on Karelian craton.
1.73-1.55	Gothian orogeny	Multiple		From south and west	Western margin of Fennoscandian shield affected but extent of penetration to Karelian craton is limited.
1.79-1.77	Post orogenic collapse				Migmatisation, granite emplacement in the Central Lapland Granitoid Belt
1.82-1.79	Svecofennian/Svecokarelian orogeny	Nordic orogeny	Amazonia	From west	N-S deformation of high temperature, low-moderate pressure.
1.84-1.80		Svecobaltic orogeny	Sarmantia	Obliquely from south	All areas north of the Bergslagen microcontinent (including Karelian craton) stable, no magmatism
1.89-1.87		Fennian orogeny	Bergslagen and Uusimaa	From south	Created fold and thrust belt across Keitele microcontinent into the Karelian craton. May have closed rift and failed rift basins in the north of the Karelian craton, such as the Central Lapland Greenstone Belt (CGLB).
1.93-1.89		Lapland-Savo orogeny	Norbotton, Keitele and Bothnia microcontinents	From south and west	The Kittilä allochthon emplaced onto the Central Lapland Greenstone Belt in the Kittilä greenstone area. Accretion of several island arcs onto the edges of the Karelian craton. Orogenic collapse inhibited by the Fennian orogeny, resulting in extensive wet and dry granitoid magmatism, resulting in granite domains such as the Central Lapland Granitoid Complex (CGLC).
1.96-1.90		Lapland-Kola orogeny	Assorted Archaean and Palaeoproterozoic terranes including the Murmansk craton, Kola province and Inari terrane	From north	Kola region accreted onto the north side of the Karelian craton. Extensive deformation and metamorphism of the early continent.
2.5-2.1		Rifting of the Karelian craton			
3.2-2.6	Accretion of the Karelian craton				The Karelian craton is assembled from small crustal nuclei.

Table 2.1 – Timeline of accretion focusing on the subdivisions of the Svecofennian orogeny (Åhäll and Larson, 2000; Korja et al., 2006; Lahtinen et al., 2005; Vaasjoki and Sipila, 2001). Coloured to match Fig. 2.1

2.2 The Karelian craton

The large Karelian domain is the nucleus of the Fennoscandian shield with an array of microcontinents accreting onto this core. It is comprised of Archaean basement rocks with Palaeoproterozoic supracrustal rocks, the latter category including the CLGB.

The Archaean rocks of the Karelian craton are granodiorite and monzogranites, with gneiss complexes, and greenstone and metasedimentary belts between plutons (Sorjonen-Ward and Luukkonen, 2005). The majority of exposed Karelian Archaean rock in Finland is granitic gneisses. The gneissic basement which underlies the CLGB is termed the Pomokaira terrane and is exposed as inliers such as the Möykkelmä dome and the Tojottamanselkä dome (Fig. 2.4). Multiple studies analysing zircons from the Tojottamanselkä dome provide an age of ~3.1 Ga (Lauri et al., 2012; Sorjonen-Ward and Luukkonen, 2005). Archaean greenstone belts are mainly found in the south of Finland, trending north-south.

Palaeoproterozoic rocks exist across the Karelian craton as both supracrustal volcanic and sedimentary successions and both mafic and felsic intrusions. In the north of Finland the largest areas of Palaeoproterozoic rocks are the CLGB and the Central Lapland Granitoid Complex (CLGC; see Figure 2.2). In the southern part of the Karelian craton in Finland the supracrustal rocks occur mainly as fragmented basins (Lahtinen et al., 2009).

The CLGB is a succession of sediments and volcanics formed from ~2.5-1.9 Ga in the rifting event which preceded the Svecofennian orogeny (2.1.2.1). The succession conforms to rifting models, with a deepening of sedimentary facies with decreasing age. However the timescale of 600 million years is not comparable with modern day rift systems. The CLGB hosts the Sakatti deposit and so the geology is discussed in detail in section 2.3.

The CLGC is a 'late-orogenic' granite intrusion ~1.8 Ga (Nironen, 2005) to the south of the CLGB. It is thought to have occurred as a result of the Fennian orogeny impeding the Lapland-Savo orogenic collapse, and the subsequent Fennian orogenic collapse.

2.3 The Central Lapland Greenstone Belt

The CLGB sits on the Karelian craton in the core of the Fennoscandian shield. The CLGB in Finland focuses around the Kittilä greenstone area, the Sodankylä schist belt and the Salla greenstone (Fig. 2.2). The term CLGB is occasionally used to refer to just these three central areas, however it can also be used to cover the Kuusamo schist area, the Peräpohja schist belt and even the Karasjok belt in northern Norway. The Sakatti deposit is located in the Sodankylä schist area, near to the Kittilä greenstone area. The same lithologies are found in the three central areas and can be traced from the Salla greenstone area (mainly the older Salla, Onkamo and Kuusamo groups (Manninen and Huhma, 2001)) through the Sodankylä schist area (mainly the intermediate Sodankylä and Savukoski groups (Räsänen and Huhma, 2001; Saverikko, 1987) to the Kittilä greenstone area (mainly the younger Kittilä, Lainio and Kumpu groups; (Rastas et al., 2001)).

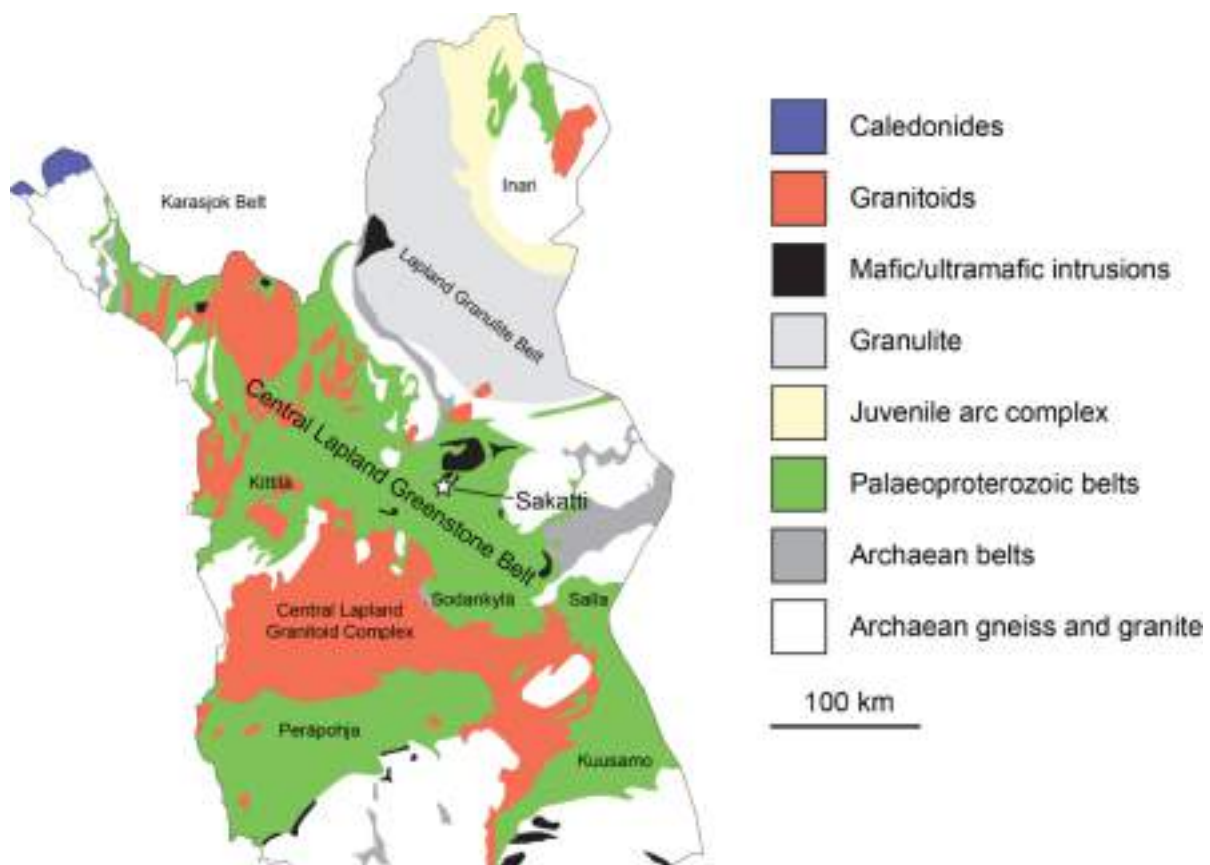


Figure 2.2 – Simplified geological map of northern Finland showing the main rock-forming events and the five areas of the CLGB (after Hanski and Huhma, 2005).

2.4 Local Geology – The Sodankylä area

The Sakatti deposit is in the north of the Sodankylä schist area (Fig. 2.4). Because of the lack of exposed rock in this area of Finland the geological maps rely heavily on geophysical data and so cannot be treated as wholly reliable. The current geological map shows the location of the Sakatti deposit as being a mafic sill within the Sodankylä quartzites (Fig. 2.4), however this is not compatible with the lithologies seen at Sakatti.

The majority of the stratigraphy of the Sodankylä area is the Lapponi supergroup which sits upon Archaean basement, exposed in small inliers. There is also a large layered mafic intrusion, the Koitelainen intrusion, a suite of intruded mafic-ultramafic dykes and sills and the Kevitsa ultramafic-mafic intrusion (Hanski and Huhma, 2005).

2.4.1 The Lapponi supergroup

The Lapponi supergroup has been subdivided into five groups: the Salla group, the Onkamo group, the Sodankylä group, the Savukoski group and the Kittilä group (Lehtonen et al., 1998). The first four of these groups are the most important and are all present in the Sodankylä area (Figure 2.3) while the Kittilä group is only found further to the west. The Salla is at the base of the supergroup, found directly on Archaean basement, followed by the komatiitic Onkamo volcanics. These are overlain by the shallow marine quartzites of the Sodankylä group then the sulphide bearing phyllites of the lower Savukoski group (the Matarakoski formation). The stratigraphically highest part of the Lapponi supergroup in the Sodankylä area is the extensive komatiitic volcanics of the upper part of the Savukoski group (the Sattasvaara formation). Both the Onkamo and Savukoski groups have extensive komatiitic volcanism (Fig. 2.3). The whole sequence is thought to be a widening rift from ~2.5-1.9 Ga which was curtailed and closed by the Svecofennian orogeny (Hanski and Huhma, 2005). This interpretation is not compatible with the timescale of modern day plate tectonics, where the partial opening of a rift does not last 600 Ma.

The overlying Kittilä group is a 6 km deep predominantly tholeiitic volcanic pile which is thought to be allochthonous, emplaced during the Lapland-Savo orogeny (Hanski and Huhma, 2005).

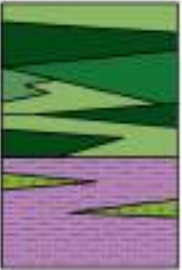
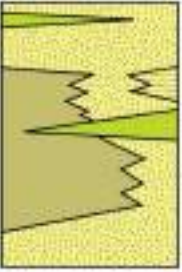


Group	Lithology	Setting	Age	Location
Savukoski	 <p><i>Sattasvaara formation</i> - Extensive ultramafic volcanics shown to be a komatiite-picrite association (Hanski et al., 2001a). In the vicinity of Sodankylä (the Sattasvaara area) komatiites are dominant. Spinifex textures have only identified very rarely (Räsänen, 1996, cited in Hanski et al., 2001). Interlayered with the komatiites are komatiitic basalts and high Mg basalts.</p> <p><i>Matarakoski formation</i> - Meta-phyllites and black schists interspersed with mafic volcanics and tuffs, chemically Fe-tholeiites (Lehtonen et al., 1998). The black schists are sulphide bearing, typically with abundant pyrite.</p>	The Sattasvaara formation is a resumption of volcanism. The Matarakoski formation is a deepening of marine facies, possibly a further widening rift.	Indoect 2056 ± 25 Ma at Jeesjärvi (Hanski et al., 2001a) Minimum, Kevissa, 2058 ± 4 Ma (Mutanen and Huhma, 2001)	Both formations follow a broad E-W trend north of Sodankylä and immediately north of Sakatti.
Sodankylä	 <p>Sedimentary group, mainly quartzite and mica schist. Orthoquartzites, sericite quartzites and mica schist with minor carbonate and mafic metavolcanic lenses. Fuchsite, Cr-bearing mica, is abundant often staining the unit characteristically green. Sedimentary structures are abundant such as graded and cross bedding, herringbone structures and mud cracks (Lehtonen et al., 1998). Stromatolitic structures have been identified in the carbonate (Hanski and Huhma, 2005). Felsic layers within the unit have been identified as lahars and ignimbrites (Lehtonen et al., 1998), however subsequent zircon dating has shown them to be Archaean age with unknown origin (Räsänen and Huhma, 2001).</p>	A hiatus of volcanic activity. Shallow marine facies could be associated with a widening rift setting.	Minimum ultramafic sills -2200 Ma (Hanski and Huhma, 2005)	The Sodankylä group is the most common lithology in the Sodankylä area.
Onkamo	 <p>Alternating mafic and ultramafic units, ultramafic dominated at the base and mafic dominated at the top.</p> <p>Top unit is basalt dominated, mainly intercalated tuffs and lavas, with occasional amygdaloidal andesite flows and ultramafic tuffs and lavas.</p> <p>Lower unit is ultramafic. It is best classified as a komatiitic basalt as the MgO contents ranges from 11.7-21.4%, averaging 15.5% (Räsänen et al., 1989). At the Möykkelmä dome the unit is dominantly volcanoclastic meaning it contains the only komatiite with convincing pyroclastic features that has been reported (Barnes and Lesher, 2008). The basal volcanic breccia contains clasts of the Archaean gneiss basement (Hanski and Huhma, 2005).</p>	Erupted directly onto Archaean crust and on the Salla group.	Possible max, Koitelainen, 2439 ± 3 Ma Coeval Venery suite 2449 ± 35 Ma or 2416 ± 34 Ma (Puchtel et al., 1997)	The Onkamo group is present as inliers in the Sodankylä group, particularly the Möykkelmä dome. It is also found atop the Salla group around Koitelainen.
Salla	 <p>A series of extensively metamorphosed andesite, dacite and rhyolite lavas and volcanoclastics. Generally contain abundant amygdalae. Microstructures in tuffs and the absence of a sedimentary component suggests that, in the Sodankylä area, this group was mostly erupted sub-aerially. Geochemical studies have shown the andesites and dacites most likely derive from the same tholeiitic parent subject to crustal contamination. However the rhyolites probably derive from a different source (Lehtonen et al., 1998).</p>	Erupted directly onto Archaean crust. Possibly early rifting of the proposed supercontinent.	2438 ± 14 Ma (Manninen and Huhma, 2001) 2438 ± 11 Ma (Räsänen and Huhma, 2001) At least some older than Koitelainen 2439 ± 3 Ma	In the Sodankylä area, the Salla group is only present around the Koitelainen intrusion.

Figure 2.3 – Lithological characteristics of the Salla, Onkamo, Sodankylä and Savukoski groups of the Lapponi supergroup. The column is diagrammatic to assist with interpretation of the geological map in figure 2.4 (Hanski et al., 2001a; Hanski and Huhma, 2005; Manninen and Huhma, 2001; Mutanen and Huhma, 2001; Puchtel et al., 1997; Räsänen and Huhma, 2001).

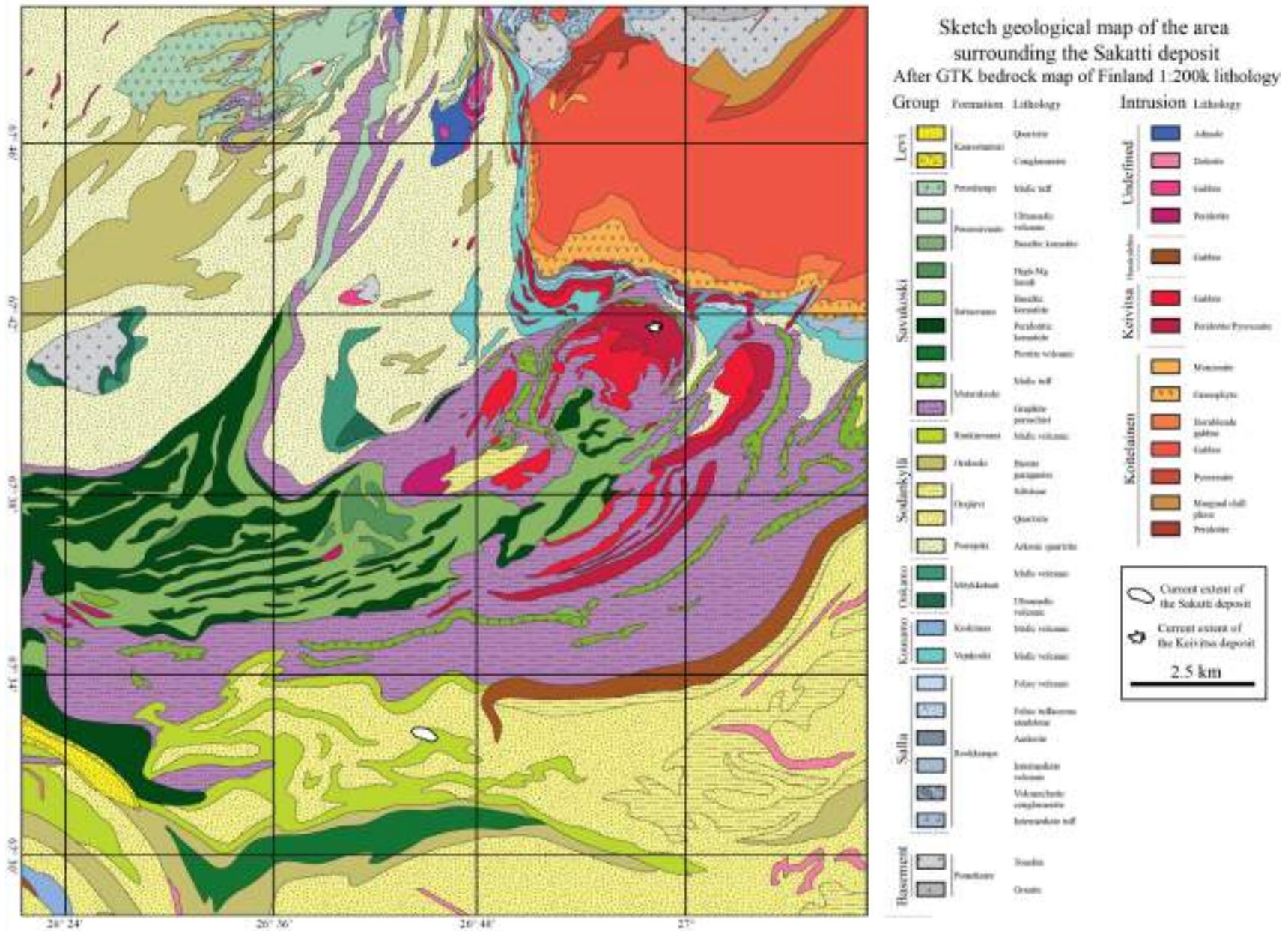


Figure 2.4 – Geological map of the CLGB in the Sodankylä area, after the publicly available GTK bedrock map.

2.4.2 Higher stratigraphy

The Lainio and Kumpu groups are later units that occurred following a hiatus after formation of the rest of the CLGB. Despite being initially classed as separate units (Lehtonen et al., 1998) it has since been shown that they are very similar and should not be distinguished (Hanski and Huhma, 2005). The group is sedimentary, mostly conglomerates with interbedded greywacke. The conglomerates are formed from a wide array of clasts from the lower successions of the CLGB. The facies is interpreted as possible alluvial fan or braided river deposits (Hanski and Huhma, 2005). Age dating and comparisons of clasts in the conglomerates with known units has shown that the Lainio and Kumpu group was most likely deposited after 1.88 Ga, post or during the waning stages of the Fennian orogeny.

2.4.3 Metamorphism of the CLGB

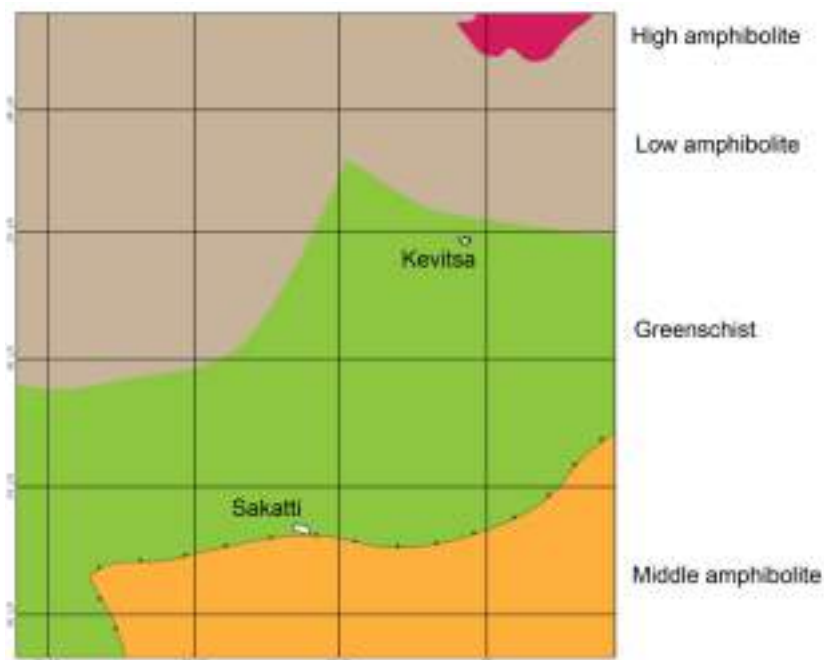


Figure 2.5 – Duplicate map of Fig. 2.4 showing metamorphic facies in the Sakatti area, after the publically available GTK metamorphic map and Hölttä et al. (2007). The Tojottamanselkä basement inlier within the Koitelainen intrusion exhibits high amphibolite facies while the Sakatti deposit is in greenschist facies, immediately underlain by a thrust in the Sodankylä quartzites and middle amphibolite facies to the south.

The Central Lapland Greenstone Belt is bordered by the Central Lapland Granitoid Complex to the south and the Lapland Granulite Belt to the north (Fig. 2.2). The area has undergone extensive metamorphism throughout its tectonic history, primarily during the Svecofennian orogeny (Table 2.1).

The early structural evolution of the CLGB consists of sub-horizontal folds and foliations (D1+D2) created by northern tectonic movement at potentially 1.88-1.87 Ga (Hölttä et al., 2007). This stage probably initiated a series of east-west thrust faults. Later deformation (D3) is

considerably more variable and complex with a wide array of fold vergences and reactivating the earlier thrusts. (Hölttä et al., 2007).

To the south of the Sakatti deposit a complex thrust duplex has been identified (Evins and Laajoki, 2002). Sakatti exists above a thrust fault that places the deposit above higher grade Sodankylä quartzites. This thrust cuts the base of the deposit, therefore post-dating it, and forms part of the footwall. This thrust can be considered as part of the duplex process associated with northern tectonic movement of D1 deformation, although it also probably reactivated in later stages of deformation.

The Sakatti deposit itself is located within a zone of greenschist metamorphism (Fig. 2.5) that is one of the lowest grade metamorphic areas in the Central Lapland Greenstone Belt. Rocks in this zone, termed zone IV by Hölttä et al. (2007), have preserved magmatic textures and the ultramafic rocks present also have preserved magmatic mineralogy (as seen at Sakatti).

Central Lapland has undergone extensive regional metasomatism resulting in scapolite occurrences throughout the CLGB (Frietsch et al., 1997). The source of this scapolitisation has been suggested to have occurred from brines generated by fluids mobilised from basins with evaporitic sequences (Frietsch et al., 1997).

2.4.4 The Koitelainen Layered Igneous Intrusion

The Koitelainen intrusion is a round intrusion ~30 x 25 km across and with an estimated maximum thickness of 3200 m (Mutanen, 1997). It appears to have intruded at the contact between the Salla group and the underlying Archaean basement gneiss, which is exposed in the centre of the anticlinal intrusion. Koitelainen has been dated at 2439 ± 3 Ma (Mutanen and Huhma, 2001) in the upper suite. The lower suite has not been dated.

The Koitelainen intrusion is a layered mafic intrusion and hosts small PGE reef-style mineralisation. It is comparable with 20 layered mafic intrusion of a similar age across Finland including Portimo, Penikat, Akanvaara and Koillismaa. Koitelainen is the closest of these to Sakatti.

The stratigraphy of the Koitelainen intrusion is contentious and had been categorised into upper, main and lower zones all resulting from one intrusive event (Mutanen, 1997), however it has since been shown that part of the lower zone is in fact an earlier phase of intrusion termed the lower suite (Hanski et al., 2001b).

2.4.4.1 The lower suite

The base of the lower suite (Fig. 2.6) is cumulate peridotites including dunite, which grades upwards into clinopyroxene-dominated pyroxenites followed by gabbros and then monzodiorites (Hanski et al., 2001b). This layered series can be over 600 m thick and is interpreted as a separate earlier batch of magma as it is texturally and lithologically distinct from the main Koitelainen intrusion (Hanski et al., 2001b). It is the only place where ultramafic cumulates are found. It is also referred to as an earlier mafic sill and a pre-Koitelainen intrusion (Latypov et al., 2011) and therefore left out of any models interpreting the formation of the Koitelainen intrusion and should not be considered a part of the intrusion. The forsterite content of the olivine decreases upwards from 84.5% to 77.0% in the peridotite and pyroxenite, showing an evolution of the parental magma up the layered series. Unfortunately no direct dating of the lower suite can be found in the literature. The contact between the upper and lower suite is not exposed and has not been intersected by drilling.

2.4.4.2 The upper suite

This is the main Koitelainen intrusion and it is petrologically quite distinct from the lower suite (Fig. 2.6). The less than 200 m thick base of the unit has been called a microgabbro and a pigeonite gabbro with a chilled lower margin on the Archaean gneiss. The lower margin has been identified as a marginal reversal series (Latypov et al., 2011) meaning that it becomes more primitive upwards, contrasting with the traditional overlying layered series.

The basal pigeonite gabbro is overlain by an orthopyroxenite that hosts the 'lower chromite' reefs over 40-60 m (Hanski et al., 2001b). The pyroxenite is mainly cumulus orthopyroxene and chromite with intercumulus plagioclase, clinopyroxene and phlogopite (Mutanen, 1997).

The orthopyroxenite is overlain by a thick sequence of noritic gabbros. It hosts two thin ultramafic interlayers near the base, the lowest hosting a 5 cm chromite band termed the 'middle chromite' (Mutanen, 1997). Abundant unusual accessory minerals, such as chlorapatite, zircon, baddeleyite and galena, strongly imply contamination of the melt as the cause of these layers. The noritic gabbro itself is mainly mesocumulates of plagioclase, orthopyroxene and clinopyroxene.

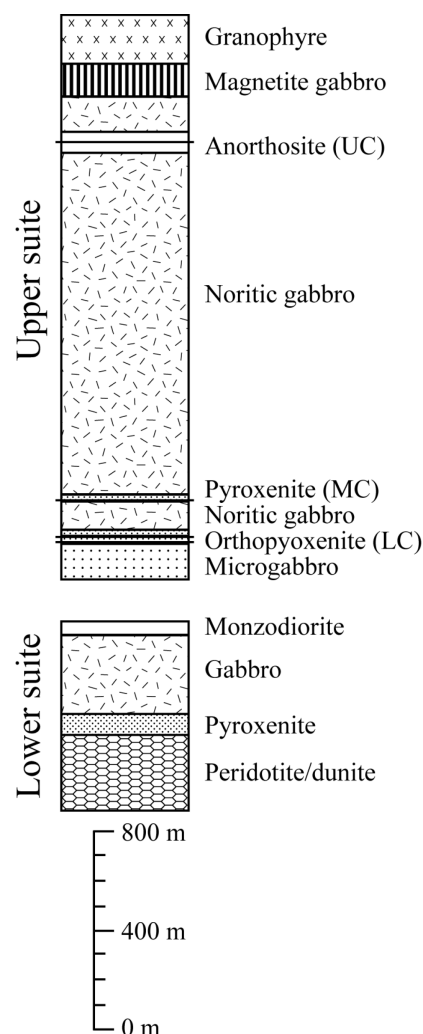


Figure 2.6 – Simplified stratigraphy of the Koitelainen intrusion (Hanski et al., 2001b).

Above the noritic gabbro is a 40 m thick anorthosite, which contains the 1-2 m thick 'upper chromite' reef, overlain by interlayered gabbros and anorthosites, with decreasing amounts of anorthosite upwards. This is topped by a V-rich magnetite gabbro and the final unit is a granophyre which reaches up to 400 m (Hanski et al., 2001b).

2.4.4.3 Metamorphism and alteration of the Koitelainen intrusion

The Koitelainen intrusion reached middle amphibolite facies metamorphism mostly replacing the primary silicate assemblages in the upper part, although in the lower part the ultramafic rocks have survived with their primary mineralogy largely intact (Hanski et al., 2001b).

During regional metamorphism the Koitelainen behaved like a large unyielding block and as a result has an array of lithologies piled up on its flanks. These areas are complex and lacking in exposure but provide a substantial source of information about the volcano-sedimentary stratigraphy of the CLGB.

2.4.5 The Kevitsa-Satosvaara Intrusion

The Kevitsa-Satosvaara intrusion comprises two separate areas of intrusive ultramafic-mafic rocks. These are suggested to be the same intrusion separated by faulting (Mutanen, 1997). The Kevitsa part of the intrusion hosts a low grade disseminated Cu-Ni-PGE deposit, the Kevitsansarvi deposit, discovered by the Geological Survey of Finland (GTK) and currently being developed by First Quantum Minerals Ltd.

The Kevitsa part is a semi-circular structure, between 5-6 km across, and the Satosvaara part is more linear, roughly 8 km long and 2 km wide. The Satosvaara part is thought to be higher up the cumulate succession than Kevitsa, having been lowered by 2-3 km to its present height (Mutanen, 1997).

Dating of skeletal zircon grains in the fresh pyroxenite from the Kevitsa intrusion has given an age of 2058 ± 4 Ma (Mutanen and Huhma, 2001). These zircons have been shown not to be inherited due to their skeletal nature.

2.4.5.1 Marginal zone

This is a small chill zone at the base of the intrusion, between 0-8 m thick. It is a microgabbro which grades rapidly upwards into cumulates, becoming an olivine pyroxenite (Mutanen, 1997). The microgabbro as a whole shows extensive contamination, in places bearing significant quartz.

2.4.5.2 Ultramafic zone

This zone is up to and possibly exceeding 2 km thick. It hosts the Kevitsansarvi mineral deposit. The microgabbro of the marginal zone grades into a pyroxene-olivine cumulate with intercumulus plagioclase. This transition can be 40 m thick and has abundant high-U zircon from contamination (Mutanen, 1997).

The main ultramafic zone is an olivine-clinopyroxene-orthopyroxene-magnetite cumulate with intercumulus hornblende and biotite and smaller amounts of plagioclase and sulphides. Olivine constitutes ~15-25% of the rock (Mutanen, 1997) meaning that the rocks are classified as olivine websterites. The olivine is generally between 75-85% forsterite. The olivine in the Ni-PGE ore type has an exceptionally high Ni content, up to 1.7% Ni (Mutanen, 1997; Yang et al., 2013). Olivines often have clinopyroxene inclusions indicating that clinopyroxene was forming simultaneously or prior to olivine formation.

Pyroxene and olivine shows reverse fractionation, increasing in magnesium content up to the Ni-PGE ore layer, after which magnesium content decreases upwards (Mutanen, 1997). Orthopyroxene occurs mostly as oikocrysts with clinopyroxene, olivine and minor plagioclase inclusions, indicating orthopyroxene formed later in the crystallisation sequence.

2.4.5.3 Gabbroic zone

The gabbroic zone is an unlayered unit above the ultramafic zone. It is principally pyroxene gabbro, ferrogabbro and magnetite gabbro. The unit exceeds 500 m in thickness and occasionally contains rafts of pelitic hornfels and minor komatiites (Mutanen, 1997).

2.4.5.4 Kevitsansarvi Cu-Ni-PGE-Au deposit

The Kevitsansarvi ore deposit is a low grade disseminated deposit found at several levels in the Kevitsa intrusion. Sulphides within the Kevitsa intrusion have been classified into the following five categories.

i. False ore

The 'false ore' type is a mineralised cumulate rich in disseminated pyrite and pyrrhotite generally better looking than the regular ore. However, it has very low Ni, typically >0.1%, and PGE is proportional to the Ni grade (Mutanen, 1997). Sulphide mantled orthopyroxene is a diagnostic characteristic of the false ore. This is the most abundant sulphide mineralisation in the Kevitsa intrusion.

ii. Regular ore

The 'regular ore' type is the bulk of the Kevitsansarvi mineral deposit. The sulphide is pyrrhotite and pentlandite, typically 4-7% Ni and good ore contains 0.5-1 ppm PGE+Au (Mutanen, 1997). It is a similar disseminated style to the false ore type and can be heterogeneous over hundreds of metres.

iii. Transitional ore

This ore type is a transition between the regular ore type and the Ni-PGE type. It has a lower sulphide content which is richer in Ni (15-23%), consequently more dominated by pentlandite. It is found at higher levels in the deposit where the regular ore meets the Ni-PGE type (Mutanen, 1997).

iv. Ni-PGE type ore

This ore has very low sulphide content which is very rich in Ni (40-60%) in the form of pentlandite. It also has the highest PGE grades which do not correlate with S contents (Mutanen, 1997). The PGE minerals are typically (Pt,Pd)Te₂ to (Pt,Pd)Bi₂ and it is argued that the presence of the bismuthide minerals (and evidence of PGE minerals found inside hydrous alteration minerals) suggests a post-magmatic alteration related reworking of the PGE (Gervilla and Kojonen, 2002).

v. Massive sulphide veins

Massive sulphide veins are common but they are insufficiently voluminous to be significant. They are false ore type (predominantly pyrrhotite, poor in Ni and PGE-Au) and have sharp contacts with fresh peridotite with minimal contact effects (Mutanen, 1997).

2.4.6 Gabbro-Wehrlite 2.2 Ga associations

The 'gabbro-wehrlite associations' are sills which intrude the Sodankylä group quartzites among other units. They are referred to as differentiated albite diabases in the older literature as well as karjalites and Haaskalehto-type intrusions, although gabbro-wehrlite associations is the favoured term (Hanski, 1987). There are numerous U-Pb zircon ages which closely fall between 2.1-2.2 Ga (Vuollo and Huhma, 2005). The sills are found over an area 300 by 600 km in extent, well outside the CLGB. They can be several hundred metres thick and usually are identifiable over at least several kilometres strike extent (Hanski and Huhma, 2005). They are strongly layered, with gabbro at the top down to olivine-clinopyroxene (wehrlite) cumulates at

the base. The wehrlite cumulates may contain orthopyroxene but in very minor quantities. Olivine chemistry is between ~82% and 70% forsterite (Hanski and Huhma, 2005).

A large example of these sills is the Rantavaara-Särkivaara intrusion which runs east-west in close proximity to Sakatti (Fig. 2.4). It is 30 km long, 40° N dipping sill up to one kilometre thick (Mutanen, 2005). The Rantavaara gabbro is dated at 2148 ± 11 Ma using U-Pb zircon measurements (Räsänen and Huhma, 2001). The age of the Savukoski sediments is not well constrained although the use of the Rantavaara intrusion as a minimum age constraint (Lehtonen et al., 1998) is doubtful as the contact appears to indicate that intrusion may have existed first with the sediments unconformably deposited on it (Räsänen and Huhma, 2001).

The Kaikkivaltiaanlehto intrusion has been intersected by the Finnish Geological Survey below the Rantavaara-Särkivaara intrusion, although very little information is available. Very high PGE-Au grades have been suggested (Mutanen, 2005).

North of the Savukoski group but within 20 km of the Sakatti deposit the Ponostama intrusion also conforms to the occurrence of the gabbro-wehrlite sills, although it has not been directly dated (Mäkimattila, 2015). The Ponostama sill exhibits olivine with depleted (<500 ppm) Ni content, unlike Kevitsa or Sakatti, suggestion depletion by sulphide melt, although the deposit is poorly mineralised (Mäkimattila, 2015).

The Pikku-Vaiskonselkä sill is 1 km north of the Kevitsa deposit is another differentiated gabbro-wehrlite sill in the Sodankylä area and it has also not been dated (Suvanto, 2014)

2.5 Discussion

The Sakatti host rocks are ultramafic cumulates and fine-grained mafic rock. Having been intersected by drilling, their relationship to surrounding lithologies is unknown. The geology of the Sodankylä schist area features several generations of mafic/ultramafic bodies which could host Cu-Ni-PGE deposits.

A principal aim of this project is to determine whether the Sakatti deposit could be related to one of these known generations of magmatic activity. The oldest and least likely is the 2.5 Ga Koitelainen intrusion. The ~2.2 Ga gabbro-wehrlite intrusions, such as the Rantavaara intrusion, and the younger 2.06 Ga Kevitsa intrusion are magmatic events that are considerably more likely to have also resulted in an intrusion at Sakatti.

However ultramafic cumulates are also formed as lower parts of extruded komatiites. The Onkamo and Sattasvaara komatiites are both within 15 km of the Sakatti body and so these

could also be related to the same phase of activity which gave rise to the ultramafic cumulates at Sakatti.

A considerable amount of data exists on these five different ultramafic occurrences and so a large part of this project will be producing equivalent data at Sakatti and comparing them to see how the Sakatti host fits into the regional framework.

The regional metamorphism and metasomatism have affected the Sakatti deposit, although it is worth noting that the Sakatti deposit sits within a thrust block that is one of the least metamorphosed areas of the CLGB at greenschists facies (Hölttä et al., 2007).

Comparisons with Kevitsa will be an inevitable part of the project as it is a Ni-PGE deposit within 15 km of Sakatti. The controversial conclusions drawn from Kevitsa about alteration-related PGE remobilisation (Gervilla and Kojonen, 2002; Mutanen, 1997) and disputed by some (Le Vaillant et al., 2016) are tested at the Sakatti deposit. Studying the mineralogy that hosts the PGE and whether they are related to sulphide is a key aim of this project.

The Matarakoski black schists are sulphide-bearing sediments in the immediate vicinity of the Sakatti deposit. It is therefore a likely candidate for sulphide contamination of the Sakatti deposit and is tested as part of the project. Sulphur isotope data of the Matarakoski formation in the vicinity of the Kevitsa intrusion have been found in the range $\delta^{34}\text{S} +15$ to 20 (Hanski et al., 1996, cited in Hanski and Huhma, 2005).

3 Silicate geology and geochemistry

3.1 Introduction

3.1.1 Key questions

The Sakatti magmatic body hosts sulphide mineralisation and consequently must be investigated to determine the sources of S and the contained metals as well as the reasons behind the formation and concentration of a potentially economic deposit.

What is the nature of the parent melt from which the mineralisation formed?

The silicate rock hosting mineralisation is the most likely unit to have originated from the same parent melt as the sulphide mineralisation. Petrography and thorough examination of mineral chemistry can indicate whether this unit has derived from S-saturated melt and provide information about the causes of sulphide formation.

How does the deposit fit with the regional stratigraphy?

In the absence of field relationships between the deposit and units that are clearly identifiable as part of the regional stratigraphy, geochronology has been utilised as the preferred method for placing the deposit within the well constrained age ranges of units in the Central Lapland Greenstone Belt (CLGB). Both Sm/Nd and U/Pb methodologies have been attempted on the silicate host rock of the mineralisation.

Is there any layering of different pulses of magmatism coherent with mineralisation?

Closely-spaced sampling focused on particular drill holes can resolve vertical differentiation within the host rock. Cryptic layering may be identifiable only in magmatic mineral chemistry, and the optimal situation would be to provide a chemical 'fingerprints' for olivine cumulate that is below mineralisation, hosts mineralisation and is above mineralisation (Eg. Bulle and Layne, 2015).

Is there any alteration that affects mineralisation?

The nature of alteration around the mineralisation is examined petrographically and geochemically in order to determine if there is a remobilising, upgrading or downgrading effect associated with hydrothermal alteration of the deposit, such as that suggested at Kevitsa (Gervilla and Kojonen, 2002).

What is the relevance of the Aphanitic Unit?

The Aphanitic Unit is present as both the footwall and, in part, the hanging wall of the deposit and exhibits an unusual texture at the contact with the Olivine Cumulate Unit. The relationship between these two units will be examined petrographically and geochemically to determine its nature and whether it has any relevance to the processes that resulted in the formation of sulphide mineralisation.

3.1.2 Geological Setting

The Sakatti deposit is located within the Palaeoproterozoic CLGB, which extends across Lapland from northern Norway to the Finnish-Russian border. It is a complex succession containing sedimentary rocks as well as volcanic rocks ranging from komatiitic to rhyolitic in composition. The evolution of the CLGB spans around 600 Ma, starting with andesitic volcanism at ca. 2.5 Ga and ending with deposition of molasse-type coarse-clastic sediments at <1.9 Ga (Hanski and Huhma, 2005). The belt is also host to several mafic-ultramafic intrusions, having a range of ages which at the one end includes the 2439±3 Ma Koitelainen layered intrusion and at the other end includes the 2058±4 Ma Kevitsa intrusion (Mutanen and Huhma, 2001). The geology of the CLGB is described in chapter 2.

The stratigraphic level at which Sakatti has been emplaced within the CLGB has not yet been resolved as the units so far intersected do not correspond conclusively to any particular part of the CLGB succession. Regionally the deposit is surrounded by the Matarakoski Formation pelitic metasediments and the Sodankylä Group quartzites, which were deposited between ca. 2.3 and 2.06 Ga (Räsänen and Huhma, 2001). However, neither of these rock formations has been identified directly in drill core at the Sakatti deposit. For reference the Ni-Cu ore-bearing Kevitsa intrusion, which is located ca. 15-20 km NE of Sakatti, was emplaced into the mica schists and black schists of the Matarakoski Formation.

3.1.3 Deposit overview

Based on current understanding, the Sakatti deposit consists of three spatially distinct mineralised bodies of olivine cumulate named 'main body', 'north-east body' and 'south-west body' (Fig. 3.1). Mineralisation in all three is hosted within or at a basal contact of the olivine cumulate. In hand specimen, there are no discernible petrological differences between these three bodies.

The major host and wall rock units of the deposit comprise the Olivine Cumulate or Peridotite Unit, Aphanitic Unit, Mafic Suite, Breccia Unit and Volcanosedimentary or Volcaniclastic Unit. These units are defined below and their

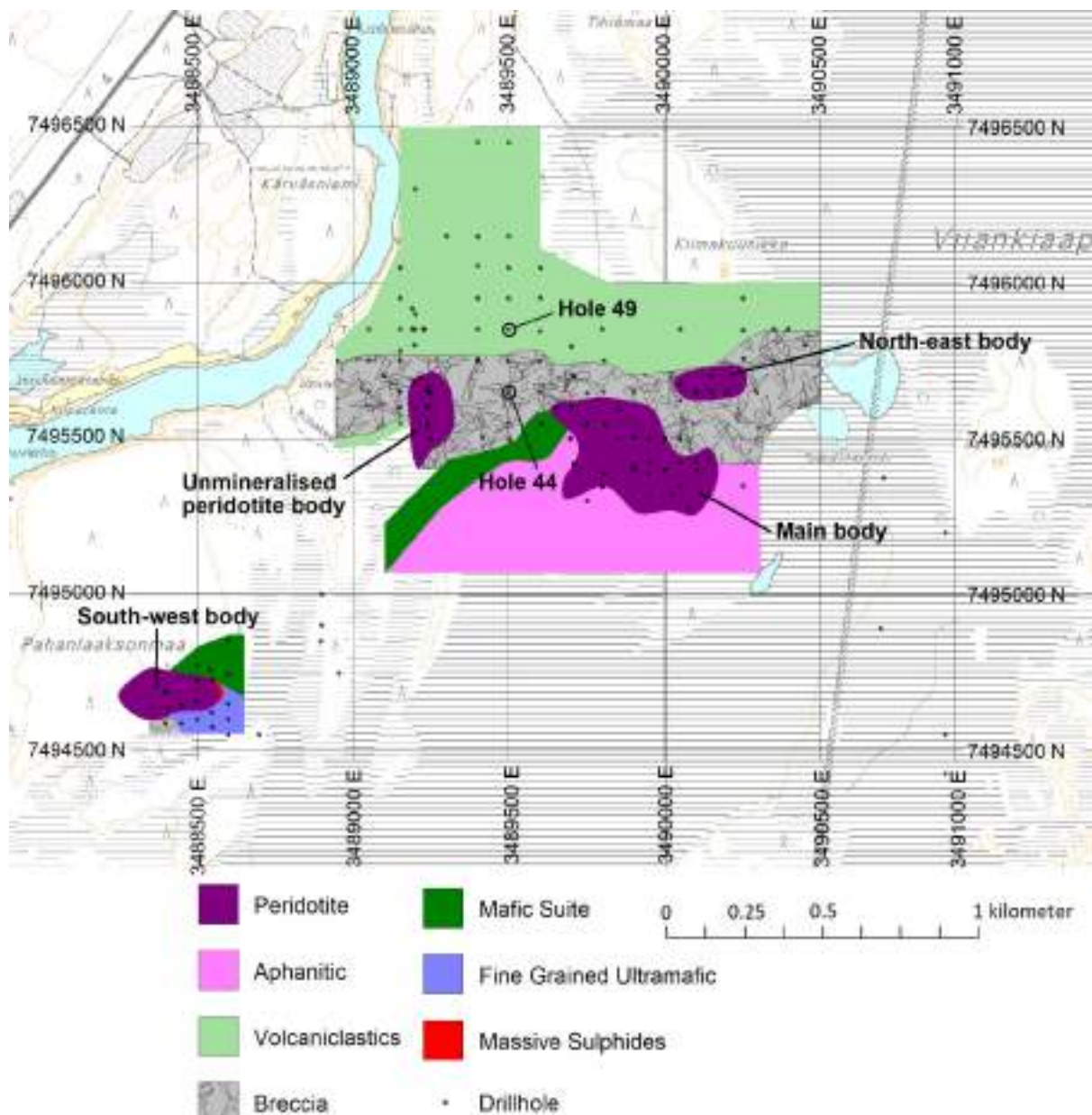


Figure 3.1 - Plan map of the Sakatti deposit showing the interpreted geology and drill hole locations (Brownscombe et al., 2015). The locations of holes 44 and 49 are marked as they were the site of the majority of silicate sampling in this project.

relationship is illustrated in figures 3.2, 3.3 and 3.4. The composition and location of these units are briefly described and their mineralogical and chemical compositions are discussed in more detail in Section 3.3.

3.1.3.1 Key lithologies

The key lithologies are presented below with the unit names that are used on site at the Sakatti exploration project. Where these names are not geologically satisfactory and alternative name is suggested.

Olivine Cumulate or Peridotite Unit

The Olivine Cumulate Unit is the principal constituent of the main cumulate body, which itself can be over 400 m thick. This is an olivine cumulate with variable oikocrystic pyroxene content and rarely minor interstitial plagioclase. Most of the unit is pervasively serpentinised, and should technically be termed a serpentinite. However, the cumulate texture is preserved therefore the rock can be considered in terms of its protolith. Textures within the main body range from adcumulate to orthocumulate with the groundmass typically also composed of serpentine with minor talc.

The *Altered Ultramafic* is a logging unit interpreted to be a talc-carbonate alteration product of the Olivine Cumulate Unit. This unit is invariably present where the Olivine Cumulate Unit is in direct contact with the overlying Breccia Unit. The *Dunite* is another logging subunit of the Olivine Cumulate Unit. It is an olivine adcumulate marked by an almost complete lack of serpentinisation and forms a continuous, discrete package at the base of the Olivine Cumulate Unit in the north-western part of the main body. Primarily in the upper part of the Olivine Cumulate Unit, the Pegmatoidal Gabbro Sub-Unit may occur. These gabbroic rocks display sharp contacts with the Olivine Cumulate Unit and comprise intersections of between 50 cm and 15 m.

Plagioclase-rich Picrite or Aphanitic Unit

The Aphanitic Unit, so named because of its grain size and likely volcanic origin, forms the hanging wall, footwall and sidewall to much of the main cumulate body, notably along the southern edge and the far western side.

Referring to a unit as aphanitic is clearly problematic as it is not an adequate rock name. This name has endured because the unit has proved difficult to classify. The mineralogical and textural features of this unit all point towards a volcanic origin.

Where it is within 50 m of the contact with the Olivine Cumulate Unit, the Aphanitic Unit exhibits an unusual texture containing injections of the Olivine Cumulate Unit. Further from the contact this texture is not present and the rocks merely show serpentine veining.

The *Footwall Mafic Rock* is a logging unit referring to what is interpreted as an alteration product of the Aphanitic Unit. The rock consists mainly of chlorite, phlogopite and talc, accompanied by carbonate vein and fracture fill.

Mafic Suite

In addition to the Aphanitic Unit, the hanging wall of the Sakatti deposit contains several other lithological units, including the Mafic Suite. It is present in the south-western part of the deposit where it occurs between the Olivine Cumulate or Aphanitic Units and the Breccia Unit. It comprises three separate logging units: the Mafic Volcanic Rock, the Scapolite-Mica Rock and the Hanging-Wall Gabbro. The Mafic Volcanic Rock is a strongly chlorite-amphibole-altered lithology that, when in close proximity to the Breccia Unit, has undergone in-situ brecciation and precipitation of matrix and vein calcite. The Scapolite-Mica Rock is a strongly foliated, almost schistose rock with a biotite matrix hosting scapolite porphyroblasts. The Hanging-Wall Gabbro comprises a series of gabbroic sills that intrude the mafic volcanic and scapolite-mica rocks but do not intrude the main cumulate body. At the contact between the scapolite-mica rock and the Aphanitic Unit, a cryptocrystalline serpentine unit is frequently present.

Breccia Unit

The Breccia Unit is a 100-300 m thick hematite-dolomite-albite-talc-altered, and exceptionally heterogeneous, polymict breccia package that lies stratigraphically above the main cumulate body. Various zones can be differentiated within the Breccia Unit, including those with predominantly albite or carbonate (calcite/dolomite) alteration, as well as polymict zones where rounded to angular clasts of talc, chlorite and quartz typically occur in a calcite matrix.

Volcano-sedimentary or Volcaniclastic Unit

The Volcano-sedimentary Unit is the stratigraphically uppermost unit in the hanging wall of the Sakatti deposit. It is a phyllite with biotite porphyroblasts and a crenulation cleavage throughout. It is interpreted as a metamorphosed volcano-sedimentary package. The thickness of this unit is at least 600 m.

Footwall units

In the eastern part of the deposit, where the Aphanitic Unit forms the primary footwall below the Olivine Cumulate Unit, a clay-rich zone, interpreted as a fault structure, is present beneath the Aphanitic Unit. In the west, this fault structure occurs directly at the base of the Olivine Cumulate Unit and has often necessitated the cessation of drilling. Beneath this fault, a strongly

laminated carbonate-rich metasediment is present. No sulphides have been observed in this metasediment.

3.1.3.2 Morphology of the Sakatti deposit

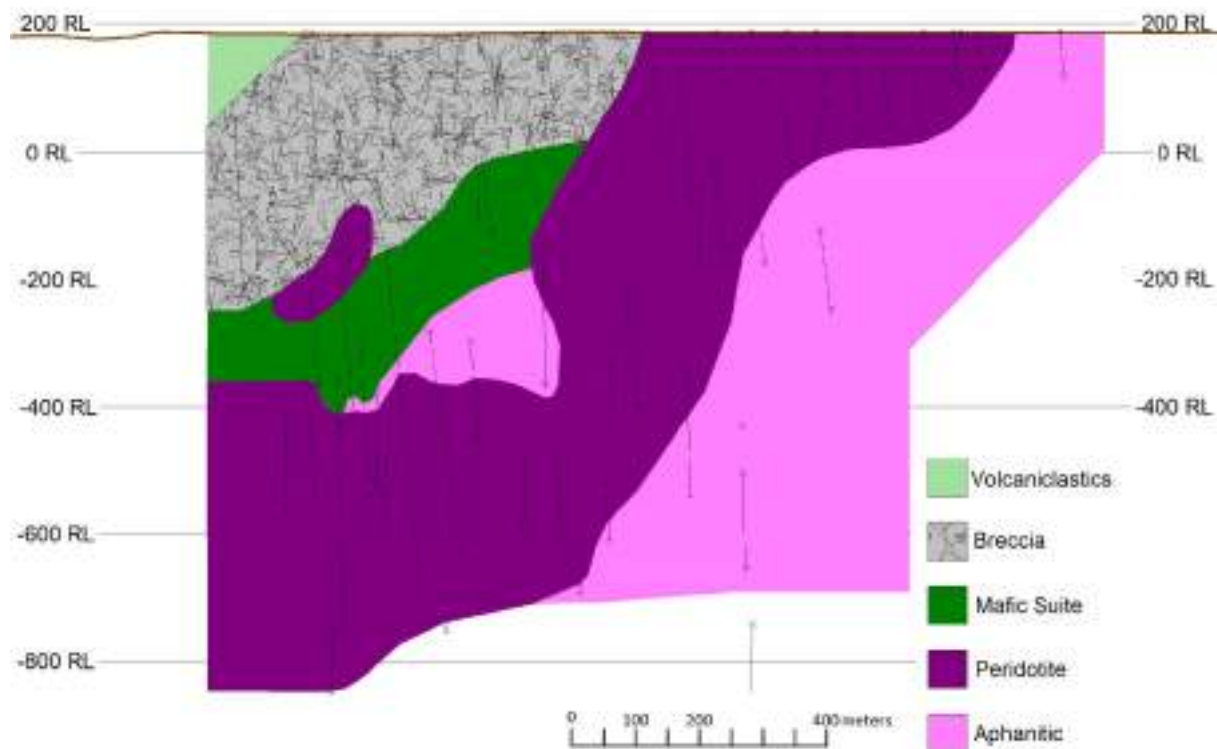


Figure 3.2 - WNW-ESE angled section, +/-25 m clipping, through the main body of the Sakatti deposit at 110° through centre point 3489600E 7495600N showing the changing geometry of the cumulate body and the crosscutting relationship of the cumulate with both the Mafic Suite and the Aphanitic Unit (Brownscombe et al., 2015).

The main cumulate body

The north-west plunging main cumulate body is by far the largest of the three cumulate bodies (Fig. 3.1), with a currently delineated extent of more than 1100 m down plunge from surface to a depth of 1220 m below surface, and a maximum thickness of more than 400 m. The cumulate body is roughly tubular, yet irregular in shape, with a shallower plunge near surface in the east and at depth in the north and west. These two shallowly plunging parts are connected by a more steeply plunging NNW-SSE orientated part of the body (Fig. 3.2).

Broadly speaking, the main cumulate body occurs stratigraphically below the Breccia Unit but above the Aphanitic Unit; however, the exact stratigraphic setting is locally more complex.

The geology in the eastern portion of the main body is relatively simple (Fig. 3.3). The Olivine Cumulate Unit sub-crops beneath the glacial till cover, and a mixture of Aphanitic Unit and altered aphanitic rocks form the southern sidewall and basal contact to the cumulate body.

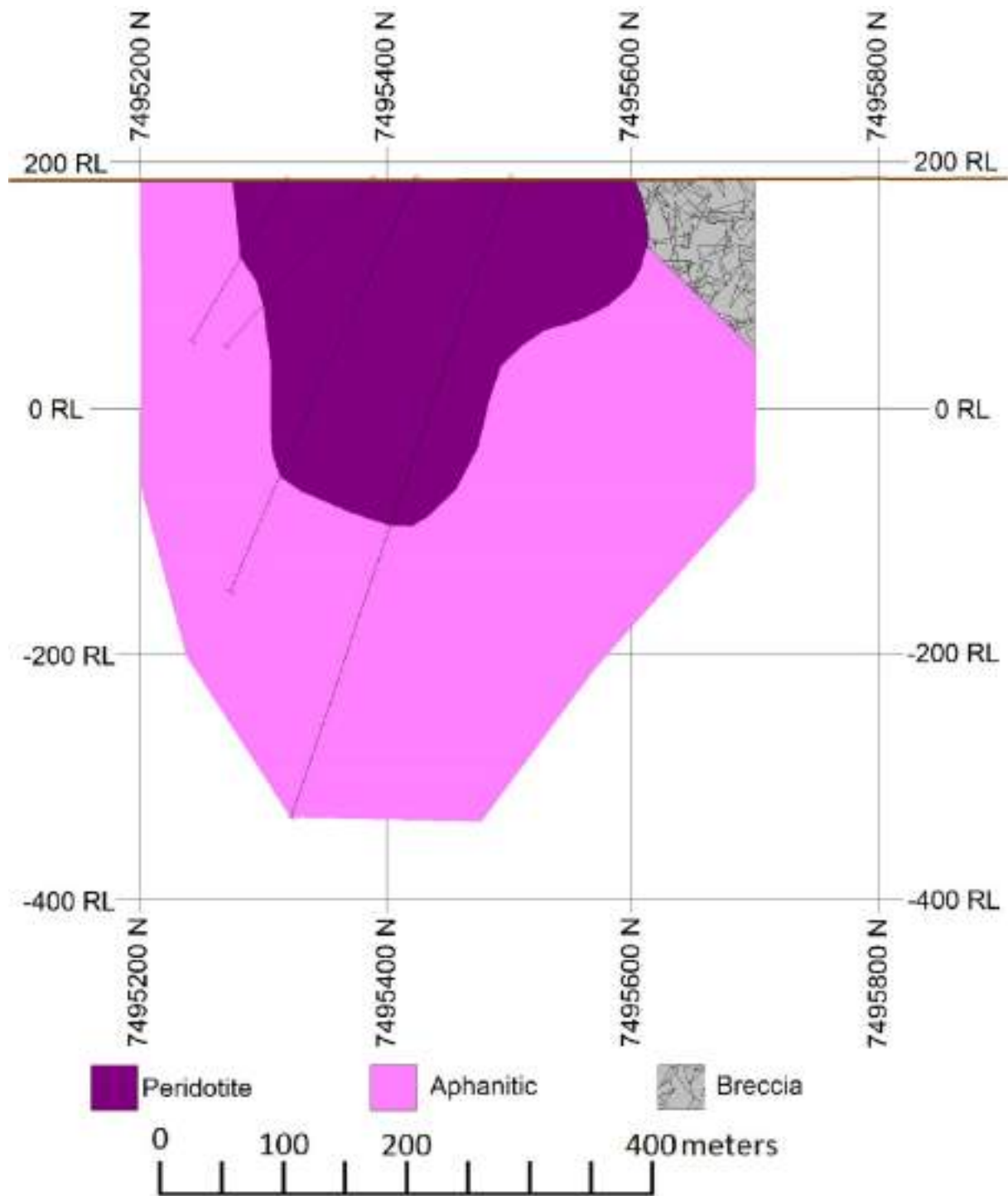


Figure 3.3. S-N cross section, +/-25 m clipping, through the main body of the Sakatti deposit on 3489950E showing the aphanitic footwall surrounding the main cumulate body and a small portion of the hanging-wall breccia (Brownscombe et al., 2015).

With increasing depth, further to the west, an extensive package of non-mineralised hanging wall rocks is encountered before reaching the cumulate body (Fig. 3.4). In this western part of the deposit, the Aphanitic Unit constitutes both the hanging wall and part of the footwall of the cumulate body, the remainder of the footwall is a fault structure.

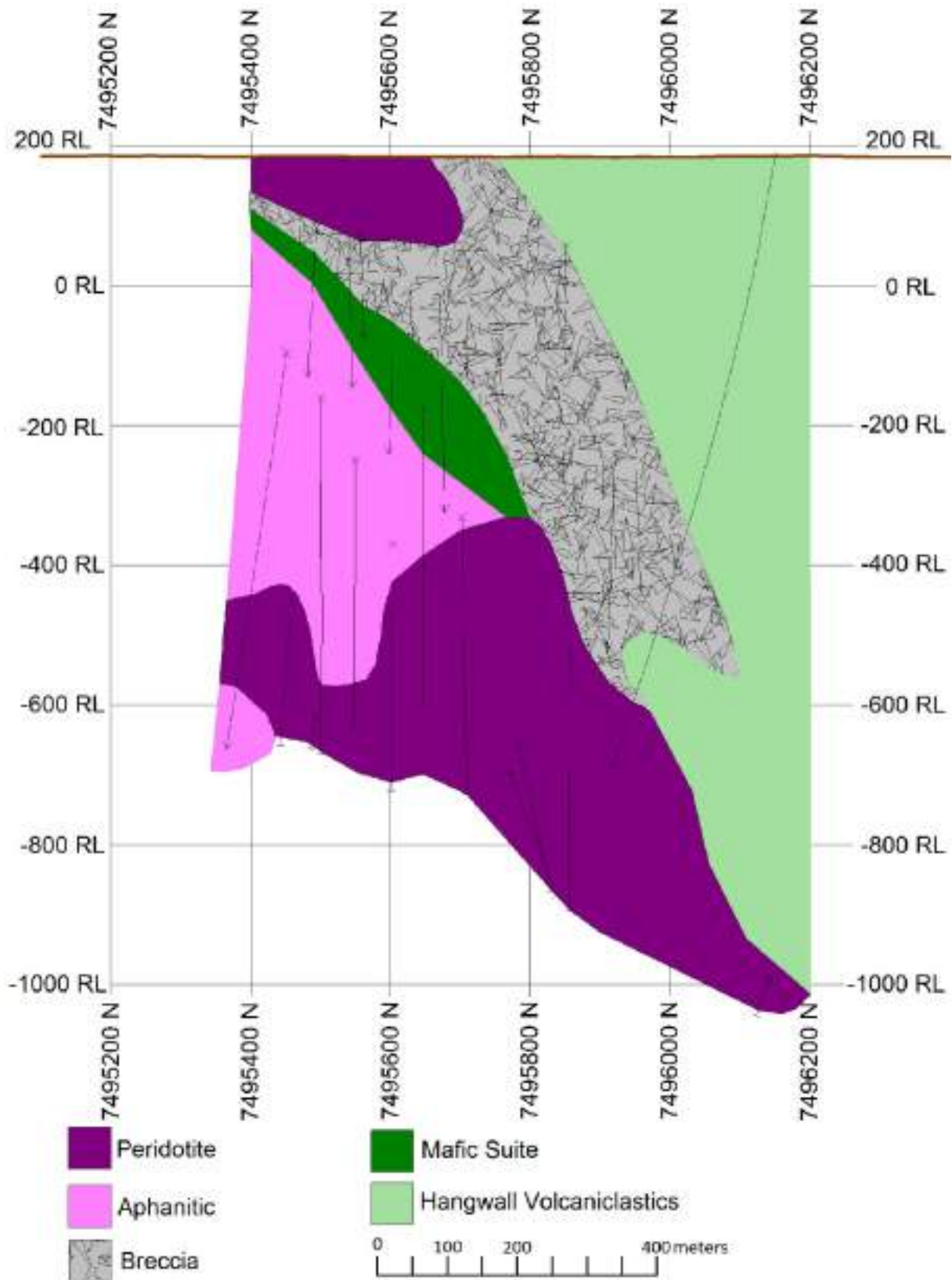


Figure 3.4 – S-N cross section, +/-25 m clipping, through the main body of the Sakatti deposit on 3489300E. The hanging wall contains volcano-sediments, breccia, the Mafic Suite and an unmineralised Olivine Cumulate Unit (Brownscombe et al., 2015). The Aphanitic Unit is present both above and below the Olivine Cumulate Unit. The base of the cross section is a faulted contact.

The upper contact of the Aphanitic Unit with the remainder of the hanging wall is always marked by a cryptocrystalline serpentinite unit. Stratigraphically above the Aphanitic Unit and the serpentinite is the north-west dipping Mafic Suite. Above this package is the Breccia Unit that also dips to the north-west and appears to be concordant with the underlying Mafic Suite. Towards the north, the package of Aphanitic Unit, serpentinite and Mafic Suite pinches out and the cumulate body is in direct contact with the Breccia Unit. Further to the north, the Breccia Unit itself pinches out to leave the Volcano-sedimentary Unit in contact with the cumulate body. An apparently isolated non-mineralised olivine cumulate body sub-crops at surface within the Breccia Unit in this western portion (Fig. 3.4), without any established links to the main cumulate body.

The north-east cumulate body

Based on the evidence of current drilling, the north-east cumulate body is smaller than the main cumulate body and more cylindrical, albeit with an elongate tail to depth, giving it an inverted teardrop-like shape (Fig. 3.5). It has an east-west strike and gently plunges to the east. Occurring at a different stratigraphic level to the main cumulate body, it is bound by the Volcano-sedimentary Unit to the north and the Breccia Unit to the south and at depth. Talc-carbonate-altered ultramafic rocks are also more common when compared to the main cumulate body, particularly to the east. In the west, a 20-30 m thick cryptocrystalline serpentinite body occurs within the Olivine Cumulate Unit, almost perpendicular to the contact between the cumulate body and the Volcano-sedimentary Unit. Only one drill hole has extended from the north-east cumulate body towards the main cumulate body and this hole intersected a fault at depth.

The south-west cumulate body

The south-west cumulate body is ovoid in shape, with a central sub-cropping portion and a gently dipping eastern edge. The western edge is untested by drilling. Scapolite-mica rocks occur to the north of the cumulate body, and a breccia occurs at depth and to the south. At surface in the south-east is a fine-grained amphibole-rich ultramafic rock that has not been intercepted elsewhere within the Sakatti area.

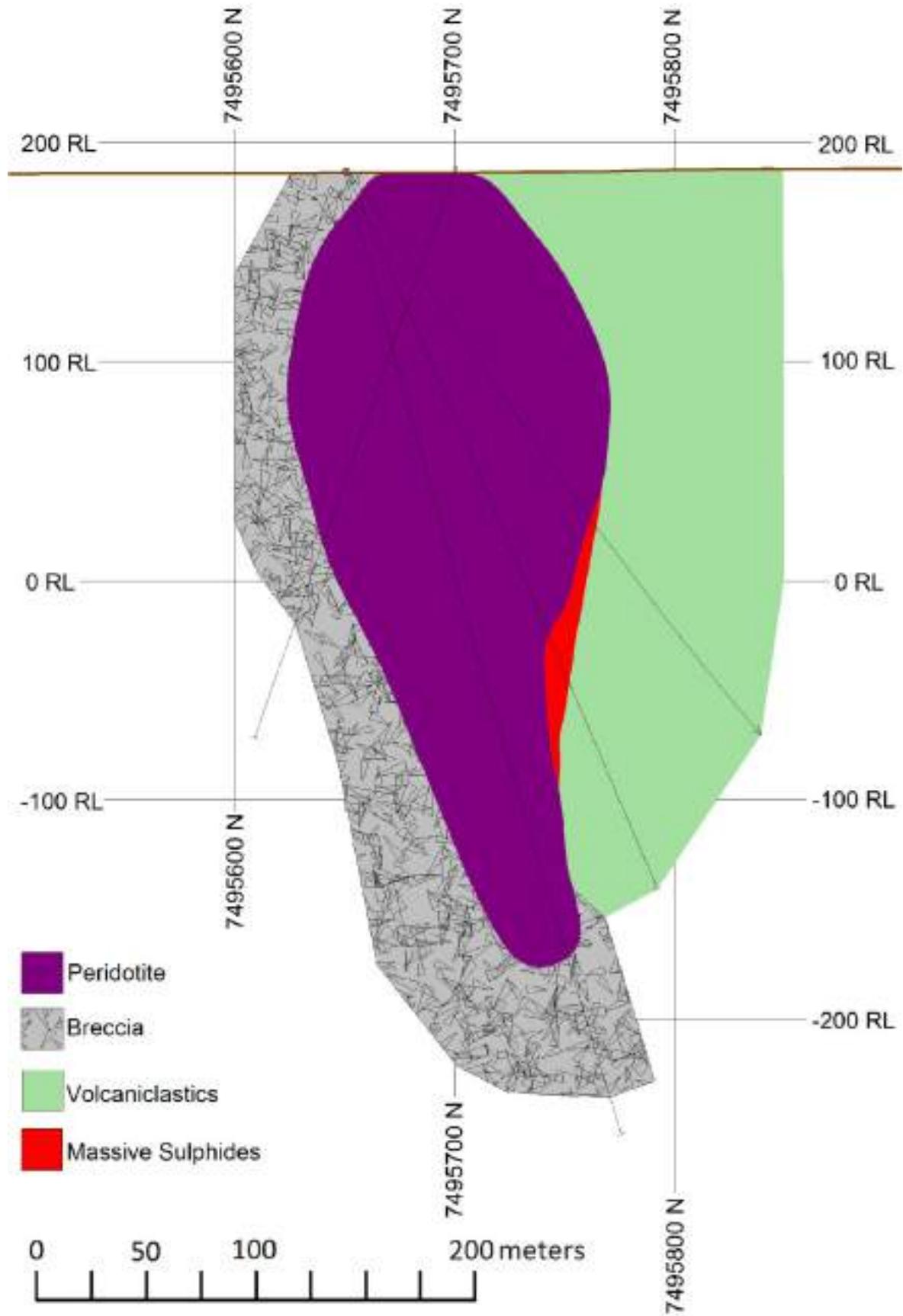


Figure 3.5. S-N cross section through the NE body of the Sakatti deposit on 3490150E. The Olivine Cumulate Unit occurs between the Breccia Unit and the Volcano-sedimentary Unit (Brownscombe et al., 2015).

3.2 Sampling

The techniques section is located in the appendix to avoid repetitions between chapters.

Thin sections were taken for this study (85) and combined with previously existing thin sections on the Sakatti deposit (30). Ten holes were logged in detail and numerous other intersections were examined under the guidance of the company geologists. Two holes were chosen to concentrate thin section sampling in order to provide downhole continuity, with sporadic and representative samples taken from other holes (Fig. 3.6). These thin sections focused on the Olivine Cumulate Unit and the contact between the Olivine Cumulate Unit and the Aphanitic Unit. Relatively few sections (10) were taken in the hanging wall lithologies as the focus of the study is the mineralised body.

Whole-rock geochemistry samples were initially taken from the pulp rejects (unused portions of samples that have been assayed in a commercial laboratory) of assay intervals for samples that matched thin section sampling. These samples were also taken for XRD in addition to quarter core samples in the non-assayed core.

In the latter stages of the project whole-rock geochemistry was taken from top to bottom on several holes, including the hole that was the focus of downhole thin section analysis.

Sm/Nd samples were chosen on the basis of pyroxene content and lack of alteration after thin section analysis. U/Pb samples were chosen by the company geologists in part using advice from this study.

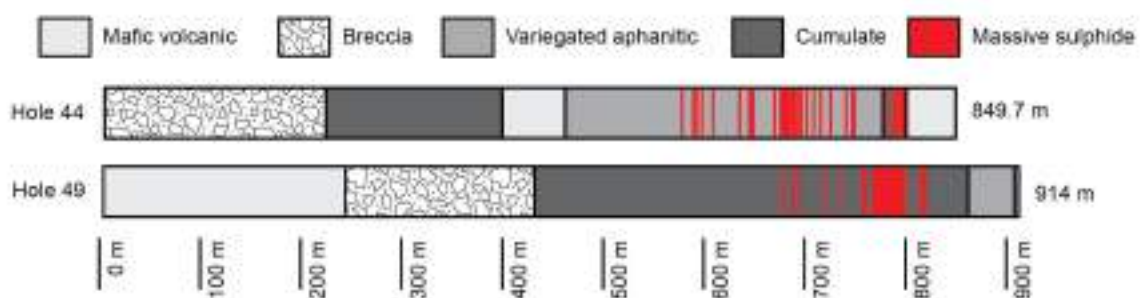


Figure 3.6 – Cartoon logs of the two holes that were the target of the majority of sampling for this project.

3.3 Petrography

3.3.1 Volcano-sedimentary Unit

The Volcano-sedimentary (also erroneously termed Volcaniclastic) Unit located above the Sakatti deposit is a low-grade metamorphic rock that is interpreted as having a volcano-sedimentary protolith. Despite being locally variable the majority of the unit comprises elongate fine-grained (approximately 50 μm) chlorite and muscovite surrounded by quartz and feldspar. The rock has mm-scale compositionally layering, visible from hand specimen (Fig. 3.7a) and two types of porphyroblasts.

The lighter layers have abundant plagioclase and quartz (Fig. 3.7j). More abundant mafic phases, rutile and phlogopite make up the darker layers (Fig. 3.7h). The elongate minerals are aligned in a well-defined crenulation cleavage which is not aligned with the compositional layering (Fig. 3.7g).

Type 1 porphyroblasts (Fig. 3.7d and i) are primarily quartz with chlorite and calcite inclusions in the centre and clay minerals around the periphery. Inclusions within these porphyroblasts are straight and orientated approximately 20 degrees off the prominent compositional trend in the surrounding rock. These porphyroblasts are not visible in hand specimen, presumably because of their compositional similarity to the rest of the rock.

Type 2 porphyroblasts (Fig. 3.7f) are elongate and composed of chlorite and phlogopite. These porphyroblasts have prominent quartz pressure shadows (σ -type mantling) indicating exposure to shear stress. Inclusions are aligned in straight lines showing that the porphyroblasts formed prior to shearing or formation of the crenulation cleavage.

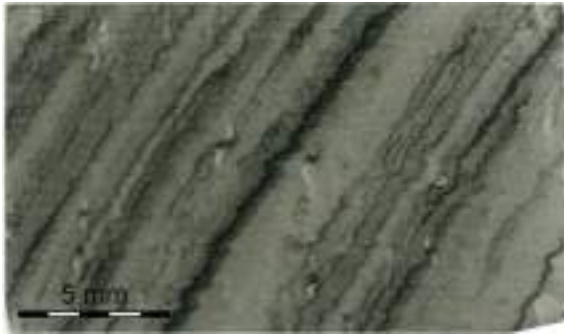


Figure 3.7a – Compositional layering and abundant porphyroblasts. A crenulation cleavage is evident at a different angle to the compositional layering.

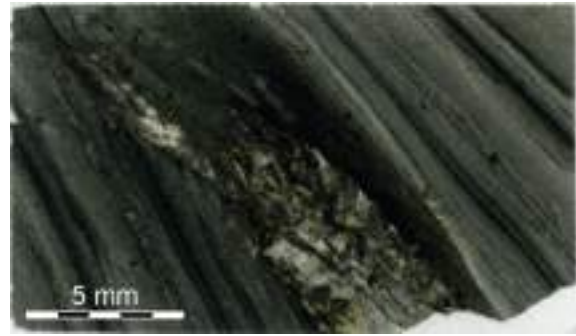


Figure 3.7b – Coarser scapolite-carbonate-chlorite patch within compositional layering.

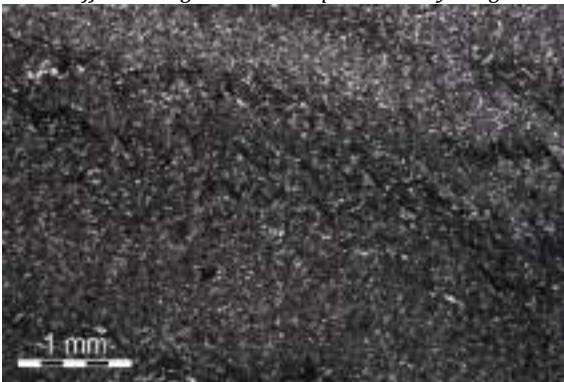


Figure 3.7c – Darker and lighter layers in transmitted light.

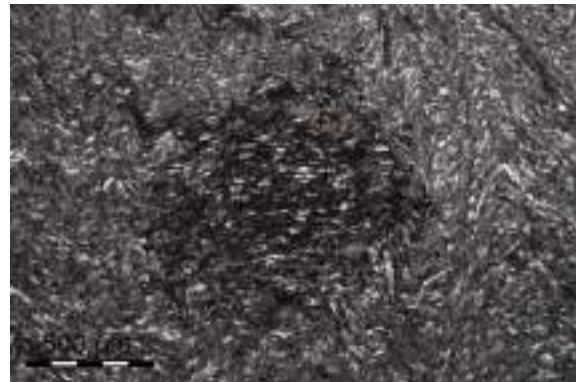


Figure 3.7d - Type 1 porphyroblasts are equant up to 1 mm across and zoned (Fig. 3.7i).

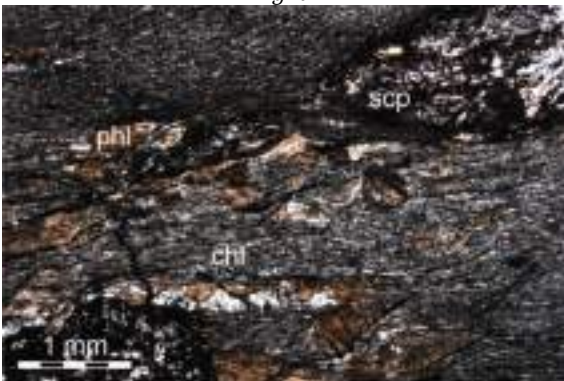


Figure 3.7e - Coarser patches feature easily distinguished rounded scapolite grains (2-3 mm) in a carbonate matrix, along with large crystals of phlogopite and chlorite.

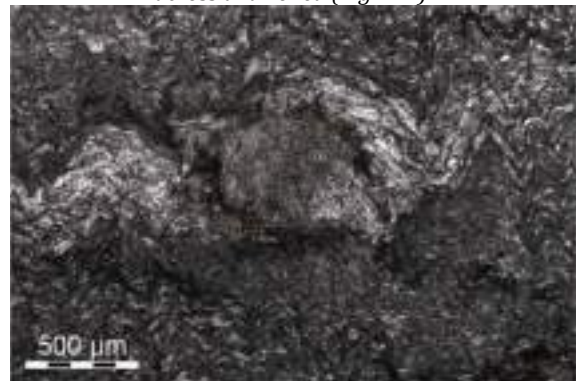


Figure 3.7f - Type 2 porphyroblasts are elongate and composed of chlorite and phlogopite.

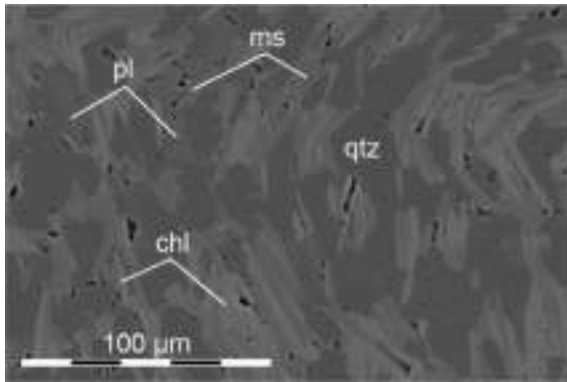


Figure 3.7g - The lighter layers have abundant plagioclase and quartz.

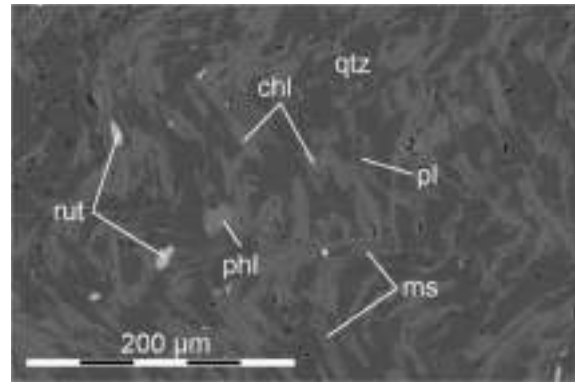


Figure 3.7h - The darker layers have more abundant rutile and phlogopite and less abundant plagioclase and quartz.

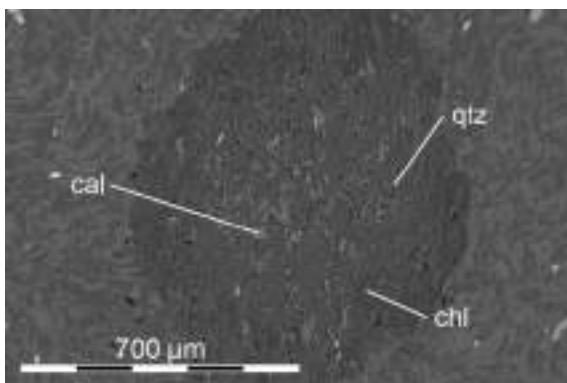


Figure 3.7i - Type 1 porphyroblasts composed of quartz, chlorite and calcite. The porphyroblasts are equant and difficult to see in hand specimen.

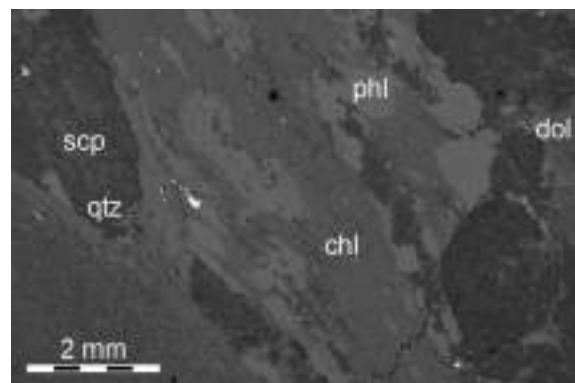


Figure 3.7j - Coarse scapolite grains (2-3 mm) in a carbonate matrix, along with large crystals of phlogopite and chlorite. The coarse patch is haloed by fine-grained chlorite, similar in composition to the main rock but notable because the accompanying minerals are not present.

Figure 3.7 - Images of the Volcano-sedimentary Unit

3.3.2 Breccia Unit

The highly variable Breccia Unit was not extensively sampled as part of this study. This is because it is so variable that the number of samples required to get adequate representation of the unit would have been so great that they would have diverted resources away from the principal focus of the study which was the Sakatti deposit below.

For that reason a Master's project, linked to this PhD project, was conceived studying solely this unit and was undertaken by Katherine Jillings of Imperial College London. The observations from this project are summarised below (Jillings, 2015).

In that study 29 thin sections were taken from the Breccia Unit with a focus on two holes for which there was whole-rock geochemical data throughout the breccia package (Jillings, 2015). Several sub-units were identified within the breccia package on the basis of their phyllosilicate

content, monomictic clast, polymictic clast and carbonate content (Fig. 3.8). The variation between these end-members is complete with large intersects of pure dolomite present, extensive albitisation and scapolitisation and a layered chlorite-talc rock, being the phyllosilicate end-member.

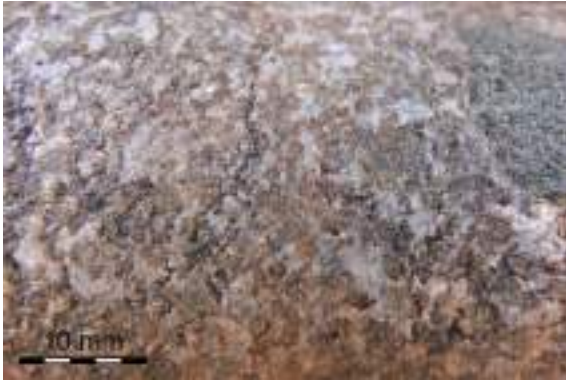


Figure 3.8a – Brecciated quartzite with carbonate and hematite and a phyllosilicate clast.



Figure 3.8b – The dolomite sub-unit of the Breccia Unit.



Figure 3.8c – Carbonate matrix around clasts of feldspar

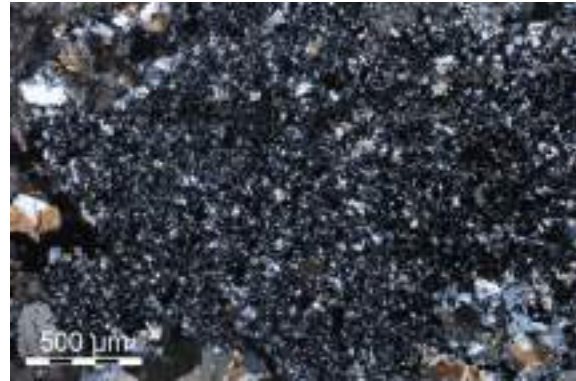


Figure 3.8d - Clast of arkosic quartzite within the breccia

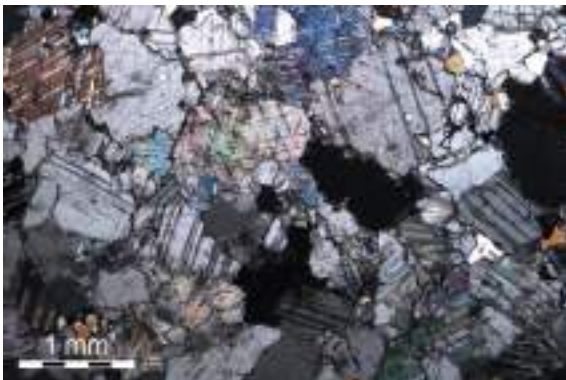


Figure 3.8e – Dolomite from the Breccia Unit.

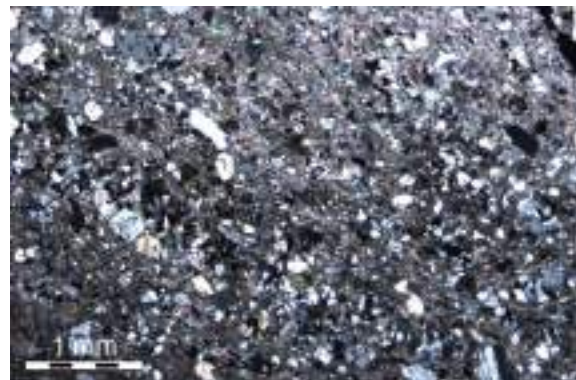


Figure 3.8f – The phyllosilicate sub-unit of the breccia with quartz clasts amongst chlorite and carbonate.

Figure 3.8 – Photographs and thin section images of the Breccia Unit

3.3.3 Mafic suite

It is doubtful whether this unit was actually present in the holes sampled as part of this project. It is clearly present further to the west. The contact between the Breccia Unit and the Olivine Cumulate Unit or Mafic Suite is very heavily altered and subject to complete mineralogical replacement, making identifying units complicated even in the broadest sense.

The samples taken from in this zone are composed primarily of chlorite, scapolite and carbonate assemblages that could be included within the breccia classification of phyllosilicate but could also be scapolite-mica rock of the Mafic Suite (Fig. 3.91-b). There is no discrete horizon where the Olivine Cumulate Unit starts but the first identifiable sample occurs at 429.50 m (Fig. 3.9c-d). Here the rock consists primarily of amphibole, but relict cumulus shapes can be seen within relict oikocryst outlines, now all replaced by amphibole.

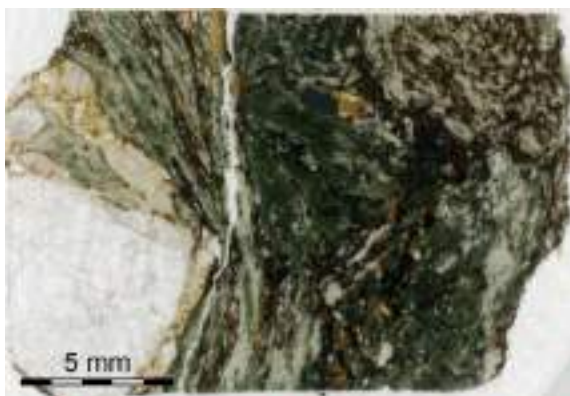


Figure 3.9a – Dolomite, chlorite and scapolite are present in the altered zone above the deposit which may or may not be the Mafic Suite Units.

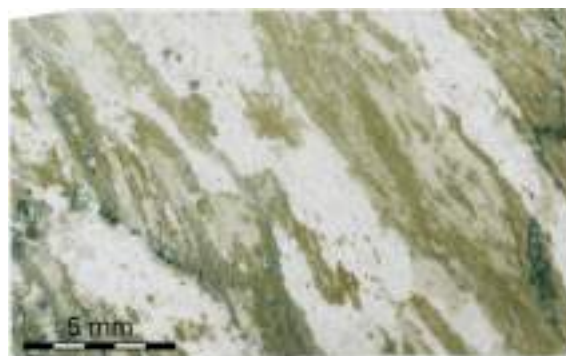


Figure 3.9b – Chlorite and dolomite are pervasive meaning the protolith lithology is difficult to distinguish.

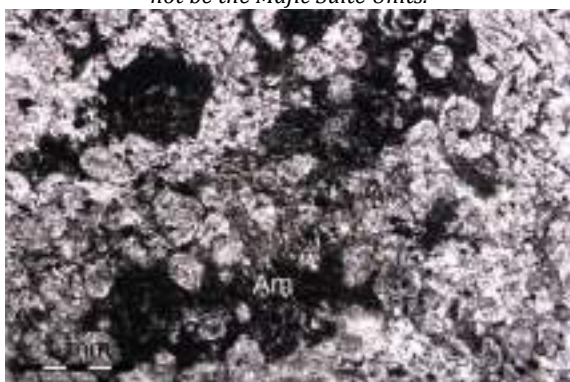


Figure 3.9c – The highest sample identifiable as having a Olivine Cumulate Unit protolith.

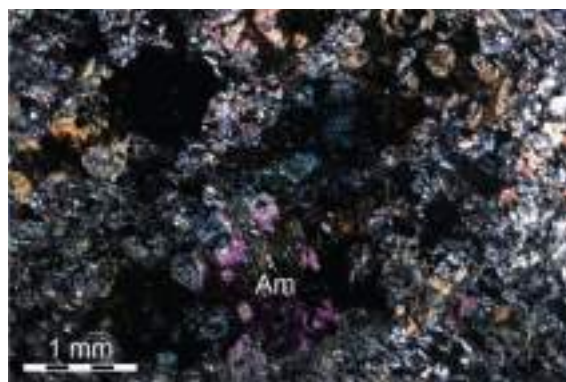


Figure 3.9d - The highest sample identifiable as having a Olivine Cumulate Unit protolith contains amphibole porphyroblasts that contain relict olivine cumulus textures within the amphibole.

Figure 3.9 – Images of the altered samples between the Breccia Unit and the Olivine Cumulate Unit.

3.3.4 Host Olivine Cumulate or Peridotite Unit

The Sakatti deposit shows extensive serpentinisation yet in the majority of samples studied the magmatic texture of the olivines (typically 0.5-2 mm in width) is preserved and observable by the naked eye. This means a textural interpretation can be drawn even though the vast majority of the original magmatic minerals are no longer present. Though the serpentinised olivines are relatively easy to identify, it is more difficult to interpret the precursor phases in the serpentinised groundmass.

Oikocrysts of pyroxene (up to 2 cm across) can be identified when fresh, when altered to amphibole they are variably apparent depending primarily on their shade relative to the surrounding groundmass. This can be either light or dark, but still serpentine, depending on the magnetite content. These difficulties have meant that no systematic behaviour has been observed in the cumulus textures which can vary from adcumulate to orthocumulate on a local scale, making larger scale differences difficult to discern.

With those caveats, estimated original olivine proportions in this unit are 60-95% with pyroxene content varying from 0-40%. Fig. 3.1a-n is intended to show the variation in this unit downhole and the varying extent of serpentinisation. Grain sizes are discussed on a phase by phase basis below.

3.3.4.1 Olivine

Due to pervasive serpentinisation, most samples do not contain primary olivine (eg. Fig. 3.10j) but in a number of samples it is preserved. The main cumulus phase is olivine (typically 0.5-2 mm in width) and the cumulate shapes vary from relatively euhedral to subhedral. Because they are almost invariably serpentinised, the colour of the olivine shapes varies from black to brown, sometimes becoming difficult to distinguish from the intercumulus.

It is common for the olivine to exist only as small patches within the former cumulate shape. In these cases the separate olivine patches are crystallographically aligned to the other patches within one cumulate shape. This suggests that they are remnant olivine rather than being of metamorphic origin.

The rock varies from orthocumulate to adcumulate on the 10^{-2} to 10^2 m scale. Orthocumulate is more abundant towards the top of the succession, although there is local variability throughout (Fig. 3.10c-n). No evidence of layering has been observed within the Olivine Cumulate Unit, the variation in olivine grain size does not fit conventional layering and accumulation models.

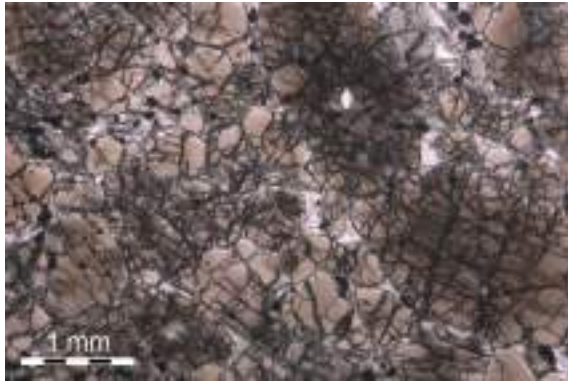


Figure 3.10a – Adcumulate olivine with minimal intercumulus or oikocrystic pyroxene, entirely preserved olivine in the Dunite sub-unit M8055 988.30 m

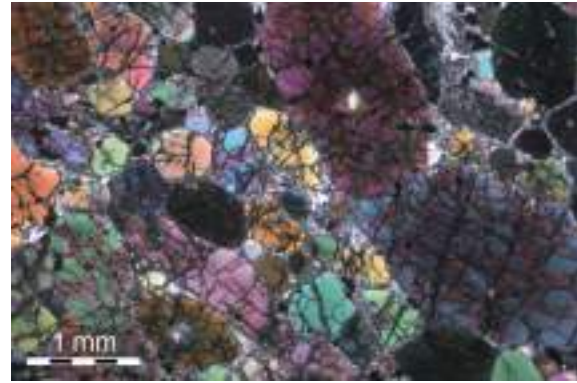


Figure 3.10b - Adcumulate olivine with minimal intercumulus or oikocrystic pyroxene, entirely preserved olivine in the Dunite sub-unit M8055 988.30 m

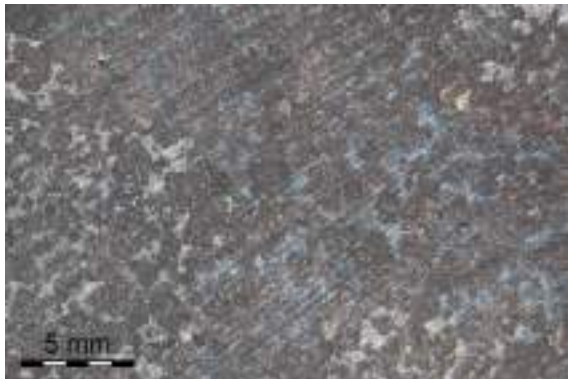


Figure 3.10c – Meso-orthocumulate olivine in pyroxene and serpentine, well preserved M8049 668.14 m

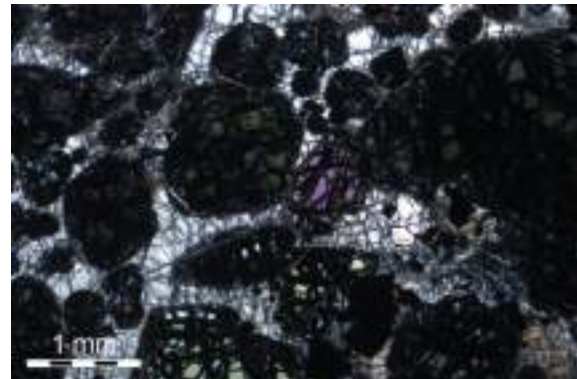


Figure 3.10d – Meso-orthocumulate olivine in pyroxene and serpentine, well preserved M8049 668.14 m

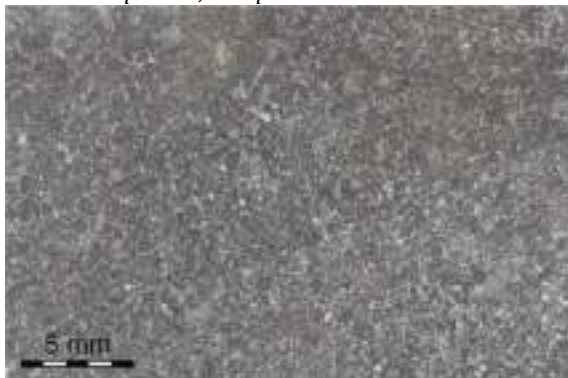


Figure 3.10e – Smaller mesocumulate olivine in pyroxene and serpentine, well preserved M8049 678.23 m

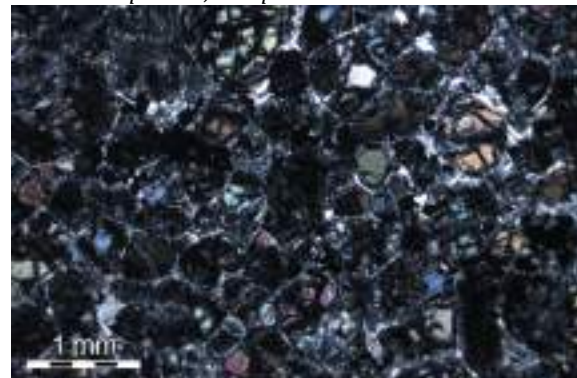


Figure 3.10f - Smaller mesocumulate olivine in pyroxene and serpentine, well preserved M8049 678.23 m

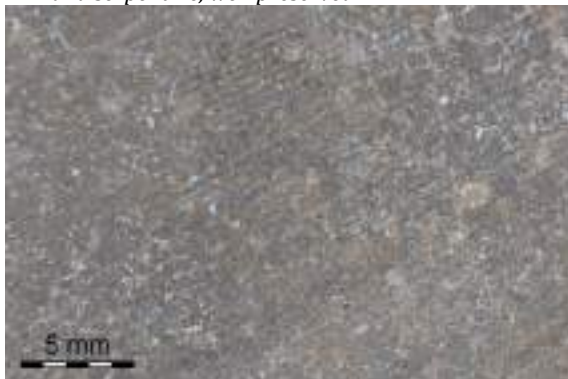


Figure 3.10g – Mesocumulate serpentinised olivine in serpentinised groundmass M8049 693.63m

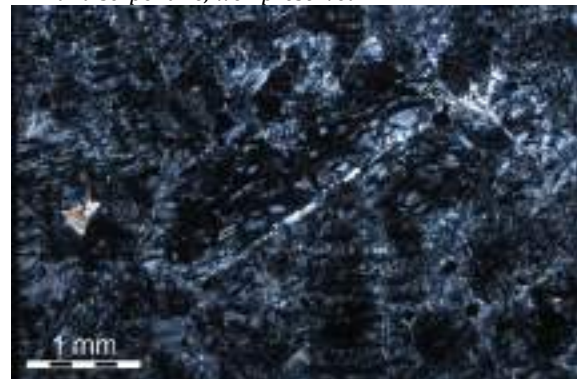


Figure 3.10h - Mesocumulate serpentinised olivine in serpentinised groundmass M8049 693.63m

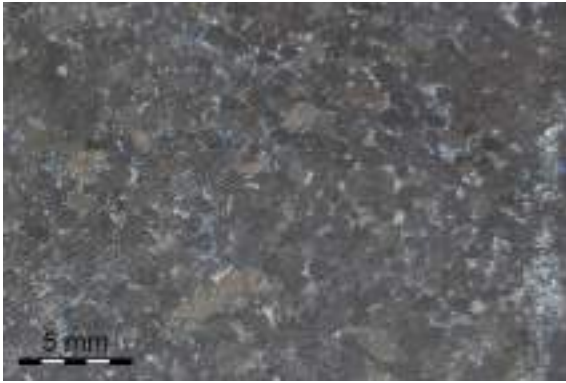


Figure 3.10i - Larger serpentinised olivine in serpentinised groundmass M8049 708.51 m

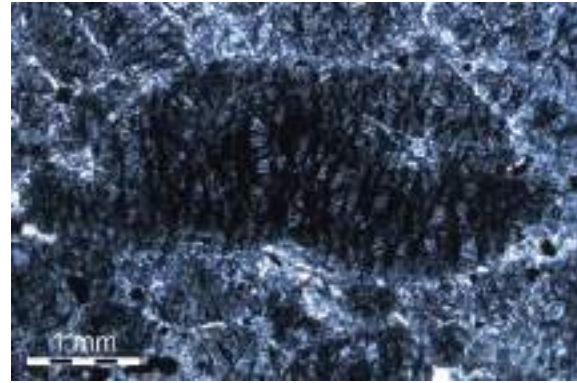


Figure 3.10j - Larger serpentinised olivine in serpentinised groundmass M8049 708.51 m

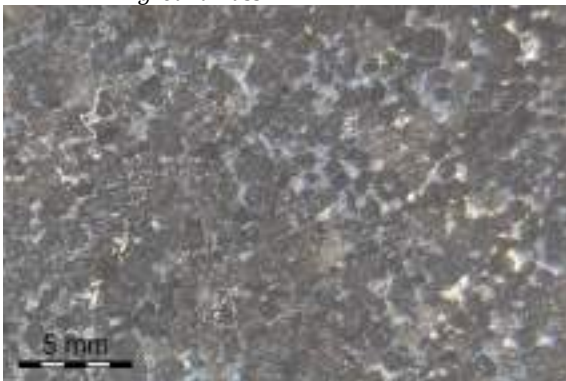


Figure 3.10k - Partially preserved mesocumulate olivine in serpentinised groundmass - M8049 711.71 m

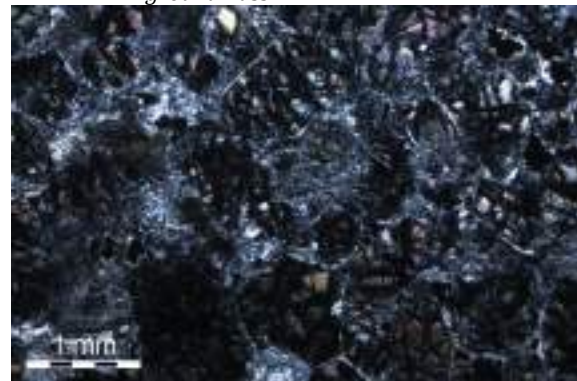


Figure 3.10l - Partially preserved mesocumulate olivine in serpentinised groundmass - M8049 711.71 m

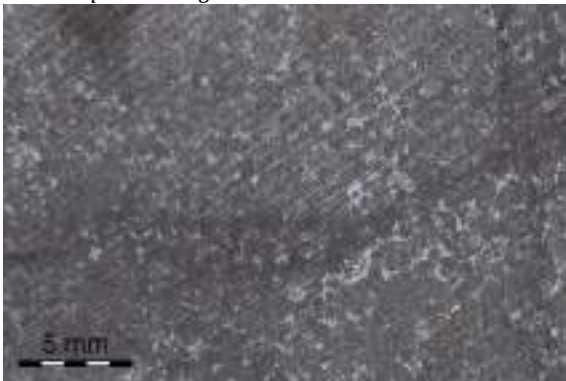


Figure 3.10m - Fully serpentinised mesocumulate olivine in serpentinised groundmass M8049 720.22 m

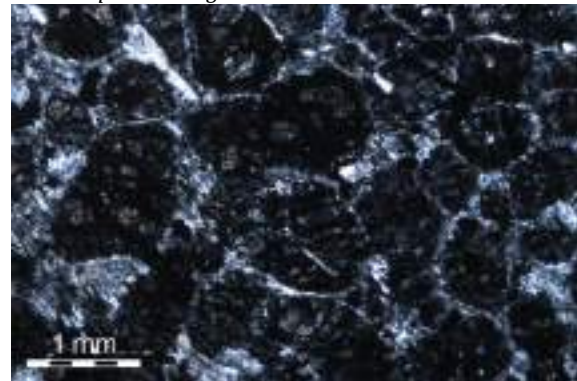


Figure 3.10n - Fully serpentinised mesocumulate olivine in serpentinised groundmass M8049 720.22 m

Figure 3.10 - Images of olivine within the Olivine Cumulate Unit including a downhole succession of samples.

3.3.4.2 Chromite

Chromite is the other cumulus phase alongside olivine. It is present as euhedral-subhedral crystals generally between 0.2-1 mm and is variably altered to chrome-bearing magnetite. The extent of alteration can be assessed by the proportion of the original cumulate crystal that is made up of chromite, usually visible both in reflected light and backscattered electron imaging. In some samples the cores can be up to 95% of the grains whereas others do not have chromite cores.

This cumulus phase is ubiquitous throughout the core and present as between 0.5-3% of the rock mass. No systematic variation of abundance of chromite with depth has been observed. Magnetite is also present as a product of serpentinisation but this is very fine-grained, in-situ and therefore cannot be confused with cumulus chromite, although there are overgrowths on cumulus chromite that are potentially associated with serpentinisation. The boundaries of the euhedral chromites are generally smooth but can feature undulations that could either be a result of magmatic resorption of the cumulus phase (Fig. 3.11a) or the aforementioned overgrowth of serpentine-related magnetite (Fig. 3.11b).

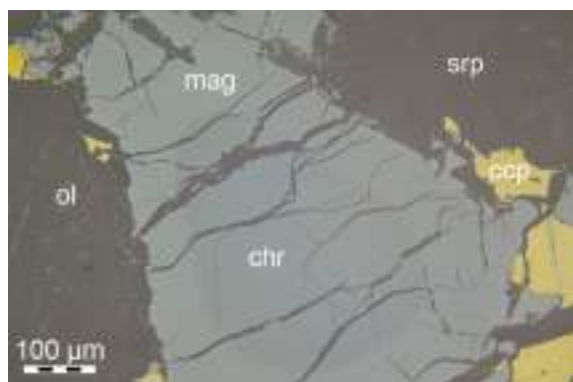


Figure 3.11a – Cumulus chromite core with altered Cr-rich magnetite rim. Undulating edges may indicate resorption.

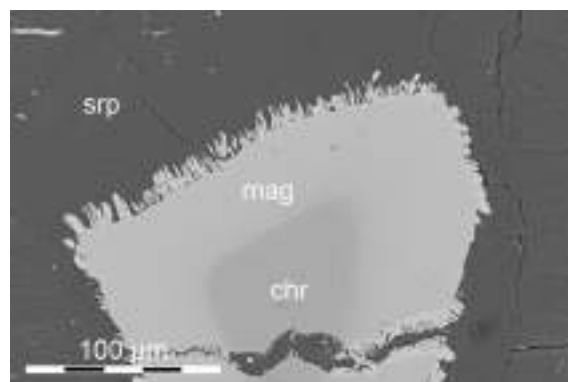


Figure 3.11b - Cumulus chromite core with altered Cr-rich magnetite rim. Undulating edges may indicate growth of magnetite during serpentinisation.

Figure 3.11 – Images of cumulus chromite within the Olivine Cumulate Unit.

3.3.4.3 Pyroxene

Clinopyroxene is the most common intercumulus mineral, occurring as oikocrysts up to 2 cm across that are frequently altered to tremolite (Fig. 3.12). Orthopyroxene also forms oikocrysts, but is less abundant. These oikocrysts, particularly the orthopyroxene ones, frequently 'shield' the olivine from alteration and it is not uncommon to find preserved olivine within pyroxene oikocrysts while all the olivine without pyroxene oikocrysts has been serpentinised.

Clinopyroxene is readily identifiable in thin section due to ubiquitous exsolution lamellae of orthopyroxene and prominent cleavage planes. Both of these features are not pronounced in the

orthopyroxene oikocrysts. As with the olivine, these primary phases can be rapidly found using reflected light microscopy and relying on their greater polishing hardness leading to greater relief than the surrounding alteration intercumulus minerals (serpentine or chlorite and talc).

Orthopyroxene at the Sakatti deposit is difficult to distinguish from olivine using backscatter electron imaging as they have very similar backscatter coefficients, compared to clinopyroxene which has a higher coefficient. Olivine can be identified as separate to orthopyroxene in backscatter electron images as it has characteristic serpentine filled cracks throughout that are more prominent than those in the orthopyroxene, giving it the impression of having greater relief.

It is difficult to accurately distinguish the proportion of pyroxene present in a particular part of the cumulate by eye because the oikocrysts vary in shade and level of degradation. The surrounding groundmass also varies meaning that in some instances the pyroxene oikocrysts are particularly obvious whereas in others they are invisible despite still being present. This makes the extent of pyroxene difficult to quantify meaningfully downhole. The extent of the pyroxene oikocrysts is also not well suited to thin section quantification due to their size (1-2 cm) meaning that thin section sampling is not a valid sampling technique. Two bulk techniques were therefore chosen to quantify the extent of pyroxene (whole-rock geochemistry and XRD).

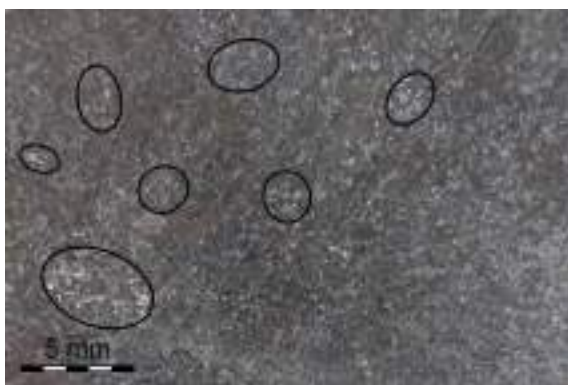


Figure 3.12a – Oikocrystic pyroxene can be identified in core when well preserved.

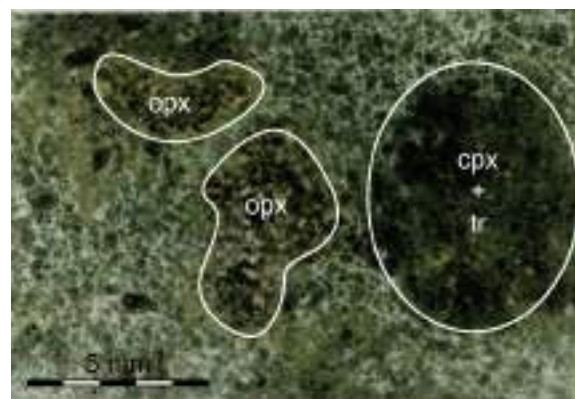


Figure 3.12b – Oikocrysts are easily identifiable in thin sections but are not well represented by thin section size sampling.

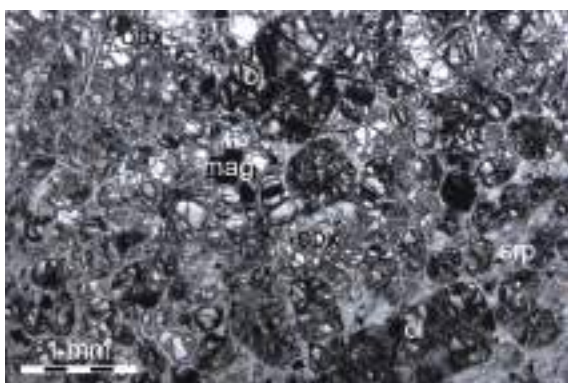


Figure 3.12c – Well preserved orthopyroxene oikocryst

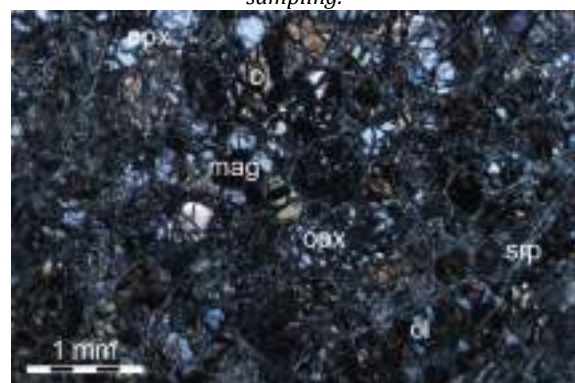


Figure 3.12d - Well preserved orthopyroxene oikocryst

resulting in preservation of olivine.

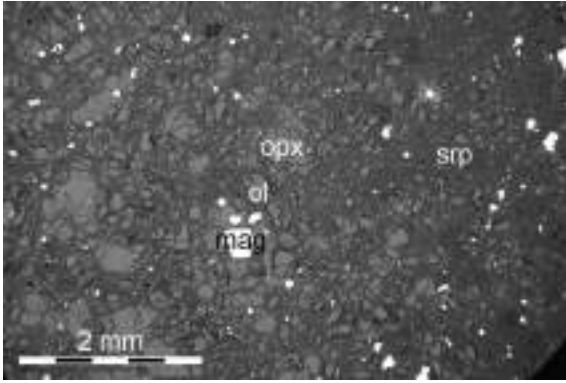


Figure 3.12e - Well preserved orthopyroxene oikocryst resulting in preservation of olivine.

resulting in preservation of olivine.

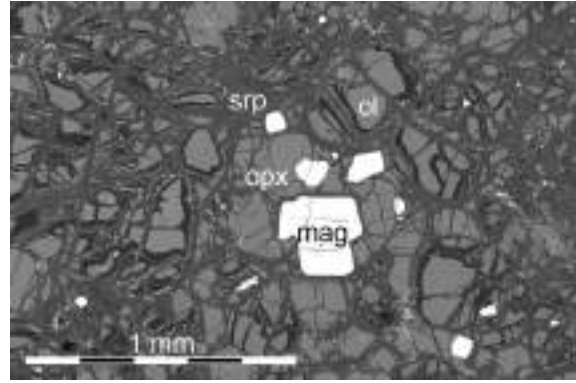


Figure 3.12f - Well preserved orthopyroxene oikocryst resulting in preservation of olivine. The close backscatter coefficients of orthopyroxene and olivine make them difficult to distinguish.

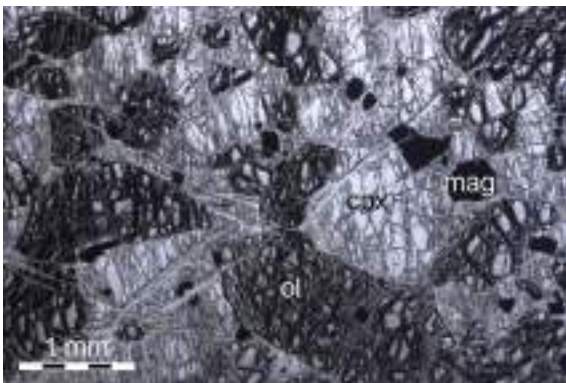


Figure 3.12g - Well preserved clinopyroxene and olivine within large oikocryst.

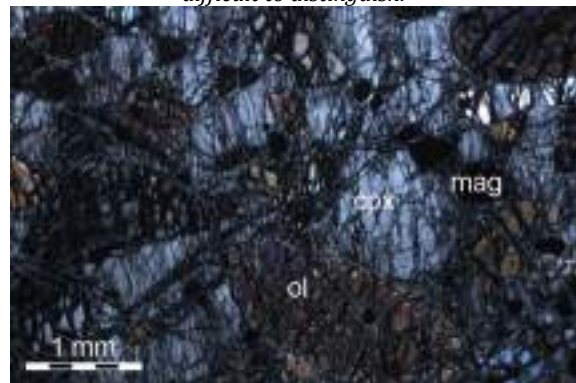


Figure 3.12h - Well preserved clinopyroxene and olivine within large oikocryst.

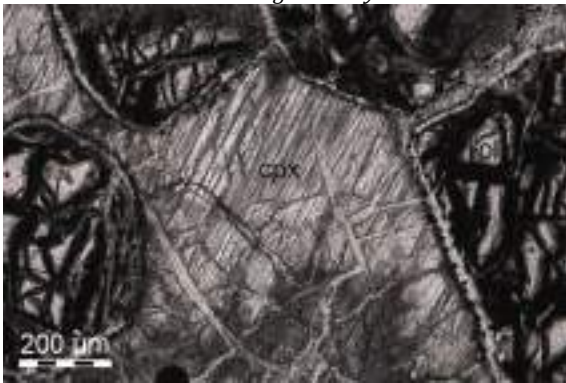


Figure 3.12i - Cleavage planes and exsolution lamellae of orthopyroxene within clinopyroxene.

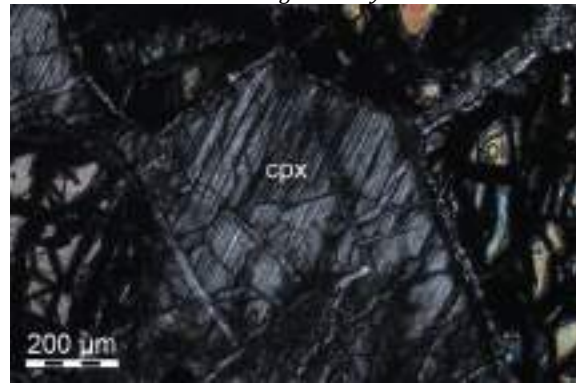


Figure 3.12j - Cleavage planes and exsolution lamellae of orthopyroxene within clinopyroxene.

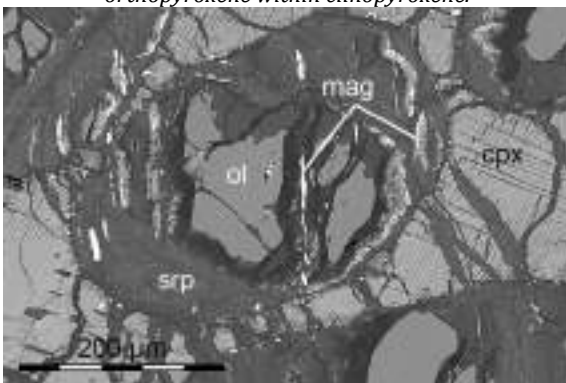


Figure 3.12k - Partially preserved olivine within clinopyroxene oikocryst.

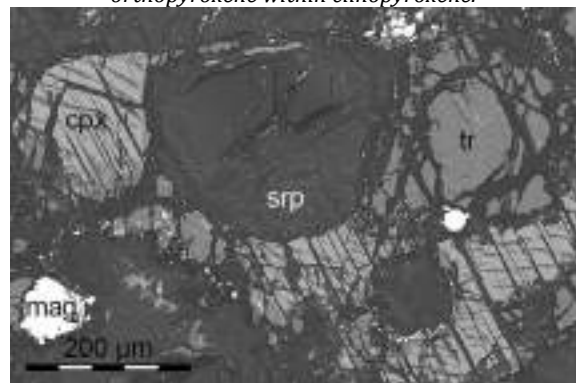


Figure 3.12l - Serpentinised olivine cumulate shapes within clinopyroxene that is partially altered to tremolite

Figure 3.12 - Images of oikocrystic pyroxene within the Olivine Cumulate Unit

3.3.4.4 Amphibole

Amphibole is an evident alteration product of clinopyroxene throughout the Olivine Cumulate Unit. This amphibole is the most abundant type in the Olivine Cumulate Unit and frequently comprises entire oikocrysts, pseudomorphing clinopyroxene. It is texturally unremarkable and can be difficult to identify in hand specimen. It can be different shades of light and dark depending on the surrounding mineralogy and the amount of inclusions within it.

There is also a further amphibole population present alongside unaltered pyroxene texturally consistent with the two minerals co-forming and not that one is an alteration product of the other (Fig. 3.13). This separate population of amphibole is texturally distinct, frequently exhibiting 60-120 cleavage angles in thin section and it has been identified as pargasite. The pargasite occurs as both colourless and also brown in thin section, this has been established to be two separate sub-populations of pargasite with differing Ti contents.

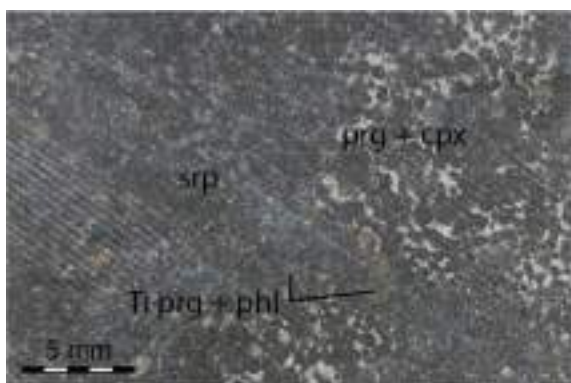


Figure 3.13a – Ti-rich pargasite is more easily identified in hand specimen whereas normal pargasite is difficult to distinguish from clinopyroxene.



Figure 3.13b – Ti-rich pargasite can be separately identified from normal pargasite due to a reddish brown colour compared to normally colourless pargasite.

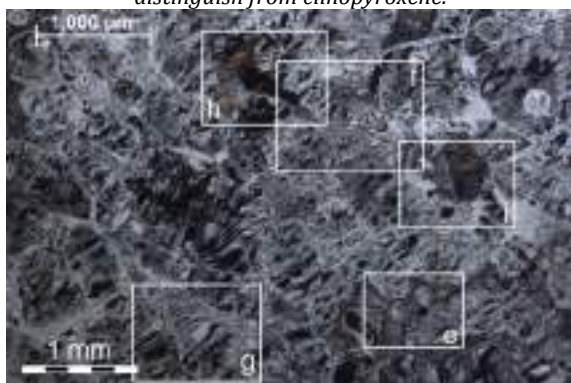


Figure 3.13c – Brown Ti-rich pargasite with phlogopite distinct from pargasite and clinopyroxene.

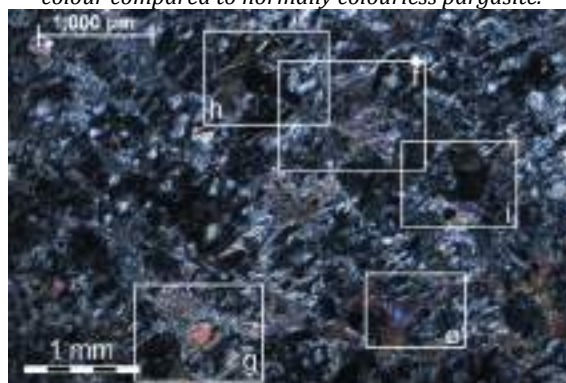


Figure 3.13d - Brown Ti-rich pargasite with phlogopite distinct from pargasite and clinopyroxene.

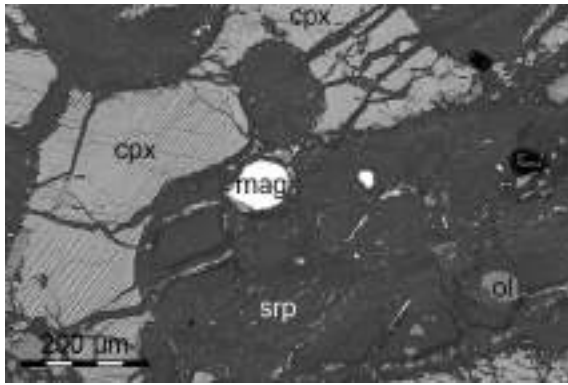


Figure 3.13e – Oikocrystic clinopyroxene with magnetite contrasts with serpentinised olivine.

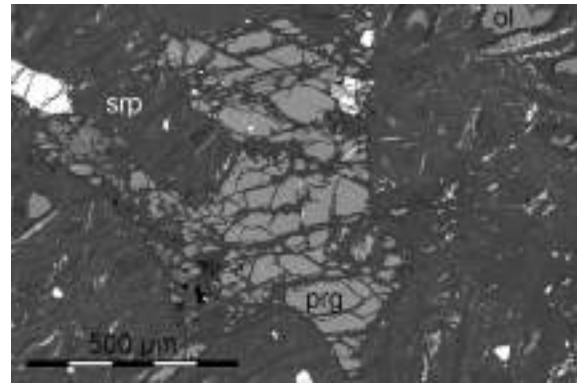


Figure 3.13f – Oikocrystic pargasite with serpentinised olivine.

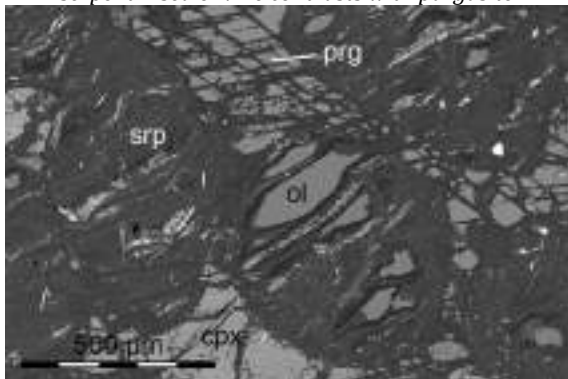


Figure 3.13g – Both pargasite and clinopyroxene around partially preserved olivine.

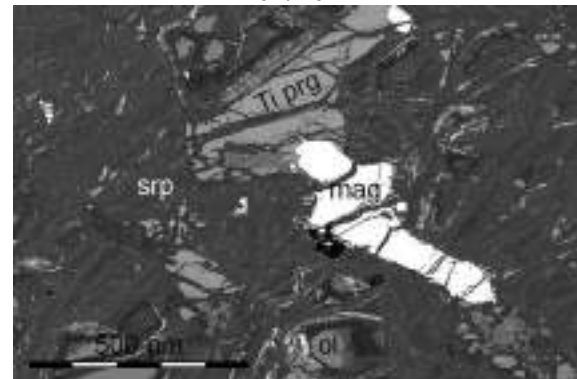


Figure 3.13h – Ti-rich pargasite with magnetite and partially preserved olivine.

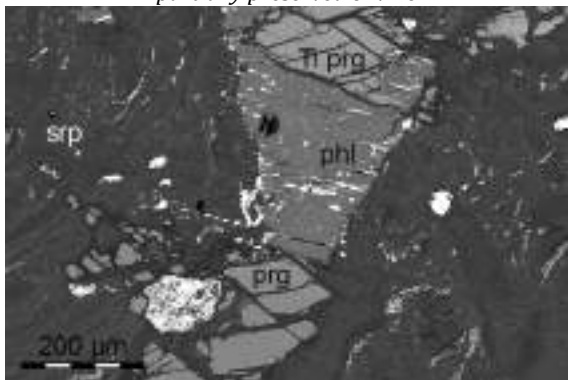


Figure 3.13i – Phlogopite with both Ti-rich pargasite and normal pargasite, distinguishable due to different backscatter coefficients.

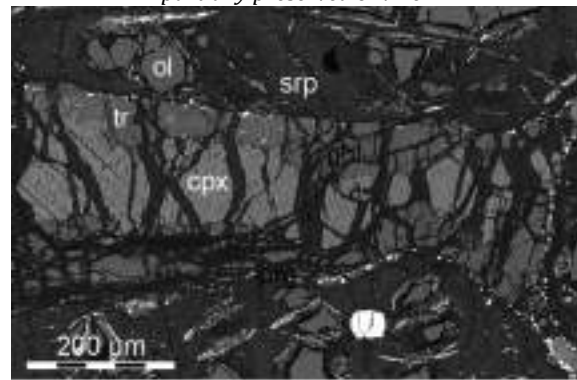


Figure 3.13j – Tremolite present as a partial alteration product of oikocrystic clinopyroxene.

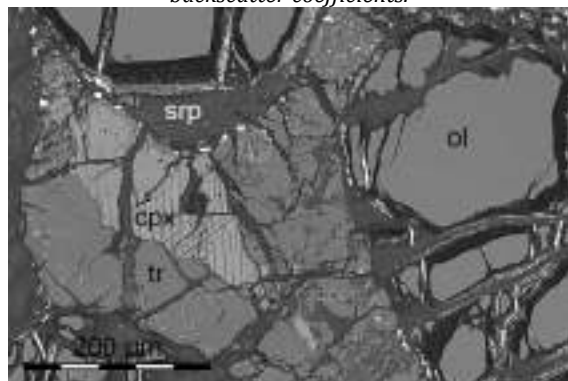


Figure 3.13k - Tremolite present as a partial alteration product of oikocrystic clinopyroxene.

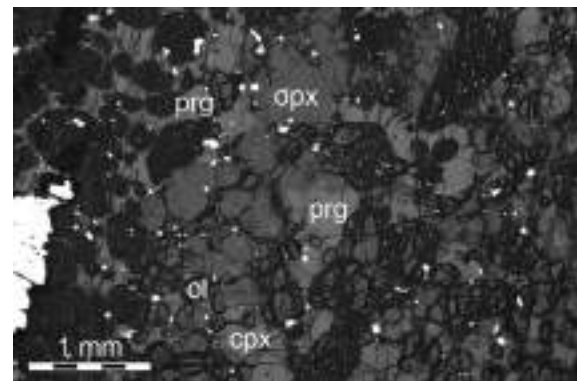


Figure 3.13l – Pargasite, orthopyroxene and clinopyroxene together with straight grain boundaries indicating that pargasite is not an alteration product of the pyroxenes.

Figure 3.13 – Images of magmatic and alteration amphibole within the Olivine Cumulate Unit

3.3.4.5 Plagioclase

The Olivine Cumulate Unit itself does not contain plagioclase by definition and it has not been observed as an accessory phase in the main part of the intrusion. However, towards the very base of the Olivine Cumulate Unit plagioclase begins to occur in the more abundant intercumulus. It occurs as an intercumulus phase, co-crystallised with pyroxene.

Plagioclase is also a major coarse component of the Pegmatoidal Gabbro Sub-Unit and so this is dealt with separately below.

3.3.4.6 Sub-units

Dunite

The Dunite Sub-Unit is an adcumulate situated at the base of the intrusion. The olivine is texturally and chemically the same as the overlying Olivine Cumulate Unit. Rather than being distinct on a textural or primary mineralogical basis, it is different from the rest of the cumulate primarily because of an almost complete preservation of magmatic olivine (Fig. 3.14). The level of preservation is exceptional given the antiquity of the deposit and the tectonic history of the region (2.1). The absence of intercumulus phases and the lack of serpentinisation may be interrelated.

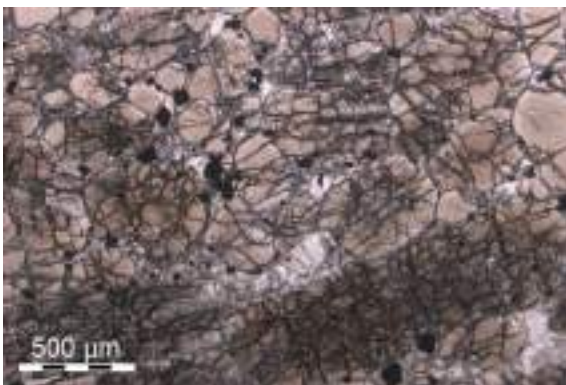


Figure 3.14a – Almost complete olivine adcumulate with several small grains of clinopyroxene

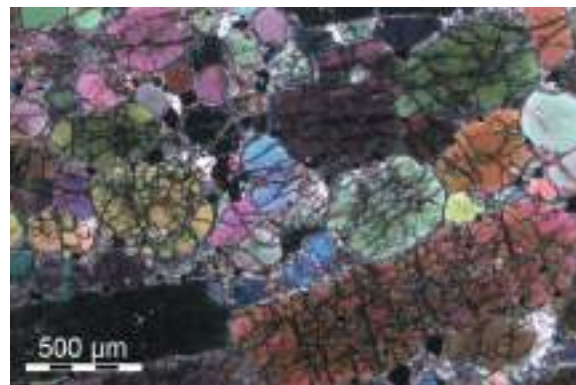


Figure 3.14b - Almost complete olivine adcumulate with several small grains of clinopyroxene

Figure 3.14 – Images of the Dunite Sub-Unit

Pyroxenite

There are multiple occurrences within the Olivine Cumulate Unit package where cumulus olivine is absent and the rock is a coarse pyroxenite. These drill core intersections are generally less than 15 cm wide and are composed of up to 3 cm sized diopside grains as well as minor enstatite. These intersections could represent stratigraphically important levels, such as the top

of separate pulses of magmatism; however, to date they do not correlate with the identified chemistry and mineral chemistry changes presented later in this section.

Pegmatoidal Gabbro

Pegmatoidal Gabbro Sub-Unit is similar to the pyroxenite in that it contains very coarse pyroxene and the latter unit could simply be a less evolved form of this sub-unit. The Pegmatoidal Gabbro Sub-Unit is particularly prevalent in the central and eastern portions of the main cumulate body, and also towards its top. The downhole thickness of the gabbroic intervals varies from less than 0.5 m up to 15 m although the angle between the contacts and the core axis is very variable and thus the true thickness remains unclear.

The Pegmatoidal Gabbro Sub-Unit contains large euhedral plagioclase grains in addition to pyroxene and, possibly secondary, amphibole (Fig. 3.15). Unusually, the plagioclase is black in colour while the pyroxene is lighter grey. The plagioclase can be altered to scapolite, particularly around the edges while the pyroxene is commonly altered to tremolite.

The pegmatoidal gabbros have sharp contacts with the surrounding cumulate and are frequently associated with mineralisation (Fig. 4.4), either where the sulphides are interstitial within the gabbro or as massive sulphides adjacent to the gabbro. It has not been possible to connect coarse grained pyroxenites or pegmatoidal gabbros laterally between drill holes.

The gabbroic nature of this unit was used as a rationale for targeting it for ultimately successful U/Pb geochronology that is not included in this project.



Figure 3.15a – Coarse lath shaped plagioclase is black in hand specimen. There are abundant alteration phases, mostly tremolite and chlorite.

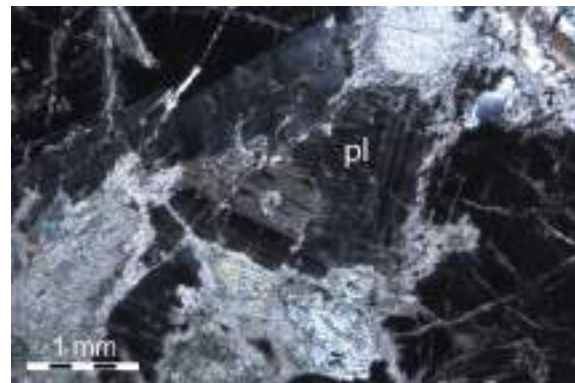


Figure 3.15b – Black with alteration phases including talc, prehnite and pumpellyite.

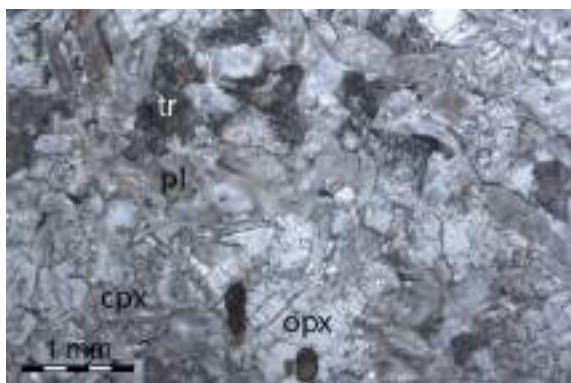


Figure 3.15c - Well preserved pegmatoidal gabbro with plagioclase and pyroxene. Note the unusually dark plagioclase in plane polarized transmitted light.

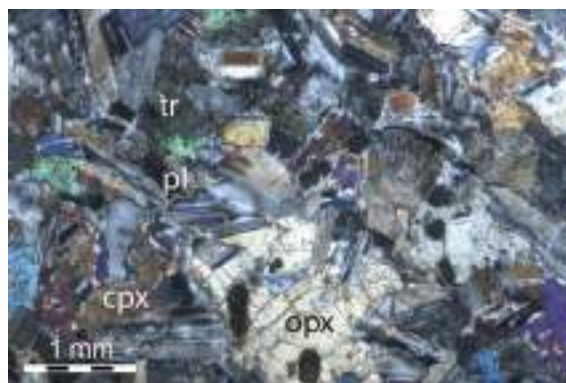


Figure 3.15d - Well preserved pegmatoidal gabbro with plagioclase and pyroxene.



Figure 3.15e - Large plagioclase lath with alteration phases. Note the black colour in plane-polarised transmitted light.

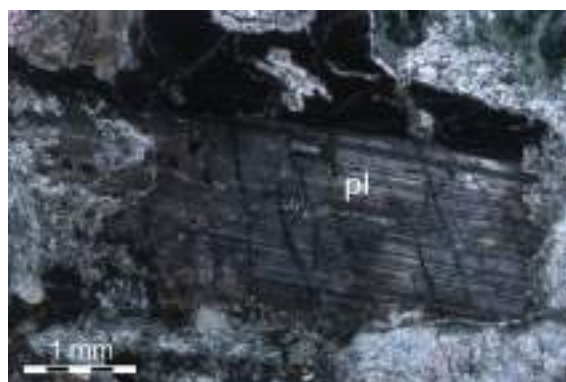


Figure 3.15f - Large plagioclase lath with alteration phases. Continuous polysynthetic twinning indicating that it is all one crystal.

Figure 3.15 - Images of the Pegmatoidal Gabbro Sub-Unit from the Olivine Cumulate Unit

3.3.5 Aphanitic Unit

The unit is composed of a groundmass of fine-grained (20-50 μm) interlocking plagioclase and pyroxene in roughly equivalent proportions (approximately 35-45% of groundmass each) and a smaller amount of fine-grained olivine (approximately 15-20% of groundmass).

3.3.5.1 Phenocrysts

Phenocrysts of olivine and rare plagioclase make up about 10% of the rock (Fig. 3.16a-d), although the olivine phenocrysts are generally less than 1 mm in size and difficult to see in hand specimen. Olivine phenocrysts form elongate, narrow grains, with the longest observed one being a 4 mm by 0.2 mm single crystal (Fig. 3.16c). The cores of phenocrysts are frequently hollow. These are interpreted as extrusive olivine textures, which are compatible with the fine-grained nature of the groundmass.

Plagioclase is present as small crystals in the groundmass and as larger crystals (up to 3 mm in length, Fig. 3.16e-f) containing numerous inclusions of olivine but not pyroxene (Fig. 3.16j). This indicates that they crystallised prior to pyroxene formation, thus these plagioclase grains are

interpreted as phenocrysts. Pyroxene is present only as a groundmass phase. As in the Olivine Cumulate Unit, both orthopyroxene and clinopyroxene are present as enstatite and diopside. These two pyroxenes are present in distinct domains, so that part of a sample is enstatite-dominated, whereas other parts are dominated by diopside (Fig. 3.16d).

The phenocrysts are concentrated in lineations throughout the unit as well as sporadically amongst the groundmass. These lineations of phenocrysts appear to be a focus for the limited serpentinisation that has occurred in this unit, creating a network of fine black veins (Fig. 3.18a).

3.3.5.2 Groundmass

Texturally, the rock exhibits considerable variability and domaining of minerals at the microscopic and hand specimen scale. Unaltered samples of this rock appear relatively homogenous, with minor serpentine veining being the only discernible texture. However, in more altered samples separate domains become more obvious. Finer grained (<<1 mm), moderately brecciated domains alternate with few coarser grained (<1 mm) more homogenous layers.



Figure 3.16a - Euhedral olivine in fine-grained pyroxene and plagioclase groundmass, typical of the Aphanitic Unit



Figure 3.16b - Potential 'hopper' type olivine in fine-grained groundmass.

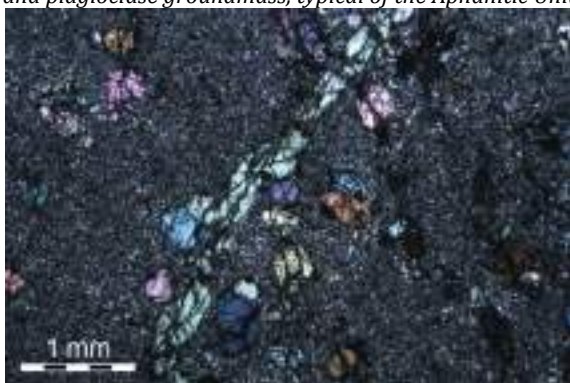


Figure 3.16c - Elongate individual crystal of olivine and numerous smaller phenocrysts

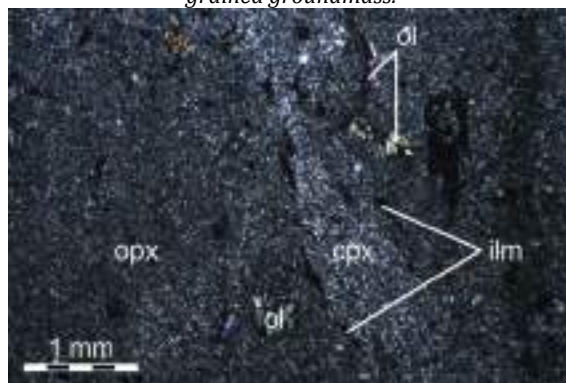


Figure 3.16d - Domaining of orthopyroxene- and clinopyroxene-dominated groundmass;

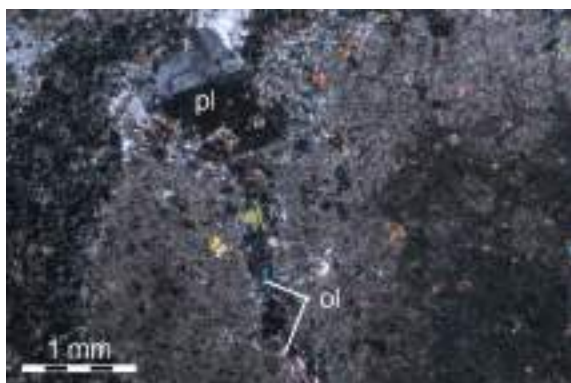


Figure 3.16e - Large plagioclase and olivine phenocrysts with serpentine veining



Figure 3.16f - Large plagioclase and olivine phenocrysts with serpentine veining

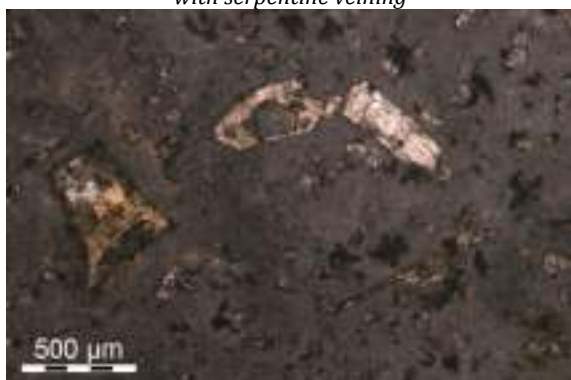


Figure 3.16g - Altered aphanitic sample still retains phenocryst shapes

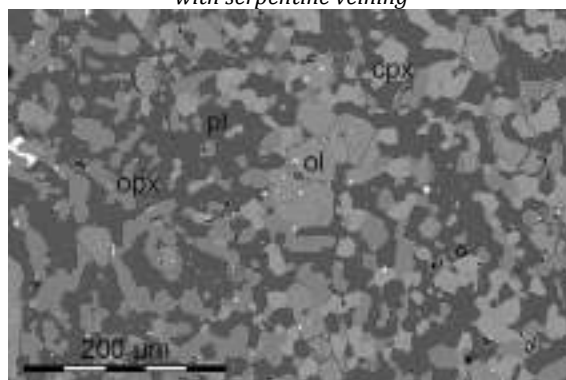


Figure 3.16h - Fine-grained olivine, clinopyroxene, orthopyroxene and plagioclase.

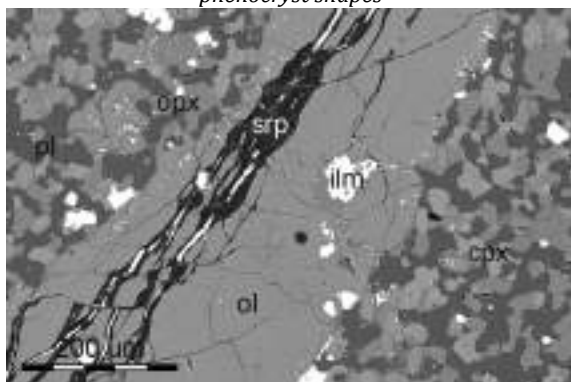


Figure 3.16i - Elongate olivine a focus for serpentinisation.

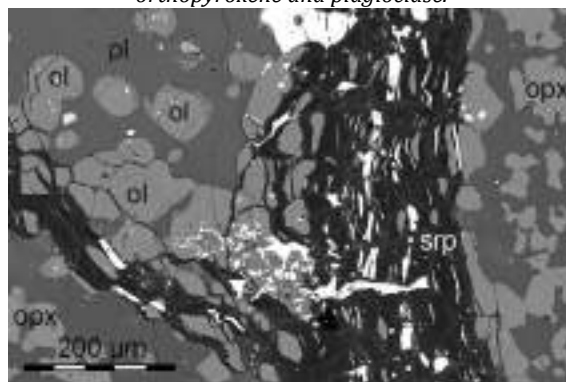


Figure 3.16j - Serpentine vein alongside large plagioclase containing only olivine inclusions

Figure 3.16. Images of thin sections from the Aphanitic Unit

3.3.5.3 Alteration

One of the most striking characteristics of the Aphanitic Unit is that it is in general remarkably unaltered and composed almost entirely of fine-grained primary magmatic minerals. Small black serpentine veinlets are concentrated around lineations of phenocrysts, and the long axes of olivine crystals appear to be particularly susceptible. These fine black serpentine veinlets become a characteristic logging feature of the otherwise featureless fine-grained unit.

In some occurrences, the Aphanitic Unit can be more pervasively altered. This does not appear to be spatially related to the Olivine Cumulate Unit. Instead, strongly altered segments can occur

sporadically within the Aphanitic Unit, but particularly so in the vicinity of the contact with the hanging wall lithologies (Mafic Suite or Breccia Unit).

3.3.6 Contact between the Olivine Cumulate Unit and the Aphanitic Unit

There are two styles of contact between the Aphanitic Unit and the Olivine Cumulate Unit, the first is a seemingly gradational contact that is generally present at the base of the intrusion and the second is a micro-intruding contact that is dominant on the sidewall and upper contacts of the intrusion. This micro-intruding contact is also evident at the basal contact but it is less pronounced.

Gradational contact

In drill core, at its base, the Olivine Cumulate Unit becomes increasingly pyroxenitic (3.4.1.3) and the transition into the underlying fine-grained Aphanitic Unit can be hard to distinguish, especially as the larger pale pyroxene oikocrysts and darker groundmass begins to resemble the characteristic aphanitic texture while larger pyroxene crystals are present within the aphanitic, potentially recrystallisations (Fig. 3.17). The Ni content of olivine has an abrupt change from Olivine Cumulate Unit to Aphanitic Unit and is the clearest indication that the boundary in hole 49 lies between 864.22 m and 865.83 m (3.4.1.4, Fig. 3.21).



Figure 3.17a – 864.22 m sample has oikocrystic pyroxene and interstitial mineralisation.

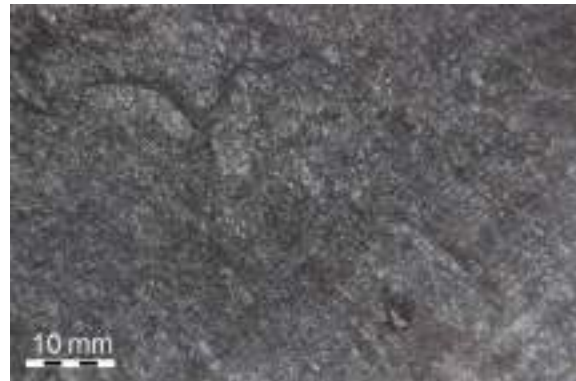


Figure 3.17b – 865.83 m sample has similar superficial appearance but is much finer.

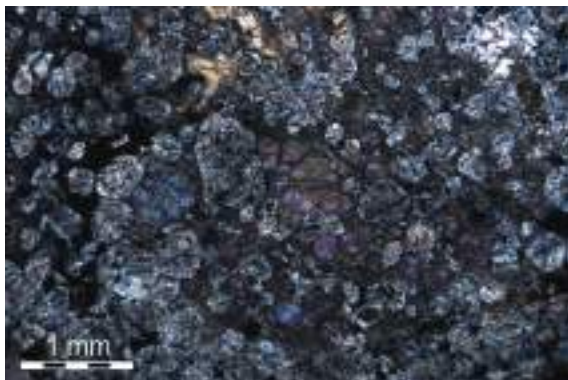


Figure 3.17c – 864.22 m cumulus olivine, orthocumulate in abundant pyroxene



Figure 3.17d - 865.83 m fine-grained olivine and pyroxene.



Figure 3.17e - 864.22 m cumulus olivine, orthocumulate in abundant pyroxene

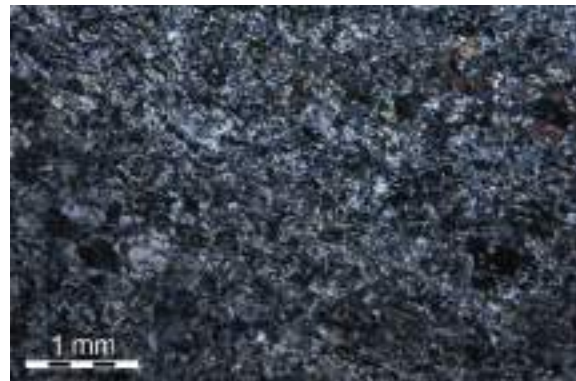


Figure 3.17f - 865.83 m fine-grained olivine and pyroxene.

Figure 3.17 – Images of basal contact between the Olivine Cumulate and Aphanitic Units

Network contact

The network contact gives the aphanitic its characteristic texture that led to it first being described as ‘tiger rock’ (Fig. 3.18). This texture was encountered extensively in holes that tracked down the sidewall of the deposit, seemingly going in and out of the Aphanitic Unit. The fine-grained nature of the rock made it difficult to classify by eye.

A network of dark vein-like domains are visible throughout the rock (Fig. 3.18a-b). Within these vein-like domains coarse (2 mm) olivine identical in appearance to those in the olivine cumulate unit (Fig. 3.18c), These are particularly accentuated by the presence of mineralisation, within the darker parts of the texture.

Microscopy confirmed the observation of the darker network being contained larger olivine similar to those in the Olivine Cumulate Unit, generally more clinopyroxene rich than the orthopyroxene rich aphanitic parts (Fig. 3.19a-d). The darker parts of the network are also more serpentinised than the well preserved aphanitic parts of the rock (Fig. 3.19b).

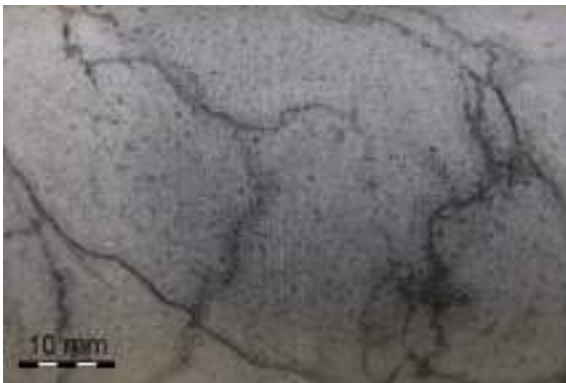


Figure 3.18a – The Aphanitic Unit not near the contact to the Olivine Cumulate Unit. Small olivine phenocryst can be observed and serpentine veining.

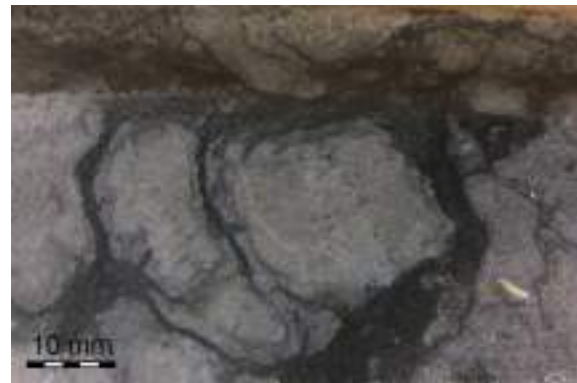


Figure 3.18b – The Aphanitic Unit near the contact with the Olivine Cumulate Unit. Large serpentine ‘veins’ give the unit a characteristic texture.



Figure 3.18c – Near the Olivine Cumulate Unit these serpentine ‘veins’ can be mineralised. The mineralisation reveals cumulate large olivine from the Olivine Cumulate Unit indicating that they are micro-intrusions as opposed to veins.

Figure 3.18 - Photographs of the Aphanitic Unit



Figure 3.19a – Dark areas of serpentinised cumulate and light areas of Aphanitic Unit.

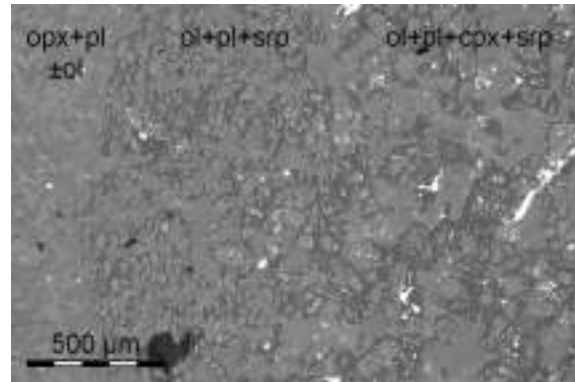


Figure 3.19b – Transition between the aphanitic light part, plagioclase with olivine inclusions then cumulus olivine on the right side.

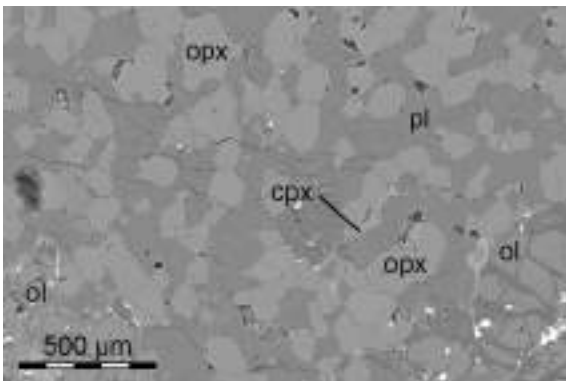


Figure 3.19c – Aphanitic part of thin section with fine grained orthopyroxene, plagioclase and olivine phenocryst

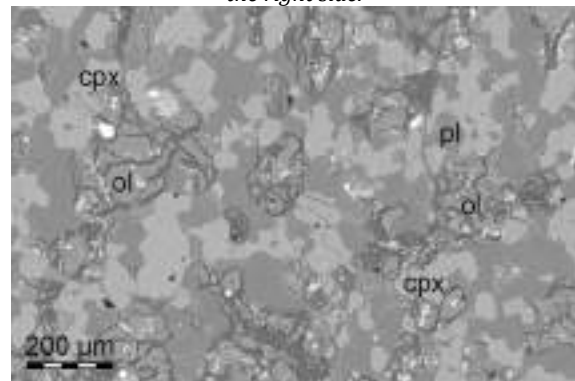


Figure 3.19d – Darker part of thin section with olivine, clinopyroxene and plagioclase.

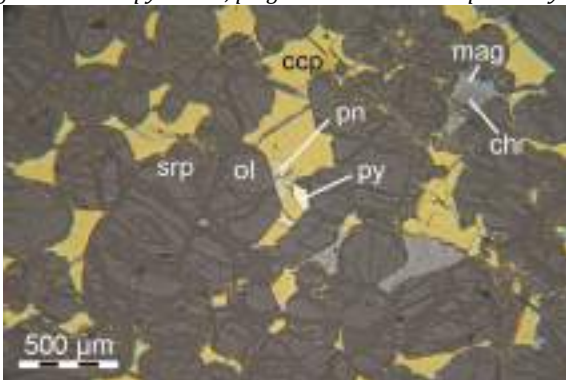


Figure 3.19e – Cumulus olivine in mineralised intercumulus within a micro-intrusion within the Aphanitic Unit.

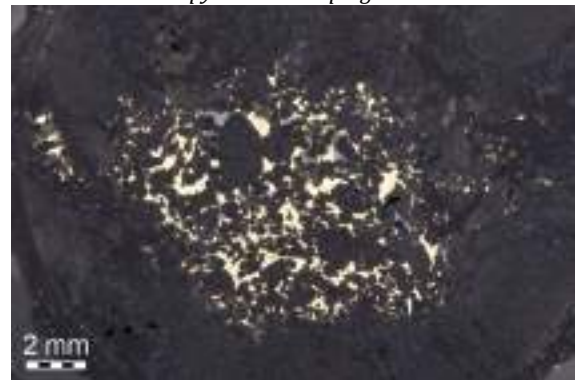


Figure 3.19f – Patch of mineralised cumulus olivine within a micro-intrusion within the Aphanitic Unit.

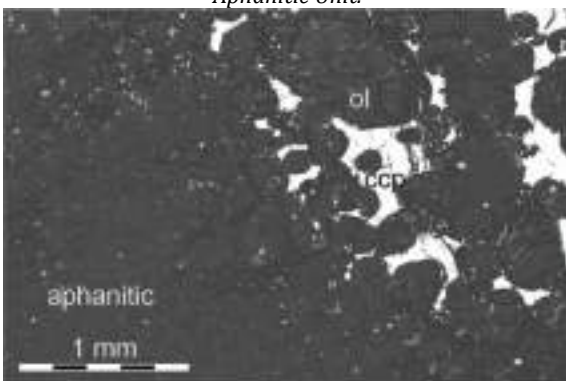


Figure 3.19g – Fine-grained Aphanitic Unit contact with mineralised cumulate olivine micro-intrusion.

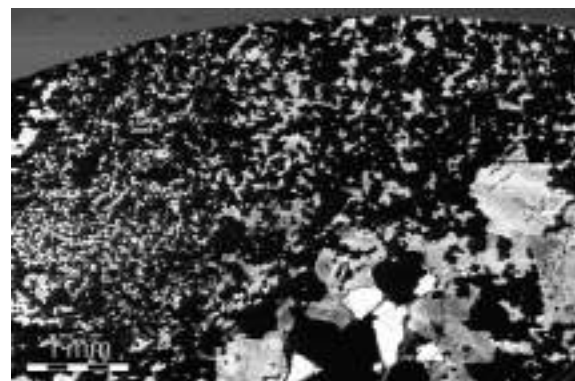


Figure 3.19h – Cathodoluminescent image showing differing crystal size of plagioclase between the Aphanitic Unit and a micro-intrusion of Olivine Cumulate Unit.

Figure 3.19 – Images of the micro-intrusional texture of the Olivine Cumulate Unit into the Aphanitic Unit.

3.3.7 Petrographic interpretations

3.3.7.1 Volcano-sedimentary Unit

This is clearly a metamorphic rock, however the mineral assemblage, particularly the porphyroblasts being chlorite, mica and quartz, implies that it has undergone extensive retrogression. Therefore it is difficult to assess the grade this rock may have reached. It could be hesitantly suggested that, due to the equant nature, zoning and abundant inclusions that type 1 porphyroblasts are after garnet or scapolite while type 2 porphyroblasts maybe have originally been chlorite or phlogopite (Fig. 3.7), meaning this would be a greenschist-facies schist or even phyllite.

The compositional layering could either be the result of migration of elements due to metamorphism or original compositional layering. Migration of elements into compositional bands is typically associated with high grade metamorphism. Original compositional layering could have been laminations associated with a sedimentary or volcano-sedimentary rock such as a tuff. The abundant mica and chlorite in the rock points towards significant clay mineral content in the protolith suggesting that it could have been pelitic sediment. The presence of plagioclase means the situation may be more complex as the texture could be either metamorphic or original, the latter suggesting a volcanic component in the protolith.

3.3.7.2 Breccia Unit

The Breccia Unit has clearly undergone extensive alteration, as it is composed primarily of alteration minerals and textures, but variability in the original protolith most likely also accounts for some of the differences within the unit. The protolith of parts of the Breccia Unit is sedimentary, with clasts primarily being made of albitised quartzite. However other samples from within the breccia contain euhedral amphibole pseudomorphing pyroxene suggesting a mafic igneous protolith. The extensive dolomite is thought to be sedimentary in origin (Jillings, 2015).

3.3.7.3 Olivine Cumulate Unit

The rock should be classified as a serpentinite according to the International Union of Geological Sciences (IUGS) definition (Fettes et al., 2007). Due to the ease with which the protolith olivine contents can be observed the Olivine Cumulate Unit protolith would have been coarse grained, ultramafic and contained >40% olivine therefore should be classed as a peridotite according to the IUGS definition (Le Maitre et al., 2002).

Cumulate olivine units can be found at the base of komatiite and picrite flows meaning that they are not intrusive as the classification 'peridotite' would imply. However in this case it is explicitly recommended that the intrusive terminology be used (Arndt et al., 2008).

3.3.7.1 Serpentinisation

The wide array of samples in different degrees of serpentinisation means that the progression of serpentinisation on the micro-scale can be established. The pattern of serpentinisation of olivine is uniform with the first phase of serpentinisation being the formation of serpentine along the undulatory cracks that are a diagnostic feature of olivine. This serpentinisation occurs in all samples, except those from the dunite sub-unit. It characteristically results in the formation of larger needles of magnetite (Fig. 3.20a), or increased concentration of fine-grained magnetite compared to the rest of the serpentine (Fig. 3.20b).

The next stage of serpentinisation leaves small 'islands' of olivine preserved in amongst a majority of serpentine. This serpentine generally contains diffuse fine-grained magnetite. Most of the olivine at the deposit is found in this condition, usually as only a small portion of a mostly serpentinised thin section (Fig. 3.20a-d).

The final step of serpentinisation is the replacement of these last 'islands' of olivine with serpentine. The outlines of the 'islands' remains, and are identifiable by eye. This makes identification of samples with preserved olivine exceedingly difficult because the same texture is preserved and indistinguishable in both hand specimen and also plane-polarised transmitted light. It becomes obvious in cross polarised transmitted light or reflected light showing the higher polishing hardness of olivine. Generally this last stage does not have magnetite within it.

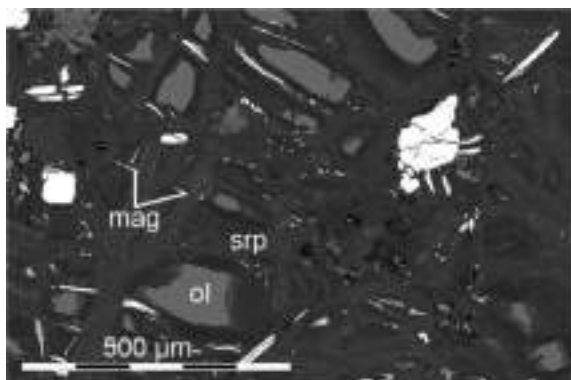


Figure 3.20a – Partially serpentinised olivine cumulate with needle-like magnetite from early stage serpentinisation.

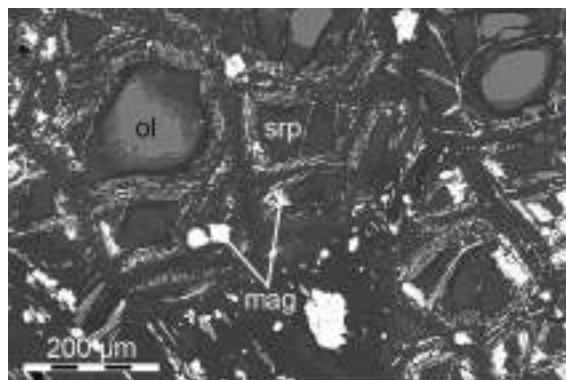


Figure 3.20b – Needle-like and disseminated magnetite around 'islands' of preserved olivine.

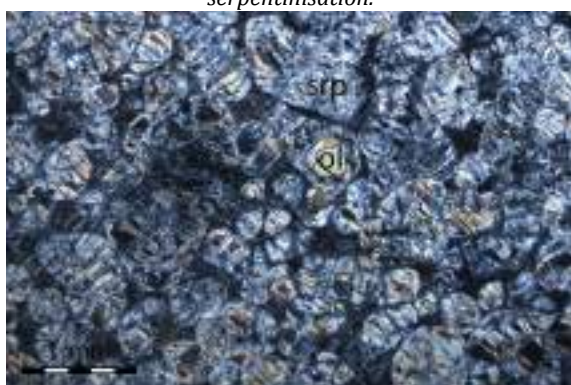


Figure 3.20c – Partially serpentinised olivine cumulate in cross polarized transmitted light

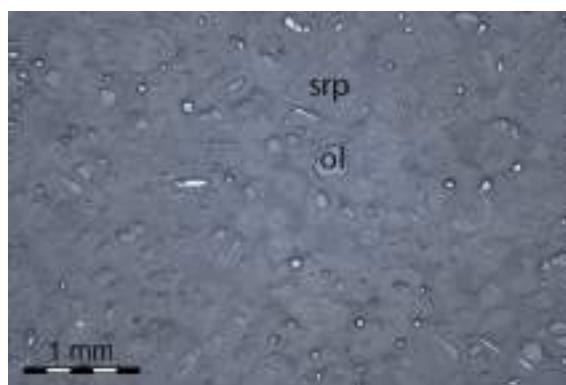


Figure 3.20d - Partially serpentinised olivine cumulate in reflected light. The polishing hardness of olivine means it is more readily identifiable.

Figure 3.20 – Images of serpentinised samples from the Olivine Cumulate Unit indicating the progression of serpentinisation on a mineral scale

3.3.7.2 Aphanitic Unit

The Aphanitic Unit itself as described in 3.3.5 is a relatively simple volcanic unit that is defined in 3.5.5 using whole rock chemistry. The unaltered nature of the rock is remarkable for the CLGB and the small spidery serpentine veins remain its only distinguishing feature in hand specimen.

The domaining of clinopyroxene and orthopyroxene is difficult to explain and is interpreted as a primary magmatic feature in the absence of strain indicators or metamorphic minerals indicating later transformation. It is suggested auto-brecciation could produce different domains. On the larger scale alternating finer, more brecciated bands and few slightly coarser more homogenous bands are interpreted as flow-tops and cumulate portions, respectively. The relatively thin cumulate portions (<20 m) are distinct from the peridotites of the main cumulate

body in that the former are finer-grained, much less serpentinised, and have exclusively orthocumulate textures.

The rock was first encountered in contact with the Olivine Cumulate Unit, both above below and on the sidewall, where it is texturally considerably more complex (Fig. 3.18). The presence of larger preserved olivines, matching those of the Olivine Cumulate Unit, and also mineralisation meant that the Aphanitic Unit was originally interpreted as an alteration product of the Olivine Cumulate Unit, where the lighter domains were altered.

However, on-site XRD analysis on over 100 samples showed the Aphanitic Unit to contain limited to no alteration minerals within the lighter domains (Fig. 3.18c). Microscope analysis revealed that lighter domains are in fact the volcanic unit described above, and later further drilling away from the Main Cumulate Body returned samples of this unit without the Olivine Cumulate Unit texture.

Figures 3.19a+b show this texture and the transition from the fine-grained volcanic to the larger olivines. Figures 3.19e-g show the presence of large, cumulus shaped olivine within this contact. Microprobe analysis revealed that these olivines were high-Ni cumulate type whereas the olivines in the lighter part were low-Ni Aphanitic Unit phenocrysts, distinguishing them further.

The presence of olivine grains derived from the Olivine Cumulate Unit within a network extending both into the hanging wall and footwall volcanics has led to the interpretation that this network is a micro-intrusion of the Olivine Cumulate Unit into the Aphanitic Unit. The potential reasons behind this are discussed in section 3.7.6.

3.4 Mineral chemistry

The chemistry of magmatic minerals has long been used to record cryptic layering in mafic and ultramafic intrusions (Eg. Wager, 1968). No systematic layers or pulses have been observed during the logging of the Sakatti deposit and so an attempt was made to examine the mineral chemistry of the magmatic minerals that are still present and establish if these revealed separate layers or episodic pulses of magmatic activity (Table 3.1 and 3.2).

The presence of magmatic minerals was difficult to establish in all but the most well preserved samples. The most common manifestation of this problem is that samples where the degree of serpentinisation was 90-95% were not distinguishable from those where the degree of serpentinisation was 100%. This meant that of the 100 samples taken downhole approximately 4/5ths of them did not contain preserved magmatic minerals. This has resulted in an unavoidable paucity of mineral chemistry data, leaving parts of the Olivine Cumulate Unit that are more serpentinised unrepresented.

Olivine Cumulate	Na ₂ O	MgO	Al ₂ O ₃	SiO ₂	K ₂ O	CaO	TiO ₂	Cr ₂ O ₃	V ₂ O ₃	MnO	FeO	CoO	NiO	Totals
Olivine	<0.0 5	48.7 3	<0.0 4	40.3 4	<0.0 5	0.03	0.04	<0.0 4	<0.0 4	0.13	10.2 2	<0.0 6	0.42	100.0 3
Serpentine	<0.0 5	36.0 6	0.22	40.5 6	<0.0 5	0.11	0.03	<0.0 4	<0.0 4	0.27	8.4	<0.0 6	0.44	86.12
Diopside	0.35	17.4 7	3.52	51.8 7	<0.0 5	20.8 3	0.5	1.04	<0.0 4	0.13	4.36	<0.0 6	0.06	100.1 7
Tremolite	0.34	19	2.2	51.4 7	<0.0 5	20.5 4	0.24	1.26	<0.0 4	0.11	3.5	<0.0 6	0.13	98.82
Enstatite	<0.0 5	31.8 8	1.43	56.3 7	<0.0 5	2.26	0.14	0.54	<0.0 4	0.17	7.51	<0.0 6	0.12	100.4 6
Pargasite	2.37	19.0 2	10.4 6	46.5 6	0.57	11.6 5	1.18	1.81	0.06	0.03	4.61	<0.0 6	0.09	98.41
Plagioclase	2.26	0.05	32.8 5	47.8	0.07	16.3 3	<0.0 2	<0.0 4	<0.0 4	<0.0 3	0.51	<0.0 6	<0.0 2	99.87
Chromite	na	5.52	12.9 6	<0.0 3	na	<0.0 2	0.35	33.0 4	0.14	0.61	43.6	<0.0 6	0.07	96.34
Magnetite	na	1.45	1.29	<0.0 3	na	<0.0 2	0.43	11.6 3	0.17	0.23	78.8 2	<0.0 6	0.14	94.19

Table 3.1 – Representative WDS data of primary magmatic minerals and alteration phases in the Olivine Cumulate Unit

Aphanitic	Proportion of each	NaO	MgO	Al ₂ O ₃	SiO ₂	CaO	TiO ₂	Cr ₂ O ₃	MnO	FeO	Total
Phenocrysts											
Olivine (phenocryst)	0.15	nd	42.2	nd	39.4	nd	nd	nd	nd	18.5	100.1
Plagioclase (phenocryst)	0.05	5.4	nd	27.6	54.7	10.8	nd	nd	nd	0.7	99.2
Groundmass											
Enstatite	0.15	nd	31	0.7	56.9	1.2	nd	nd	nd	11.8	101.6
Diopside	0.2	0.7	16	2.1	52.8	21.5	0.8	0.7	nd	5.4	100
Olivine	0.15	nd	42.9	nd	40	nd	nd	nd	nd	17.2	100.2
Plagioclase	0.29	7.3	nd	25.5	59.2	7.7	nd	nd	nd	0.5	100.3
Ilmenite	0.01	nd	3.6	nd	nd	nd	52.9	nd	0.6	42.9	100.1

Table 3.2 – Representative EDS data of primary magmatic minerals in the Aphanitic Unit

3.4.1 Olivine

3.4.1.1 Olivine overview

The olivine in the Olivine Cumulate Unit is characterised by Mg# ($\text{Mg\#} = \text{atomic Mg}/(\text{Mg}+\text{Fe})$) between 0.85-0.91 and Ni contents clustering between 3000-3700 ppm (Fig. 3.21). Compared to olivine from most other mafic-ultramafic intrusions with comparable Mg#, the Ni contents are relatively high, inconsistent with crystallisation from a melt that was S saturated (Brenan and Caciagli, 2000).

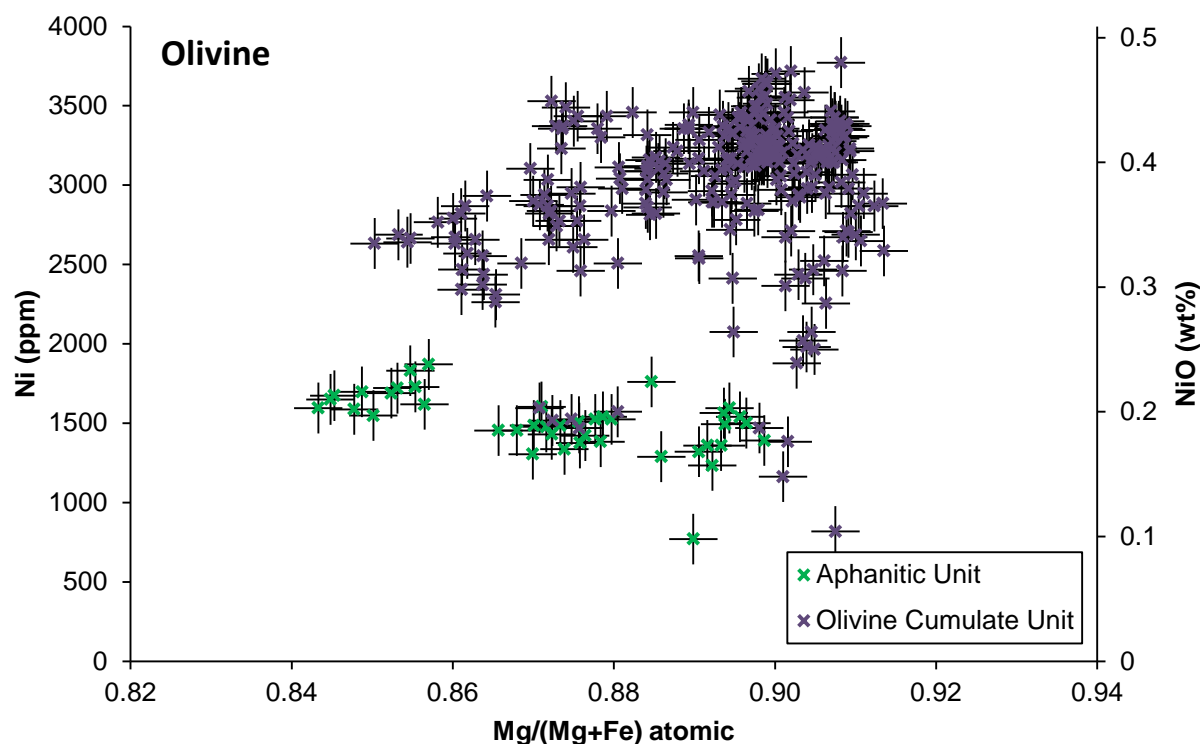


Figure 3.21 - Olivine chemistry from the main cumulate body in the Sakatti deposit and the aphanitic footwall. Ni (ppm) and NiO (wt%) are both included for reference only. Typical 3σ errors on analyses are 160 ppm Ni and 0.003 Mg#

The Ni content of olivine in the intrusion is generally high, however, some samples contain variable olivine Ni compositions, which are considered below.

Overall, the olivine Ni and Mg# compositions are broadly comparable with 'main ore' olivine chemistry reported (500-2000 ppm and 77-86 Mg#) from the Kevitsa deposit (Mutanen, 1997; Yang et al., 2013). At Sakatti, however, no olivine has been identified that approaches the unusual ultra-nickeliferous (up to 14,000 ppm) composition found in the 'Ni-PGE ore' at Kevitsa (Yang et al., 2013).

3.4.1.2 Olivine in the Aphanitic Unit

Olivine is present within the Aphanitic Unit both as phenocrysts and also smaller olivines within the groundmass. These could not be distinguished from one another on the basis of their chemistry. The Aphanitic Unit olivines are distinct from the Olivine Cumulate Unit olivines on the basis of their Ni content, 1000-2000 ppm for the former compared to 2500-3700 ppm for the latter. Unlike the Olivine Cumulate Unit olivines, the Aphanitic Unit olivines do not exhibit the expected decrease in Ni content with Mg#. This suggests that the aphanitic olivine have originated from a parent melt that has been depleted in Ni.

3.4.1.3 Olivine in the Olivine Cumulate Unit

General chemistry

The vast majority of the olivine within the Olivine Cumulate Unit plot on a trend of decreasing Ni content with decreasing Mg# as expected (De Hoog et al., 2010). This trend runs approximately from Mg# 0.91 and 3600 ppm Ni to Mg# 0.85 and 2600 ppm Ni. This trend occurs with decreasing depth in the deposit (Fig. 3.22) with the least magnesian olivines being the shallowest olivines observed (453.5 m). However it also occurs at a horizon in the middle of the Olivine Cumulate Unit, with the highest analysed olivine being 666.16 m and

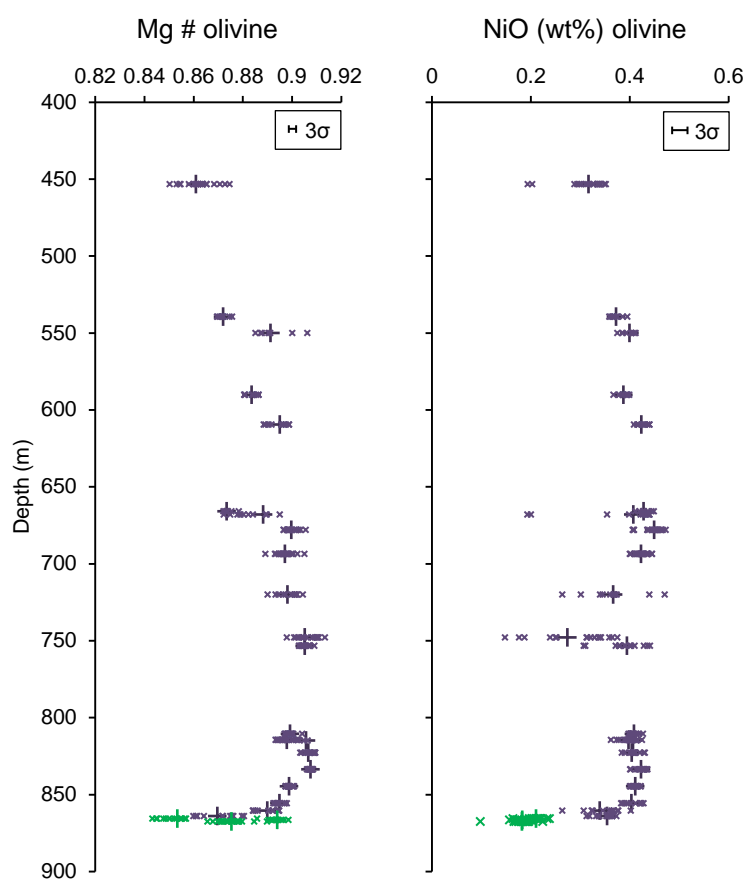


Figure 3.22 – Depth profile of hole 49 showing olivine mineral EPMA chemistry. Olivine Cumulate Unit is shown in purple with averages as large cross marks and Aphanitic Unit is shown in green. Mg# is atomic proportions and NiO is wt%. Three areas of the NiO profile are the focused on: the contact with the Aphanitic Unit; two bimodal samples at 453.5 m and 668.14 m; and olivine with Ni-depleted rims between 720.22 m and 753.36 m.

there is also more evolved olivine at the very base of the intrusion. The general decrease in Mg#

upwards suggests that the Olivine Cumulate Unit has evolved upwards and suggests that the deposit is the correct way up. The majority of the Olivine Cumulate Unit clusters at higher Mg# and Ni content with these relatively limited more evolved portions filling the lower Mg # and Ni content part of the trend (Fig. 3.21).

There are several departures from the Mg# Ni trend and these are considered separately below.

Contact with Aphanitic Unit

The base of the Olivine Cumulate Unit where it contacts the Aphanitic Unit is complex and differs from the general trend of the rest of the Olivine Cumulate Unit. In numerous drill holes it is difficult to establish precisely when the Olivine Cumulate Unit ends and the Aphanitic Unit underneath begins. The Olivine Cumulate Unit itself is less ultramafic towards the base as the plagioclase content increases. This is also shown in the whole-rock data (Fig. 3.23). This decrease could be down to assimilation of the more mafic Aphanitic Unit or a marginal reversal that is frequently seen at the base of cumulate ultramafic intrusions (Latypov et al., 2011).

The Mg# of the olivine also shows a slight gradual decrease towards the very base of the intrusion, however it is not as pronounced as the whole-rock data. The Ni content of the olivine is more revealing, potentially because, as opposed to Mg#, the Ni content of the aphanitic olivine is different from those in the the Olivine Cumulate Unit. There is a slight decrease in Ni content with increasing depth, associated with Mg#, until between 864.22 m and 865.83 m when there is an abrupt shift in Ni content from an average of 0.35 wt% oxide to 0.21 wt% oxide (Fig. 3.24). This is consistent with the petrological differences observed in thin section (3.3.6).

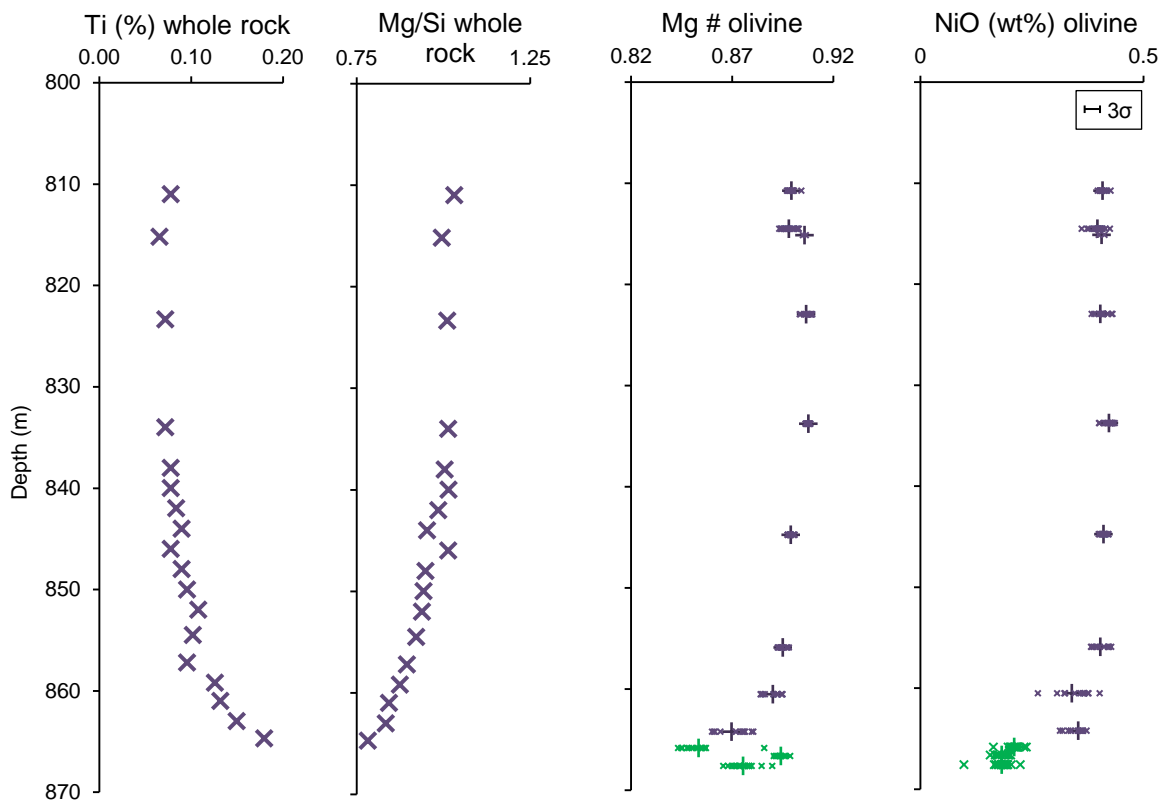


Figure 3.23 - Depth profile of the base hole 49 showing whole-rock chemistry and olivine mineral chemistry. While whole-rock chemistry is gradual towards the Aphanitic Unit, the olivine NiO values show an abrupt change between units. Olivine Cumulate Unit is shown in purple with averages as large cross marks and Aphanitic Unit is shown in green. Mg# is atomic proportions and NiO is wt%. 3σ error on measurements is below the size of the data points, with the exception of NiO, where it is 0.02 wt%.

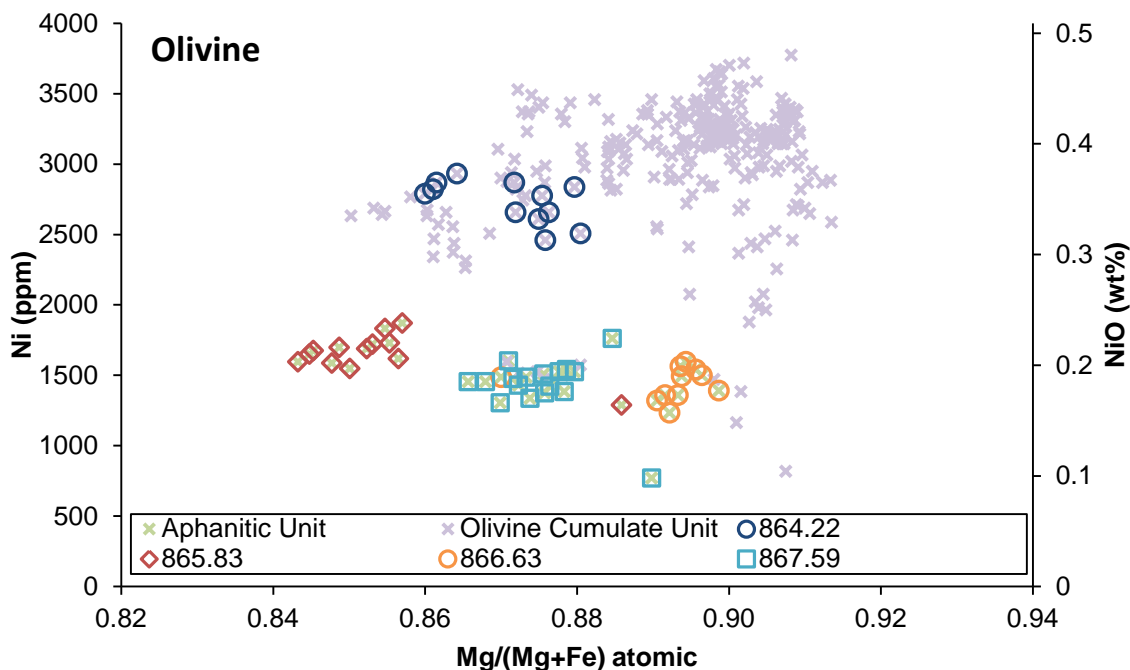


Figure 3.24 - Olivine chemistry from the main cumulate body in the Sakatti deposit and the aphanitic footwall. Ni (ppm) and NiO (wt%) are both included for reference only. The lowest Olivine Cumulate Unit sample (864.22 m) and the aphanitic samples below are highlighted.

This basal contact differs texturally from the observed side-wall and top contacts where the characteristic micro-intrusive texture is present. Similarly in these cases the Ni content of the olivine changes abruptly between the aphanitic parts and Olivine Cumulate Unit parts of the individual samples.

3.4.1.4 Ni depleted olivine

The most significant departure from the Mg# and Ni decrease trend is from four samples that show depleted Ni despite relatively high Mg# (Fig. 3.25). These four samples occur in the centre of the mineralisation and are themselves well mineralised. The Ni depletion is not uniform across individual olivine. Lower Ni values were recorded in olivine in close proximity to the boundary of the original olivine cumulus grain whereas the centres of the grains carry Ni levels similar to the rest of the olivine cumulate.

This variation in Ni content in the olivine could either be a result of olivine growth in a changing parental melt, resulting in zoning, or it could be diffuse loss of Ni from olivines that are not in equilibrium with their surrounding melt or minerals. EPMA maps of Ni content within the olivine show that the Ni content is preserved in serpentine but also that Ni does not seem to be zoned in a distinct pattern but that the loss of Ni appears more diffuse.

That these olivines occur within samples that host significant sulphide mineralisation suggests that they are unlikely to have been in equilibrium with the host melt and that they may have lost Ni either directly to sulphide melt or to Ni-depleted silicate melt that has itself lost Ni to sulphide melt. The Ni distribution does not vary where the olivine is located adjacent to sulphide and so it is reasonable to assume that this process occurred between the olivines and melt rather than a latter process where Ni has diffused from olivine into solid sulphide minerals.

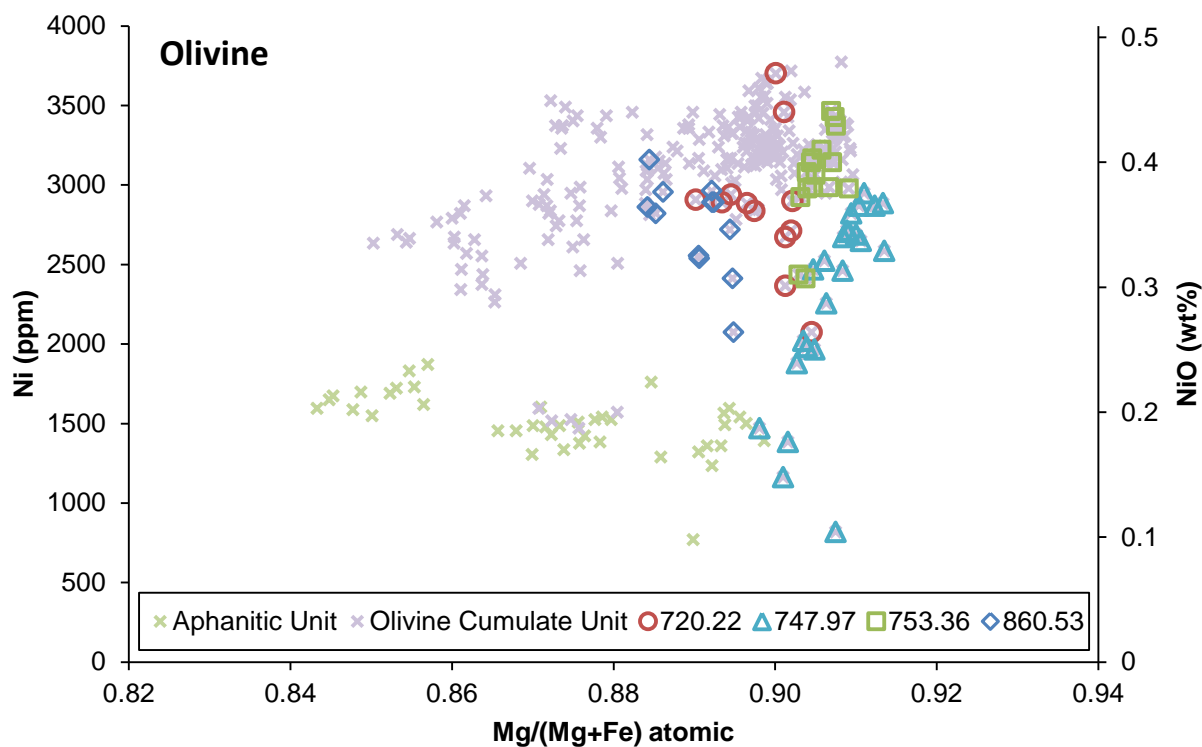


Figure 3.25 - Olivine chemistry from the main cumulate body in the Sakatti deposit and the aphanitic footwall. Ni (ppm) and NiO (wt%) are both included for reference only. Four samples that contain olivine with low Ni rims are highlighted.

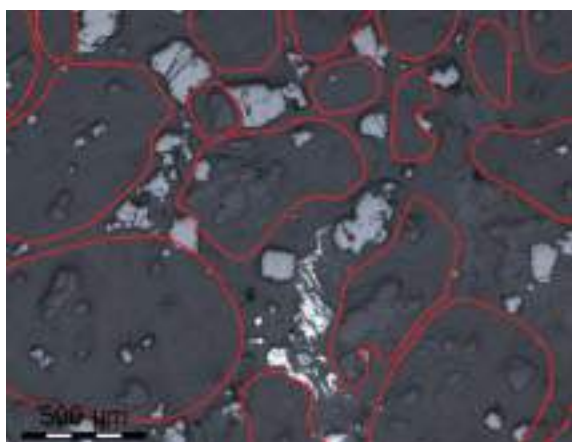


Figure 3.26a - Reflected light image showing preserved olivine

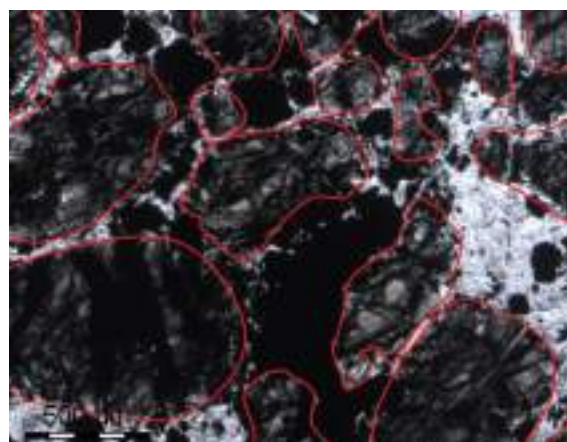


Figure 3.26b - Transmitted light image showing olivine cumulus shapes, which have been outlined.

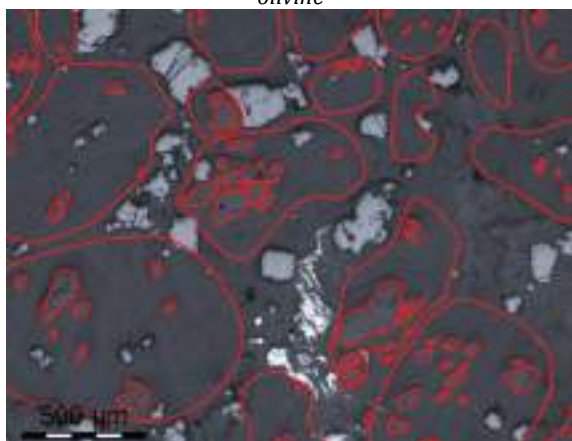


Figure 3.26c - Reflected light image on which preserved

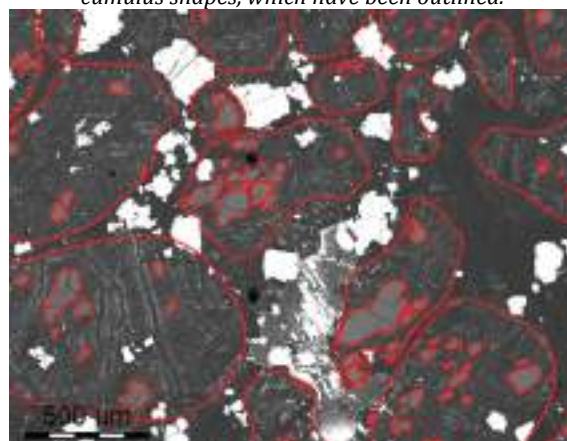


Figure 3.26d - Backscatter electron image showing

olivine has been outlined in addition to cumulus shapes.

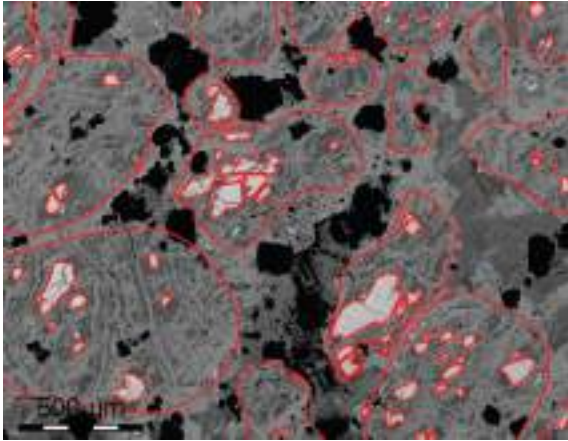


Figure 3.26e – EPMA map showing Mg highlighting preserved olivine.

preserved olivine.

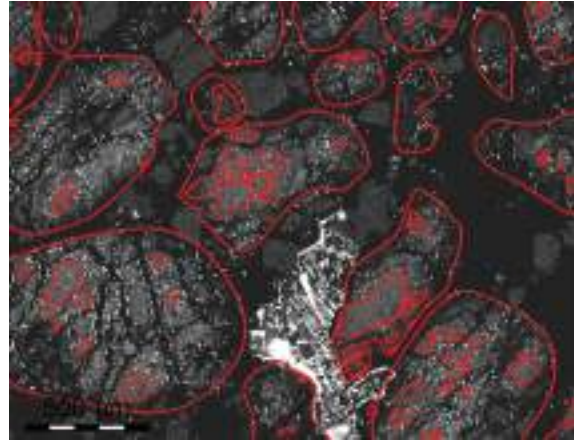


Figure 3.26f –EPMA map showing Ni. Ni content is lower around the rims of the cumulus shapes. Note that this is true in both olivine and serpentine. Also note preserved olivine is not identifiable based on Ni content.

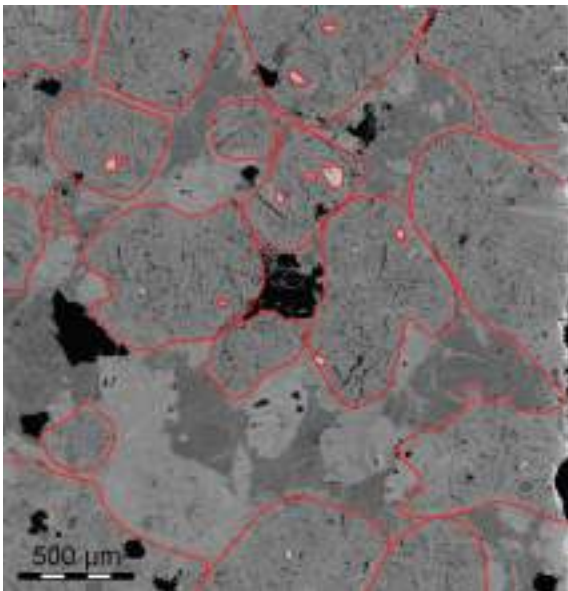


Figure 3.26g - EPMA map showing Mg highlighting preserved olivine.

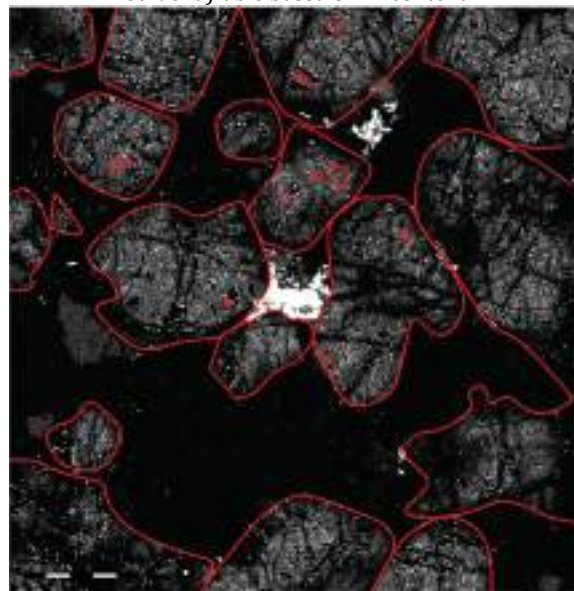


Figure 3.26h - EPMA map showing Ni. Ni content is lower around the rims of the cumulus shapes. Note that this is true in both olivine and serpentine.

Figure 3.26 – EPMA maps showing variable Ni content in olivine

Aphanitic olivines incorporated into the Olivine Cumulate Unit

There are two samples within the Olivine Cumulate Unit that have atypical olivine within them (Fig. 3.27). In contrast to the Ni-depletion these olivines formed a distinct low Ni population, rather than a diffuse decrease in Ni at the edge of olivine grains. They are three small grains (~50 μm) that are not part of a larger cumulus grain (Fig. 3.28).

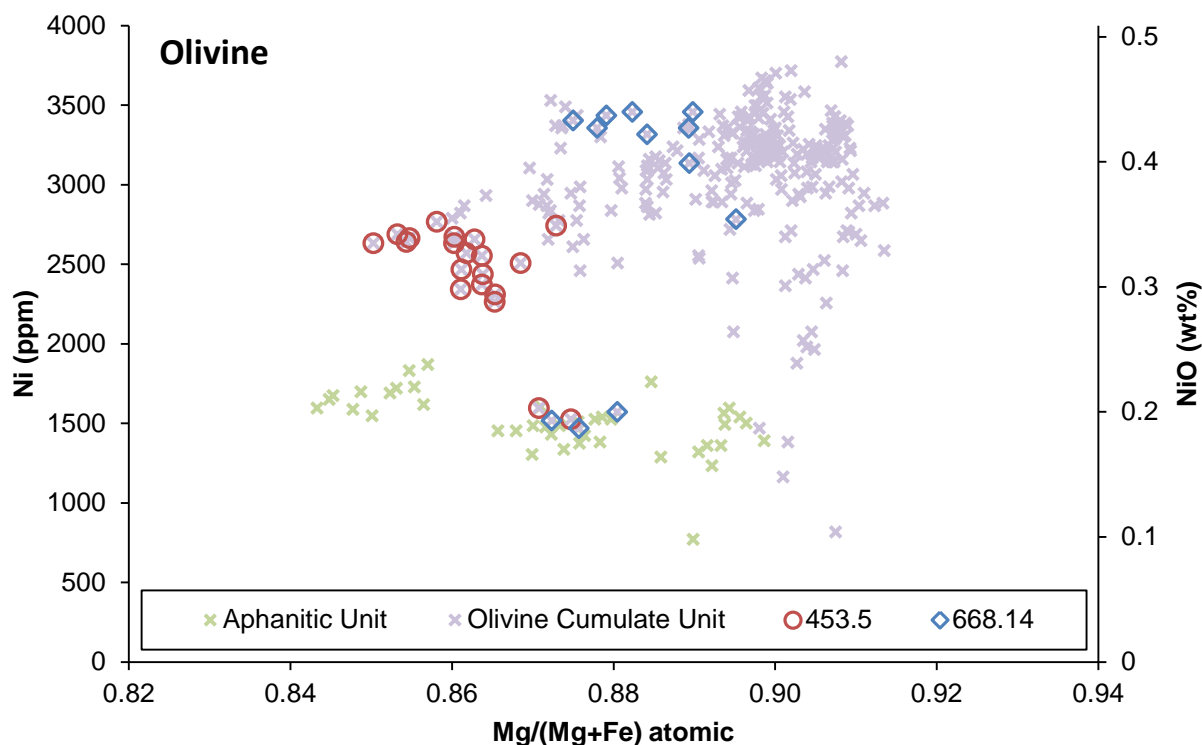


Figure 3.27 - Olivine chemistry from the main cumulate body in the Sakatti deposit and the aphanitic footwall. Ni (ppm) and NiO (wt%) are both included for reference only. Two samples that contain bimodal Ni contents are highlighted.

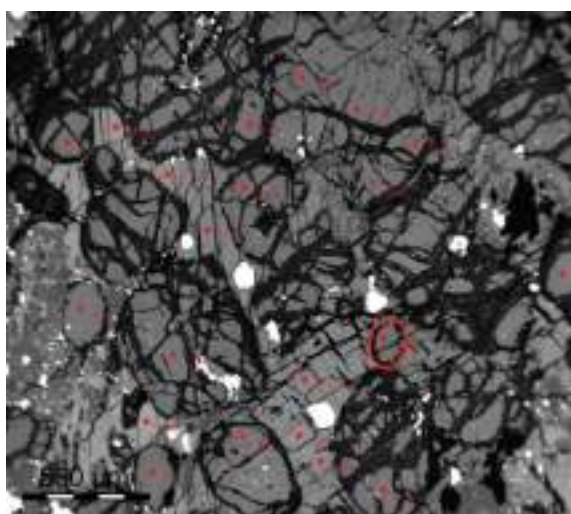


Figure 3.28 – Image showing low Ni olivine amongst normal cumulus olivine

Due to their similarity to the aphanitic olivine Ni content it is suggested that these are incorporated aphanitic olivines. That they occur at 666.16m and 453 is significant as these are not in close proximity to the footwall and this suggests that assimilation of the aphanitic footwall could be a widespread occurrence throughout the deposit.

LA-ICP-MS analysis was undertaken to ‘fingerprint’ these olivines and determine if they originated from the Aphanitic Unit.

Unfortunately as LA-ICP-MS requires the production of blocks in place of thin sections, these blocks made from the offcut of the thin section did not contain any olivine with less than 2000 ppm Ni. Furthermore the small size of the olivines that were found would have limited the potential for successful LA-ICP-MS analysis.

3.4.1.5 Serpentinisation

Notably, Ni appears to be immobile during pervasive serpentinisation. This is evident in a Ni distribution map of olivine cumulate (Fig. 3.26), showing similar Ni contents in preserved olivine and serpentine. This has significant implications for exploration as it means the high Ni content of the olivine is preserved, resulting in a high proportion of the Ni measured in the disseminated mineralisation being as unrecoverable silicate Ni.

3.4.1.6 Trace element chemistry of olivine

Trace element partitioning in olivine has been split into three behavioural groups by De Hoog et al. (2010); those that show limited range (Ni,Mn,Co,Cu,Zn,Li), those mainly controlled by temperature and pressure (Cr,Al,V,Sc,Ca,Na) and those principally controlled by bulk rock contents (Ti,Zr,Nb,Y,P). That study is concerned mainly with mantle olivine and the situation considered here is somewhat different with potentially greater variations in host melt concentrations of elements that will inevitably affect the amount incorporated in to olivine.

Zirconium in olivine can be expected to reflect principally the melt concentrations of Zr and so will be a proxy for evolution of that melt. Concentrations are highest, and also most variable, in the Aphanitic Unit (Fig. 3.29). Concentrations in the Olivine Cumulate Unit evolve from low values at the base to 678.18 m and are then reset to lower values at 666.16 m which again evolve to higher values with decreasing depth.

While Zr could be a proxy for overall evolution of the melt, led by fractional crystallisation, V could be expected to reflect crystallisation of chromite, to which it would be preferentially lost (Barnes, 1998). The very base of the intrusion has relatively high values which then decrease. Above 666.16 m the V concentration is higher but also more variable. Zinc content in olivine increases with decreasing depth, being particularly variable in the highest sample in the intrusion, the potential controls on Zn crystallisation are not well constrained, but it does indicate a systematic change in the parent magma. Scandium is variable throughout but it should be noted that Sc levels are high in Aphanitic Unit olivine as opposed to Olivine Cumulate Unit olivine. This conforms with the same effect in aphanitic enstatite and most likely reflects the lower amount of diopside crystallisation from the parent melt of the Aphanitic Unit.

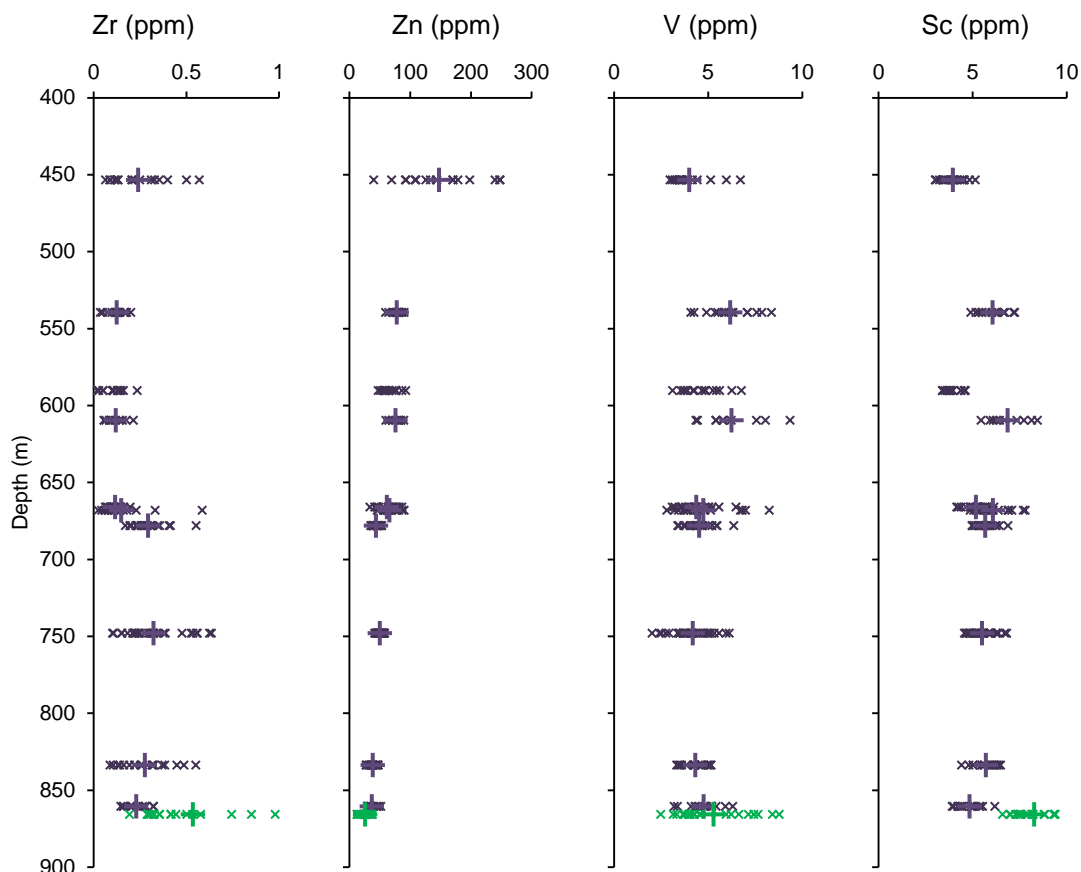


Figure 3.29 – Depth profiles showing trace element contents of olivine. Analysed by LA-ICP-MS (detection limits: Zr: 0.004 ppm, Zn: 0.160 ppm, V: 0.022 ppm, Sc: 0.091 ppm. Analytical error: Zr: 13.7% Zn: 7.2% V: 9.4% Sc: 13.4%).

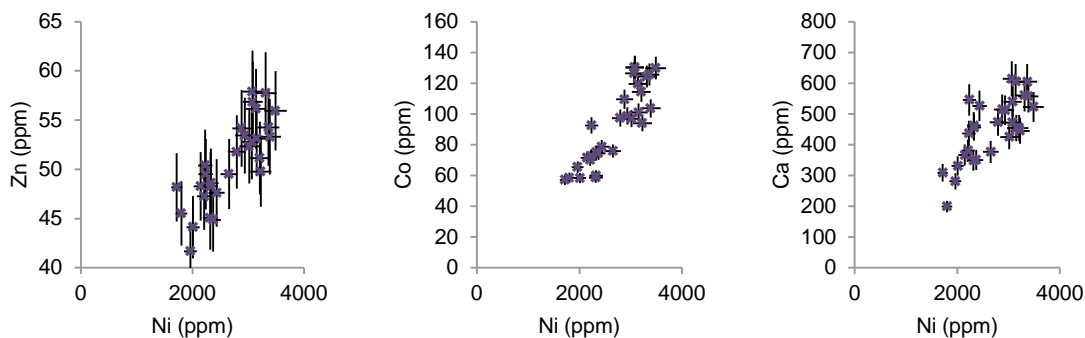


Figure 3.30 – Low Ni-rim olivine analysis shows variable Ni correlates with Zn, Co and Ca.

Trace element analysis of the low Ni rims of olivine show that variable Ni correlates with Zn, Co and Ca (Fig. 3.30), which are also divalent ions. Zinc and Co could be expected to be lost by diffusion to a sulphide-depleted melt however Ca is not chalcophile and has a much larger ionic radius.

3.4.2 Chromite

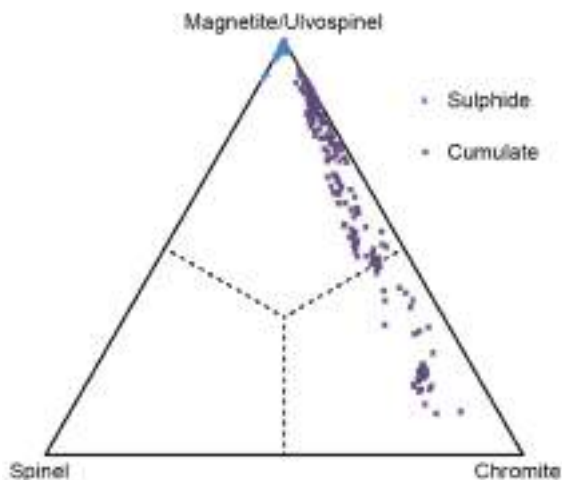


Figure 3.31 – EPMA data of magnetite and chromite showing the difference between sulphide-derived magnetite and cumulus chromite-derived magnetite

Chromite grains are euhedral and form the only other cumulus phase besides olivine. Most cumulus chromite has been altered to chromium-bearing magnetite (Fig. 3.31). However, the grains frequently contain cores of chromite that potentially reflect the original composition. These cores have Cr_2O_3 contents between 27-37 wt% and Ni contents of 1000-2500 ppm. The presence of cumulus chromite suggests that the parental melt had an MgO content below 24 wt%, as otherwise chromite would not have been on the liquidus (Barnes, 1998).

Nickel content in the chromite was found to be systematically variable, compared to other elements (eg. Al, Ti, Mn). Nickel content in chromite could be expected to vary depending on the Ni content of the parent melt which would itself depend on the degree of either olivine crystallisation or any sulphide formation. The Ni contents of the chromite decreases from the base of the Olivine Cumulate Unit upwards and increases again at the 666.16 m. The upper portion of the Olivine Cumulate Unit has higher Ni in the chromite than the lower portion (Fig. 3.32).

The trace element chemistry is largely unperturbed by the transition from chromite to chrome-bearing magnetite. The chromites and its alteration magnetite are clearly distinguishable from sulphide-derived magnetite due to their Cr contents. Chromium is below EPMA detection limits the sulphide-derived magnetite.

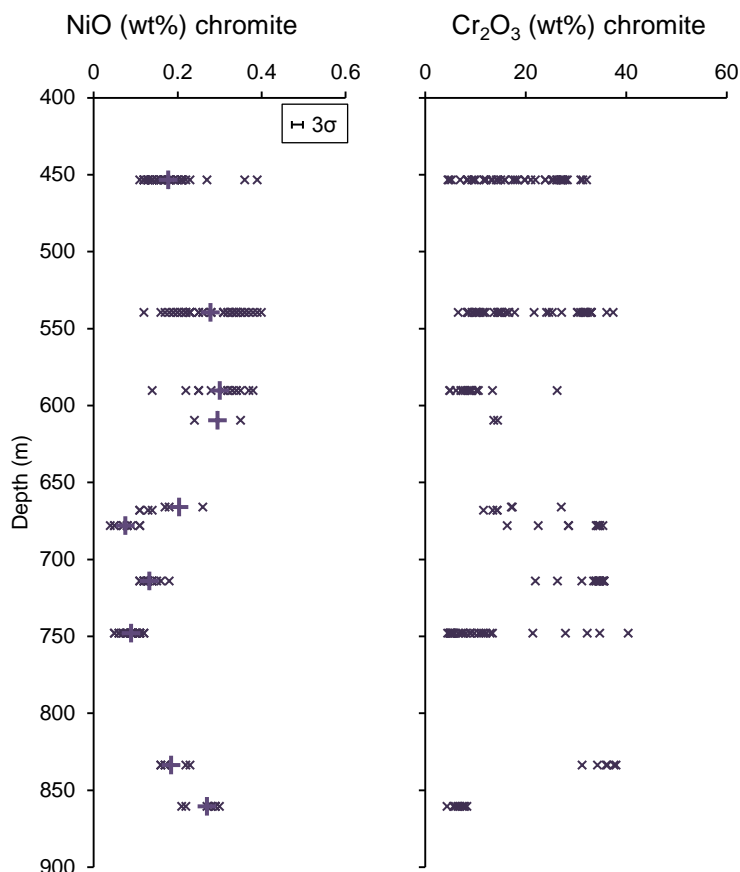


Figure 3.32 – Hole 49 depth profiles of EPMA data of Ni and Cr in chromite and magnetite derived from chromite, as seen in the bimodal chromite distribution. Detection limits are 0.02 wt% NiO and 0.01 wt% Cr₂O₃. 3σ analytical error is 0.03 wt% NiO and 0.01 wt% Cr₂O₃.

3.4.3 Pyroxene

Olivine Cumulate Unit pyroxene

Pyroxene in the Olivine Cumulate Unit is invariably oikocrystic, surrounding and encompassing smaller cumulus olivine. Oikocrysts may be 1-2 cm wide and consist of either enstatite or diopside (Fig. 3.34). The pyroxene is frequently altered to tremolite-actinolite. In some cases, unaltered oikocrysts contain preserved olivine whereas surrounding olivine has been serpentinised. Enstatite oikocrysts have Mg# of 0.80-0.90 (or Enstatite:Ferrosilite proportion) and Ni contents in the range of 400-1000 ppm, whereas diopside oikocrysts have Mg# of 0.85-0.92 (or Diopside:Hedenburgite proportion) and Ni contents of 200-600 ppm (Fig. 3.33).

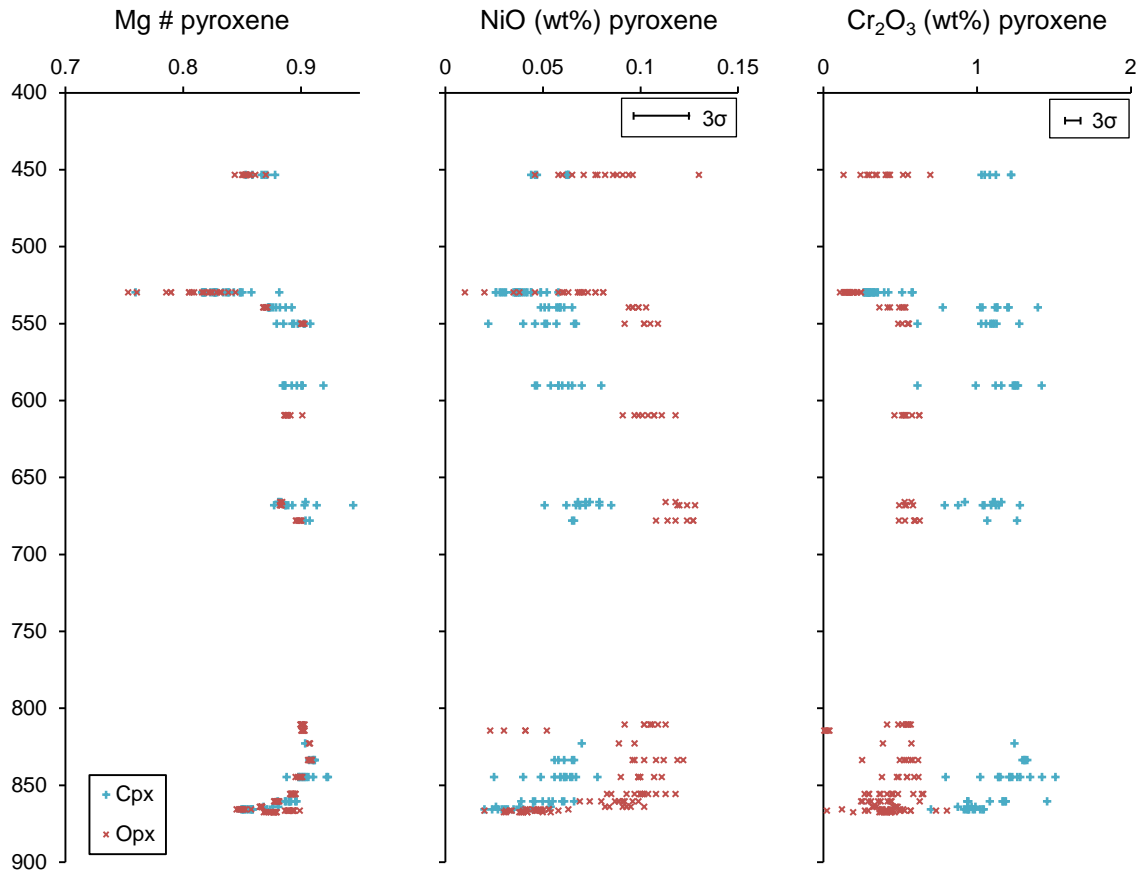


Figure 3.33 – Hole 49 EPMA depth profiles of clinopyroxene (blue) and orthopyroxene (red). Sparse data is due to the absence of preserved minerals. Mg# is (Mg/Mg+Fe). Detection limits are 0.02 wt% NiO and 0.01 wt% Cr₂O₃.

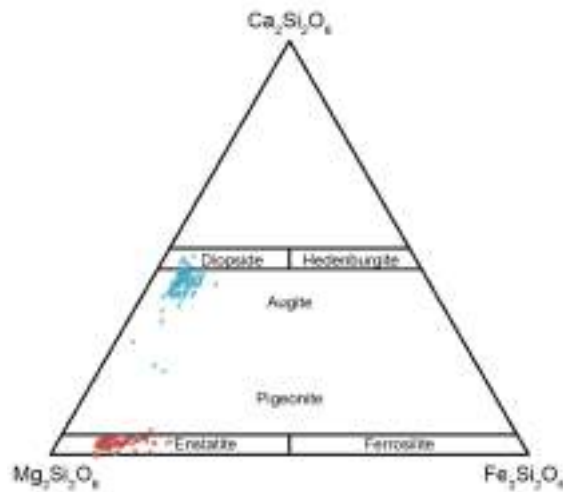


Figure 3.34 – Compositions of pyroxene in the Olivine Cumulate Unit in Hole 49.

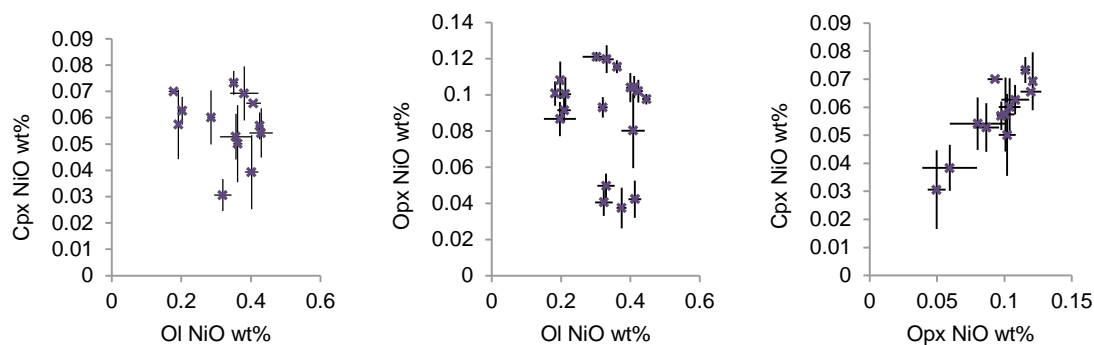


Figure 3.35 – Average EPMA NiO values with 3σ error bars for olivine and pyroxene in each sample. The pyroxenes correlated with each other while olivine does not correlate with either orthopyroxene or clinopyroxene.

Pyroxene shows limited chemical variation compared to olivine, yet the proportions of orthopyroxene to clinopyroxene varies as discussed in the petrology section (3.3.4.3). Sample 529.80 m is part of the Pegmatoidal Gabbro Sub-Unit and has less magnesian and nickeliferous values. Excluding this sample the general chemistry of the pyroxenes does not seem to evolve with depth. The base of the intrusion has abundant preserved pyroxene and here the same reversal trend can be seen that is observed in the olivine chemistry (3.4.1.3).

The pyroxene Ni content, while correlating between the pyroxenes does not correlate with Ni values in the olivine (Fig. 3.35). This confirms the textural observation that the oikocryst pyroxene has probably formed from quite different melt conditions to the earlier cumulus olivine which is merely being deposited in the location of pyroxene formation.

Aphanitic pyroxene

Pyroxene in the Aphanitic Unit is dominated by enstatite (35%) but also has significant diopside (5%). The major element (EPMA) chemistry does not distinguish the Aphanitic Unit pyroxene from the Olivine Cumulate Unit pyroxene, except that they are marginally more evolved (0.85 En:Fs compared to 0.9 En:Fs).

Trace element chemistry

Trace element analysis of pyroxene at the Sakatti deposit did not reveal systematic changes with depth. They both carry characteristic REE signatures with enstatite being enriched in HREE (Fig. 3.37) while diopside has a flatter profile with minor depletion at both the most light and most heavy REE (Fig. 3.38). They all have negative Eu anomalies suggesting that plagioclase has crystallised from the melt at some earlier stage (Rollinson, 1993).

The distinct nature of the diopside in the Pegmatoidal Gabbro Sub-Unit was confirmed, having lower Cr content (1500-3500 ppm compared to 6000-10000 ppm), elevated LREE and showing

a more pronounced negative Eu anomaly ($Eu/Eu^* 0.74$ compared to $Eu/Eu^* >0.8$, German et al., 1991) relative to the other Olivine Cumulate Unit diopside (Figs. 3.36 and 3.38).

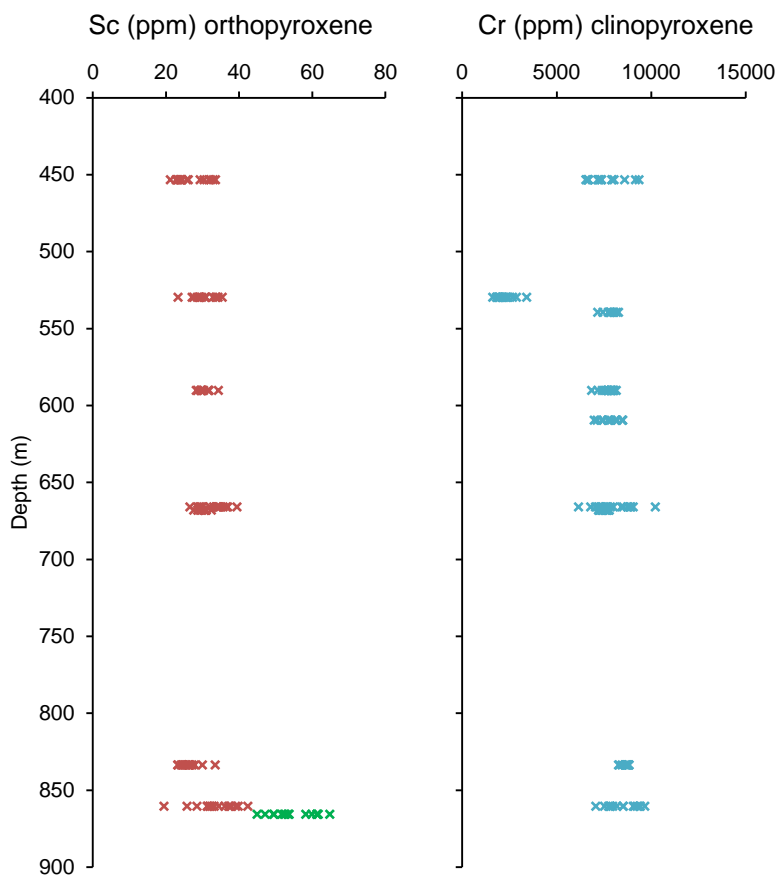


Figure 3.36 – Trace element depth profiles of Sc in orthopyroxene, showing elevated Sc in the Aphanitic Unit and Cr in clinopyroxene showing depletion in the Pegmatoidal Gabbro Sub-Unit (Detection limits Sc: 0.079 ppm Cr: 0.388 ppm Analytical error Sc: 9.3% Cr: 1.2%).

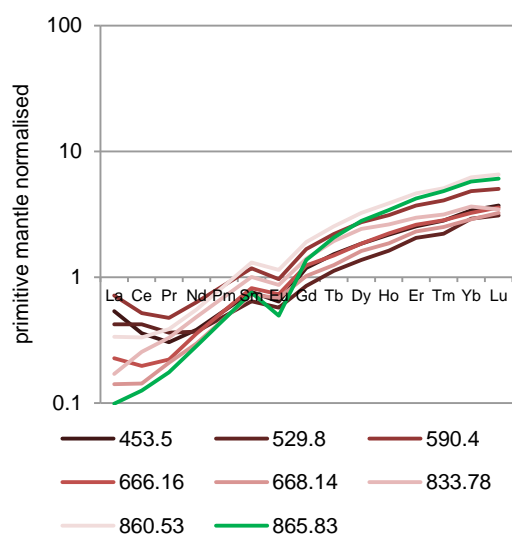


Figure 3.38 – REE profiles of orthopyroxene in the Olivine Cumulate Unit and the Aphanitic Unit (in green) from hole 49 with depth in m shown in legend.

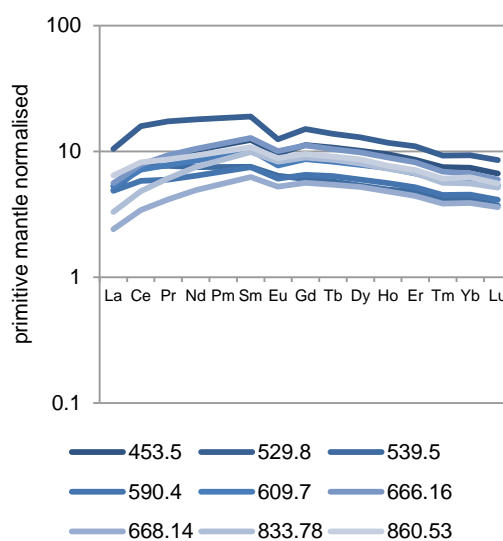


Figure 3.37 – REE profiles of clinopyroxene in the Olivine Cumulate Unit from hole 49 with depth in m shown in legend.

Lower Cr content and elevated LREE is consistent with a more evolved melt that has lost HREE to olivine and orthopyroxene crystallisation and a more pronounced negative Eu anomaly is likely to be due to the co-crystallisation of plagioclase in this sub-unit.

Mineral phases in the Aphanitic Unit are sub-optimal for LA-ICP-MS due to their fine-grained nature. The lack of diopside means that it was not analysed for trace elements. Enstatite in the Aphanitic Unit carries a distinct higher Sc content (Fig. 3.36). Scandium is usually accommodated in clinopyroxene (Arndt et al., 2008) and so an elevated Sc presence in the enstatite within the Aphanitic Unit conforms with the observation of limited clinopyroxene presence in this unit.

3.4.4 Plagioclase

Olivine Cumulate Unit

Plagioclase is rarely present in the Olivine Cumulate Unit, except as an intercumulus phase near the contact with the Aphanitic Unit. Plagioclase is also present in the Pegmatoidal Gabbro Sub-Unit where it is black in hand specimen (Fig. 3.15). In both cases, the plagioclase is anorthite, although the Na:Ca ratio is variable. The black nature of the plagioclase appears to be down to micro-inclusions of Fe (Eg. Lindsley et al., 2010), the plagioclase mineral chemistry did not exhibit any unusual characteristics.

Aphanitic Unit

Plagioclase is present within the Aphanitic Unit as both larger patches, interpreted as phenocrysts and as smaller groundmass. These larger patches have a high Ca content relative to the groundmass plagioclase, conforming to their interpretation as phenocrysts.

3.4.5 Amphibole

Amphibole major elements

Chemical analyses reveal that there are two distinct populations of amphibole. Amphiboles of the tremolite-actinolite series are the predominant type and are texturally identifiable as alteration products of pyroxene. In addition, there is a significant population of pargasite (up to 5% of sample) that is interpreted as a primary magmatic phase, based largely on texture (Fig. 3.13). This pargasite is split into sub-populations on the basis of Ti content, affecting colour.

The two amphiboles are geochemically easily distinguishable as pargasite has an A site occupied with Na as opposed to the vacant A site in tremolite (Deer et al., 2013). End-member tremolite contains no Al or Na, whereas the tremolite at Sakatti is undergoing primarily edenite substitution ($\text{SiVacant} \rightleftharpoons \text{AlNa}$) but also about twice as much tschermak substitution ($\text{MgSi} \rightleftharpoons \text{AlAl}$), meaning it is a trend towards a pargasite-hornblende middle ground (Fig. 3.39). The pargasite population is on a trend of equal amounts of edenite and tschermak substitution, this is 'perfect' pargasite substitution (Waters, 2004).

There is a higher Ti sub-population of pargasite present (Fig. 3.40), suggesting two stages of magmatic amphibole formation. This higher Ti sub-population can be seen by plotting the data as amphibole end-member vectors pargasite (itself a combination of the edenite and tschermak vectors) against a theoretical Ti tschermak end-member (Fig. 3.41) indicating that Ti tschermak substitution is responsible the elevated Ti (Deer et al., 1997; Veblen, 1981; Waters, 2004). This means that the mineral is going towards kaersutite, however as the Ti content is not high enough it should be referred to as titanian pargasite (Deer et al., 1997).

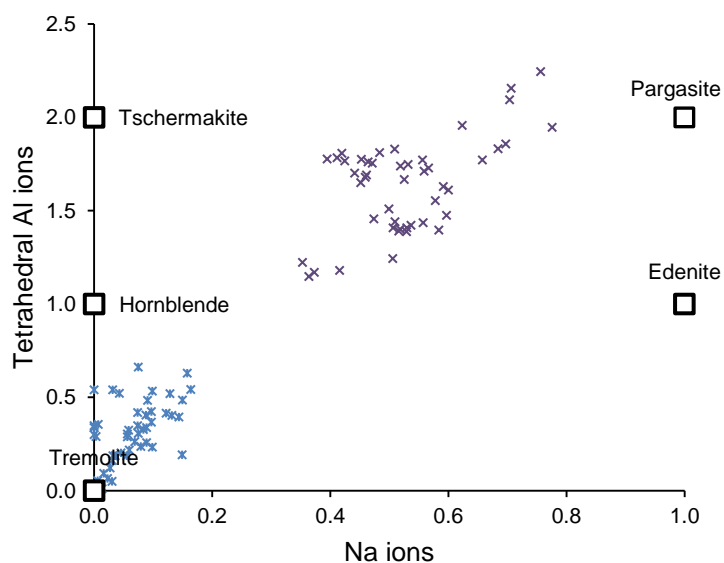


Figure 3.39 – Ions per formula unit (calculated on the basis of 23 O) of Na and Al in the tetrahedral site. Alteration tremolite is distinct from pargasite. Tremolite exhibits a steep trend closer to tschermak substitution while pargasite has a shallower trend similar to 'pargasite' substitution.

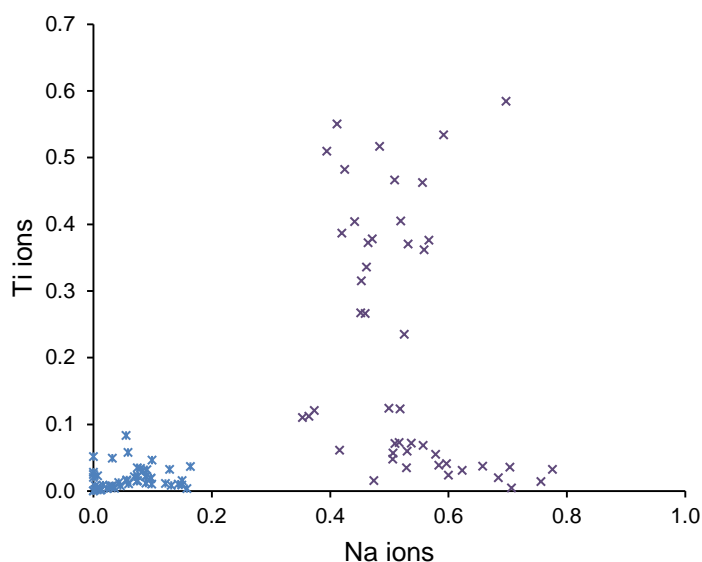


Figure 3.40 – Ti ions show that pargasite is split over different Ti contents.

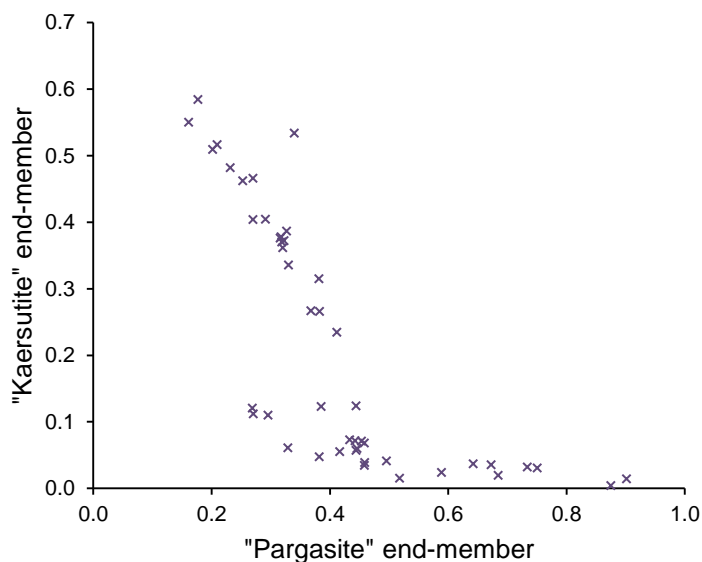


Figure 3.41 – End-member vectors calculated for hypothetical 'pargasite' and 'kaersutite' or Ti-tschermak substitution. Only pargasite is plotted. The Ti-rich pargasite exhibits a clear trend towards the 'kaersutite' end-member.

Amphibole trace elements

Trace element analysis of the pargasite led to the identification of three separate sub-populations based on Ti content (Fig. 3.42 and 3.43), these populations persisted in most samples in which amphibole was present suggesting different generations of pargasite formation. These populations are low Ti (<15000 ppm) and low Zr (<300 ppm); mid Ti (10000 ppm to 26000 ppm) and high Zr (> 400 ppm); and high Ti (>25000 ppm) and mid Zr (100 to 400 ppm). These three populations suggest a complex evolution with amphibole forming at different stages in the crystallisation history.

All of the amphiboles show REE profiles depleted in the heavy elements and also depleted in La and Ce (Fig. 3.44). The latter two populations have similar high REE profiles with a pronounced negative Eu anomaly. The low Ti, low Zr has lower REE profiles with a small negative Eu anomaly if at all and limited La and Ce depletion. The tremolite has much lower REE profiles with a positive or no Eu anomaly, these profiles are similar to the REE profiles of the pyroxene.

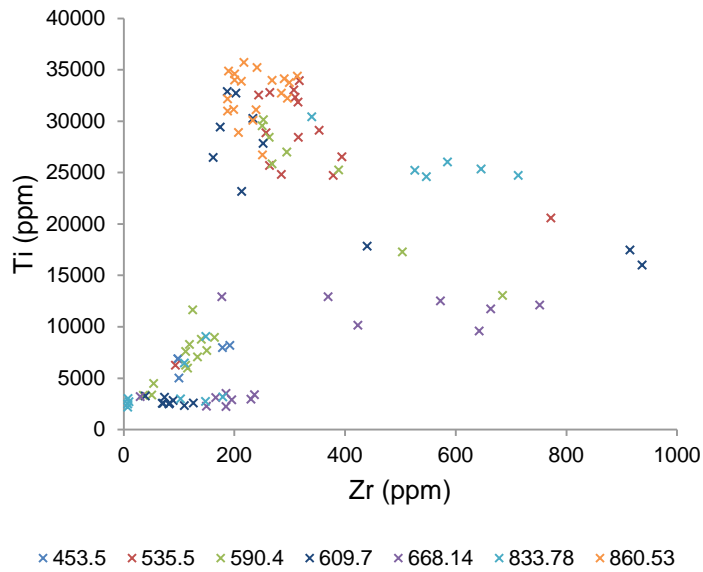


Figure 3.42 – Trace element analysis splits pargasite in hole 49 into three populations depending on Ti and Zr contents. These are present in many samples rather than being related to depth.

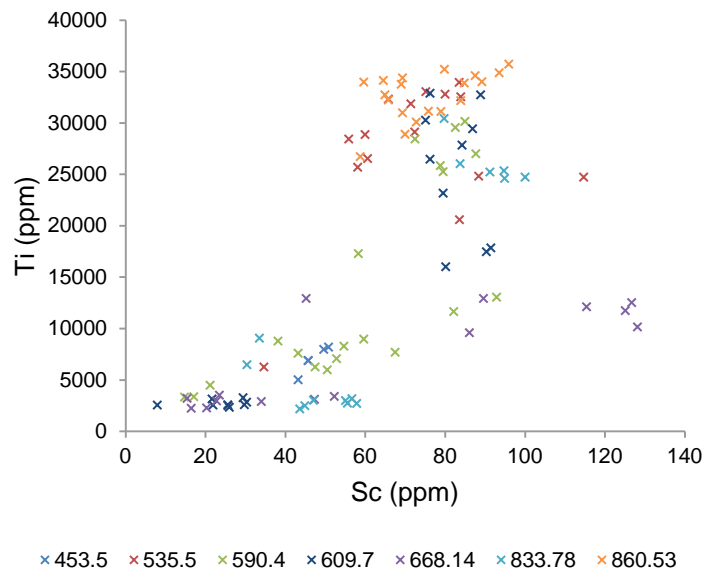


Figure 3.43 - Trace element analysis splits pargasite in hole 49 into three potential populations depending on Ti and Sc contents. These are present in many samples rather than being related to depth

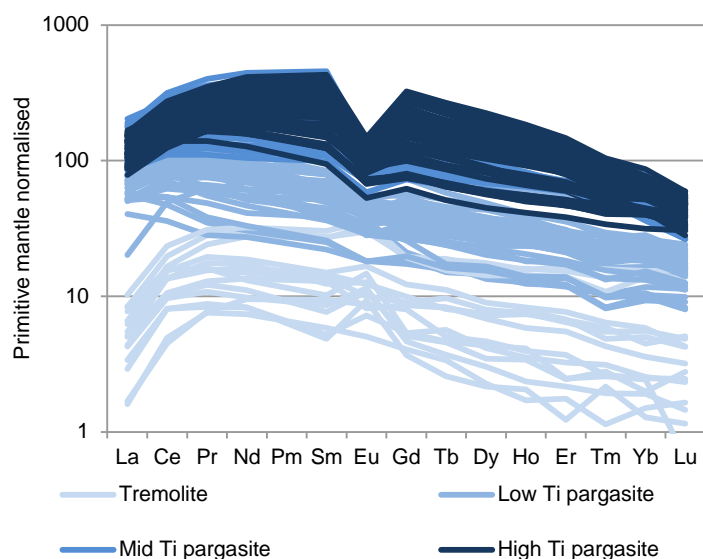


Figure 3.44 – REE profiles of amphibole in hole 49 showing lower REE concentrations and a positive Eu anomaly in alteration tremolite whereas higher levels in low Ti pargasite and higher levels still with strong Eu depletion in high Ti pargasite.

3.5 Whole-rock geochemistry

3.5.1 Summary

The whole-rock geochemical data for the majority of samples from the Olivine Cumulate Unit at Sakatti indicate primary control by abundance of olivine (Fig. 3.45, 3.48 and 3.49). Whereas the Aphanitic Unit is more complex and controlled by co-abundance of olivine and plagioclase rather than trending towards one particular end-member mineral.

Whole-rock geochemical data within cumulate systems must be treated with caution as the trends exhibited are both a reflection of mineral chemistry but also proportional accumulation of those minerals. For example Mg# in a cumulate rock can be expected to considerably exceed that of a parental melt as it is a concentration of olivine and not the residual melt.

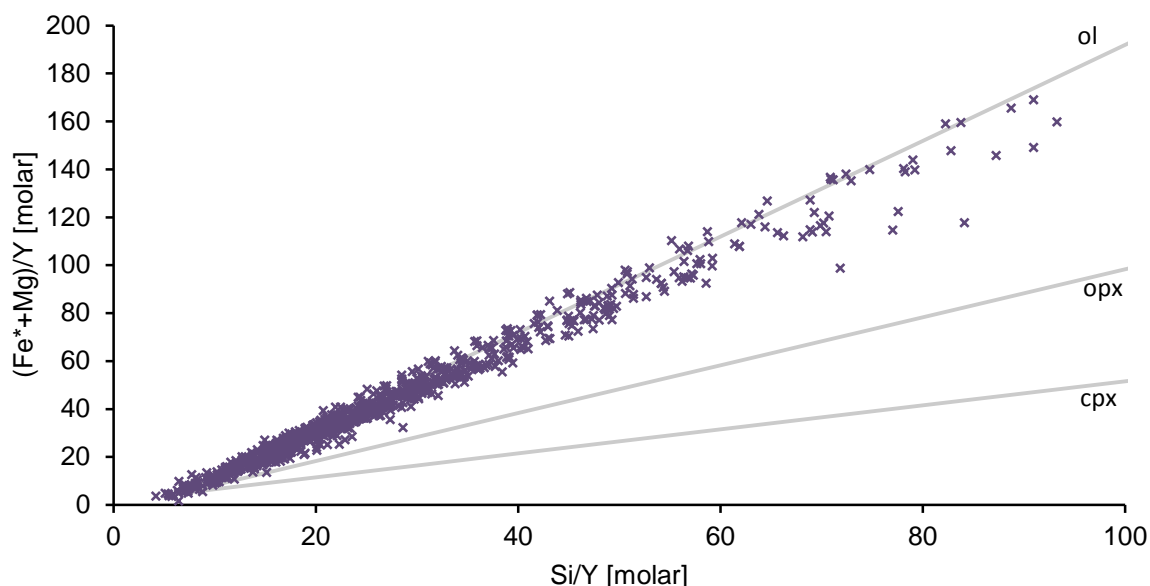


Figure 3.45 – Pearce Element Ratio plot showing $Fe^* + Mg$ vs. Si for the Olivine Cumulate Unit in molar proportions. Olivine (ol), Orthopyroxene (opx) and Clinopyroxene (cpx) lines are calculated using WDS mineral data. All data recalculated volatile free, Fe^* corrected to remove sulphide Fe. The data are divided by a common denominator of Y which is assumed to be constant in crystallisation and accumulation processes following the methodology of Pearce (1989).

3.5.2 Parental melt

The MgO content of the parental melt from which the Olivine Cumulate Unit had formed can be estimated at approximately 19% (Fig. 3.46) using whole-rock MgO and FeO contents, as well as olivine compositions (Arndt et al., 2008; Bickle, 1982; Nisbet et al., 1993). This method of estimation is subject to several assumptions and should be treated with some caution (Arndt et al., 2008). These are principally that the value used for the partition coefficient is applicable,

that the estimation of Fe³⁺ is correct, that the FeO contents measured are representative of the unit and that the most primitive olivine has been measured.

The partition coefficient of $K_D = (Mg/Fe)_{liq}/(Mg/Fe)_{ol} = 0.30$ has been used (Roeder and Emslie, 1970).

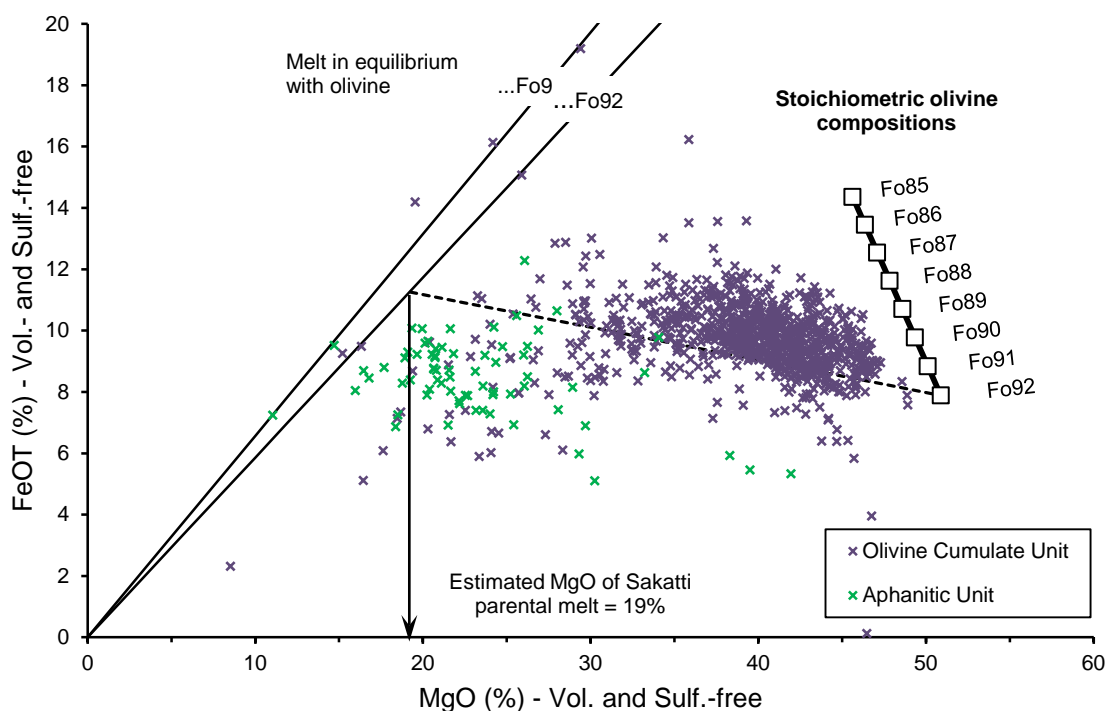
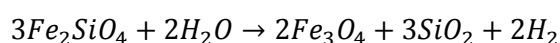


Figure 3.46 - Binary variation plot of whole rock FeOT vs. MgO in Olivine Cumulate Unit and Aphanitic Units. Data have been normalised to volatile and sulphide free compositions. Melt-olivine equilibrium lines have been calculated assuming $K_D (FeO/MgO_{ol})/(FeO/MgO_L) = 0.3$ (Roeder and Emslie, 1970).

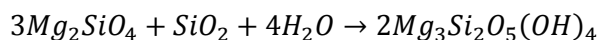
3.5.3 Layering or Serpentinisation

Identifying layering or separating different pulses of magmatism within the deposit has not been conclusive from simple drill core observations as the cumulate rocks are texturally relatively homogenous. Whole-rock chemical data have been used to delineate distinct pulses within the cumulate body (Fig. 3.47).

The ratio $(Mg+Fe)/Si$ can be controlled by modal proportions of olivine to pyroxene. In each drill core for which whole-rock geochemistry data are available it is possible to identify at least three separate magma pulses.



Equation 3.1 - Conversion of fayalite to magnetite and aqueous silica during serpentinisation



Equation 3.2 – Conversion of forsterite and aqueous silica to serpentine

Serpentinisation of fayalite will decrease the (Mg+Fe)/Si ratio (Equation 3.1) whereas serpentinisation of forsterite will increase the (Mg+Fe)/Si ratio (Equation 3.2). The Mg# of olivine at the Sakatti deposit is around 0.9 therefore at nine forsterite units to every one fayalite unit one would expect a net increase in the (Mg+Fe)/Si ratio during serpentinisation.

The difficulty in distinguishing changes in whole rock chemistry and that caused by subsequent serpentinisation is the principal reason that the project focuses on magmatic mineral chemistry.

Nonetheless potential separate layers can be identified although whether they are depicting serpentinisation or original magmatic chemistry is not clear. These are compared to the mineral chemistry data in the discussion (3.7.4).

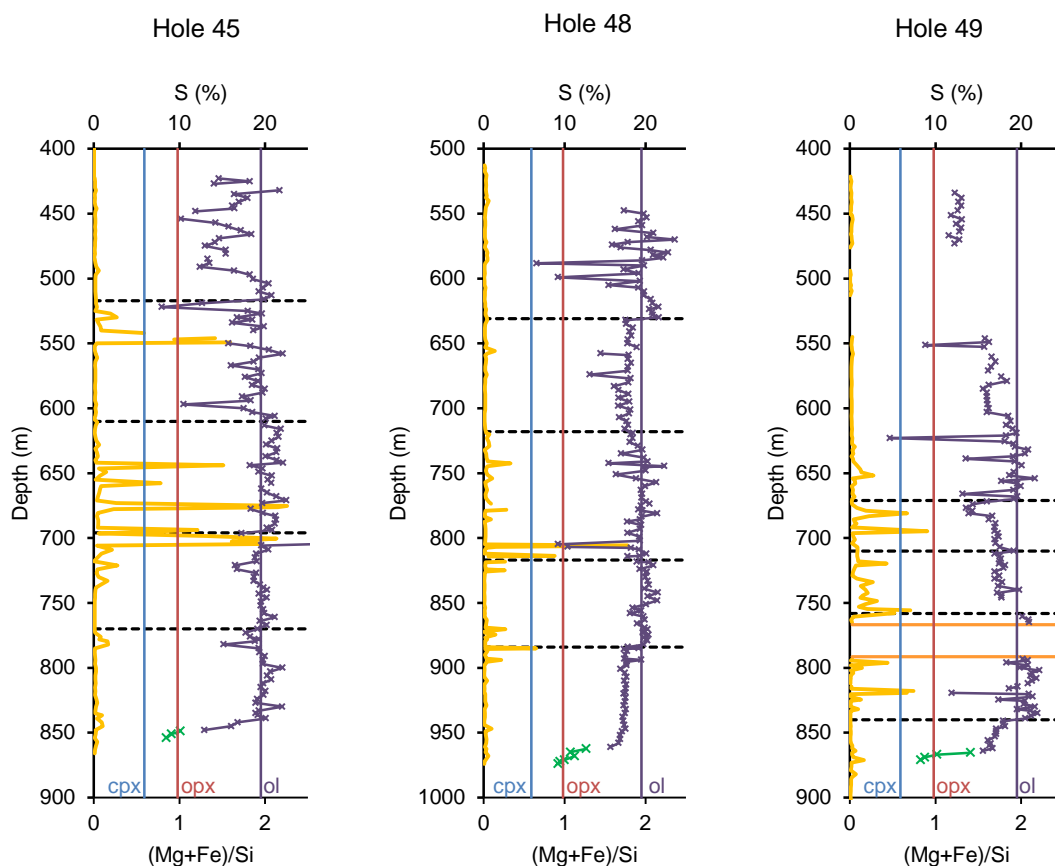


Figure 3.47 – Downhole whole-rock (Mg+Fe)/Si. Values are anhydrous and Fe values are corrected based on S values to remove sulphide Fe. Hole 49 is the one on which the sampling in this project has focused. (Mg+Fe)/Si values for averaged probe data for olivine, orthopyroxene and clinopyroxene are shown for comparison to the whole-rock. Whole-rock S content is shown in yellow and proposed magmatic pulses marked by dotted lines.

SiO ₂	TiO ₂	Al ₂ O ₃	Fe ₂ O ₃	FeO	MnO	MgO	CaO	Na ₂ O	K ₂ O	P ₂ O ₅	LOI	C	S	Se	Ni	Cu	Co	Cr	V	Sc	Zn	Rb
%	%	%	%	%	%	%	%	%	%	%	%	%	%	ppm	ppm	ppm	ppm	ppm	ppm	ppm	ppm	ppm
Olivine Cumulate																						
46.96	0.22	4.39	1.61	9.67	0.11	29.21	6.48	0.11	0.02	<0.01	8.5	0.26	0.5	2.1	2645	172	109.2	3808	102	22	9.1	0.7
43.85	0.19	2.21	1.59	9.54	0.16	39.76	0.9	0.07	0.09	0.01	13.1	0.13	0.2	1.1	2843	376	130.7	7469	66	9	24.5	4
41.8	0.25	3.15	1.69	10.15	0.17	37.88	1.98	0.24	0.21	0.05	11.9	0.15	0.9	5.5	2625	5337	131.3	7317	78	12	34.3	6.3
43.42	0.17	2.2	1.45	8.72	0.18	41.53	0.76	<0.01	0.05	0.01	14.8	0.13	0.43	0.5	2745	30	125.1	6212	57	10	37.1	2.5
39.79	0.08	1.16	1.32	7.94	0.18	46.12	1.48	<0.01	0.01	0.04	15	0.55	0.13	0.6	3077	94	131.5	9348	37	6	8.7	1.2
47.42	0.36	4.57	1.4	8.39	0.22	30.74	5.22	0.49	0.21	0.03	9.3	0.11	0.23	0.4	1544	58	93.7	3738	128	21	83.7	5.5
43.25	0.15	2.05	1.54	9.24	0.14	40.09	1.03	<0.01	<0.01	<0.01	14.4	0.21	0.66	2.3	2914	303	133.7	11826	39	8	22.9	1.1
40.48	0.14	1.66	1.32	7.91	0.13	46.26	0.57	<0.01	0.04	0.02	15.3	0.13	0.11	0.1	2786	10	117.4	7023	51	10	6.3	1.8
42.59	0.18	2.56	1.48	8.88	0.18	41.55	0.8	<0.01	0.12	0.04	14.1	0.18	0.14	0.7	2497	18	131.2	8139	75	12	31.4	4.7
43.52	0.33	2.54	1.6	9.59	0.16	38.74	1.61	0.05	0.08	0.05	12.1	0.1	0.53	3.9	2588	2021	111	6228	85	13	31.9	2.9
40.91	0.2	2.42	1.76	10.54	0.13	40.5	1.21	<0.01	<0.01	0.03	13.4	0.24	1.23	9.6	2574	7265	182.5	3906	87	10	45.9	1.2
Dunite																						
41.36	0.1	1.19	1.4	8.39	0.13	44.51	0.79	0.07	0.13	0.02	7.8	0.08	0.19	0.9	3088	74	144.8	9478	54	6	18.7	5.9
42.09	0.11	1.38	1.5	8.98	0.14	42.92	0.95	0.05	0.04	<0.01	4.9	0.09	0.29	1.5	2795	1443	128.8	7943	41	7	19.4	2.8
Altered Ultramafic																						
46.98	0.32	5.38	1.42	8.52	0.18	29.53	6.35	0.18	0.06	0.01	8.9	0.25	0.27	0.1	1630	85	90.8	4739	120	18	27.6	2.2
41.48	0.17	2.17	1.27	7.6	0.14	37.85	7.9	0.04	0.12	0.01	21.4	5.28	0.27	1.3	2990	923	92.5	4327	71	10	3	5
40.67	0.36	6.63	0.9	5.37	0.09	26.62	16.84	1.59	0.07	0.25	23.9	5.3	<0.02	0.1	1406	41	47	2643	112	13	6.5	3.7
Aphanitic																						
50.01	0.82	9.5	1.34	8.02	0.13	20.7	6.65	2.25	0.09	0.02	2.5	0.15	0.06	<0.1	676	41	67.8	1875	188	29	11.8	2.4
49.53	0.48	9.62	1.37	8.21	0.14	20.51	7.39	2.08	0.18	0.02	2.5	0.13	0.12	0.2	668	47	71.1	1947	140	32	17.9	4.8

Table 3.3 - Representative whole-rock geochemistry for major units of the Sakatti deposit. FeO and Fe₂O₃ concentrations were calculated from Fe₂O₃T using a molar Fe₂O₃/FeO ratio of 0.15, typical of mantle-derived mafic/ultramafic magmas. All data are corrected to anhydrous compositions.

Sr	Ba	Th	U	Nb	Zr	Hf	Y	La	Ce	Pr	Nd	Sm	Eu	Gd	Tb	Dy	Ho	Er	Tm	Yb	Lu	Anhydrous Totals
ppm	ppm	ppm	ppm	ppm	ppm	ppm	ppm	ppm	ppm	ppm	ppm	ppm	ppm	ppm	ppm	ppm	ppm	ppm	ppm	ppm	ppm	%
Olivine Cumulate																						
11.5	7	0.3	<0.1	0.4	12	0.4	4	1.5	2.5	0.28	1.7	0.42	0.12	0.75	0.12	0.63	0.14	0.42	0.06	0.42	0.06	99.50
7.4	42	0.5	<0.1	0.1	13.6	0.5	2.2	1.3	3.4	0.39	2.2	0.47	0.13	0.44	0.08	0.48	0.09	0.27	0.04	0.26	0.06	99.48
13.8	74	0.6	0.1	<0.1	22.9	0.6	3.9	2.4	5	0.67	1.7	0.81	0.18	0.66	0.12	0.77	0.12	0.41	0.06	0.31	0.06	99.14
5.9	6	0.5	0.1	0.6	12.1	0.2	2.4	1	1.9	0.31	1.4	0.29	0.12	0.48	0.07	0.44	0.08	0.32	0.04	0.29	0.04	99.42
7.4	33	<0.2	<0.1	<0.1	5.5	0.2	0.8	0.7	1.2	0.14	1.1	0.14	0.05	0.24	0.04	0.18	0.04	0.08	0.02	0.11	0.01	99.41
47.6	359	0.8	0.2	0.9	22.6	0.8	5.1	2.2	6.3	0.75	3.5	0.8	0.3	1.06	0.18	1.11	0.26	0.7	0.08	0.6	0.09	99.66
3.8	2	<0.2	<0.1	<0.1	15.6	0.4	1.4	0.4	0.7	0.11	0.6	0.17	0.05	0.27	0.05	0.27	0.06	0.17	0.02	0.19	0.02	99.02
4.5	42	0.2	<0.1	<0.1	10.4	0.2	1.4	0.7	1.7	0.23	1.2	0.37	0.11	0.38	0.07	0.32	0.06	0.18	0.02	0.2	0.04	99.54
8	87	0.2	<0.1	0.4	18.3	0.5	3.2	1.2	3.1	0.4	1.8	0.27	0.13	0.6	0.08	0.63	0.14	0.27	0.05	0.29	0.04	99.48
7.3	8	0.6	<0.1	1.6	30.9	0.8	4.2	1.1	2.9	0.48	2.2	0.63	0.16	0.76	0.14	0.76	0.15	0.42	0.07	0.37	0.06	99.38
5	15	0.2	<0.1	0.7	14.8	0.3	3.3	1.7	3.5	0.5	2.3	0.5	0.13	0.71	0.12	0.57	0.14	0.34	0.05	0.4	0.06	99.12
Dunite																						
3.6	13	<0.2	<0.1	14.6	6.2	<0.1	1.7	0.9	1.4	0.19	0.8	0.2	0.08	0.24	0.06	0.22	0.06	0.18	0.02	0.13	0.02	99.38
8.8	21	<0.2	<0.1	0.2	7	0.2	1.4	0.7	1.6	0.13	0.9	0.17	<0.02	0.2	<0.01	0.21	<0.02	0.12	<0.01	0.11	<0.01	99.41
Altered Ultramafic																						
16.8	18	0.7	0.2	0.7	18.6	0.6	5.7	1.2	3.2	0.5	2.8	0.72	0.21	1.01	0.18	0.89	0.22	0.62	0.08	0.57	0.07	99.60
36.6	4	<0.2	<0.1	1.2	13.2	0.4	3.5	1.9	2.7	0.32	1.7	0.4	0.05	0.54	0.09	0.64	0.15	0.44	0.05	0.38	0.05	99.58
83.3	46	2.2	2.1	2.6	52.4	1.5	11.4	13.6	30.7	3.11	11.5	2.29	0.6	2.08	0.36	1.93	0.49	1.02	0.16	1.2	0.17	99.83
Aphanitic																						
96.7	74	0.9	<0.1	1.6	57.9	1.6	9.3	2.8	7	1	5.4	1.39	0.38	1.79	0.32	1.76	0.38	0.97	0.13	0.91	0.13	99.86
91.8	62	0.4	<0.1	1.1	25.9	0.9	7.2	2.1	4.4	0.74	3.5	0.97	0.34	1.32	0.23	1.4	0.27	0.81	0.13	0.8	0.09	99.83

Table 3.3cont – Representative whole-rock geochemistry for major units of the Sakatti deposit. All data are corrected to anhydrous compositions.

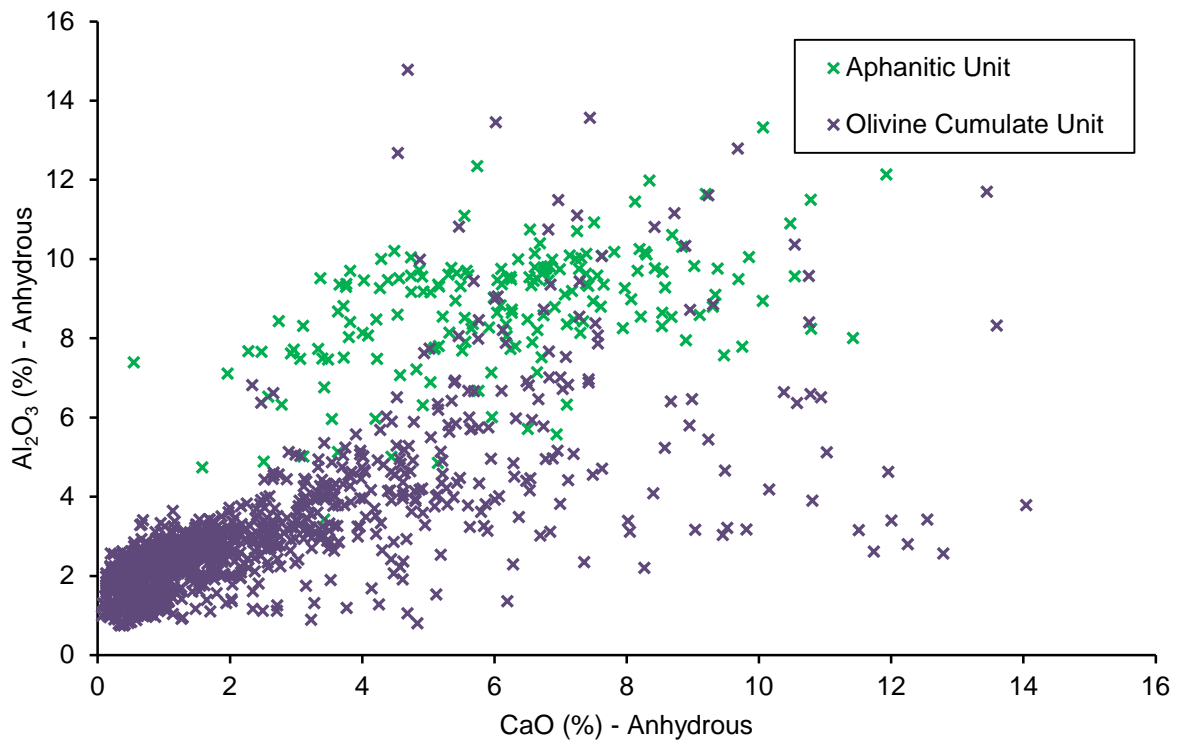


Figure 3.48 - Binary variation diagram of whole-rock CaO vs. Al₂O₃ for the Olivine Cumulate Unit and the Aphanitic Unit. Note the separate trends for the 2 units.

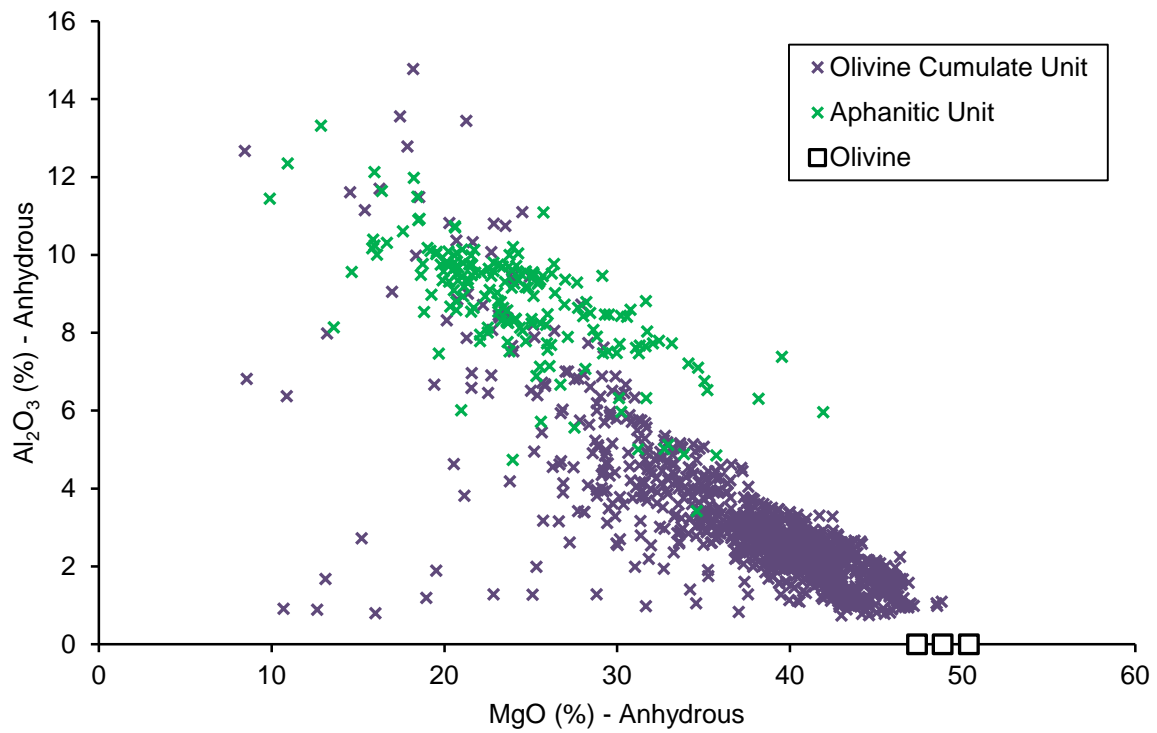


Figure 3.49 - Binary variation diagram of whole-rock MgO vs. Al₂O₃ showing both the Olivine Cumulate Unit and the Aphanitic Unit. Olivine end member chemistry is shown for Fo 92, 90 and 88. The trend in the Olivine Cumulate Unit is

consistent with olivine accumulation/dilution while the Aphanitic Unit shows a higher Al trend. This is potentially due to the presence of both olivine and plagioclase phenocrysts together.

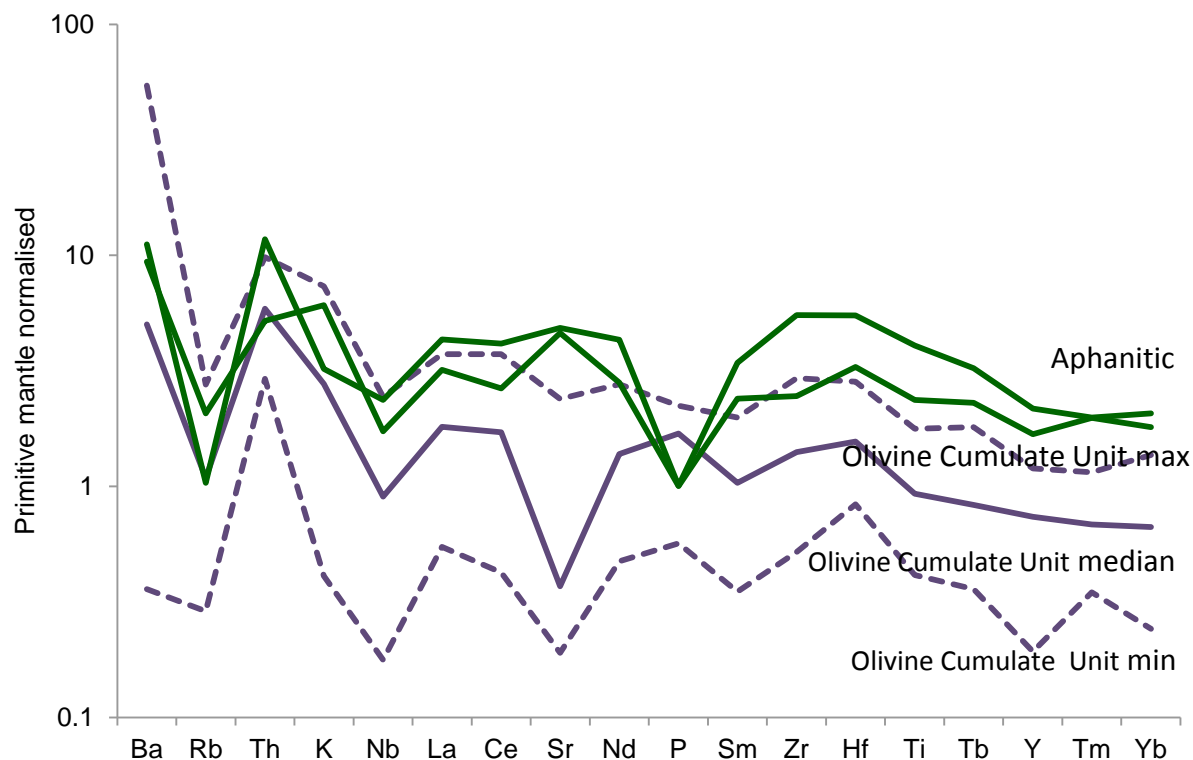


Figure 3.50 - Trace element concentrations in representative samples of the Olivine Cumulate Unit and the Aphanitic Unit. Elements are in order of compatibility and normalised to primitive mantle (McDonough and Sun, 1995).

3.5.4 Aphanitic Unit

As this unit is relatively unaltered, the whole-rock chemistry is particularly reliable in reflecting the original magmatic composition (Table 3.3). The MgO contents of the rocks typically range between 19-22 wt% but may reach up to 30 wt%. Incompatible trace elements show that the Aphanitic Unit is distinct from the Olivine Cumulate Unit geochemically (Fig. 3.50).

Such a high MgO content could at first appear to be in disagreement with petrological results, which show the unit to contain up to 35% plagioclase (Table 3.2). However, the mineral chemistry (Table 3.4) and the approximate proportions of each mineral from petrological observations were found to be in good agreement with the whole-rock geochemistry. The typical Na content of 1.5-2.5 wt% in the whole-rock is reflective of the plagioclase content and is not related to alteration.

The observed variations in whole-rock major element geochemistry within the Aphanitic Unit are not consistent with simple addition and subtraction of olivine, but rather suggest the presence of plagioclase and olivine phenocrysts (Fig. 3.48 and 3.49).

3.5.5 Classification of the Aphanitic Unit

	Approx. proportion	NaO	MgO	Al ₂ O ₃	SiO ₂	CaO	FeO	Total
Olivine (phenocryst)	0.1		42.18		39.39		18.5	100.08
Plagioclase (phenocryst)	0.05	5.41		27.57	54.74	10.84	0.66	99.23
Enstatite	0.35		30.97	0.68	56.93	1.17	11.82	101.56
Diopside	0.05	0.67	16.00	2.05	52.81	21.54	5.43	100.01
Olivine	0.1		42.93		39.98		17.24	100.15
Plagioclase	0.35	7.32		25.54	59.21	7.71	0.54	100.31
Estimated whole-rock	1	2.9	20.2	10.7	54.0	4.7	8.2	100.6

Table 3.4 – Representative WDS data from the Aphanitic Unit and an estimated whole-rock value using their proportions. This is in agreement with the measured whole-rock values (Table 3.3).

The rocks cannot be readily defined as ultramafic because they contain more than 10% felsic minerals; nor can they be defined as ultrabasic because they have more than 45 wt% SiO₂ (Le Maitre et al., 2002). High MgO content of more than 18 wt% precludes classification as basalt. The lack of alteration and the high plagioclase content suggest that the Na values reflect the original magmatic values.

According to Arndt et al. (2008), the term komatiite should 'be reserved solely for lavas with characteristic spinifex-textured olivines, or lavas that can be related directly, using field or petrological criteria, to lavas of this texture'. Olivine spinifex or harrisite texture is clearly identifiable in a 2 m section of one drill hole at the contact between the Aphanitic Unit and the Olivine Cumulate Unit. However, at present this is the only documented occurrence of olivine spinifex texture that has been observed in 155 drill holes and 99,388 m of diamond drilling. For the purposes of this study it is deemed that this single occurrence of spinifex, lacking clear field relationships, is insufficient basis on which to classify this unit as komatiitic. Furthermore the high plagioclase content of this rock, meaning it is mafic rather than ultramafic, would make it an atypical komatiite. It is therefore termed a "plagioclase-rich picrite" on the basis of its high MgO content (Fig. 3.51). However, it is acknowledged that with the discovery of more olivine spinifex textured rocks, with clear field relationships, this definition could well be revised to a komatiite.

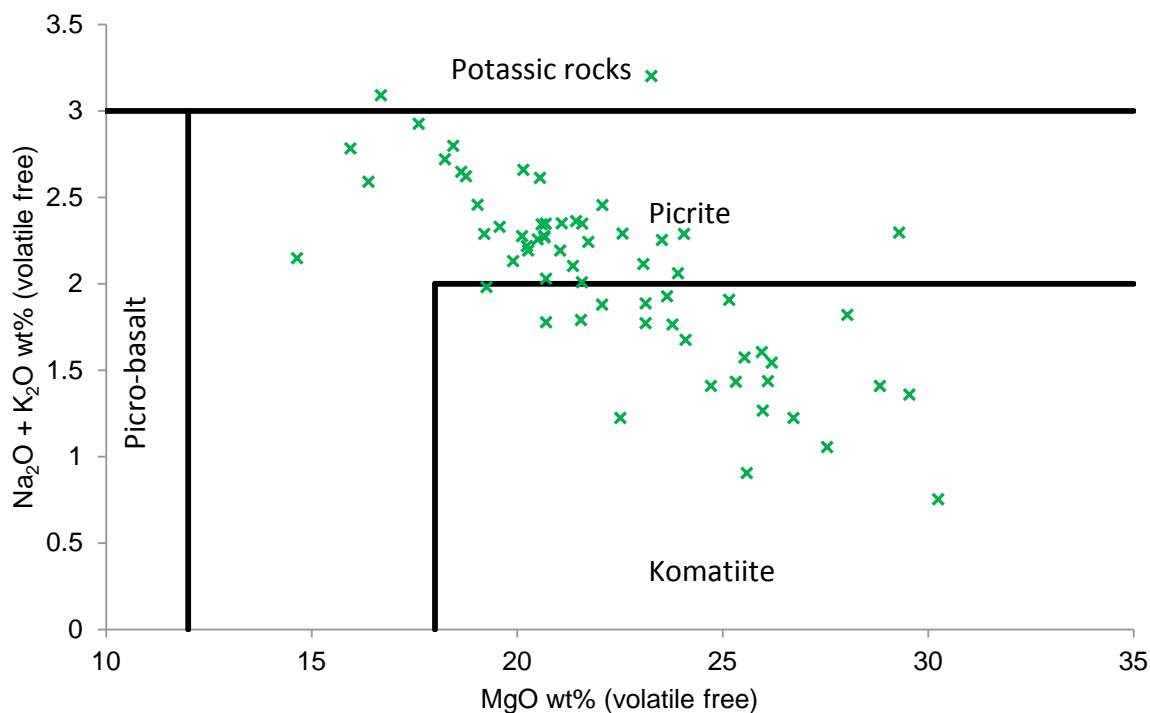


Figure 3.51 - Whole-rock geochemistry of the Aphanitic Unit plotted according to the IUGS komatiite-picrite definition (Le Maitre et al., 2002) for the aphanitic unit. All values are anhydrous.

3.6 Isotopic studies

This is the first academic study of the Sakatti deposit and as such focuses primarily on simple petrology. Stable isotopes have not been used examining the silicates, although these might be insightful when determining the origin of alteration at the deposit. Two radiogenic isotope systems were examined in the silicate minerals in order to attempt to establish a geochronological reference for the Sakatti deposit. This is particularly necessary because there are no established field relationships with the CLGB lithologies that allow the deposit to be placed in the established stratigraphy, which is itself very well constrained geochronologically (Hanski and Huhma, 2005).

3.6.1 Sm/Nd

3.6.1.1 Attempted geochronology

Sm/Nd analysis was undertaken as an attempt to date the deposit, which is possible if the mantle-derived melt has not received significant contamination by evolved crustal material. Minerals are separated, as the varying Sm and Nd contents within them will provide a range over which an isochron can be plotted. Olivine, orthopyroxene, clinopyroxene and plagioclase were separated. Whole rock analyses were also undertaken and these are presented below.

The isochron produced from this work has a large degree of scatter, which exceeds the possibility of analytical error and therefore must be the result of a genuine variation in the samples, which makes them invalid as a geochronological tool.

For Sm-Nd analysis to provide a valid isochron the samples must...

- Be the same age
- Have the same starting ϵ_{Nd} value
- Derive from the mantle or a reservoir of mantle composition
- Sm/Nd should have been unperturbed since formation

It can be assumed that the samples are the same age given their geochemical similarity and presence in a continuous cumulate stack therefore their lack of isochroneity must result from one or several of the other reasons. The ϵ_{Nd} values are between samples exhibit considerable scatter (Table 3.5).

Hole No	Sample no. (depth)	$^{143}Nd/^{144}Nd$	$^{143}Nd/^{144}Nd$ normalised	Sm/Nd	$^{147}Sm/^{144}Nd$	ϵ_{Nd} (today)	Int. Error in ϵ_{Nd} (2 σ)
49	529.08	0.512016	0.512011	0.2629639	0.163117	-12.23	0.07
49	539.5	0.511972	0.511967	0.2669617	0.165595	-13.09	0.09
49	666.16	0.511983	0.511978	0.2754881	0.170884	-12.87	0.09
49	668.2	0.511799	0.511794	0.249827	0.15496	-16.46	0.09
49	678.23	0.512053	0.512048	0.277707	0.172263	-11.51	0.11
49	744.75	0.51208	0.512075	0.2769231	0.171778	-10.98	0.38
49	822.2	0.512057	0.512052	0.2647334	0.164216	-11.42	0.18

Table 3.5 – Measured Sm/Nd isotopic values in whole rock samples and calculated ϵ_{Nd} (today). Data are normalised to correct JNdi reference to $^{143}Nd/^{144}Nd = 0.512115$ (Tanaka et al., 2000)

3.6.1.2 Assessment of crustal contamination

Assimilation of crustal material will disrupt Sm/Nd contents of a mantle-derived melt and this can be examined if the age of the unit is known from another means.

The system of ϵ_{Nd} is usually corrected for the age of the rock (t) so that it represents the initial ϵ_{Nd} . This can then be compared with the depleted mantle at the time of formation. This correction is made using the following equations.

$$\epsilon_{Nd}^i = \left[\frac{^{143}Nd/^{144}Nd_{rock,t}}{^{143}Nd/^{144}Nd_{CHUR,t}} - 1 \right] \times 10^4$$

Equation 3.3 - Where $^{143}Nd/^{144}Nd_{rock,t}$ is given by equation 3.3

$$\left[\frac{^{143}Nd}{^{144}Nd} \right]_{rock,t} = \left[\frac{^{143}Nd}{^{144}Nd} \right]_{rock,today} - \left[\frac{^{147}Sm}{^{144}Nd} \right]_{rock,today} \times [e^{\lambda t} - 1]$$

Equation 3.4 - Where the decay constant $\lambda = 6.54 \times 10^{-12} \text{ yr}^{-1}$

The age of the deposit is currently unknown. However the ϵ_{Nd} values can be corrected for a variety of different possible ages and plotted against time (Fig. 3.55). It can be seen that at any possible age the Sakatti samples are significantly more negative than the depleted mantle values. The implication of this is that the samples must have assimilated a significant amount of continental crust during their ascent.

The initial ϵ_{Nd} values at Sakatti are not the same. This variety could arise from differing degrees of contamination in the cumulate stack. Therefore it is worth assessing how the ϵ_{Nd} values change with depth and how they compare with any identified change in the magma chemistry at these levels.

There are two tentatively proposed layers in the deposit depicted in the mineral chemistry, particularly olivine chemistry. The general trend is for olivine to become more ferroan, and therefore more evolved, with decreasing depth. This trend is broken between 620 and 660 m, and it is suggested that a new layer of cumulate occurs above this, starting from more magnesian again. The top layer is poorly sampled due to the lack of well preserved (unserpentinised) samples.

There is a paucity of whole-rock samples in this ϵ_{Nd} as a significant number of samples were devoted to the separates in pursuing an unsuccessful aim of achieving an isochron. However the samples that are present follow this trend which suggests that the increasing evolution from top to bottom could be due to increasing contamination. Nb/Th values in the samples analysed for Nd isotope analysis exhibit a similar pattern, however when this is compared to the more complete data set of Nb/Th the same trend is only marginally shown, potentially due to lower precision in the whole-rock geochemical lab data (Fig. 3.52).

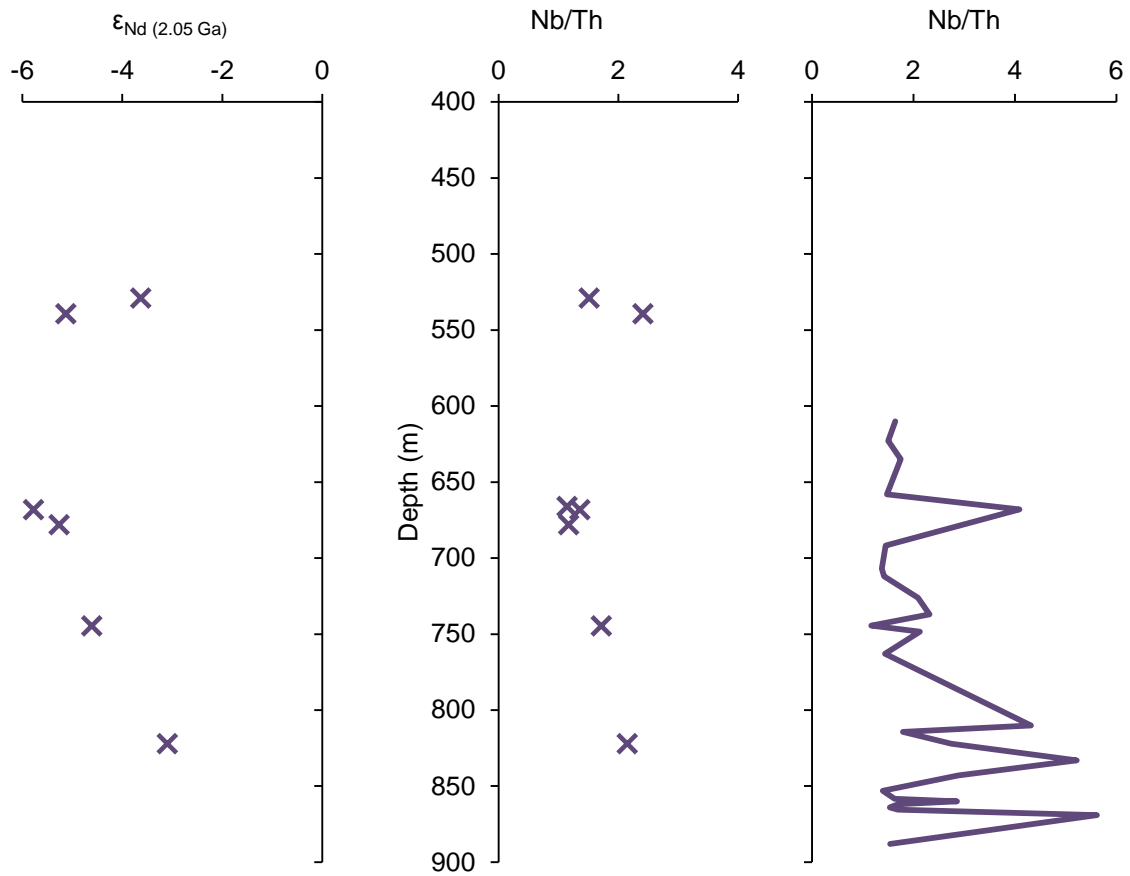


Figure 3.52 –Depth profiles of ϵ_{Nd} and Th/Nb in those same samples in hole 49. For comparison whole-rock undertaken at the NHM is compared, with more abundant sampling but lower precision.

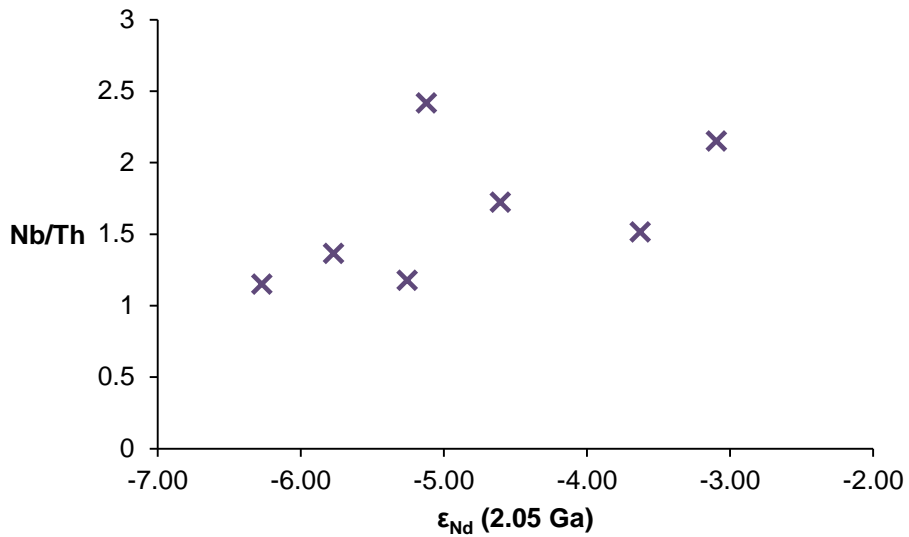


Figure 3.53 – Comparison of ϵ_{Nd} with the Nb/Th as an indicator of crustal contamination.

3.7 Discussion

3.7.1 Intrusive vs. extrusive

The Sakatti main cumulate body has been interpreted as both a shallow level conduit-like intrusion (Brownscombe et al., 2015) and also as an extrusive cumulate portion of the Aphanitic Unit (T. Halkoaho, pers. comm., 2014). While it is true that the Sakatti main cumulate body is located within a volcanic footwall and hanging wall, and ultramafic volcanic (e.g., komatiite and komatiitic basalt) successions are known to have associated peridotitic to dunitic cumulate bodies, there are several lines of evidence that suggest that Sakatti is not a lava channel cumulate but an intrusion into a lava flow field.

- The tubular shape of the cumulate body (Fig. 4.3).
- The Olivine Cumulate Unit has an apparent intrusive contact with the Aphanitic Unit both above and below the cumulate body, with micro-intrusions of cumulate within the aphanitic footwall and hanging wall (Section 3.3.6).
- The cumulate body is texturally and chemically different from the whole Aphanitic Unit, which itself has evidence of separate, distinct interlayered cumulate portions (Section 3.3.5 and 3.5).
- The cumulate body is large and homogenous. It is more than 400 m thick in sections with no clear evidence of flow tops or chilled margins (Section 3.1.3.2).

The points outlined above could be explained by the main cumulate body being a very large lava tube-type structure (T. Halkoaho, pers. comm., 2014) rather than a simple flow bottom. Leaving aside the compositional differences between the Aphanitic Unit and the main cumulate body discussed earlier, which are difficult to reconcile with such a scenario, the point at which a shallow conduit-like intrusion is distinguished from an extrusive lava tube becomes an issue of semantics. It is suggested that the aphanitic volcanism and the emplacement of the main cumulate body are probably related to the same overall magmatic event and the same magmatic feeder system, but that the main cumulate body formed slightly later as a shallow intrusion.

3.7.2 Crustal contamination

Crustal contamination of the parental silicate melt is an important factor in the formation of Ni-Cu-PGE deposits as the addition of silica has been identified as a potential cause for sulphide saturation (Li and Naldrett, 1993; Li and Ripley, 2005).

There is a dichotomy in the crustal contamination assessment at Sakatti. Both ϵ_{Nd} and various trace element ratios suggest that there has been significant contamination of the silicate melt with crustal material. On the contrary the olivine is highly magnesian, indicating that it is primitive, and the overall composition is ultramafic and so has not been particularly disrupted by large amounts of crustal material. The correlation of Mn and Zn in the low Ni edges of Sakatti cumulate could suggest reequilibration with a crustally contaminated melt (Bulle and Layne, 2015) meaning that the cumulus olivine and the intercumulus melt are not at equilibrium.

REE and other indicators of crustal contamination are present only at very low concentrations within the olivine at Sakatti whereas they are several orders of magnitude more abundant in clinopyroxene and amphibole. The REE pattern of the overall whole-rock at Sakatti closely matches that of the clinopyroxene (Fig. 3.54), suggesting that this mineral phase is the dominant control on the REE concentrations and therefore the isotope ratios within those REE at the Sakatti deposit. This is in agreement with the observation that clinopyroxene is the most abundant magmatic phase excluding olivine.

Unit		ϵ_{Nd} (2.05 Ga)	SiO ₂ (%)	Nd (ppm)	Sm (ppm)	Th (ppm)	La (ppm)	Nb (ppm)	Yb (ppm)
Parent melt		3.4	40	1	0.2	0.3	1	0.3	0.2
Granite	Möykkelmä Dome	-10	71.1	36.1	4.33	15.5	64.6	3.25	0.279
Quartzite	Sodankylä		76	10.7	1.89	2.69	12.9	2.66	0.603
Black schist	Matarakoski		55	12.1	3.2	12.7	9.66	6.72	1.97

Table 3.6 – Hypothetical parent melt concentrations of key crustal contamination indicators compared to potential contaminants. Comparison data from the publically available Bedrock Database of Finland (Hanski et al., 2001b; Makkonen and Huhma, 2007).

ϵ_{Nd} (2.05 Ga)	Archaean granite proportion	Parental melt proportion	Silica content	Th/Nb	Th/La
-2	1.5%	98.5%	40.5	0.7	0.27
-3	1.8%	98.2%	40.5	0.6	0.27
-4	2.0%	98.0%	40.6	0.6	0.27
-5	2.3%	97.7%	40.7	0.6	0.26
-6	2.6%	97.4%	40.8	0.5	0.26

Table 3.7 – Mass balance for different ϵ_{Nd} values found at Sakatti and the proportions of Archaean granite and hypothetical parental melt required to produce those values. Data from Table 3.6.

The very low concentrations of REE in ultramafic systems means that only a small proportion of contamination could come to dominate the ϵ_{Nd} signature of the melt simply because Sm and Nd are present in such higher quantities in the contaminant (Table 3.6). Table 3.7 shows that the ϵ_{Nd} range found at Sakatti requires <3% contamination by Archaean granite, and that this would have limited effect on the silica content of the melt. The same is true of the trace element ratios that are typically used to indicate crustal contamination.

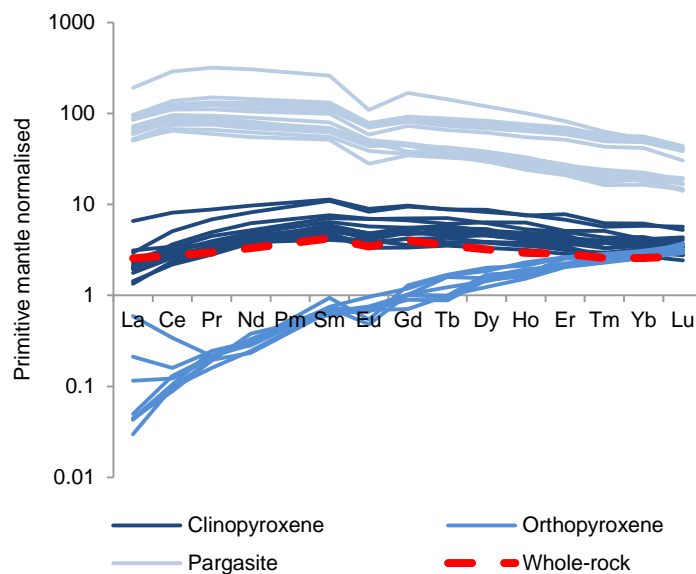


Figure 3.54 – REE profiles for an individual sample showing the whole-rock value and orthopyroxene, clinopyroxene and pargasite. The whole-rock value is very similar to clinopyroxene and is probably dictated by amphibole and clinopyroxene. Olivine is not shown because the REE values are mostly below detection limits.

Caution must be taken in cumulate systems given the separation in time and melt evolution between intercumulus and cumulus mineral phases. As the clinopyroxene is the dominant host of REE (and assorted others including Nb and Th) then both the trace element parameters and the ϵ_{Nd} must be treated as reflecting the degree of crustal contamination of the intercumulus melt.

The point of olivine crystallisation and olivine deposition do not have to be in close proximity in a dynamic flowing system and it is possible that the primitive olivine is carried in a continuously evolving and potentially contaminated melt before being deposited in a structural trap.

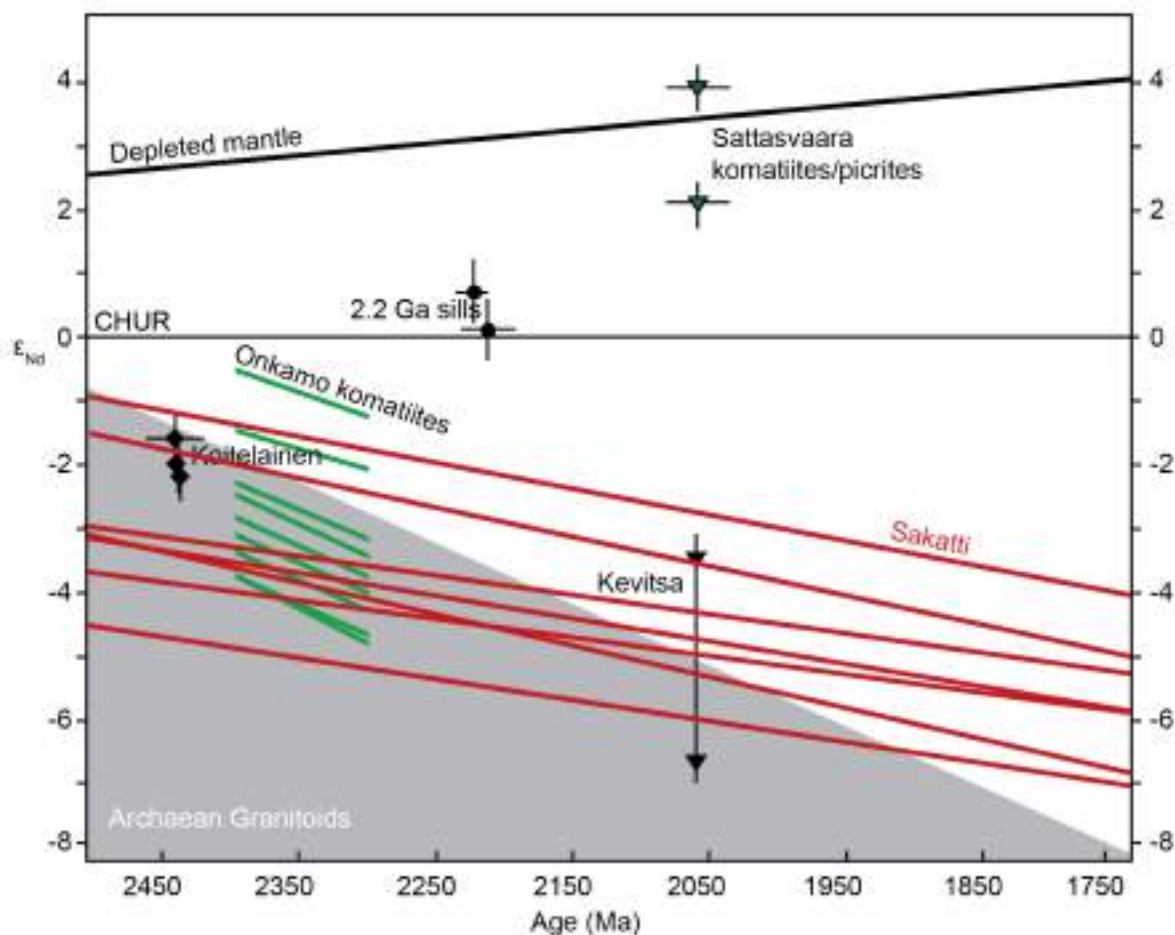


Figure 3.55 – ϵ_{Nd} values at Sakatti compared with other lithologies in the CLGB (Hanski and Huhma, 2005, and reference therein; Peltonen et al., 2014).

Likely contaminants for an ultramafic magma would be high in Sm and Nd, have a lower melting point than ultramafics and have a negative ϵ_{Nd} (Table 3.6). The most obvious candidate is the Achaean basement through which the magma will have travelled (Fig. 3.55).

The ϵ_{Nd} of Sakatti is similar to the Onkamo komatiites and the Koitelainen intrusion. These are both ultramafic-mafic units and as such would not be a significant contaminant. It could be argued that they have a shared history, however these units are both older than Sakatti is thought to be. Sakatti intrudes younger units above so cannot be genetically tied to these two magmatic events.

It is clear that Sakatti is similar to the Kevitsa deposit. The ϵ_{Nd} values (Fig. 3.55) being similar between these two Ni-Cu-PGE hosting deposits points towards them having a shared genetic history. If not actually being related to the same magma, then a very similar process appears to have happened to them.

There is also marked ϵ_{Nd} dissimilarity between Sakatti and the 2.2 Ga intrusions, suggesting that it is unlikely that these two are related (Fig. 3.55). The samples are also different from the Savukoski komatiites. These komatiites are of unknown exact age but have positive ϵ_{Nd} values indicating they are not crustally contaminated. They therefore cannot be an extrusive equivalent of the Sakatti deposit and if they do share any similar mantle heritage then they have developed along a different path in that they have survived the journey through the crust uncontaminated, unlike Sakatti. The komatiites are unlikely to host any Ni-Cu-PGE deposits as crustal contamination is critical to the genesis of these deposits in ultramafic systems.

3.7.3 Comparison with regional geology

Mineralogically the Sakatti intrusion is similar to all three of the proposed similar intrusions posited in chapter 2. Differences are most clear in the overall structure of the deposit and the absence of similar features.

3.7.3.1 2.4-2.5 Ga intrusions

These large layered mafic intrusions are not particularly similar to the Sakatti deposit which is neither large, layered nor mafic. They share similar mineralogical constituents, in particular the cumulate peridotite at the base of the lower suite in the Koitelainen intrusion (2.4.4.1).

The intrusions of the Tornio- Näränkäväära belt (Tornio, Kemi, Penikat, Portimo, Koillismaa) are all large layered mafic intrusions of similar age to Koitelainen (Iljina and Hanski, 2005).

The Sakatti deposit is within younger terrane and it is not geologically feasible for it to be as old as these intrusions. Furthermore the style of mineralisation in these intrusions is dissimilar to Sakatti. The Koillismaa complex hosts the bushveld-style chromite PGE-bearing Rometölväs reef hosted by gabbronorite (Karinen, 2010). The Penikat intrusion several reefs in the Sompujärvi, Ala-Penikka and Paasivaara reefs (Alapieti and Lahtinen, 1986). Mineralisation at Sakatti by contrast is disordered non-chromite bearing massive sulphide.

The Portimo complex hosts PGE-enriched Cu-Ni sulphides in the thick marginal series at the base as well as the PGE reef type deposits (Iljina and Hanski, 2005). However, the structure and layered stratigraphy bears no similarity to the Sakatti deposit which is a small chonolith. It is deemed exceedingly unlikely that the Sakatti deposit is related to these intrusion in any way.

3.7.3.2 2.2 Ga intrusions

The 2.2 Ga gabbro-wehrlite sills are more similar in form to the Sakatti deposit. There are several sills in close proximity to the Sakatti deposit, the Rantavaara-Särkivaara intrusion, the Ponostama intrusion and the Pikku-Vaiskonselkä sill.

Sakatti is lacking the gabbro part of the gabbro-wehrlite association. The Haaskalehto and Runkausvaara sills have been analysed for Sm-Nd (Hanski and Huhma, 2005) and show ϵ_{Nd} values closer to depleted mantle than Sakatti (Fig. 3.55). The Ponostama intrusion has olivine Fo# of 60-70 and Ni content >500 ppm (Mäkimattila, 2015). The Pikku-Vaiskonselkä sill by contrast has olivine with Fo# 84.3-85.4 and Ni content up to 2300 ppm (Suvanto, 2014). These are both more evolved and Ni-poor olivine than at Sakatti.

3.7.3.3 2.05 Ga Kevitsa intrusion

The Kevitsa deposit provides the most pertinent comparison to the Sakatti deposit. They are mineralogically similar although structurally different. The Kevitsa deposit has similar ϵ_{Nd} values to Sakatti (Fig. 3.55). The olivine is generally between 75-85% forsterite. The olivine in the Ni-PGE ore type has an exceptionally high Ni content, up to 1.7% Ni (Mutanen, 1997; Yang et al., 2013). The Kevitsa host rock is more evolved than the Sakatti host rock, being pyroxenitic rather than peridotitic and having lower Fo# olivine. The comparison between the styles of mineralisation in chapters 4 and 5 is necessary in order to fully evaluate the similarity between the two deposits.

3.7.4 Multiple pulses within the intrusion

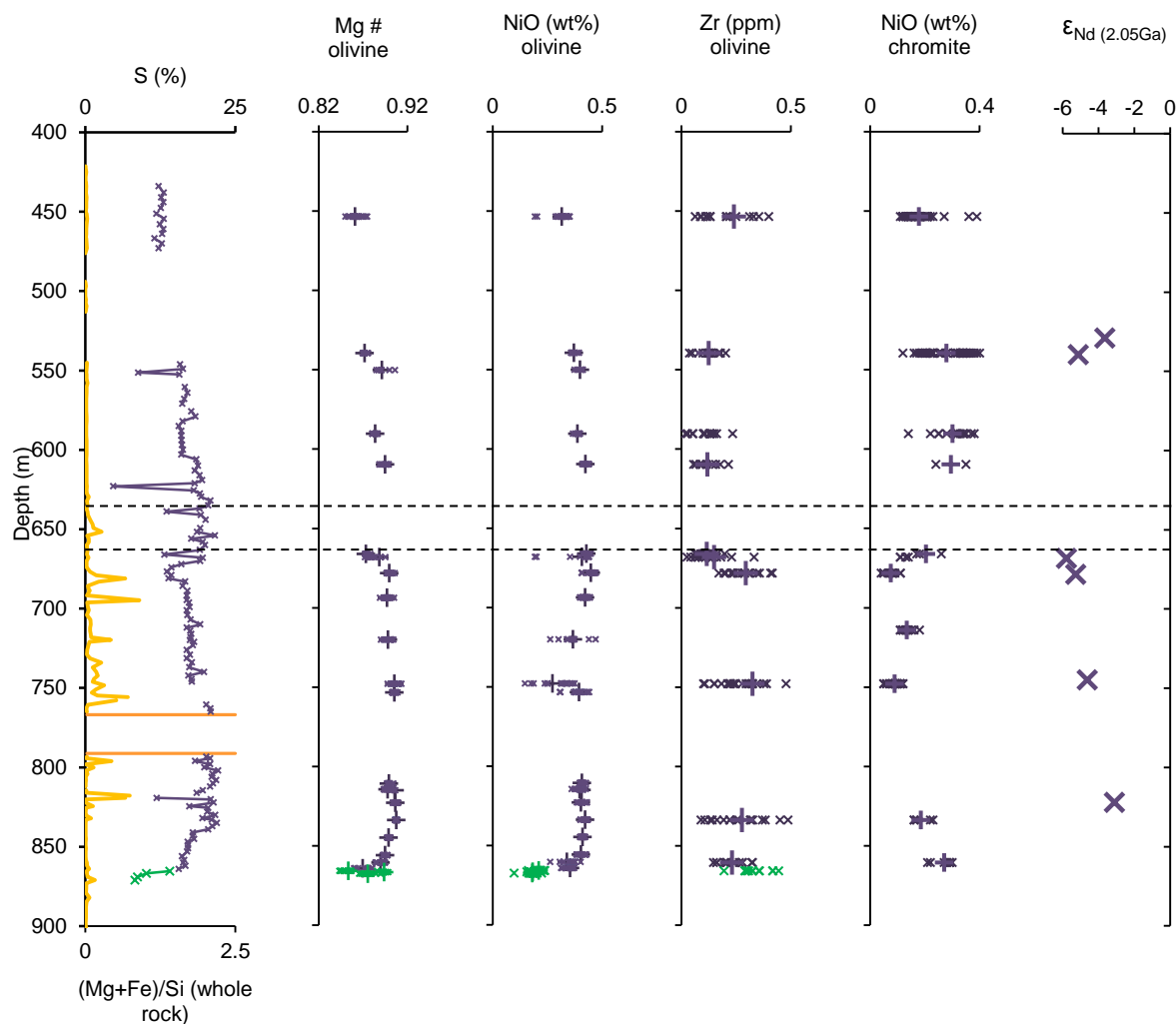


Figure 3.56 - Downhole plot showing whole-rock geochemistry and mineral chemistry data. Plotted from left to right are: whole-rock S%, whole-rock Mg+Fe/Si normalised to Zr (volatile and sulphide corrected), WDS data for Mg/(Mg+Fe) in olivine, NiO wt% in olivine and NiO wt% in chromite. Layers can be identified in the whole-rock geochemistry and these correlate broadly with subtle changes in mineral chemistry. The dotted lines indicate the potential top of the mineralised pulse which is reflected in the mineral chemistry. Detection Limits NiO olivine: 0.031 % Zr olivine: 0.004 ppm NiO chromite: 0.02 %. Analytical error NiO olivine: 0.02 absolute wt% 3σ (EPMA), Zr olivine: 13.7 relative % (LAICPMS) NiO chromite: 0.01 absolute wt% 3σ (EPMA).

The sampling strategy of this project focused on one particular drill hole, hole 49 (Fig. 3.1) with an array of techniques in order to assess any separate pulses or layers within the intrusion. A paucity of preserved magmatic minerals has led to an incomplete record downhole but using more complete whole-rock data has meant that these gaps can be extrapolated between. In this hole there are up to six separate pulses identifiable in the whole-rock (Mg+Fe)/Si values. Mineralisation is present in throughout the four pulses near the base. The magmatic mineral chemistry of these pulses did not reveal any particularly chemical fingerprint that identifies them as hosting mineralisation. Mg# in olivine broadly conforms to the separate whole-rock pulses. However the pulse directly above the main massive mineralisation is identified as being

more pyroxenitic while having the highest Mg# olivine suggesting that it is the mineral proportions that are controlling the whole-rock signature. Olivine does not show a more evolved signature despite more pyroxene being present, suggesting olivine mineral chemistry is independent of the intercumulus melt evolution.

3.7.5 Base of the intrusion

The base of the intrusion shows a more evolved signature in the whole-rock geochemistry and olivine chemistry. The Ni values within olivine, however abruptly change from Aphanitic Unit type to Olivine Cumulate Unit type. The whole-rock variation is likely to be assimilation of the Aphanitic Unit, given the micro-intrusional contact between the two units. It is also common for the base of ultramafic cumulate bodies to have a more evolved signature as a marginal reversal (Latypov et al., 2011). It cannot be resolved whether the more evolved signature is due to a marginal reversal or more contamination by the more felsic Aphanitic Unit, however the abrupt change in Ni values distinguishes that where the Olivine Cumulate Unit magmatic processes occur the silicate melt was not Ni-depleted.

3.7.6 Nature of contact with the Aphanitic Unit

The unusual contact between the Aphanitic Unit and the cumulate unit is present at both hanging wall and footwall contacts between the two units. As described in the petrology section, the darker, network-like parts of the texture contain olivine grains matching in composition with the cumulate olivine while the rest of the rock contains lower Ni aphanitic olivine. It seems clear from the network-like texture that the cumulate unit has intruded the Aphanitic Unit on the micro-scale.

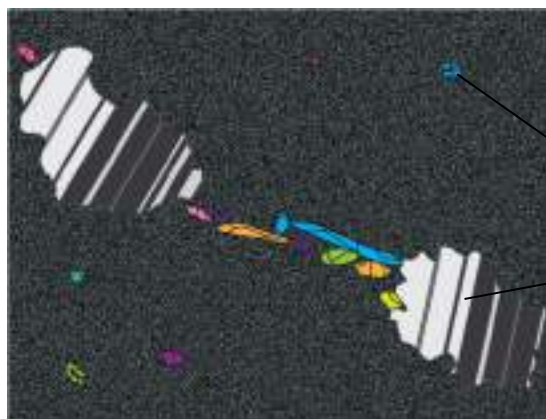


Figure 3.57a – Fresh samples of the Aphanitic Unit, at a considerable distance from the Olivine Cumulate Unit, have olivine and plagioclase phenocrysts that are aligned, potentially due to a volcanic texture such as autobrecciation.

Olivine phenocrysts
Plagioclase phenocrysts

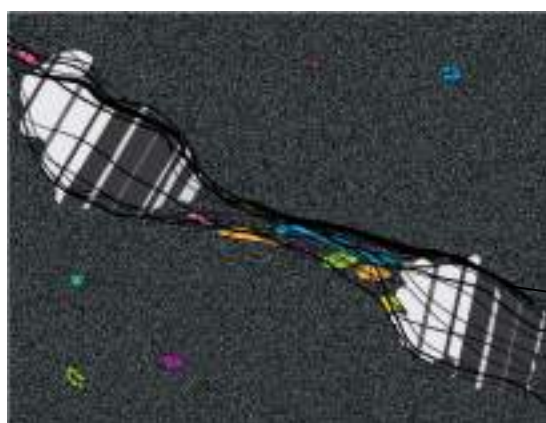


Figure 3.57b –Serpentinisation is focused along the long axes of phenocrysts resulting in a network of serpentine veins that are present in and around the plagioclase and olivine phenocrysts. The groundmass remains unserpentinised. The serpentinising fluid may have been related to the intrusion.

Serpentine veins



Figure 3.57c –During melting of the Aphanitic Unit due to the emplacement of an ultramafic conduit, the Olivine Cumulate Unit preferentially melts along the serpentine veins. The presence of plagioclase with hydrous phases would be particularly unstable at high temperature. Cumulate olivine along with sulphide melt are injected into the Aphanitic Unit along these melting paths.

Emplacement of Olivine Cumulate Unit
Cumulate olivine
Sulphide



Figure 3.57d –Due to the hydrous nature of the intercumulus and the openings from the Olivine Cumulate Unit micro-intrusions, these are preferentially serpentinised. The aphanitic groundmass remains unserpentinised. The olivine cumulate shapes are only visible where mineralisation highlights them. Preserved olivine retains the Ni-undepleted signature of the Olivine Cumulate Unit compared to the Ni-depleted signature of the aphanitic phenocrysts.

Serpentinisation of cumulate olivine

Figure 3.57 – Cartoon showing serpentinisation then micro-intrusion as a proposed model for the origin of the Olivine Cumulate Unit – Aphanitic Unit contact texture.

This pattern of micro-intrusions suggests that the cumulate unit exploited a pre-existing texture or weakness in the Aphanitic Unit. Petrographic examination of samples of the Aphanitic Unit that are more than 100 m from the intrusion reveal an heterogeneous texture defined by concentrations of olivine and plagioclase phenocrysts and differing pyroxene chemistry. While these samples are remarkably unaltered given their antiquity, there is a minor network of fine serpentine veins that are concentrated along these phenocrysts.

A suggested interpretation of the origin of this structure is that minor serpentine veining occurred prior to emplacement of the main cumulate body, potentially associated with it. The presence of these hydrated micro-veins along with plagioclase phenocrysts would consequently have a lower solidus than the rest of the aphanitic rock resulting in preferential melting along the network structure created by the veins (Fig. 3.57).

3.7.7 Pegmatoidal Gabbro Sub-Unit

A Pegmatoidal Gabbro Sub-Unit has been identified in this study. It hosts the semi-massive style of mineralisation and is often associated with massive mineralisation. The presence of a coarse gabbro within the Olivine Cumulate Unit requires some examination. The presence of the Pegmatoidal Gabbro Sub-Unit does not relate to any identified chemical layering and cannot be correlated between drill holes. Texturally the Olivine Cumulate Unit does not grade into the pegmatoidal gabbro, rather the sub-unit has sharp contacts. This means it is unlikely to be evolved portions of melt that have crystallised without cumulate olivine forming. The sharp contacts, at variable angles, and relatively narrow proportions (0.5-15 m) suggests that these are dykes of more evolved melt. The association of mineralisation with evolved fluid-rich melt is potentially because they were both late liquid phases while the majority of the Olivine Cumulate Unit was crystalline.

3.7.8 Serpentinisation

Serpentinisation affects most of the Olivine Cumulate Unit but not the Aphanitic Unit nor the Dunite Sub-Unit within the Olivine Cumulate Unit. The presence of unserpentinised rocks means that the serpentinisation that affects most of the Olivine Cumulate Unit is not pervasive regional alteration but is specific to intrusion.

Remnant olivine within serpentinised cumulate shapes are crystallographically aligned suggesting that it is not metamorphic. There no evidence to suggest that the units have undergone significant metamorphism capable of reproducing olivine from serpentine. The regional metamorphism is greenschist facies (2.4.3). Serpentinisation and the fluids associated

with it do not significantly affect mineralisation as hydrothermal textures are not observed in the magmatic sulphide mineralogy. The silicate Ni held within olivine is transferred into serpentine as seen in EPMA mapping (Fig. 3.26)

The magnetite produced by serpentinisation makes the entire Olivine Cumulate Unit strongly magnetic. It is most likely that is in fact the magnetic anomaly of the serpentinisation that helped lead to the discovery of the deposit, rather than a magnetic anomaly of the mineralisation as supposed. The serpentinisation of high Mg olivine, such as that at Sakatti, could be expected to increase the Si content of the rocks (Equation 3.2) and will inevitably disrupt the whole rock geochemistry, meaning caution should be taken interpreting whole rock data. This is why magmatic mineral chemistry has been relied upon in this project.

Serpentinisation could result from preferential introduction of fluids to majority of the intrusion due to a structural effect. However the presence of magmatic pargasite as an intercumulus phase within the intrusion means that the intercumulus melt must have been hydrous. This raises the possibility that the intrusion auto-serpentinised due to aqueous magmatic fluid present in the intercumulus. The absence of serpentinisation in the Dunite Sub-Unit, which is an adcumulate where intercumulus is not present, could be explained if the serpentinisation was a result of auto-serpentinisation by the crystallising intercumulus phase.

3.7.9 Dissociation of olivine chemistry with mineralisation

Olivine within the main cumulate body contains high amounts of Ni, which indicates crystallisation from a melt that had not been depleted in Ni by S saturation. Considering the primitive nature of the host rocks, the deposit is overall very Cu-rich, both the disseminated and fractionated massive sulphide. The high Ni content of the olivine implies that it was not in equilibrium with the sulphide melt, melt that is also in equilibrium with a Cu- and Fe-rich sulphide, and yet both the olivine and the disseminated sulphide have been transported and emplaced together. The fact that the olivine is out of equilibrium with the sulphide-carrying melt is confirmed by the loss of Ni from the rims of olivine in some of the mineralised samples. The current silicate host cannot, therefore, be considered as the parental melt for the sulphide.

It is theoretically possible to explain both the Ni-rich olivine and the Cu-rich sulphide if the olivine crystallises first, robbing the melt of Ni and then S saturation is achieved by the intercumulus melt. In order to strip sufficient Ni to result in a Cu-dominated deposit, a considerable evolution of the melt would be required and consequently varied olivine chemistry down to low forsterite content would be expected and this is not seen at Sakatti. A second possibility is that the sulphide had already been deposited by earlier magmatic activity

“upstream” in the same conduit system and was remobilised by the current host, which also brought in the cumulus olivine.

3.8 Conclusions

The host rock of the Sakatti deposit is a primitive olivine cumulate, which is undepleted in Ni. This cumulate body is a tubular structure that sits within a plagioclase-rich picrite and cross cuts hanging wall lithologies. The plagioclase picrite is a fine-grained volcanic unit with Ni-depleted olivine phenocrysts that are distinct from the olivine cumulate.

The contact between the cumulate and the picrite is characterised by a micro-intruding texture where the cumulate unit intrudes into the plagioclase-rich picrite along a network texture, potentially following prior veins of serpentinisation within the picrite. This contact is present both above and below the cumulate body and so it is interpreted as a shallow level intrusion in an earlier but similar magmatic unit potentially related to the same phase of magmatic activity.

The olivine containing high Ni levels is out of equilibrium with a sulphide liquid suggesting that the current host rock and the sulphide mineralisation have not derived from the same parental melt. Geochemistry of the intercumulus minerals suggests a degree of crustal contamination but only potentially 3% by mass Archaean granitoids so not necessarily at odds with the primitive nature of the olivine cumulate.

3.9 Implications for exploration and further work

The most significant exploration implication of this work is it does not agree with the often cited exploration tool of searching for Ni-depleted olivine as an indicator of magmatic sulphide formation (Eg. Fleet et al., 1981; Li et al., 2001a; Rajamani and Naldrett, 1978). The Sakatti deposit demonstrates that although Ni-depleted olivine may be a theoretical product of the parent melt that produced a sulphide melt, it does not have to be the current host of an ore deposit or particularly spatially related to it.

Exploration within the CLGB should involve assessing ultramafic bodies. The presence of negative ϵ_{Nd} in both the Kevitsa and the Sakatti deposits but not the barren Savukoski komatiites could imply that assessing for crustal contamination is an important factor. The older Onkamo komatiites are not well explored in the succession, but the presence of a crustally contaminated ϵ_{Nd} within them also raises implications for potential ore bodies hosted by these units.

4 Sulphide mineralisation

4.1 Introduction

This chapter is focused on Ni-Cu-Fe sulphide mineralisation at the Sakatti deposit, both as massive sulphide and disseminations throughout the silicate host rocks. Description of the structure of the mineralisation follows the previous chapter that outlined the shape of the deposits and the host silicates. The sulphide was studied initially by core logging across the deposit, before two specific representative holes (M8044 and M8049) were chosen to target sampling for petrological work. Broader scale sampling was undertaken for other techniques, principally S isotope analysis, in order to provide a representative sample set of the whole deposit.

The Pt-Pd mineralisation is present as discrete phases within the sulphide and these are discussed in the next chapter.

4.1.1 Deposit overview

Mineralisation at Sakatti consists of disseminated, vein, semi-massive and massive sulphides. Vein, semi-massive and massive mineralisation styles are found mostly within the olivine cumulate bodies but can extend into the Aphanitic Unit footwall and hanging wall. In contrast, significant disseminated mineralisation is only found within the olivine cumulate bodies. Not all of the main cumulate body is mineralised; within the relatively thick central and eastern portions of the body typically only the bottom half hosts mineralisation. In the far west and north where the cumulate body is relatively thin, mineralisation occurs throughout the entire cumulate package.

4.1.1.1 Main body

The *massive sulphide* mineralisation is present within the Olivine Cumulate Unit and also extends into the aphanitic footwall and sidewall of the main cumulate body for up to approximately 150 m. There are several different lenses of massive sulphides, at least two of which can be correlated between drill holes. The lenses are thickest (up to 25 m) in the centre of the deposit and thin out to as little as 0.5 m towards both the north-west and south-east.

The massive and veined sulphide mineralisation within the main cumulate body shows a distinct change in Ni/Cu ratios. In the west and north-west, i.e., in the deeper portions of the deposit, massive sulphides are composed of pyrrhotite-pentlandite-chalcopyrite with overall

Ni/Cu values greater than one. The composition of the massive sulphides evolves up-plunge to become increasingly chalcopyrite-dominated (Fig. 4.1).

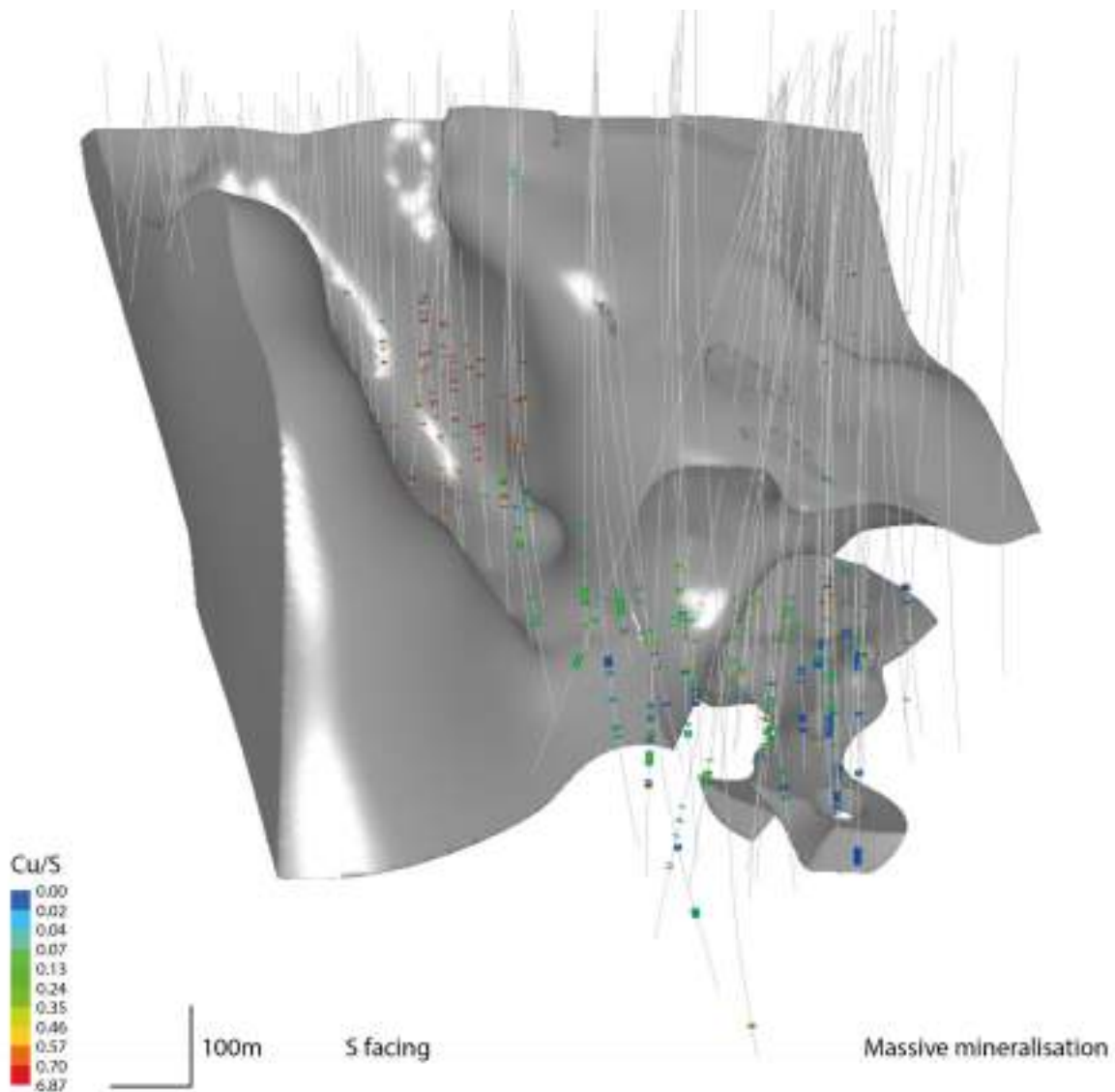


Figure 4.1 - 3D diagram showing Cu/S ratios for intersections of massive sulphides in the Sakatti deposit. Cu/S has been displayed as a proxy for $Ni_{sulphide}/Cu$ to eliminate silicate Ni. The upper contact of the Aphanitic Unit is shown in grey and the Olivine Cumulate Unit has been removed. The deposit sits in a channel within the Aphanitic Unit. Note the increase in Cu tenor of the sulphide up-plunge of the conduit-like body.

Massive sulphide lenses extending downwards from the cumulate body into the Aphanitic Unit show a concomitant decrease in thickness and Ni/Cu ratios with respect to distance from the cumulate body. Such trends occur over a much shorter distance than those observed up-plunge within the cumulate body. At the terminal extremities of the massive sulphide lenses, both within the cumulate body and the Aphanitic Unit, there is a marked increase in precious metal tenors, in particular that of Pt.

An additional style of mineralisation is typified by coarse, pegmatoidal gabbroic silicates with semi massive (interstitial) sulphides. The coarse Pegmatoidal Gabbro Sub-Unit occurs both with and without associated sulphide mineralisation.

Vein sulphides are present to a lesser extent throughout the main cumulate body, but are most abundant in its shallow south-eastern part where the massive sulphide lenses show relatively low Ni/Cu ratios and reduced thickness. The sulphide veins are mostly relatively thin with a broad range of orientations and contain predominantly chalcopyrite. As such they are judged to be distinct from the massive sulphides. The veins are generally 5-20 cm thick, but can be up to 50 cm in thickness. The use of the term “vein” is not intended to imply an epigenetic hydrothermal origin; rather, the veins are interpreted to represent fractionated apophyses of the main massive sulphide lenses (Fig. 4.2).

Disseminated sulphides or the interstitial mineralisation, as it is commonly referred to, occur predominantly in the central, steeply plunging and the south-east, shallowly plunging parts of the main cumulate body. In terms of composition, the mineralisation is generally chalcopyrite-dominated with only minor pyrrhotite, pentlandite and pyrite. The occurrence of this style of mineralisation is spatially independent of the other styles. In many places the disseminated mineralisation is cut by massive sulphide veins of varying composition and size. However, there are numerous examples where disseminated sulphides show no spatial association with massive sulphides, neither vertically nor laterally. This is especially the case at depth in the north-western part of the body.

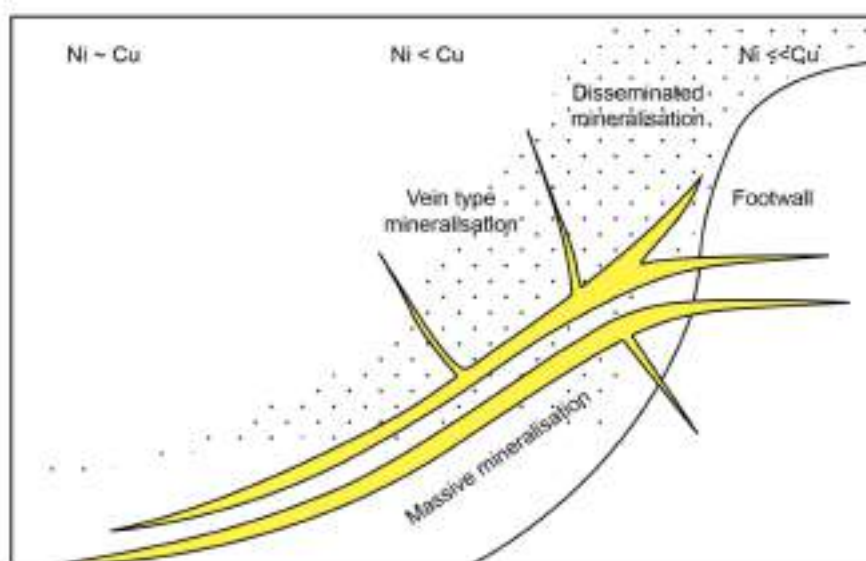


Figure 4.2 – East-west cartoon illustrating the main types of mineralisation and their approximate distribution in the Sakatti deposit along with approximate Ni/Cu values. This does not represent the actual morphology of the deposit, instead it is to illustrate the occurrence of the different mineralisation styles.

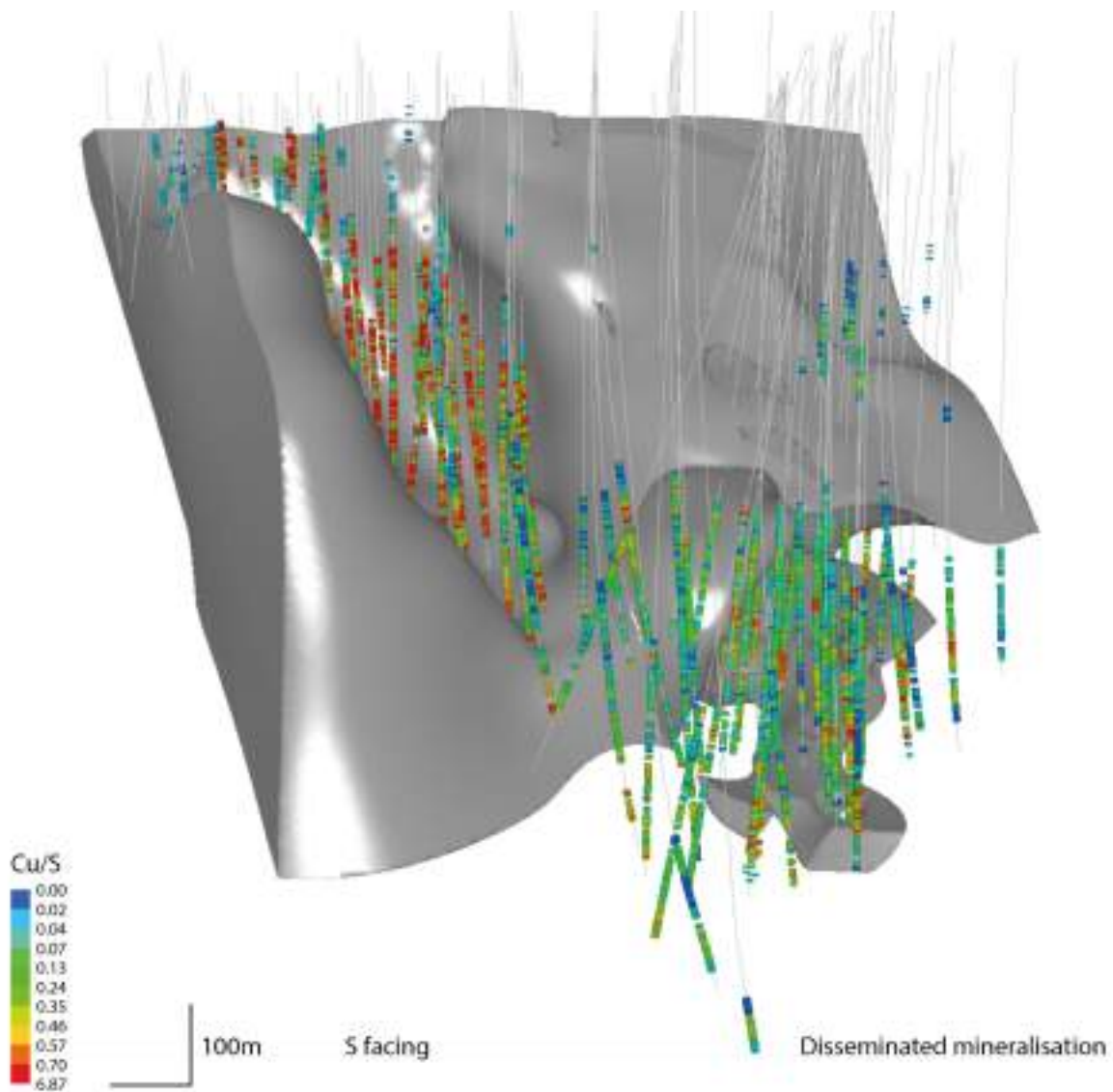


Figure 4.3 - 3D diagram showing Cu/S ratios for intersections of disseminated sulphides in the Sakatti deposit. Cu/S has been displayed as a proxy for $Ni_{sulphide}/Cu$ to eliminate silicate Ni. The upper contact of the Aphanitic Unit is shown in grey and the Olivine Cumulate Unit has been removed. The deposit sits in a channel within the Aphanitic Unit. Note the increase in Cu tenor of the sulphide up-plunge of the conduit-like body.

As discussed in greater detail later in this paper, minor interstitial chalcopyrite also occurs in small Olivine Cumulate Unit intrusions within the hanging wall and footwall Aphanitic Unit, although this is restricted to within 20 m of the contact with the cumulate body.

The disseminated sulphides are generally chalcopyrite-dominated but the Cu/S ratio shows considerable variation, being relatively Cu-poor in the deeper north-western part of the main body and relatively Cu-rich in the shallow south-eastern part (Fig. 4.3).

4.1.1.2 North-east body

Mineralisation in the north-east body is almost entirely limited to massive sulphides at the basal contact between the cumulate body and the volcano-sedimentary package. Disseminated mineralisation is of minor significance. The metal tenors of the massive sulphides are very similar to those of massive sulphides at depth in the main cumulate body; Ni contents are roughly equal to or greater than Cu contents, and Pt and Pd are present in a ratio of 2:1, although both Pt and Pd are enriched compared to massive sulphides in the main cumulate body. One notable difference when compared to the main body is the abundance of coarse-grained pyrite and the lack of pyrrhotite.

4.1.1.3 South-west body

Mineralisation in the south-west cumulate body occurs in a variety of forms. On the eastern side of the body mineralisation is massive and semi-massive and located within chlorite gouge at the upper contact of the cumulate. Moving further west, massive sulphides, semi-massive sulphides as well as clasts of massive sulphide are found within the body. All mineralisation in the south-west body is Ni-dominated with a Ni/Cu ratio of two.

4.1.2 Key questions

This is the first academic study of the deposit and as such involves characterisation and broad discovery of the style of mineralisation using conventional petrological techniques. There are also specific questions regarding the genesis of the deposit that need to be addressed and have resulted in the application of more specialised analysis.

4.1.2.1 What is the cause of S saturation?

The initial hypothesis for the Sakatti deposit is that S saturation has been achieved by contamination of the intrusion by the Matarakoski sulphide-bearing meta-sediments that are proximal to the deposit. This is tested using isotopic S analysis.

S isotopes

In magmatic Ni and PGE systems, S isotopes has been applied to determine the degree of input from externally derived S, with mantle derived S having values of $\delta^{34}\text{S}$ 0 ± 2 ‰ (Ohmoto and Rye, 1979) or 1.3 ± 3.8 ‰ (Chaussidon et al., 1989; Seal, 2006) and a crustal S input potential having a much more varied signature (Ripley and Li, 2003 and references therein). The S isotope behaviour of the Mesoproterozoic is disputed. The Archaean and early Proterozoic oceans were low sulphate with limited fractionation of $^{32}\text{S}/^{34}\text{S}$, however a change to the S cycle followed at ~ 2.4 Ga (the Great Oxidation Event), when fractionation (variability) increases due to higher oceanic sulphate levels and increased sulphate reduction through bacteria (Farquhar et al., 2010). Thus, if contamination of magmas has occurred using rocks prior to 2.4 Ga, standard $\delta^{34}\text{S}$ data has limited applicability, given the small variations seen in natural sediments prior to this period. In contrast, mass independent fractionation of S, recorded in $^{33}\text{S}/^{32}\text{S}$ ($\Delta^{33}\text{S}$) and $^{36}\text{S}/^{32}\text{S}$ ($\Delta^{36}\text{S}$), is present prior to this change in the S cycle due to special atmospheric conditions, and has been used to show contamination by Archaean sediments in Ni-PGE deposits (Fiorentini et al., 2012).

The Sakatti deposit is located in close proximity to the ~ 2.2 Ga Matarakoski black schists (Hanski and Huhma, 2005) and so S isotope analysis was used (1) to determine whether the Matarakoski black schists have a fractionated $\delta^{34}\text{S}$ signature likely therefore to show contamination using standard S isotope analyses, and, in parallel, (2) to analyse the Sakatti deposit for $\delta^{34}\text{S}$. The aim is to establish whether the Matarakoski schists have contributed significant S to the Sakatti deposit.

4.1.2.2 Why is the deposit Cu-rich?

There are several possible hypotheses that could lead to a Cu-rich magmatic Ni deposit. These are all considered in the discussion, but the principal hypothesis being tested in this chapter is

to determine whether the Cu-rich nature of the deposit results from fractional crystallisation of the sulphide melt removing the Ni-rich portion of the deposit.

The morphology of the Ni/Cu distribution is considered along with a traditional petrographic approach to determine the mineral associations present. Analyses specifically intended to test this hypothesis are detailed below.

PGE (Pt group element) behaviour – bulk sulphide and minerals

The behaviour of the PGE can be used to determine whether fractional crystallisation and loss of early MSS cumulates has occurred. This is because the IPGE (Ir group PGE) partition into the first forming MSS cumulates whereas the PPGE (Pd group PGE) are concentrated in the residual liquid (Holwell and McDonald, 2010). Analysis of the PGE contents of individual minerals and also the bulk sulphide will provide information about the degree of evolution of the sulphide melt and IPGE/PPGE content should correlate with Ni/Cu ratio if fractionation of the sulphide is the dominant control on the Ni/Cu distribution at the deposit.

Assessment of the individual mineral PGE contents will be particularly useful assessing the PGE behaviour as the less common PGE are frequently concentrated within solid solution in certain bulk sulphide minerals.

Ni isotopes

Recent studies report Ni isotope analyses that have been used in a magmatic Ni-Cu-PGE system at the Duluth Complex, Minnesota (Asp et al., 2015), the Agnew-Wiluna greenstone belt, W Australia and the Abitibi greenstone belt, Canada (Guegen et al., 2013), the Trojan and Shanghai mines, Zimbabwe (Hofmann et al., 2014) and the Creighton mine in the Sudbury igneous complex, Canada (Gall, 2011). The data from this last study are presented in this chapter with permission as a comparison to the Sakatti data (Gall, 2011). All of these studies indicate that mass dependent fractionation of Ni isotopes occurs during formation or crystallisation of magmatic sulphide liquid, and so this technique was utilised to analyse samples from the Sakatti deposit.

Magnetite

Magnetite is the only major non-sulphide phase that is present within the massive sulphide. It has derived directly from the sulphide liquid and as such has very low lithophile content when compared to magnetite that has derived from a silicate melt. However it is the only mineral that concentrates the lithophile elements from the sulphide melt and as such has the potential to

reveal information about the nature of the sulphide melt (Dare et al., 2014b). Magnetite has been shown to provide an indication of the degree of evolution of the sulphide melt as the most primitive MSS cumulates co-form with the first magnetite which scavenges lithophiles from the sulphide melt (Dare et al., 2014a). Later forming magnetite has lower lithophile content as it has formed from depleted sulphide melt.

4.1.2.3 What is the origin of the pyrite mineralisation?

The hypothesis for pyrite mineralisation is that it is present as an alteration product of the original magmatic sulphide at the deposit. This will be tested using conventional petrography and trace element geochemistry.

4.1.2.4 To what extent do hydrothermal processes affect the mineralisation?

The extent of hydrothermal alteration at the deposit is related to the origin of pyrite. Hydrothermal controls on PGE distribution at the deposit, affecting the Pt/Pd ratio will be examined and the extent of an upgrading/downgrading or redistributive component to the deposit that may have originated hydrothermal processes assessed.

4.2 Sampling

The core petrological samples were restricted to 20 polished blocks that were taken from two holes in the geographical centre of the deposit (Fig. 3.1, Table 4.2). The decision to focus purely on two holes was taken in order to observe down-hole variation rather than geographical variation.

These samples were used for several different analytical techniques, with detailed petrological knowledge obtained through microscopic analysis. Additional samples were taken spatially across the deposit more specifically for S isotope analysis but also Ni isotope analysis and an unsuccessful attempt at Re/Os geochronology.

Hole	Depth	Style	Dominant sulphide phase
44	636.93	Massive	Chalcopyrite
44	650.91	Semi-massive	Pyrite
44	684.49	Semi-massive	Pyrrhotite
44	696.16	Massive	Pyrrhotite
44	760.77	Disseminated	Chalcopyrite
44	762.54	Massive	Pyrrhotite
44	779.20	Semi-massive	Pyrrhotite
49	679.80	Massive	Chalcopyrite
49	681.86	Massive	Pyrite
49	695.74	Massive	Pyrite
49	714.15	Disseminated	Chalcopyrite
49	734.49	Massive	Pyrite
49	744.68	Disseminated	Chalcopyrite
49	757.36	Massive	Pyrrhotite
49	759.70	Massive	Pyrite
49	767.78	Massive	Pyrrhotite
49	773.57	Massive	Pyrrhotite
49	792.45	Massive	Pyrrhotite
49	820.00	Massive	Chalcopyrite
49	869.14	Disseminated	Chalcopyrite

Table 4.1 – List of primary samples made into sulphide blocks for petrological study and analysis.

4.3 Results

4.3.1 Petrography

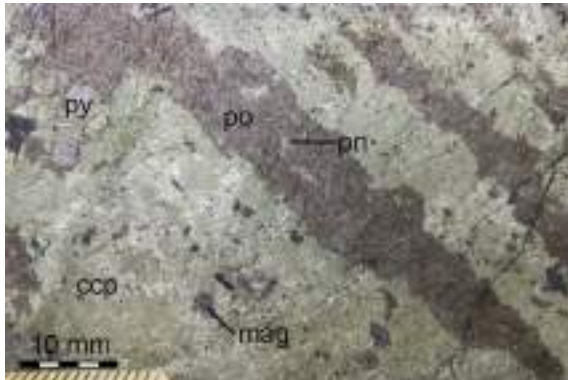


Figure 4.4a - Chalcopyrite-dominated massive sulphide mineralisation with streaks of pyrrhotite and minor pentlandite and magnetite.

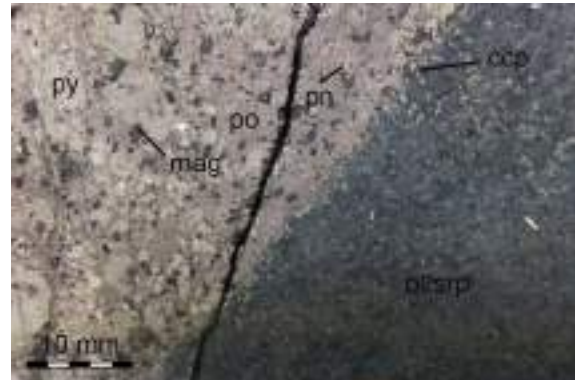


Figure 4.4b - contact of pyrrhotite-pentlandite-pyrite massive sulphide mineralisation with olivine cumulate.

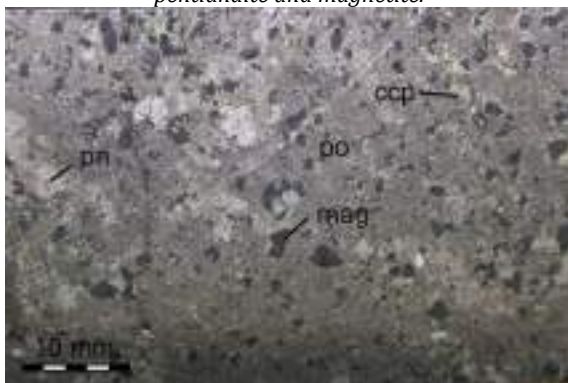


Figure 4.4c - pyrrhotite-pentlandite massive sulphides with minor chalcopyrite and euhedral magnetite.



Figure 4.4d - massive sulphides showing segregation of pyrrhotite-pentlandite and chalcopyrite.

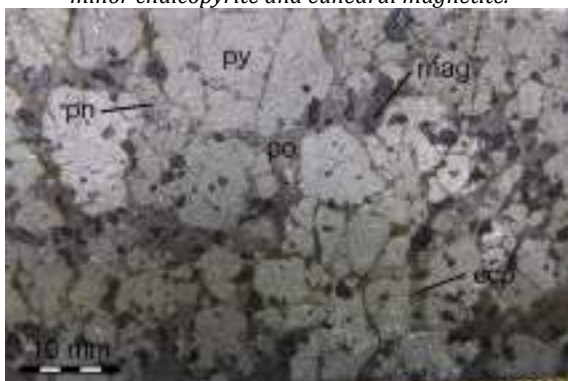


Figure 4.4e - pyrite style of mineralisation characterised by large pyrite grains, typical of, but not exclusive to the north-east body mineralisation.

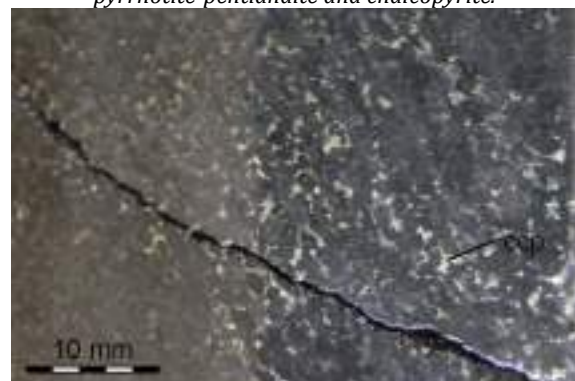


Figure 4.4f - typical chalcopyrite-dominated disseminated/interstitial mineralisation.

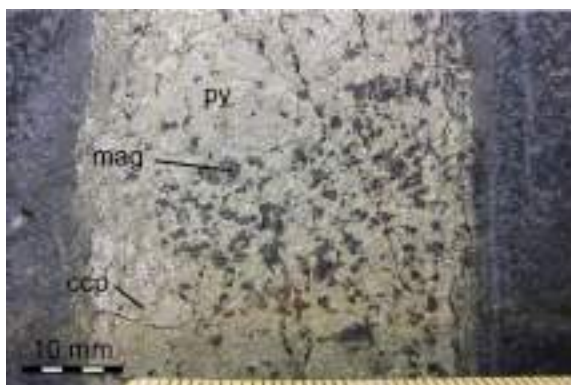


Figure 4.4g - chalcopyrite- and pyrite-rich vein-style of mineralisation.

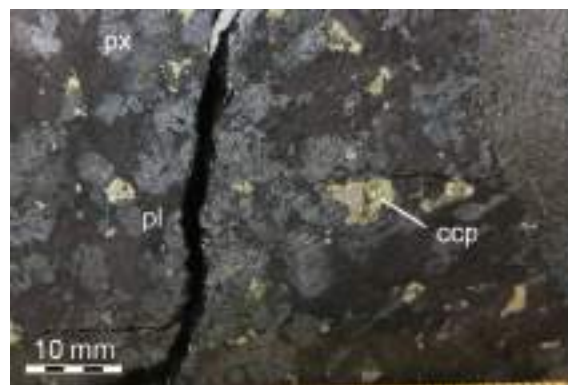


Figure 4.4h - semi-massive mineralisation hosted by pegmatoidal gabbro.

Figure 4.4 – Photographs of the key mineralisation styles at the Sakatti deposit.

In addition to the thin sections detailed in chapter 3, a series of polished blocks were taken for more detailed petrological study of the mineralisation itself. These blocks are listed in table 4.2. A summary of the petrographical information recorded for each sample in turn is included in the appendix. An overview of this petrographical information is presented below.

4.3.1.1 Massive

Thirteen of the twenty block samples were massive sulphide mineralisation. The petrology of the PGE minerals that are present within these samples is considered separately in chapter 5.

Chalcopyrite/pyrrhotite dominated samples

The mineralogy of the main massive sulphides at Sakatti is simple containing pyrrhotite, chalcopyrite and pentlandite in varying proportions (Fig. 4.4a-d and 4.5). Pyrite can also be present as a minor phase. Magnetite is euhedral and abundant with no exsolutions within it. Pentlandite is present as brittle fractured masses that are rarely altered to millerite or violarite. Pentlandite is also present throughout all samples as flame-like exsolutions within the pyrrhotite.

Silicate phases are rarely present in the samples but when they are it is as veins of serpentine, talc or chlorite. Cubanite is present in two samples associated with serpentine and voids in the sample suggesting it is the product of minor hydrothermal alteration.

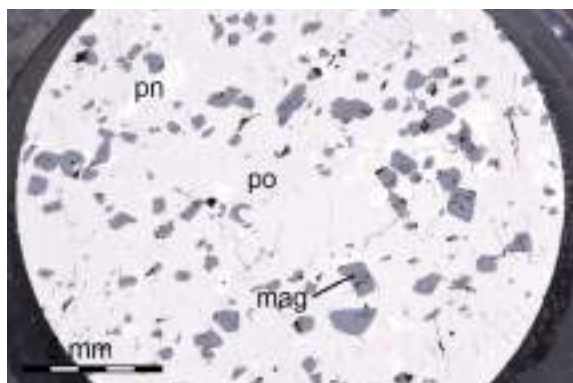


Figure 4.5a – M8044 696.19 - The mineralogy of massive sulphide samples is generally very simple, comprising of chalcopyrite and pyrrhotite in varying abundance with minor pentlandite and euhedral magnetite and in some cases pyrite.

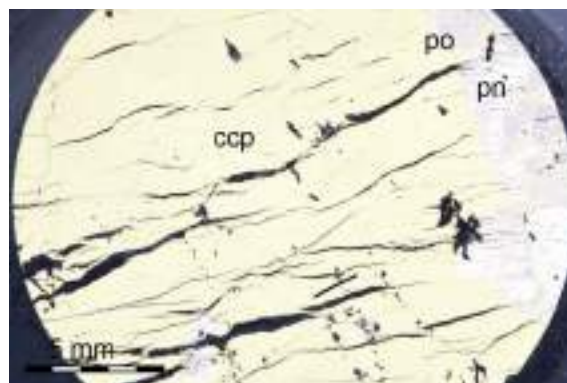


Figure 4.5b – M8049 820.00 - Silicate is usually absent from the samples, however where it is present it is serpentine or even talc veinlets presumably associated with alteration. When discrete non-sulphide, non-magnetite phases are present (as opposed to veinlets) they are chlorite, chlorapatite, phlogopite, barite or anhydrite. The apatite and phlogopite contain EDS detectable chlorine within them.

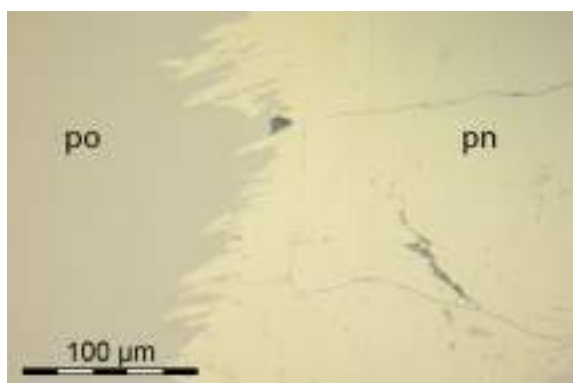


Figure 4.5c – M8049 767.78 - Pentlandite is present as discrete grains that are highly fractured due to the brittle nature of pentlandite. These grains can be partially altered to different Ni phases such as millerite and violarite, however this is more common where pyrite is present.

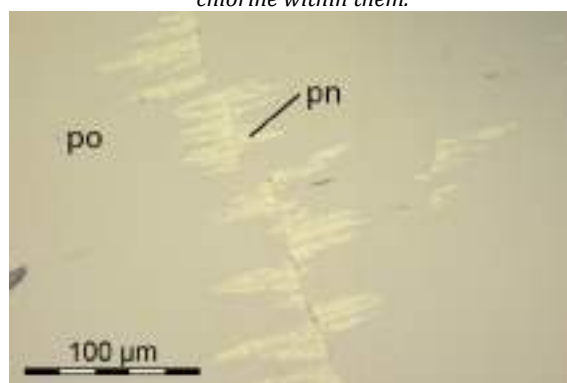


Figure 4.5d – M8049 767.78 - Pentlandite is also present as small 'flame-like' inclusions within pyrrhotite. These are generally 1-5 µm wide and up to 20 µm long but can be grouped together in masses. They are ubiquitous along pyrrhotite grain boundaries and are likely a result of exsolution from the pyrrhotite during cooling.

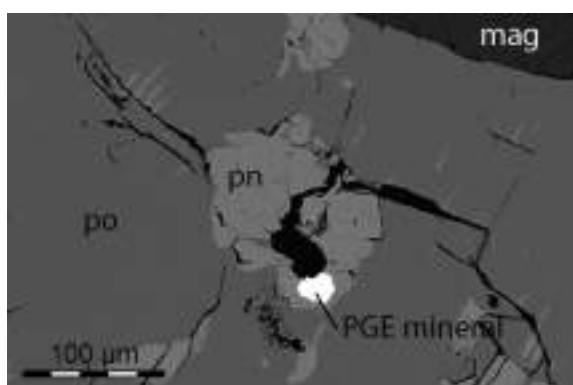


Figure 4.5e – M8044 696.19 – Small PGE phase associated with pentlandite and pyrrhotite. Pentlandite flames can be seen along the grain boundary in the pyrrhotite.

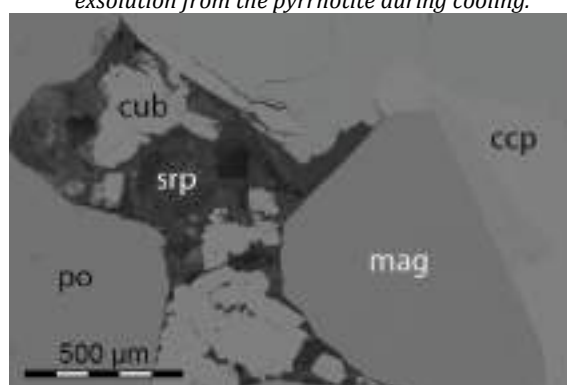


Figure 4.5f – M8049 767.78 - Cubanite is present as a very minor phase with serpentine and voids. An interpretation is that the cubanite is associated with minor hydrothermal activity within the massive sulphide.

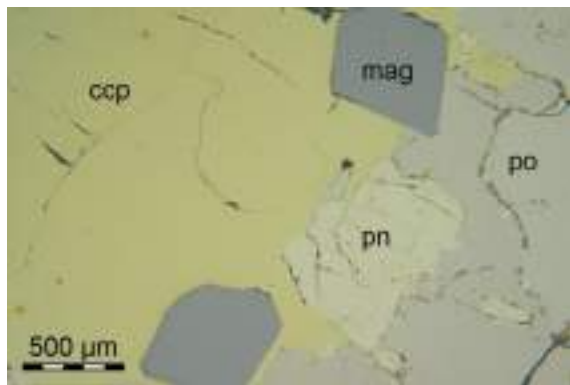


Figure 4.5g - M8049 773.57 - Magnetite is present as euhedral to subhedral cubes up to 2 mm in most samples, although in core observations magnetite up to 5 cm across was noted within the massive sulphide. The magnetite is featureless and does not contain either chromite cores or ilmenite exsolutions.

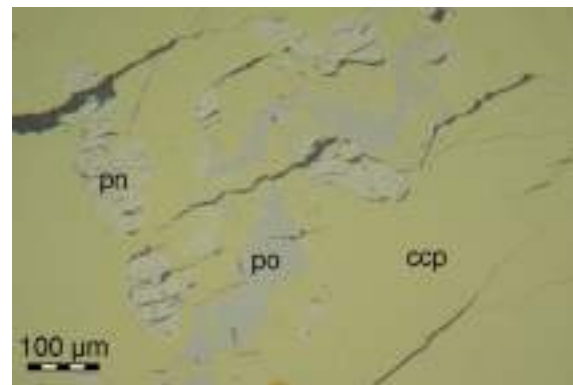


Figure 4.5h - M84049 820.00 - Pentlandite is present as discrete grains that are highly fractured due to the brittle nature of pentlandite. These grains can be partially altered to different Ni phases such as millerite and violarite, however this is more common where pyrite is present.

Figure 4.5 - Images of massive sulphide mineralisation

Pyrite dominated samples

Pyrite is present as a clear alteration product of sulphide in some parts of the Sakatti drill core, sample M8044 650.91 m is an example of this. However the more abundant mode of pyrite is as orbicular nodules that can be present as isolated 1-2 cm occurrences or can dominant multi-metre intersections (Fig. 4.4e,g and 4.6). Because of this the formation of this pyrite can be viewed as a continuum from less abundant (~50% at M8049 681.86 m) to more abundant (~99% at M8049 734.49 m). The pyrite orbicules are referred to as 'clean' because they rarely contain inclusions. Their round nature gives the rock the appearance of a breccia, although a sedimentary origin is not suggested. The surrounding 'matrix' of the orbicules is not effected by their presence where it is chalcopyrite (samples M8049 695.74 m and M8049 759.70 m) but where it is pyrrhotite it becomes concentrated with pentlandite and ultimately pyrrhotite is absent and a nickeliferous pyrite is present referred to as 'stripy' pyrite due to the presence of abundant magnetite exsolutions within it.

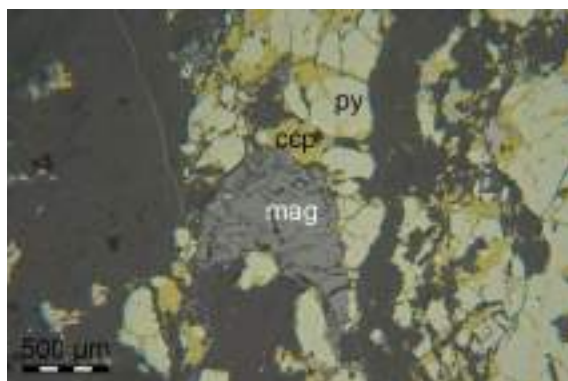


Figure 4.6a - M8049 759.70 - Pyrite mineralisation with magnetite and silicate. Chalcopyrite is unaffected by pyrite.

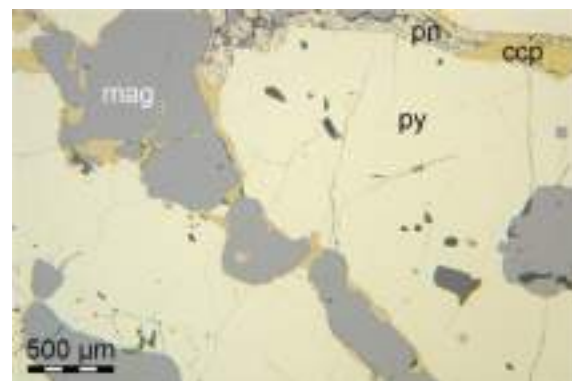


Figure 4.6b - M8049 695.74 - Pyrite 'orbicules' with a chalcopyrite and magnetite 'matrix'. The textures within magnetite and chalcopyrite are the same as in normal massive sulphide.

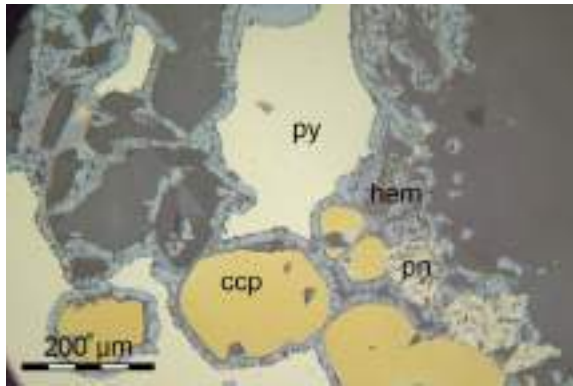


Figure 4.6c - M8044 650.91 – Pyrite present in this sample differs from the orbicular pyrite as it does not have the characteristic shape. It is also accompanied by alteration silicate and abundant hematite.

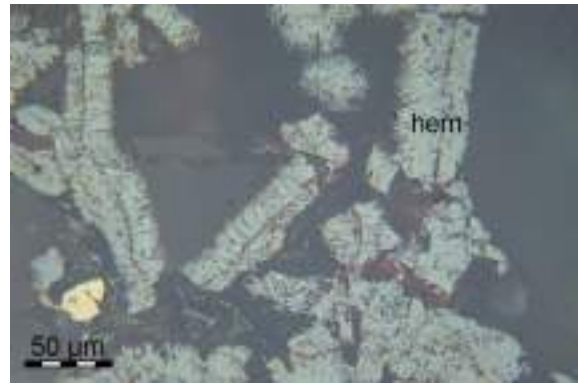


Figure 4.6d - M8044 650.91 – Hematite is present throughout alteration silicates in the alteration derived pyrite sample. This type of alteration pyrite is not typical of the majority of the deposit.

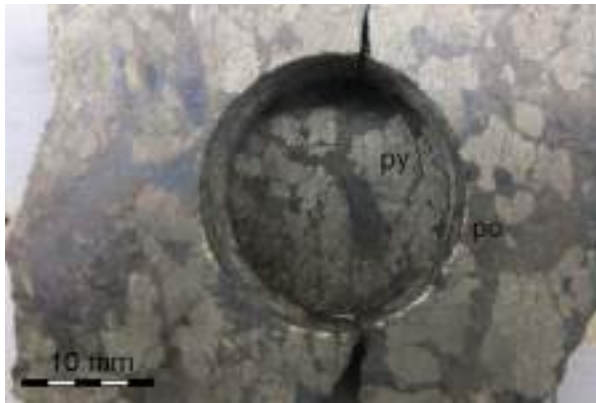


Figure 4.6e - M8049 681.86 – Drill core containing large pyrite 'orbicules' making up the majority of the sulphide but with interstitial pyrrhotite.

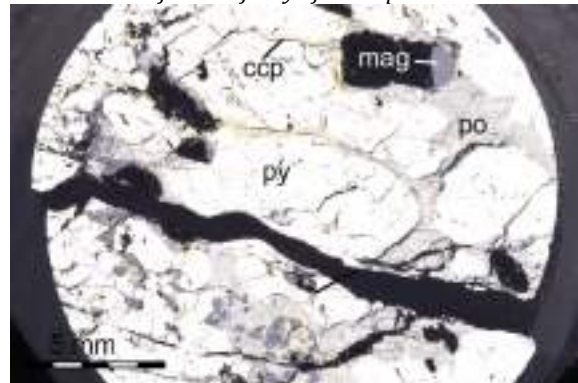


Figure 4.6f - M8049 681.86 – Polished block containing orbicular pyrite and pyrrhotite 'matrix'

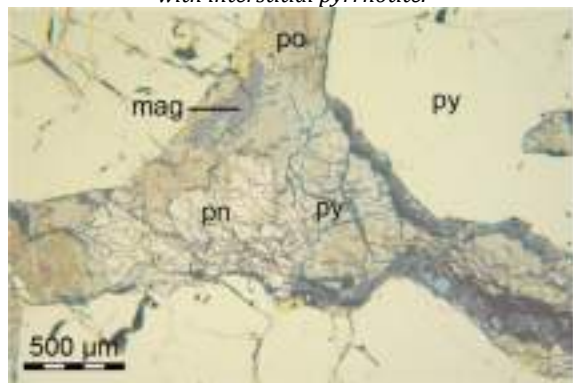


Figure 4.6g - M8049 681.86 – Triple junction of 'clean' orbicular pyrite with altered pentlandite and high-Ni pyrrhotite present as 'matrix' between.



Figure 4.6h - M8049 734.49 – 'Clean' orbicular pyrite with altered pentlandite at its edge and then 'stripy' pyrite

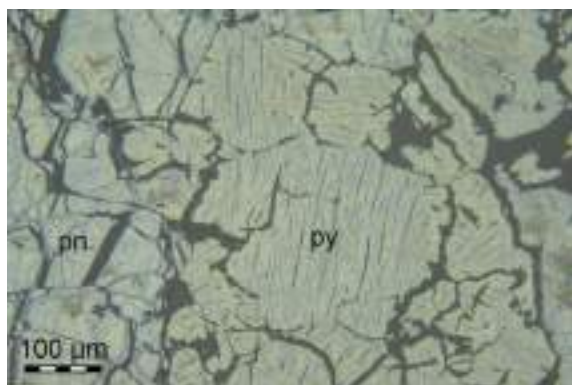


Figure 4.6i - M8049 734.49 – 'stripy' pyrite due so called due to the abundance of magnetite exsolution lines within the pyrite. Violarite networks can be seen in the pentlandite.

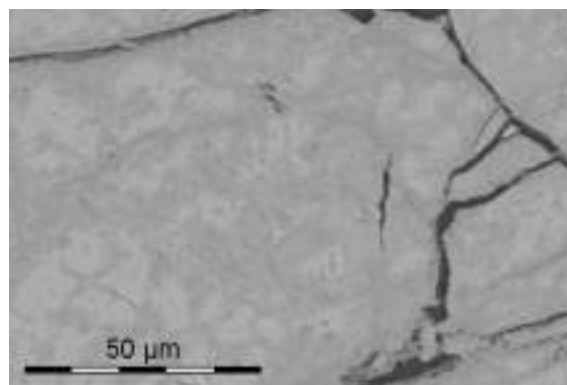


Figure 4.6j - M8049 734.49 – Alteration of pentlandite to violarite and millerite

Figure 4.6 – Images of pyrite mineralisation

4.3.1.2 Semi-massive

Three of the twenty block samples are semi-massive sulphide, meaning they contain roughly equal proportions of sulphide and silicate (Fig. 4.4h and 4.7). When the semi-massive style occurs at the Sakatti deposit it is frequently associated with the Pegmatoidal Gabbro Sub-Unit described in chapter 3. Two of the samples, M8044 684.49 m and M8044 779.20 m contain typical examples of the semi-massive style whereas sample M8044 650.91 is an example of a more heavily altered sample with only alteration silicates being present alongside calcite and minor anhydrite

The sulphide mineralogy of the semi-massive mineralisation is the same as the massive sulphide and frequently chalcopyrite rich. Magnetite present differs from that in the massive sulphide as it has abundant ilmenite exsolutions, suggesting higher Ti content at formation (Deer et al., 2011). It is also more abundant than in the massive sulphide.

The silicates present are the same as those in the Pegmatoidal Gabbro Sub-Unit, primarily black lath-shaped plagioclase and lighter pyroxene/amphibole. This are mostly altered containing abundant chlorite, scapolite and tremolite. Chlorine-bearing phases are present including phlogopite and chlor-apatite. In each sample zircon, monazite or baddeleyite have been observed, suggesting this is an evolved silicate melt.

The interpretation of this style of mineralisation is heavily interlinked with the interpretation of the coarse Pegmatoidal Gabbro Sub-Unit outlined in section 3.3.4.6.

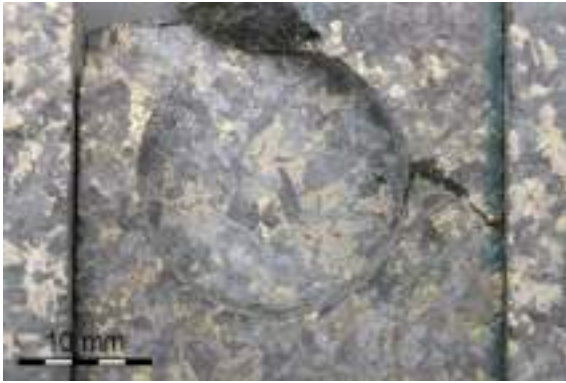


Figure 4.7a – M8044 650.91 – Semi-massive mineralisation with coarse pegmatoidal plagioclase and amphibole.

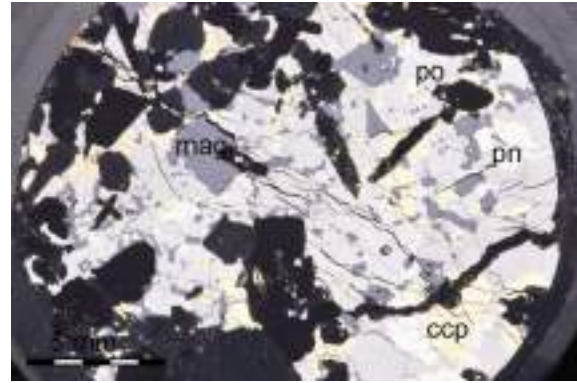


Figure 4.7b – M8044 650.91 - Semi-massive mineralisation with coarse pegmatoidal plagioclase and amphibole.



Figure 4.7c – M8044 684.49 - magnetite within these semi-massive samples exhibits exsolutions and coprecipitations of ilmenite, suggesting a higher Ti content that is likely to have been input directly from silicate melt. This titaniferous magnetite is an abundant phase constituting upwards of 5 % of the rock, and being generally less euhedral than in the massive sulphide samples.

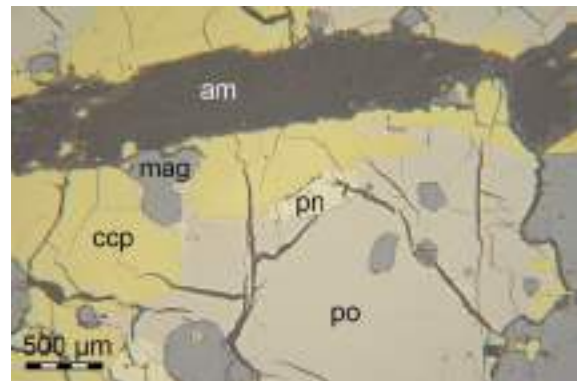


Figure 4.7d – M8044 684.49 - Amphibole is in the tremolite-actinolite series and present as an alteration product of the diopside and also potentially as discrete grains.

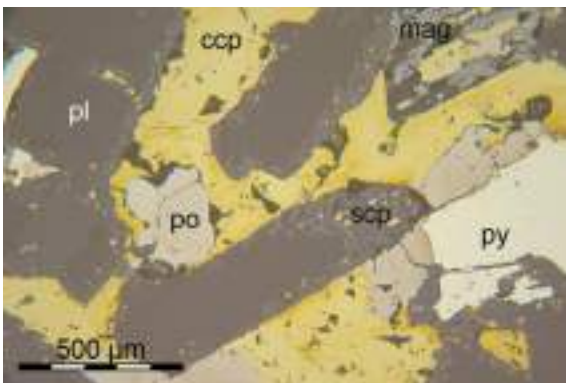


Figure 4.7e – M8044 779.20 - plagioclase laths, altered around the edges to chlorite or scapolite, in chalcopyrite pyrrhotite and pyrite.

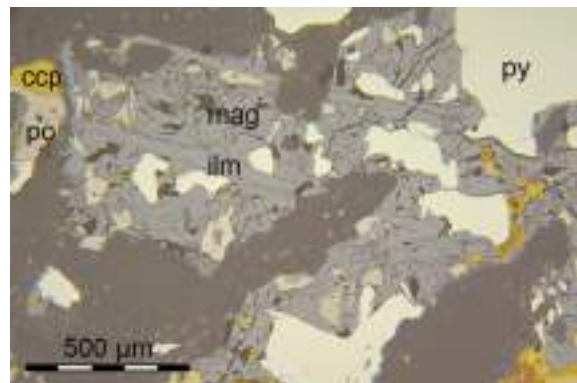


Figure 4.7f – M8044 779.20 - showing heavily fractured magnetite with 1 mm long needles of ilmenite, cut by laths of silicate. Magnetite has multiple pyrrhotite, chalcopyrite and pyrite throughout.

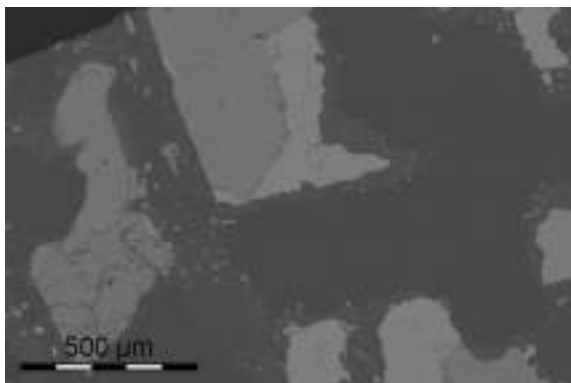


Figure 4.7g – M8044 779.20 - Backscattered electron image of plagioclase laths altering to chlorite around the rims. Interstitial chalcopyrite and pyrite.

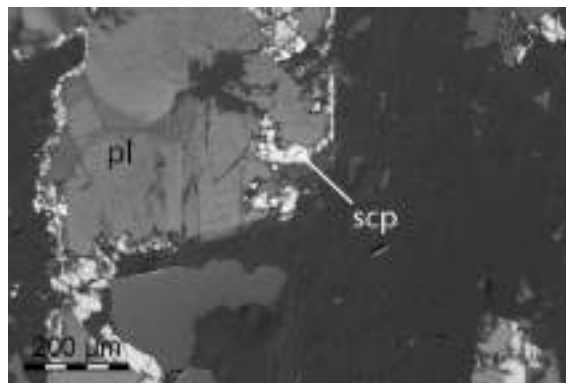


Figure 4.7h – M8044 779.20 - Cathodoluminescence image showing plagioclase with scapolite alteration around the edges. Next to amphibole and pyrite.

Figure 4.7 - Images of semi-massive mineralisation

4.3.1.3 Disseminated

Olivine Cumulate Unit

Two of the twenty block samples contain disseminated sulphide within Olivine Cumulate Unit. There are relatively few because in general thin sections were taken from disseminated samples in order to provide more useful information about the silicates (3.2).

These two blocks vary slightly in that sample M8 049 744.68 m is more altered, containing no primary silicates whereas sample M8 049 714.15 still contains olivine and amphibole. In both samples the mineralisation is dominated by chalcopyrite, which is consistent with primary observations in logging (Fig. 4.4f and 4.8).

Pyrite and pentlandite are present as minor phases. The pyrite is clean and polygonal while the pentlandite is heavily fractured and infilled with serpentine and a low Ni phase, probably bravoite.

Magnetite is present as exsolutions within the chalcopyrite but also as chrommagnetite rims around cumulus ferrichromite.

The disseminated mineralisation is not particularly well suited to microscopic examination because each sample has relatively little mineralisation present. No PGE phases were observed in any of the disseminated mineralisation blocks or thin sections.

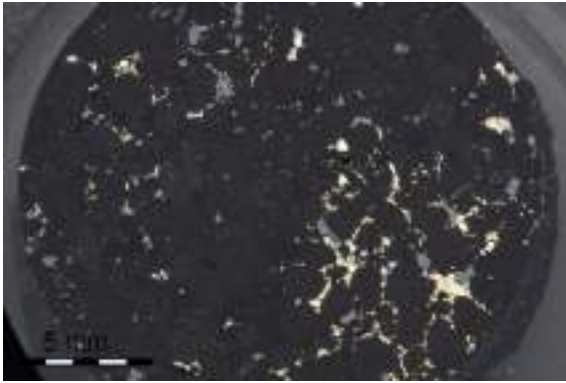


Figure 4.8a – M8049 714.15 – disseminated mineralisation interstitial to olivine cumulate.

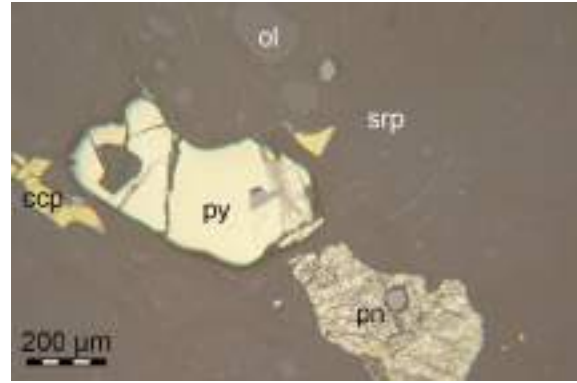


Figure 4.8b – M8049 714.15 – pyrite, pentlandite and chalcopyrite as disseminated phase with partially preserved olivine

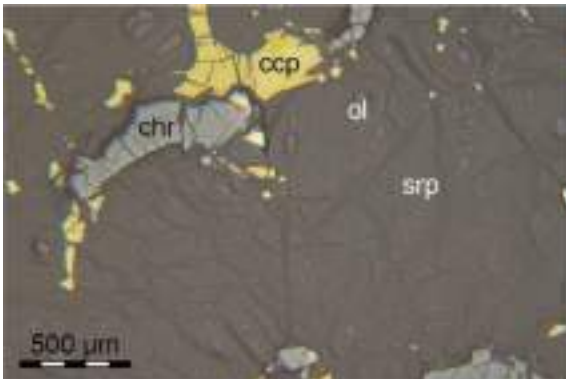


Figure 4.8c – M8049 714.15 – chalcopyrite with cumulus chromite and minor pyrite and partially preserved olivine.

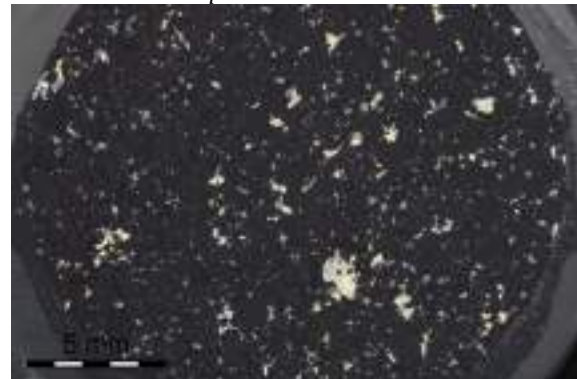


Figure 4.8d – M8049 744.68 – disseminated mineralisation with abundant chromite.

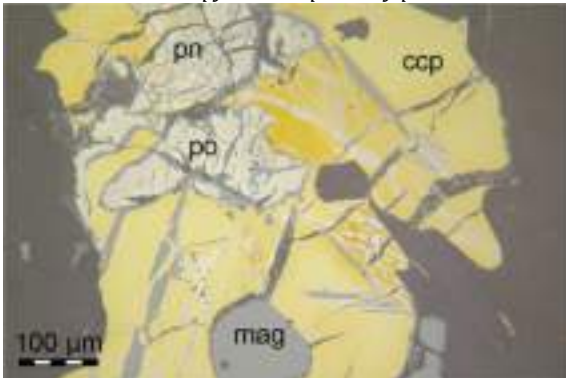


Figure 4.8e – M8049 744.68 – disseminated mineralisation with chalcopyrite, pyrrhotite and pentlandite. Chalcopyrite has characteristic magnetite lamellae and also pyrrhotite lamellae.

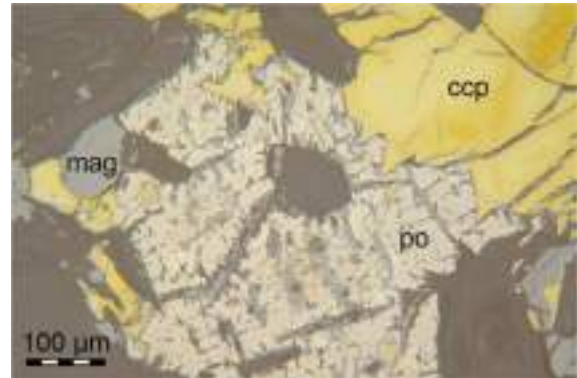


Figure 4.8f – M8049 744.68 – disseminated pyrrhotite and chalcopyrite with magnetite and minor pentlandite.



Figure 4.8g – M8049 744.68 – well mineralised Olivine Cumulate Unit.

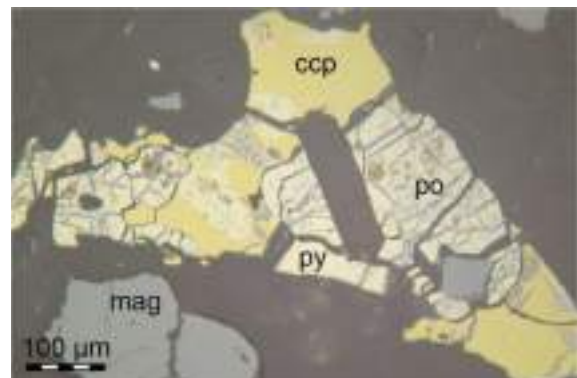


Figure 4.8h – M8049 744.68 – chalcopyrite disseminated mineralisation with pyrrhotite and pentlandite.

Figure 4.8 – Images of disseminated mineralisation

Aphanitic Unit

Two of the block samples are disseminated mineralisation within the Aphanitic Unit. Disseminated mineralisation within the Aphanitic Unit is sporadic and low grade as it only occurs within micro-intrusions of the Olivine Cumulate Unit (Fig. 4.9). It is the occurrence of this mineralisation, interstitial to cumulate olivine from the Olivine Cumulate Unit that led to the first logging observations revealing the nature of the Aphanitic Unit and the contact between the Aphanitic Unit and the Olivine Cumulate Unit (3.3.6). Sample M8 049 869.14 m is a good example of this style of disseminated mineralisation.

The central domain of the M8 049 869.14 m block is coarse olivine cumulate (0.2-3 mm) with interstitial sulphide, while the periphery of the block is mostly fine-grained pyroxene, plagioclase and minor olivine that is characteristic of the Aphanitic Unit. The sulphide itself is chalcopyrite dominated with minor pyrite, pyrrhotite and pentlandite. There are characteristic magnetite exsolutions in the chalcopyrite and also cumulus ferrichromite with chrommagnetite rims, the same as are found in the Olivine Cumulate Unit.

Sample M8 044 760.767 m is a more richly mineralised mixture of the Aphanitic Unit and Olivine Cumulate Unit. The coarse cumulus olivine of the Olivine Cumulate Unit is clearly visible in the mineralised domains of the sample, whereas the fine-grained domains do not host sulphide mineralisation. Mineralisation is chalcopyrite dominated but also with extensive pyrrhotite and minor pentlandite. There is also minor pyrite but this is heavily fractured and seems to be reverting to pyrrhotite.

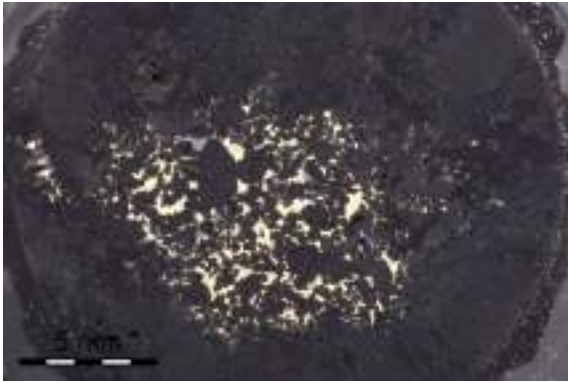


Figure 4.9a – M8049 869.14 – Patch of mineralised Olivine Cumulate Unit within the Aphanitic Unit.

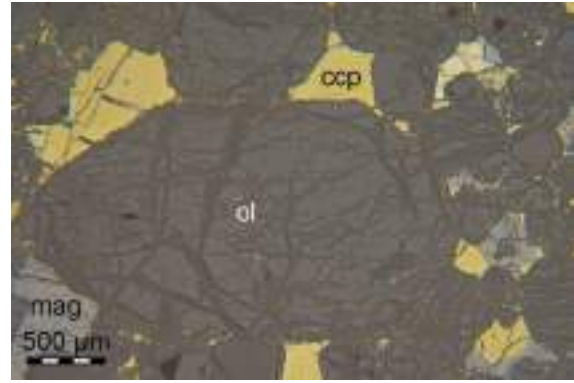


Figure 4.9b – M8049 869.14 – Cumulus olivine from the Olivine Cumulate Unit within mineralised micro-intrusions

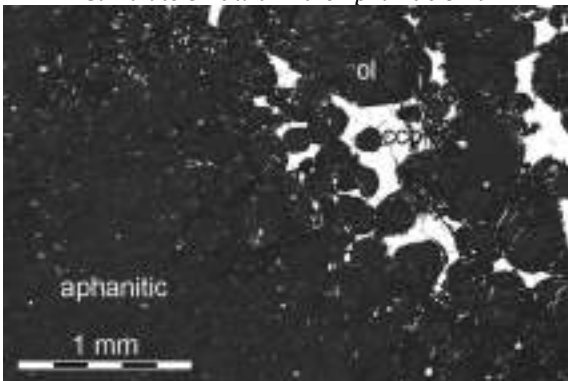


Figure 4.9c – M8049 869.14 – Mineralised cumulate olivines next to aphanitic groundmass.

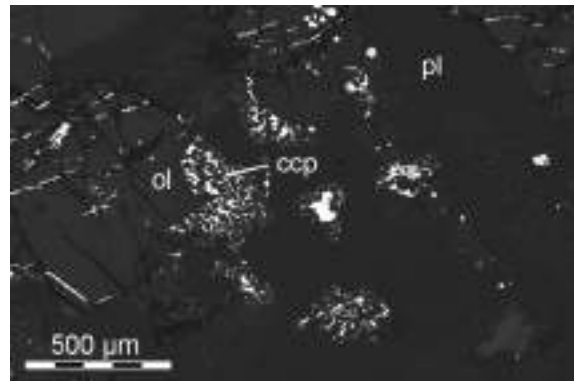


Figure 4.9d – M8049 869.14 –chalcopyrite inclusions within olivine

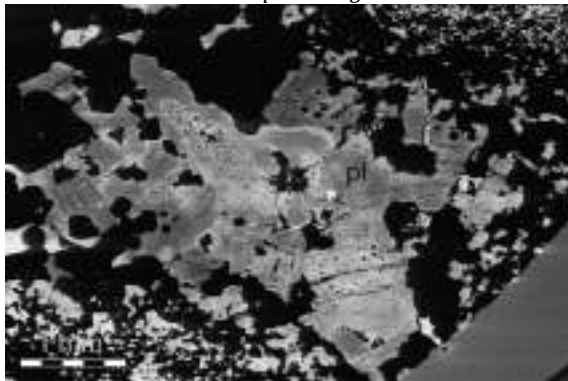


Figure 4.9e – M8049 869.14 – cathodoluminescent image showing different grain size of feldspar between the aphanitic and cumulate portions of the rock.



Figure 4.9f – M8044 760.77 – Cumulus olivines with interstitial mineralisation

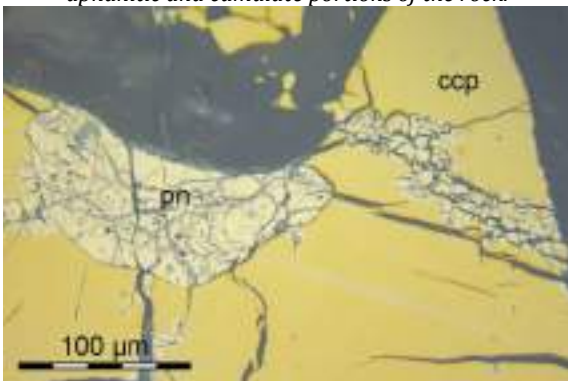


Figure 4.9g– M8044 760.77 – chalcopyrite mineralisation with pentlandite within Olivine Cumulate Unit micro-intrusion.

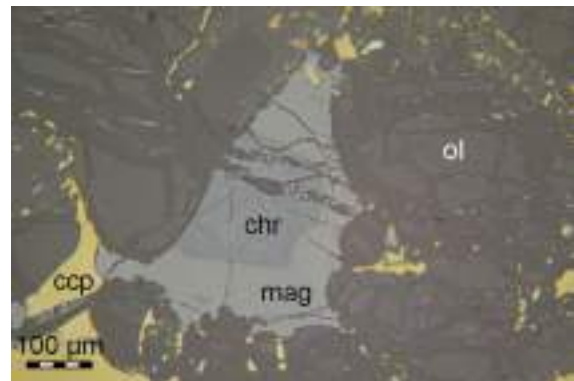


Figure 4.9h – M8044 760.77 – cumulus chromite within the Olivine Cumulate Unit micro-intrusion. Chromite is not present in the aphanitic unit.

Figure 4.9 – Images of disseminated mineralisation within Olivine Cumulate Unit micro-intrusions within the Aphanitic Unit

4.3.2 Mineral chemistry

4.3.2.1 Electron Probe Micro-Analysis (EPMA)

The sulphide mineral chemistry at the Sakatti deposit proved to be largely stoichiometric. Nonetheless extensive EPMA measurements were taken as part of the study of the PGE minerals and also as a necessary precursor for LA-ICP-MS.

Chalcopyrite

Chalcopyrite contains Cu, Fe and S at the Sakatti deposit and little else. There is detectable Co and Bi at very low levels in most samples (Table 4.2).

Hole	Depth	S	Fe	Co	Ni	Cu	Bi	Total
M8044	636.93	34.67	30.43	0.03	< 0.04	34.15	0.07	99.35
M8044	636.93	34.71	30.33	0.03	< 0.04	34.11	0.08	99.26
M8044	684.49	34.22	30.52	0.03	< 0.04	33.85	0.08	98.7
M8044	684.49	34.17	29.95	0.05	0.11	33.82	0.06	98.16
M8044	684.49	34.12	30.39	0.03	< 0.04	34.3	0.08	98.92
M8044	684.49	33.88	29.97	0.03	< 0.04	34.3	0.08	98.26
M8044	684.49	34.33	30.44	0.04	< 0.04	34.45	0.06	99.32
M8044	684.49	34.05	30.45	0.02	< 0.04	34.16	0.09	98.77
M8044	684.49	33.94	30.57	0.02	< 0.04	34.36	< 0.05	98.89
M8044	684.49	34.49	30.65	0.03	< 0.04	34.31	0.07	99.55
M8044	684.49	34.43	30.33	0.04	< 0.04	34.39	0.08	99.27
M8044	767.78	34.27	30.59	0.03	< 0.04	34.46	0.07	99.42
M8044	767.78	34.16	30.6	0.04	< 0.04	34.37	0.07	99.24
M8044	767.78	34.61	30.08	0.05	< 0.04	33.49	0.08	98.31
M8044	767.78	34.2	30.49	0.04	< 0.04	34.23	0.07	99.03
M8044	767.78	34.35	30.57	0.04	< 0.04	34.32	0.08	99.36
M8049	773.57	34.42	30.31	0.02	< 0.04	34.58	0.07	99.4
M8049	773.57	33.93	30.52	0.04	< 0.04	34.14	0.07	98.7
M8049	773.57	34.09	30.64	0.02	< 0.04	34.45	0.07	99.27
M8049	773.57	34.2	30.69	0.03	< 0.04	34.58	0.09	99.59
M8049	773.57	34.41	30.51	0.04	< 0.04	34.45	0.07	99.48
M8049	773.57	34.06	30.53	0.04	< 0.04	34.62	0.06	99.31
M8049	773.57	34.13	30.71	0.02	< 0.04	34.52	0.07	99.45
M8049	773.57	34.18	30.39	0.04	< 0.04	34.37	0.08	99.06
M8044	650.91	35.05	30.53	< 0.004	< 0.04	34.34	0.05	99.97
M8044	650.91	34.68	30.53	< 0.004	< 0.04	34.19	0.09	99.49
M8044	650.91	34.76	30.38	0.01	< 0.04	34.15	0.05	99.35
M8044	650.91	34.68	30.6	< 0.004	< 0.04	33.94	0.08	99.3
M8044	650.91	34.78	30.84	0.01	< 0.04	34.2	0.09	99.92
M8044	760.77	34.81	30.74	0.01	< 0.04	33.92	0.07	99.55
M8044	760.77	34.95	30.66	< 0.004	< 0.04	33.88	0.05	99.54
M8044	760.77	34.8	30.66	< 0.004	< 0.04	33.77	0.1	99.33
M8044	760.77	34.88	30.48	< 0.004	< 0.04	33.93	0.08	99.37
M8044	760.77	34.29	30.51	< 0.004	< 0.04	33.7	0.07	98.57
M8044	762.54	34.67	30.82	< 0.004	< 0.04	34.37	0.08	99.94
M8044	762.54	34.65	30.59	< 0.004	< 0.04	34.49	0.09	99.82
M8044	762.54	34.54	30.59	< 0.004	< 0.04	34.57	0.07	99.77
M8044	762.54	34.77	30.76	0.02	< 0.04	34.54	0.07	100.16
M8044	762.54	34.86	30.62	0.01	< 0.04	34.49	0.08	100.06
M8044	762.54	34.77	30.51	0.01	< 0.04	34.53	0.05	99.87
M8044	762.54	34.67	30.87	< 0.004	< 0.04	34.38	0.09	100.01
M8044	762.54	762.54	34.53	30.56	< 0.004	< 0.04	34.49	0.08
M8044	762.54	762.54	34.8	30.63	< 0.004	< 0.04	34.44	0.07
M8044	762.54	762.54	34.89	30.58	< 0.004	< 0.04	34.35	0.1
M8044	779.20	779.20	34.61	30.24	0.01	< 0.04	33.66	0.1
M8044	779.20	779.20	34.75	30.23	0.01	< 0.04	33.93	0.07
M8044	779.20	779.20	34.44	29.55	< 0.004	< 0.04	33.03	0.07
M8044	779.20	779.20	34.57	30.84	0.01	< 0.04	34.05	0.08
M8044	779.20	779.20	34.56	30.05	< 0.004	< 0.04	32.61	0.09
M8044	779.20	779.20	34.48	30.54	0.01	< 0.04	34.51	0.1
M8044	779.20	779.20	34.66	30.79	< 0.004	< 0.04	34.24	0.08
M8044	779.20	779.20	34.53	30.42	0.01	< 0.04	34.06	0.06
M8044	779.20	779.20	34.44	30.58	< 0.004	< 0.04	34.16	0.08
M8044	779.20	779.20	34.56	30.98	0.01	< 0.04	34.41	0.07
M8044	779.20	779.20	34.54	30.89	< 0.004	< 0.04	34.21	0.09
M8049	681.86	681.86	35.24	30.77	0.02	< 0.04	34.08	0.07
M8049	681.86	681.86	34.97	30.71	0.01	< 0.04	33.92	0.07
M8049	681.86	681.86	34.85	30.67	< 0.004	< 0.04	33.9	0.07
M8049	681.86	681.86	36.16	32.09	< 0.004	0.11	32.05	0.08
M8049	695.74	695.74	34.59	30.5	0.01	< 0.04	33.55	0.07
M8049	695.74	695.74	34.73	30.28	0.01	< 0.04	33.6	0.06
M8049	695.74	695.74	34.55	29.84	0.02	< 0.04	32.61	0.05
M8049	695.74	695.74	34.66	30.5	0.01	< 0.04	34.03	0.06
M8049	695.74	695.74	34.48	30.54	< 0.004	0.09	33.93	0.07
M8049	695.74	695.74	34.93	30.63	< 0.004	< 0.04	33.8	0.07
M8049	759.70	759.70	34.87	30.94	0.01	< 0.04	34.2	0.07
M8049	759.70	759.70	35.08	30.77	0.01	< 0.04	34.19	0.08
M8049	759.70	759.70	35.27	31.86	< 0.004	< 0.04	33.19	0.08
M8049	759.70	759.70	34.85	30.95	0.02	0.04	34.05	0.08
M8049	759.70	759.70	35.22	30.66	< 0.004	< 0.04	33.96	0.06
M8049	759.70	759.70	35.29	30.84	< 0.004	< 0.04	33.81	0.08
M8049	759.70	759.70	35	30.71	0.01	< 0.04	33.84	0.08
M8049	759.70	759.70	34.82	30.72	< 0.004	< 0.04	33.78	0.08
M8049	792.45	792.45	34.92	30.82	< 0.004	< 0.04	34.2	0.08
M8049	792.45	792.45	35.12	31.02	< 0.004	< 0.04	34.4	0.07
M8049	792.45	792.45	35.05	30.82	0.01	< 0.04	34.23	0.06
M8049	820.00	820.00	35.7	30.88	< 0.004	< 0.04	34.27	0.09
M8049	820.00	820.00	34.95	31.05	< 0.004	< 0.04	34.37	0.07
M8049	820.00	820.00	35.17	31.17	0.01	< 0.04	34.12	0.05
M8049	820.00	820.00	35.23	31.12	0.03	0.2	33.87	0.08
M8049	820.00	820.00	35.33	31.22	< 0.004	0.04	34.2	0.07

Table 4.2 – EPMA analyses of chalcopyrite at the Sakatti deposit

Pyrrhotite

Pyrrhotite at the Sakatti deposit contains detectable Ni throughout, on average 0.45 wt% but up to 1.5 wt%. There is also detectable Co and Bi (Table 4.3).

Hole	Depth	S	Fe	Co	Ni	Cu	Bi	Total
M8044	636.93	38.84	60.01	0.07	0.69	< 0.07	0.07	99.68
M8044	636.93	39.04	59.43	0.07	0.68	< 0.07	0.09	99.31
M8044	684.49	39.10	59.46	0.06	0.84	< 0.07	0.11	99.57
M8044	760.77	39.34	61.01	< 0.01	0.07	< 0.07	0.09	100.51
M8044	760.77	38.84	61.59	0.02	0.04	< 0.07	0.12	100.61
M8044	762.54	39.43	59.99	0.02	0.51	< 0.07	0.10	100.05

M8044	684.49	38.99	59.31	0.06	0.63	< 0.07	0.12	99.11
M8044	684.49	38.52	59.57	0.07	0.64	< 0.07	0.11	98.91
M8044	684.49	38.61	59.76	0.09	0.68	< 0.07	0.09	99.23
M8044	684.49	38.97	59.47	0.07	0.58	< 0.07	0.11	99.20
M8044	684.49	39.03	59.75	0.08	0.58	< 0.07	0.09	99.53
M8044	767.78	38.84	60.00	0.08	0.44	< 0.07	0.09	99.45
M8044	767.78	38.95	59.85	0.08	0.40	< 0.07	0.08	99.36
M8044	767.78	39.03	59.94	0.06	0.40	< 0.07	0.09	99.52
M8044	767.78	38.90	59.63	0.08	0.44	< 0.07	0.08	99.13
M8044	767.78	38.71	59.80	0.08	0.46	< 0.07	0.10	99.15
M8049	773.57	38.54	60.10	0.06	0.38	< 0.07	0.09	99.17
M8049	773.57	38.69	59.78	0.06	0.40	< 0.07	0.12	99.05
M8049	773.57	38.56	60.09	0.08	0.36	< 0.07	0.08	99.17
M8049	773.57	38.90	60.13	0.06	0.38	< 0.07	0.10	99.57
M8049	773.57	38.86	59.92	0.06	0.46	< 0.07	0.08	99.38
M8049	773.57	38.49	60.20	0.06	0.37	< 0.07	0.12	99.24
M8049	773.57	38.65	59.91	0.07	0.46	< 0.07	0.10	99.19
M8044	696.19	38.91	58.84	0.03	0.52	< 0.07	0.13	98.43
M8044	696.19	39.76	60.14	0.03	0.61	< 0.07	0.09	100.63
M8044	696.19	40.85	57.93	0.17	1.50	< 0.07	0.11	100.56
M8044	760.77	39.23	61.24	< 0.01	0.20	< 0.07	0.11	100.78
M8044	760.77	38.46	60.05	0.02	0.18	< 0.07	0.10	98.81
M8044	760.77	40.48	58.25	0.19	0.17	0.11	0.13	99.33
M8044	760.77	36.87	60.03	< 0.01	0.48	0.29	0.09	97.76
M8044	760.77	39.83	60.62	< 0.01	0.11	< 0.07	0.11	100.67
M8044	760.77	39.65	60.38	0.02	0.21	0.50	0.09	100.85

M8044	762.54	39.44	59.97	0.02	0.33	< 0.07	0.10	99.86
M8044	762.54	39.45	60.25	0.02	0.41	< 0.07	0.09	100.22
M8044	762.54	39.64	60.53	< 0.01	0.49	< 0.07	0.11	100.77
M8044	762.54	39.64	60.11	< 0.01	0.47	< 0.07	0.07	100.29
M8044	762.54	39.88	59.88	0.03	0.38	< 0.07	0.08	100.25
M8044	762.54	39.72	59.76	0.04	0.39	< 0.07	0.11	100.02
M8044	762.54	39.79	60.46	< 0.01	0.43	< 0.07	0.11	100.79
M8044	762.54	39.57	60.22	< 0.01	0.34	0.16	0.11	100.40
M8044	762.54	39.51	60.03	0.03	0.56	< 0.07	0.10	100.23
M8044	762.54	39.46	59.94	0.04	0.66	< 0.07	0.10	100.20
M8044	762.54	39.84	60.11	< 0.01	0.43	< 0.07	0.09	100.47
M8044	762.54	39.47	60.04	< 0.01	0.52	< 0.07	0.08	100.11
M8049	695.74	39.81	59.28	< 0.01	0.76	< 0.07	0.11	99.96
M8049	695.74	39.69	59.67	0.02	0.75	< 0.07	0.11	100.24
M8049	695.74	39.47	58.82	0.02	0.81	< 0.07	0.08	99.20
M8049	759.70	39.97	60.94	0.02	0.35	< 0.07	0.08	101.36
M8049	759.70	40.00	60.77	0.02	0.24	< 0.07	0.10	101.13
M8049	759.70	39.73	61.03	< 0.01	0.25	< 0.07	0.09	101.10
M8049	792.45	40.05	60.70	0.03	0.41	< 0.07	0.09	101.28
M8049	792.45	40.03	60.71	0.03	0.40	< 0.07	0.07	101.24
M8049	792.45	40.13	60.85	< 0.01	0.39	< 0.07	0.11	101.48
M8049	792.45	39.96	60.66	0.03	0.36	< 0.07	0.10	101.11
M8049	792.45	40.11	60.79	0.03	0.30	< 0.07	0.09	101.32
M8049	820.00	39.44	61.72	< 0.01	0.05	< 0.07	0.11	101.32
M8049	820.00	39.27	61.85	0.02	0.17	< 0.07	0.07	101.38
M8049	820.00	39.07	61.14	< 0.01	0.14	< 0.07	0.10	100.45

Table 4.3 - EPMA analyses of pyrrhotite at the Sakatti deposit

Pentlandite

Pentlandite at the Sakatti deposit contains detectable Co throughout, on average 1 wt% but up to 2.3 wt%. There is a loose inverse correlation between Co and Ni, which could be an effect of the Co displacing Ni in the pentlandite structure (Fig. 4.1). There is also detectable Bi (Table 4.4).

Hole	Depth	S	Fe	Co	Ni	Cu	Te	Bi	Total
M8044	684.49	33.44	30.43	0.93	34.49	< 0.02	< 0.04	0.09	99.38
M8044	684.49	33.16	30.14	1.14	34.96	0.03	< 0.04	0.08	99.51
M8044	684.49	32.69	29.28	1.14	35.87	0.04	< 0.04	0.09	99.11
M8044	684.49	32.82	29.54	1.26	36.22	< 0.02	< 0.04	< 0.05	99.84
M8044	684.49	32.55	29.39	1.30	36.18	< 0.02	< 0.04	0.10	99.52
M8044	684.49	32.86	28.88	1.08	36.01	0.05	< 0.04	0.06	98.94
M8044	684.49	33.39	27.90	1.03	35.19	< 0.02	< 0.04	0.08	97.59
M8044	767.78	33.76	28.44	1.22	36.05	< 0.02	< 0.04	0.10	99.57
M8044	767.78	32.94	29.86	1.18	35.84	< 0.02	0.05	0.09	99.96
M8044	767.78	32.73	29.32	1.27	35.96	< 0.02	< 0.04	0.09	99.37
M8044	767.78	33.06	29.97	1.51	35.68	< 0.02	< 0.04	0.08	100.30
M8044	767.78	33.67	30.71	1.51	33.90	< 0.02	< 0.04	0.07	99.86
M8044	650.91	33.00	28.48	0.44	37.97	< 0.02	< 0.04	0.08	99.97
M8044	650.91	34.16	26.89	0.45	37.67	< 0.02	< 0.04	0.06	99.23
M8044	650.91	35.52	26.36	0.66	35.09	< 0.02	< 0.04	0.08	97.71
M8044	650.91	32.97	28.41	0.43	37.82	< 0.02	0.05	0.09	99.77
M8044	650.91	32.74	27.10	0.50	37.32	< 0.02	< 0.04	0.08	97.74
M8044	650.91	33.08	26.60	0.47	36.97	< 0.02	< 0.04	0.07	97.19
M8044	650.91	32.99	27.65	0.43	36.56	0.03	< 0.04	0.06	97.72
M8044	696.19	32.63	28.71	0.35	37.40	0.03	0.06	0.08	99.26
M8044	696.19	33.18	29.51	0.47	37.09	< 0.02	0.05	0.08	100.38
M8044	696.19	33.51	29.82	0.53	36.49	< 0.02	< 0.04	0.09	100.44
M8044	696.19	33.63	29.77	0.47	36.96	< 0.02	< 0.04	0.10	100.93
M8044	760.77	33.18	30.49	2.71	33.99	< 0.02	< 0.04	0.06	100.43
M8044	760.77	33.18	30.27	2.68	33.82	< 0.02	< 0.04	0.09	100.04
M8044	762.54	34.59	27.64	1.18	36.21	0.23	< 0.04	0.09	99.94
M8044	762.54	33.29	29.11	1.10	36.90	< 0.02	0.05	0.08	100.53

Hole	Depth	S	Fe	Co	Ni	Cu	Te	Bi	Total
M8044	762.54	33.25	30.00	1.29	35.61	< 0.02	< 0.04	0.08	100.23
M8044	762.54	33.21	28.92	1.27	36.61	< 0.02	< 0.04	0.07	100.08
M8044	762.54	33.15	29.93	1.20	35.19	< 0.02	< 0.04	0.09	99.56
M8044	762.54	33.21	30.21	1.24	35.82	< 0.02	< 0.04	0.08	100.56
M8044	762.54	33.24	29.59	1.24	35.88	< 0.02	< 0.04	0.09	100.04
M8044	762.54	33.45	29.49	1.21	35.70	< 0.02	< 0.04	0.05	99.90
M8044	762.54	33.46	30.49	1.24	34.87	< 0.02	< 0.04	0.07	100.13
M8049	681.86	33.38	28.43	0.22	38.67	< 0.02	< 0.04	0.09	100.79
M8049	681.86	33.39	28.50	0.29	38.54	< 0.02	< 0.04	0.08	100.80
M8049	681.86	33.25	28.97	0.21	38.43	< 0.02	< 0.04	0.09	100.95
M8049	695.74	32.86	27.30	0.40	37.90	< 0.02	< 0.04	< 0.05	98.46
M8049	695.74	32.90	26.28	0.72	36.53	< 0.02	< 0.04	0.07	96.50
M8049	734.49	33.69	27.91	0.20	37.77	< 0.02	< 0.04	0.05	99.62
M8049	734.49	34.57	22.76	0.16	40.62	< 0.02	< 0.04	0.08	98.19
M8049	759.70	36.29	24.67	0.75	37.97	< 0.02	< 0.04	0.06	99.74
M8049	759.70	33.32	29.16	0.77	37.87	< 0.02	< 0.04	0.07	101.19
M8049	792.45	33.90	30.41	1.02	36.22	< 0.02	< 0.04	0.08	101.63
M8049	792.45	33.59	29.76	1.17	36.74	< 0.02	< 0.04	0.09	101.35
M8049	792.45	33.66	29.58	1.15	36.77	< 0.02	< 0.04	0.06	101.22
M8049	792.45	33.57	30.63	1.19	35.76	< 0.02	< 0.04	0.07	101.22
M8049	792.45	33.68	30.10	1.31	35.93	< 0.02	< 0.04	0.07	101.09
M8049	792.45	33.95	30.96	1.16	35.09	< 0.02	< 0.04	0.08	101.24
M8049	792.45	33.81	30.22	1.25	35.93	< 0.02	< 0.04	0.07	101.28
M8049	820.00	33.49	29.35	1.01	36.85	< 0.02	< 0.04	0.07	100.77
M8049	820.00	34.87	29.95	1.06	35.63	0.04	< 0.04	0.06	101.61
M8049	820.00	34.35	31.93	1.17	33.15	0.03	< 0.04	0.07	100.70

Table 4.4 - EPMA analyses of pentlandite at the Sakatti deposit

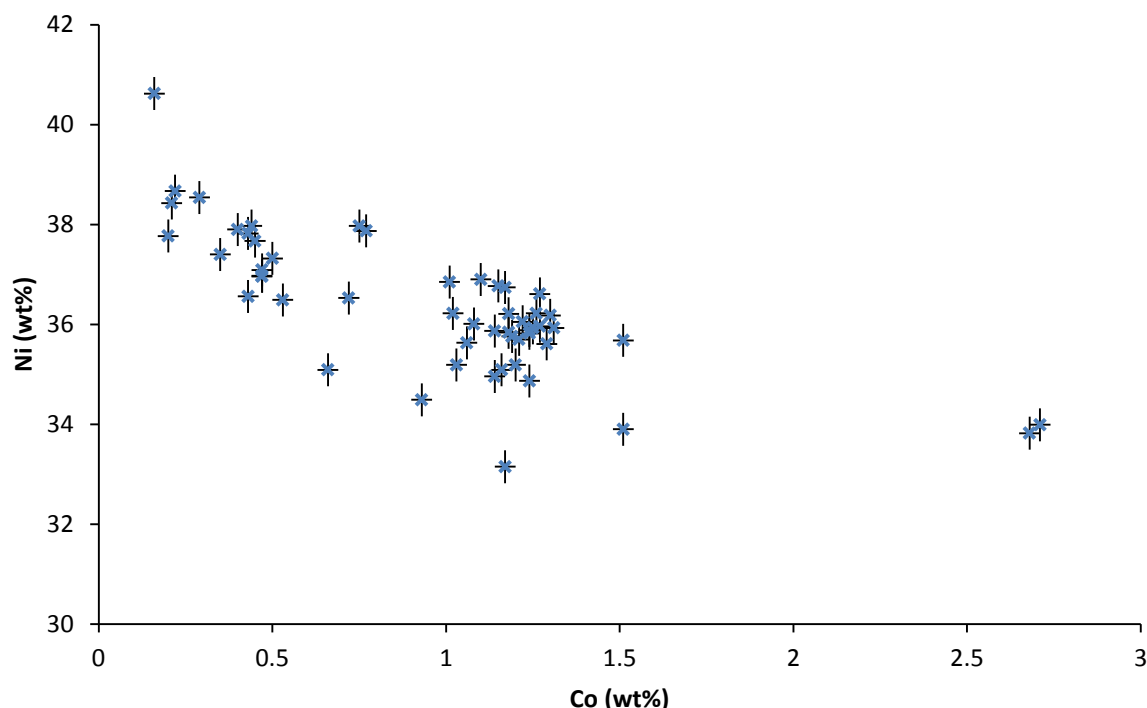


Figure 4.10 – Weight % Co and Ni in pentlandite at the Sakatti deposit showing a slight negative correlation which may be a result of Co replacing Ni. Detection limits are Ni: 0.052% and Co: 0.035%.

Pyrite

Pyrite mineral chemistry at Sakatti is bimodal (Table 4.5). The pyrite orbicules that are referred to as ‘clean’ pyrite contained up to 1 wt% Co and limited Ni (<0.035%) however the ‘stripy’ pyrite that occurred in the matrix contained up to 4 wt% Ni although averaging 1 wt% and limited Co (Fig. 4.11). The Ni content of the pyrite was highest in sample M8049 734.49 m where no pyrrhotite was present. In contrast in sample M8049 681.86 m the Ni content in the ‘stripy’ pyrite was only up to 0.5 wt%. ‘Stripy’ pyrite is particularly difficult to analyse because the backscatter coefficient of the pyrite and magnetite exsolutions is similar meaning they could not be distinguished on a backscattered electron image.

Hole	Depth	S	Fe	Co	Ni	Cu	Se	Bi	Total
M8044	636.93	52.35	46.54	0.06	<0.04	<0.05	<0.03	0.13	99.08
M8044	636.93	52.67	46.72	0.05	<0.04	<0.05	<0.03	0.12	99.56
M8044	767.78	51.17	46.32	0.07	1.18	<0.05	<0.03	0.12	98.86
M8044	767.78	52.59	46.21	0.06	0.9	<0.05	<0.03	0.12	99.88
M8044	767.78	52.66	46.59	0.05	0.59	<0.05	<0.03	0.09	99.98
M8049	773.57	51.61	46.53	0.57	0.09	<0.05	<0.03	0.11	98.91
M8049	773.57	52.63	46.37	0.62	0.07	<0.05	<0.03	0.12	99.81
M8049	773.57	52.86	46.62	0.52	0.05	<0.05	<0.03	0.14	100.19
M8049	773.57	52.56	46.29	0.77	0.09	<0.05	<0.03	0.12	99.83
M8049	773.57	52.53	46.8	0.54	0.05	<0.05	<0.03	0.14	100.06
M8049	773.57	52.76	46.61	0.67	0.07	<0.05	<0.03	0.12	100.23
M8049	773.57	53.04	46.67	0.48	0.08	<0.05	<0.03	0.12	100.39
M8044	650.91	53.61	47.84	<0.03	<0.04	<0.05	<0.03	0.12	101.57
M8044	650.91	54.16	47.32	0.51	0.04	<0.05	<0.03	0.14	102.17
M8044	650.91	53.62	47.15	0.57	0.07	<0.05	<0.03	0.15	101.56
M8044	650.91	53.79	47.5	<0.03	<0.04	<0.05	<0.03	0.13	101.42
M8044	650.91	53.24	47.39	<0.03	<0.04	<0.05	<0.03	0.13	100.76
M8044	650.91	54.33	46.8	0.36	<0.04	<0.05	<0.03	0.15	101.64
M8044	650.91	54.11	47.56	<0.03	<0.04	<0.05	<0.03	0.12	101.79

Hole	Depth	S	Fe	Co	Ni	Cu	Se	Bi	Total
M8044	779.2	53.42	45.56	1.8	0.26	<0.05	0.43	0.15	101.62
M8044	779.2	53.15	45.28	2.12	0.24	<0.05	0.26	0.16	101.21
M8049	681.86	54.27	47.29	0.55	0.04	<0.05	<0.03	0.14	102.29
M8049	681.86	54.2	47.49	0.53	0.04	<0.05	<0.03	0.11	102.37
M8049	681.86	54.14	47.68	0.41	0.06	<0.05	<0.03	0.1	102.39
M8049	681.86	53.52	47.62	<0.03	0.36	<0.05	<0.03	0.1	101.6
M8049	681.86	54.1	47.5	0.48	<0.04	<0.05	<0.03	0.11	102.19
M8049	681.86	54.18	47.26	0.67	0.04	<0.05	<0.03	0.13	102.28
M8049	681.86	54.15	47.32	0.59	0.04	<0.05	<0.03	0.13	102.23
M8049	681.86	54.06	47.24	0.58	0.04	<0.05	<0.03	0.15	102.07
M8049	681.86	54.26	47.14	0.67	0.04	<0.05	<0.03	0.12	102.23
M8049	681.86	53.27	46.84	<0.03	0.91	1.09	<0.03	0.11	102.22
M8049	695.74	53.38	45.84	0.99	0.1	<0.05	<0.03	0.12	100.43
M8049	695.74	53.19	45.1	0.65	0.1	<0.05	<0.03	0.1	99.14
M8049	695.74	53.56	46.28	1.04	0.1	<0.05	<0.03	0.11	101.09
M8049	695.74	53.02	45.35	0.99	0.1	<0.05	<0.03	0.11	99.57
M8049	734.49	54.19	46.59	0.81	0.04	<0.05	<0.03	0.16	101.79
M8049	734.49	54.14	46.65	0.78	0.05	<0.05	<0.03	0.14	101.76
M8049	734.49	54.05	46.62	0.6	<0.04	<0.05	<0.03	0.13	101.4

M8044	650.91	53.83	48	<0.03	<0.04	<0.05	<0.03	0.14	101.97	M8049	734.49	51.33	41.95	0.04	4.1	3.23	<0.03	0.13	100.78
M8044	650.91	53.65	47.64	<0.03	<0.04	<0.05	<0.03	0.14	101.43	M8049	734.49	52.16	46.13	0.96	0.09	<0.05	<0.03	0.11	99.45
M8044	650.91	53.06	47.67	<0.03	<0.04	<0.05	<0.03	0.12	100.89	M8049	734.49	52.38	46.8	0.55	<0.04	<0.05	<0.03	0.11	99.84
M8044	650.91	53.43	47.82	<0.03	<0.04	<0.05	<0.03	0.13	101.38	M8049	759.7	54.16	45.89	1.95	<0.04	<0.05	<0.03	0.1	102.1
M8044	779.2	52.76	45.2	2.01	0.16	0.05	<0.03	0.13	100.31	M8049	759.7	54.38	46.63	1.24	<0.04	<0.05	<0.03	0.13	102.38
M8044	779.2	53.36	44.64	2.83	0.24	<0.05	<0.03	0.15	101.22	M8049	759.7	54.15	45.95	1.99	<0.04	<0.05	<0.03	0.12	102.21
M8044	779.2	52.69	46.27	1.43	0.18	0.05	0.15	0.13	100.9	M8049	759.7	54.29	46.43	1.33	<0.04	<0.05	<0.03	0.13	102.18

Table 4.5 - EPMA analyses of pyrite at the Sakatti deposit

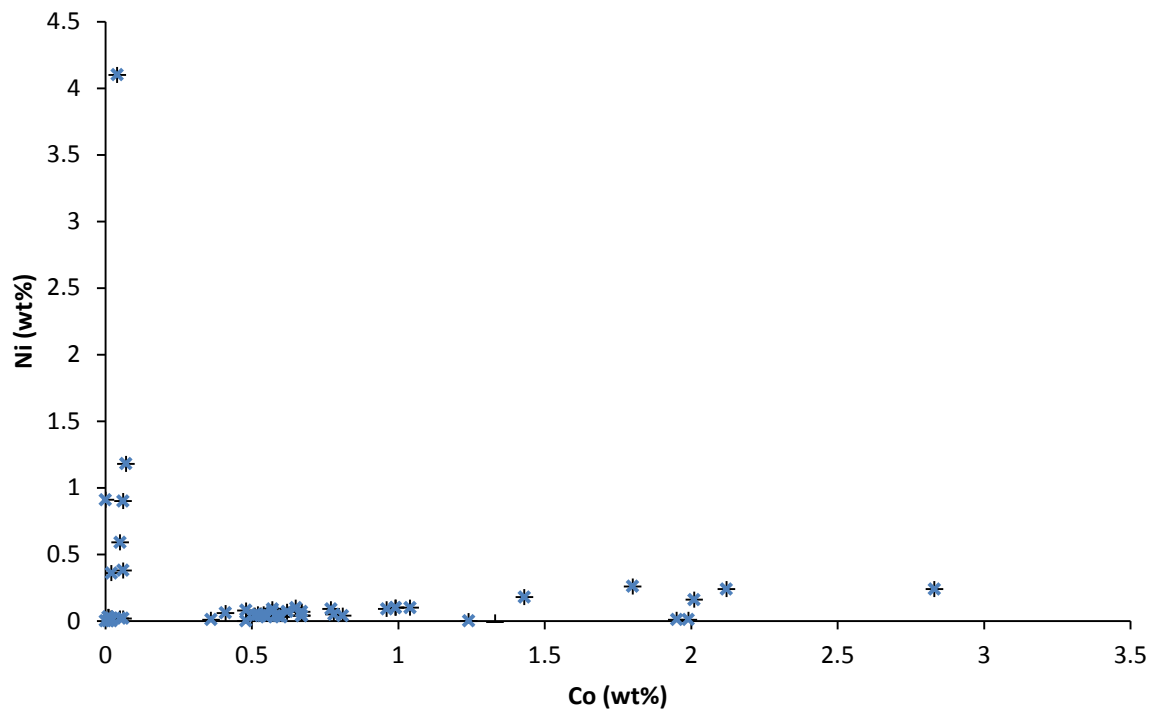


Figure 4.11 – EPMA data showing Ni vs. Co wt% in pyrite. The difference illustrates the separation of nickeliferous ‘stripy’ pyrite from cobaltiferous ‘clean’ pyrite. Detection limits are Ni: 0.035% and Co: 0.035%.

Magnetite

Magnetite is the only major non-sulphide phase that is present within the massive sulphide. Lithophile elements were present at or very close to the detection limits for EPMA (Table 4.6). It can be seen even in the EPMA data that the lithophile content increases in sulphide derived magnetite towards the base of the large massive sulphide lens that is present in hole M8 049 (Fig. 4.12).

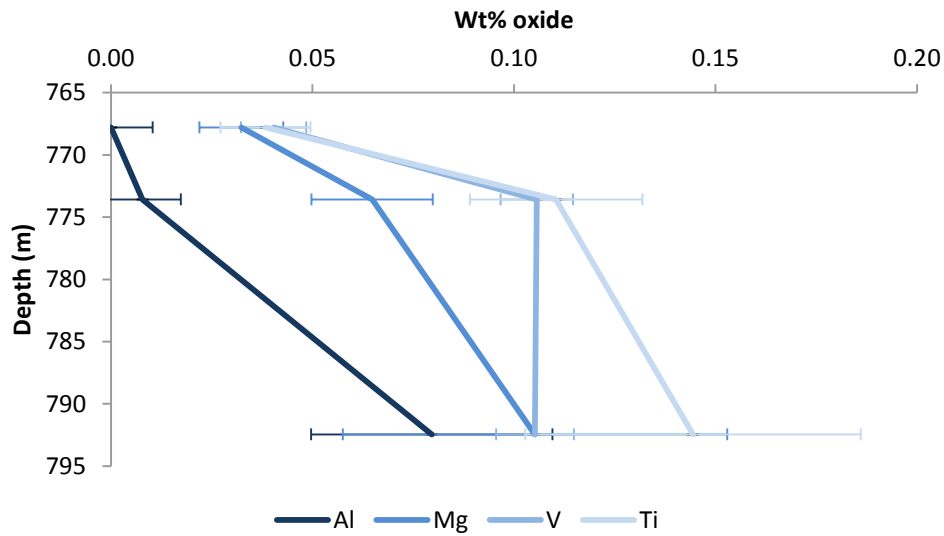


Figure 4.12 – EPMA data showing an increase in lithophile elements in magnetite with depth in one single massive sulphide lens in hole M8049.

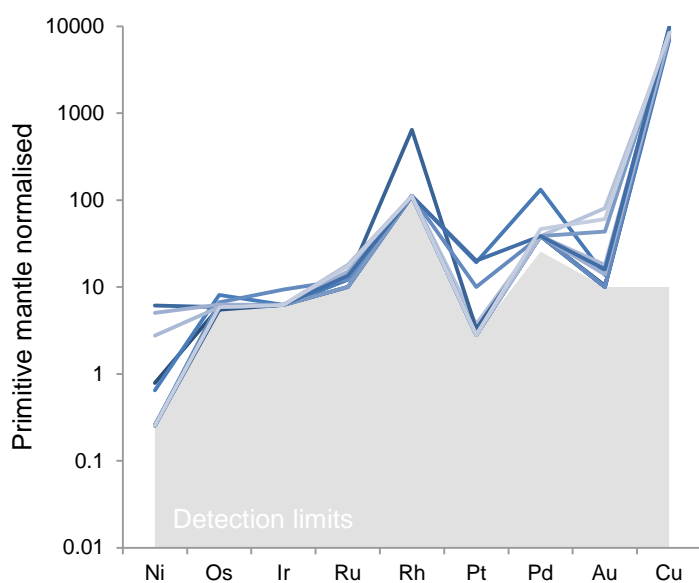
	MgO	Al ₂ O ₃	SiO ₂	CaO	TiO ₂	Cr ₂ O ₃	MnO	FeO	CoO	NiO	V ₂ O ₅	Fe ₂ O ₃	Total	
M8044	696.19	0.04	< 0.01	0.03	< 0.02	0.04	0.03	0.11	31.19	0.01	0.05	0.04	69.65	101.19
M8044	696.19	0.05	< 0.01	0.04	< 0.02	0.04	< 0.02	0.11	31.23	< 0.01	0.06	0.05	69.76	101.35
M8044	696.19	0.05	< 0.01	0.15	< 0.02	0.04	0.02	0.11	31.27	0.02	0.07	0.04	69.74	101.51
M8044	696.19	0.03	< 0.01	0.03	< 0.02	0.04	0.04	0.11	31.13	0.02	0.05	0.05	69.52	101.03
M8044	696.19	0.06	< 0.01	0.04	< 0.02	0.05	0.04	0.11	31.06	< 0.01	0.07	0.05	69.42	100.89
M8044	696.19	0.03	< 0.01	0.04	< 0.02	0.05	0.02	0.10	31.19	0.03	0.06	0.05	69.64	101.21
M8044	696.19	0.04	< 0.01	0.03	< 0.02	0.04	0.03	0.11	31.07	0.01	0.07	0.05	69.45	100.91
M8044	696.19	0.04	< 0.01	0.05	< 0.02	0.05	0.02	0.11	31.06	0.02	0.07	0.04	69.39	100.85
M8044	696.19	0.04	< 0.01	0.02	< 0.02	0.05	0.02	0.12	31.12	0.01	0.07	0.05	69.58	101.08
M8044	696.19	0.03	< 0.01	0.03	< 0.02	0.04	0.03	0.11	31.25	0.01	0.07	0.04	69.82	101.44
M8044	696.19	0.04	< 0.01	0.03	< 0.02	0.04	0.02	0.11	30.80	0.01	0.04	0.05	68.81	99.95
M8044	696.19	0.02	< 0.01	0.02	< 0.02	0.06	0.03	0.12	30.88	< 0.01	0.05	0.04	68.89	100.10
M8044	696.19	0.02	< 0.01	0.04	< 0.02	0.05	0.03	0.10	31.04	0.01	0.06	0.04	69.22	100.60
M8044	696.19	0.03	< 0.01	0.03	< 0.02	0.04	0.03	0.10	30.89	0.02	0.07	0.05	68.98	100.24
M8044	696.19	0.03	< 0.01	0.02	< 0.02	0.05	0.03	0.11	30.72	0.02	0.05	0.04	68.60	99.67
M8044	696.19	0.04	< 0.01	0.02	< 0.02	0.04	0.02	0.11	30.97	0.01	0.07	0.05	69.25	100.58
M8044	696.19	0.03	< 0.01	0.04	< 0.02	0.05	0.03	0.11	31.11	< 0.01	0.07	0.04	69.44	100.92
M8044	696.19	0.04	< 0.01	0.04	< 0.02	0.03	0.04	0.10	31.13	0.02	0.05	0.04	69.58	101.07
M8044	696.19	0.02	< 0.01	0.03	< 0.02	0.02	0.03	0.10	31.15	0.01	0.06	0.03	69.55	101.00
M8044	696.19	0.03	< 0.01	0.06	< 0.02	0.02	0.02	0.09	31.06	< 0.01	0.07	0.03	69.30	100.68
M8044	696.19	0.03	< 0.01	0.04	< 0.02	0.03	0.04	0.11	31.14	< 0.01	0.06	0.04	69.48	100.97
M8044	696.19	0.02	< 0.01	0.04	< 0.02	0.03	0.03	0.11	31.11	< 0.02	0.06	0.03	69.47	100.92
M8044	696.19	0.03	< 0.01	0.05	< 0.02	0.02	0.03	0.11	31.22	< 0.01	0.07	0.03	69.74	101.30
M8044	696.19	0.03	< 0.01	0.04	< 0.02	0.02	0.03	0.11	31.10	0.02	0.04	0.02	69.44	100.85
M8044	696.19	0.03	< 0.01	0.04	< 0.02	0.02	0.02	0.11	31.12	0.01	0.04	0.03	69.46	100.88
M8044	696.19	0.02	< 0.01	0.03	< 0.02	0.04	0.04	0.11	31.27	0.01	0.04	0.04	69.74	101.35
M8044	696.19	0.03	< 0.01	0.04	< 0.02	0.03	0.03	0.11	31.12	0.02	0.07	0.03	69.59	101.07
M8044	696.19	0.03	< 0.01	0.04	< 0.02	0.04	0.04	0.11	31.05	0.02	0.04	0.04	69.30	100.71
M8044	696.19	< 0.02	< 0.01	0.04	< 0.02	0.04	0.03	0.10	31.23	< 0.01	0.07	0.04	69.61	101.16
M8044	696.19	0.03	< 0.01	0.02	< 0.02	0.03	0.04	0.10	31.10	0.01	0.04	0.04	69.38	100.78
M8044	779.2	0.05	0.16	0.03	< 0.02	0.08	0.04	0.03	31.24	< 0.01	0.08	0.10	69.29	101.10
M8044	779.2	0.03	0.14	< 0.01	< 0.02	0.11	0.04	< 0.02	31.16	0.01	0.07	0.13	69.06	100.75
M8044	779.2	0.04	0.14	< 0.01	< 0.02	0.12	0.05	0.03	31.11	< 0.01	0.07	0.20	68.85	100.61
M8044	779.2	0.06	0.15	0.04	< 0.02	0.07	0.05	0.03	31.19	0.01	0.08	0.19	69.17	101.04
M8044	779.2	0.03	0.15	0.03	< 0.02	0.09	0.06	0.03	31.14	0.02	0.05	0.22	68.85	100.67
M8044	779.2	0.06	0.14	0.03	< 0.02	0.07	0.04	0.03	31.18	0.02	0.09	0.17	69.26	101.09
M8044	779.2	0.05	0.13	0.03	< 0.02	0.07	0.03	0.03	31.20	0.02	0.06	0.19	69.21	101.02
M8044	779.2	0.06	0.16	0.03	< 0.02	0.20	0.03	< 0.02	31.34	< 0.01	0.06	0.08	69.39	101.35
M8044	779.2	0.06	0.12	0.02	< 0.02	0.15	0.02	0.03	31.23	0.01	0.08	0.06	69.40	101.18
M8044	779.2	0.11	0.13	0.02	< 0.02	0.05	0.04	0.06	31.16	0.01	0.07	0.08	69.55	101.28
M8044	779.2	0.09	0.13	0.04	< 0.02	0.05	0.02	0.07	31.15	0.01	0.05	0.05	69.43	101.09
M8044	779.2	0.11	0.13	0.05	< 0.02	0.05	0.03	0.06	31.09	< 0.01	0.06	0.10	69.31	100.99
M8044	779.2	0.08	0.13	0.03	< 0.02	0.08	0.04	0.07	31.02	0.03	0.08	0.07	69.17	100.80
M8044	779.2	0.10	0.15	0.03	< 0.02	0.06	0.04	0.03	31.09	< 0.01	0.06	0.11	69.15	100.82
M8044	779.2	0.08	0.16	0.03	< 0.02	0.09	0.04	0.03	31.13	0.01	0.08	0.10	69.20	100.95
M8044	779.2	0.13	0.16	0.10	< 0.02	0.12	0.06	0.03	31.06	0.01	0.06	0.17	68.92	100.83
M8044	779.2	0.09	0.16	0.04	< 0.02	0.08	0.04	0.04	31.08	0.03	< 0.03	0.16	68.99	100.71
M8049	636.91	0.37	1.68	1.22	< 0.02	0.07	0.04	0.05	31.74	< 0.01	0.06	0.05	67.29	102.57
M8049	636.91	0.16	0.42	0.02	< 0.02	0.06	0.03	0.07	31.19	0.01	0.05	0.04	69.39	101.44
M8049	636.91	0.19	0.34	0.04	< 0.02	0.08	0.04	0.06	31.13	0.02	0.07	0.04	69.45	101.46
M8049	636.91	0.05	0.15	0.04	< 0.02	0.10	0.03	0.08	31.26	0.01	0.07	0.04	69.50	101.33
M8049	636.91	0.06	0.16	0.04	< 0.02	0.08	0.02	0.05	31.23	0.01	0.08	0.04	69.47	101.24
M8049	636.91	0.06	0.20	0.05	< 0.02	0.08	0.03	0.06	31.21	0.02	0.09	0.02	69.41	101.22
M8049	636.91	0.07	0.22	0.06	< 0.02	0.08	0.04	0.07	31.16	0.02	0.07	0.04	69.23	101.06
M8049	636.91	0.07	0.20	0.04	< 0.02	0.11	0.03	0.09	31.14	< 0.01	0.07	0.03	69.27	101.05
M8049	636.91	0.05	0.13	0.03	< 0.02	0.09	0.05	0.07	31.05	< 0.02	0.07	0.04	69.09	100.69
M8049	636.91	0.02	0.24	0.04	< 0.02	0.04	0.03	0.06	31.29	< 0.01	0.06	0.05	69.31	101.13
M8049	636.91	0.02	0.28	0.02	< 0.02	0.06	0.03	0.05	31.27	0.01	0.05	0.05	69.20	101.03
M8049	636.91	0.10	0.62	0.04	< 0.02	0.14	0.03	0.08	31.16	0.02	0.06	0.04	68.69	100.98
M8049	636.91	0.04	0.36	0.05	< 0.02	0.09	0.05	0.06	31.20	< 0.01	0.08	0.04	68.92	100.88
M8049	636.91	0.05	0.41	0.02	< 0.02	0.11	0.02	0.07	31.20	0.01	0.08	0.05	69.01	101.02
M8049	636.91	0.11	0.28	0.04	< 0.02	0.19	0.04	0.10	31.11	0.02	0.08	0.04	69.15	101.16
M8049	636.91	0.11	0.17	0.04	< 0.02	0.07	0.03	0.05	31.20	0.02	0.08	0.05	69.61	101.42
M8049	636.91	0.12	0.19	0.05	< 0.02	0.11	0.03	0.06	31.19	0.03	0.07	0.04	69.55	101.44
M8049	636.91	0.09	0.20	< 0.01	< 0.02	0.09	0.03	0.06	30.96	0.02	0.06	0.05	68.92	100.49

M8049	636.91	0.09	0.20	0.05	< 0.02	0.09	0.03	0.05	31.16	0.02	0.07	0.04	69.34	101.14
M8049	681.86	0.07	0.28	0.06	< 0.02	0.09	0.05	< 0.02	31.30	0.03	0.08	0.21	69.16	101.33
M8049	681.86	0.05	0.28	0.10	< 0.02	0.20	0.05	< 0.02	31.30	< 0.01	0.06	0.20	68.80	101.04
M8049	681.86	0.10	0.37	0.07	< 0.02	0.14	0.04	0.03	31.18	0.03	0.07	0.21	68.81	101.04
M8049	681.86	0.06	0.29	0.06	< 0.02	0.12	0.05	0.03	31.18	0.02	0.07	0.20	68.82	100.89
M8049	681.86	0.05	0.25	0.08	< 0.02	0.06	0.05	0.03	31.21	0.02	0.07	0.20	68.95	100.97
M8049	681.86	0.07	0.16	0.04	< 0.02	0.71	0.06	0.05	31.25	0.01	0.05	0.23	68.42	101.04
M8049	681.86	0.06	0.19	0.04	< 0.02	0.07	0.06	< 0.02	31.34	0.01	0.06	0.24	69.29	101.35
M8049	681.86	0.08	0.23	0.04	< 0.02	3.43	0.06	0.22	31.62	< 0.01	0.05	0.20	65.89	101.52
M8049	681.86	0.47	0.30	0.03	< 0.02	1.06	0.04	0.07	30.77	< 0.01	0.06	0.22	68.36	101.40
M8049	681.86	0.09	0.30	0.03	< 0.02	0.05	0.07	< 0.02	31.07	0.02	0.05	0.21	68.69	100.57
M8049	681.86	0.05	0.23	0.03	< 0.02	0.09	0.07	< 0.02	31.24	0.01	0.06	0.23	68.96	100.97
M8049	681.86	0.07	0.29	0.03	< 0.02	0.52	0.06	0.03	31.34	0.01	0.06	0.21	68.68	101.30
M8049	681.86	0.07	0.30	0.04	< 0.02	0.26	0.06	0.04	31.33	0.02	0.04	0.22	68.94	101.33
M8049	681.86	0.10	0.52	0.04	< 0.02	0.07	0.05	< 0.02	31.13	0.01	< 0.03	0.22	68.43	100.58
M8049	681.86	0.08	0.42	0.06	< 0.02	0.10	0.06	< 0.02	31.33	0.02	0.04	0.22	68.93	101.27
M8049	681.86	2.07	3.82	3.52	0.14	1.90	0.05	0.14	28.26	0.04	0.11	0.18	57.04	97.26
M8049	681.86	0.02	0.20	0.05	< 0.02	0.08	0.04	< 0.02	31.30	0.01	0.05	0.21	69.02	100.99
M8049	681.86	0.04	0.22	0.04	< 0.02	0.08	0.05	< 0.02	31.31	0.02	< 0.03	0.21	69.10	101.07
M8049	681.86	0.10	0.49	0.06	< 0.02	0.08	0.04	< 0.02	31.35	< 0.01	0.04	0.22	68.95	101.33
M8049	681.86	0.03	0.24	0.08	0.03	0.17	0.04	< 0.02	31.26	< 0.01	0.05	0.19	68.80	100.89
M8049	681.86	0.29	0.41	0.39	< 0.02	0.10	0.06	0.03	30.74	0.01	0.06	0.20	68.01	100.30
M8049	681.86	0.10	0.34	0.05	< 0.02	0.07	0.06	0.03	31.35	0.02	0.08	0.22	69.31	101.62
M8049	681.86	0.11	0.29	0.18	< 0.02	0.05	0.06	< 0.02	31.12	0.01	0.05	0.21	68.66	100.75
M8049	681.86	0.11	0.23	0.51	0.05	0.15	0.06	0.17	31.20	< 0.01	< 0.03	0.19	68.62	101.30
M8049	681.86	0.12	0.20	0.07	< 0.02	0.05	0.06	< 0.02	31.24	< 0.01	0.06	0.22	69.27	101.29
M8049	684.49	0.09	0.22	0.05	< 0.02	0.26	0.13	0.04	31.30	0.01	0.06	0.35	68.88	101.39
M8049	684.49	0.10	0.21	0.03	< 0.02	0.11	0.16	0.04	31.23	< 0.01	0.04	0.36	68.89	101.16
M8049	684.49	0.53	0.56	0.04	< 0.02	10.03	0.13	0.84	31.01	< 0.01	0.06	0.30	58.28	101.78
M8049	684.49	0.13	0.35	0.03	< 0.02	0.20	0.15	0.03	31.25	0.01	0.06	0.34	68.81	101.35
M8049	684.49	0.12	0.41	0.07	< 0.02	0.94	0.14	0.08	31.47	0.01	0.07	0.34	68.23	101.88
M8049	684.49	0.16	0.33	0.03	< 0.02	0.09	0.14	0.04	31.10	0.01	0.06	0.35	68.79	101.10
M8049	684.49	0.36	1.03	0.07	< 0.02	0.20	0.15	< 0.02	30.99	0.01	0.07	0.36	67.98	101.22
M8049	684.49	0.11	0.23	0.02	< 0.02	0.16	0.14	0.03	31.24	< 0.01	0.06	0.36	68.92	101.28
M8049	684.49	0.11	0.30	0.02	< 0.02	0.13	0.13	0.06	31.10	0.01	0.07	0.35	68.68	100.96
M8049	684.49	0.15	0.46	0.04	< 0.02	0.46	0.15	0.05	31.32	< 0.01	0.07	0.33	68.54	101.57
M8049	684.49	2.18	1.10	3.55	< 0.02	0.10	0.17	0.05	27.63	< 0.01	0.04	0.31	61.61	96.74
M8049	684.49	0.63	0.54	0.91	< 0.02	0.10	0.18	0.05	30.46	0.01	0.06	0.34	67.32	100.61
M8049	684.49	0.15	0.29	0.08	< 0.02	0.20	0.18	0.04	31.33	0.02	0.06	0.41	69.00	101.76
M8049	684.49	0.11	0.21	0.04	< 0.02	0.85	0.19	0.06	31.38	0.02	0.08	0.41	68.33	101.68
M8049	684.49	0.31	0.50	0.44	< 0.02	0.33	0.19	0.05	31.14	0.02	0.05	0.41	68.07	101.51
M8049	684.49	0.22	0.26	0.04	< 0.02	0.88	0.19	0.10	31.02	< 0.01	0.06	0.38	67.91	101.06
M8049	684.49	1.11	0.64	1.52	< 0.02	0.27	0.17	< 0.02	30.13	< 0.02	0.06	0.42	66.89	101.23
M8049	684.49	0.11	0.22	0.06	< 0.02	0.20	0.17	0.04	31.23	< 0.01	0.05	0.48	68.72	101.29
M8049	684.49	1.45	0.38	0.06	< 0.02	11.31	0.16	1.09	29.23	0.02	0.04	0.34	56.97	101.05
M8049	684.49	0.18	0.19	0.05	< 0.02	0.80	0.16	0.08	31.18	0.01	0.06	0.41	68.29	101.41
M8049	684.49	0.09	0.19	0.02	< 0.02	0.30	0.16	0.03	31.22	0.01	0.06	0.34	68.69	101.11
M8049	684.49	0.15	0.38	0.05	< 0.02	0.27	0.16	0.05	31.27	0.03	0.06	0.33	68.83	101.59
M8049	684.49	0.13	0.35	0.05	< 0.02	0.15	0.18	0.03	31.23	< 0.01	0.08	0.33	68.76	101.29
M8049	684.49	0.37	0.26	0.04	< 0.02	6.91	0.15	0.71	30.58	0.01	0.05	0.30	60.99	100.37
M8049	684.49	0.19	0.43	0.03	< 0.02	0.09	0.18	0.03	31.15	0.03	0.07	0.32	68.94	101.46
M8049	684.49	0.82	2.51	0.06	< 0.02	1.62	0.16	0.19	30.31	< 0.01	0.06	0.31	64.46	100.50
M8049	684.49	0.46	0.41	0.64	< 0.02	3.76	0.15	0.48	30.79	0.03	0.07	0.31	64.24	101.34
M8049	684.49	0.13	0.44	0.04	< 0.02	0.37	0.16	0.03	31.43	< 0.01	0.07	0.33	68.81	101.80
M8049	684.49	0.15	0.37	0.06	< 0.02	0.51	0.17	0.06	31.28	0.01	0.09	0.33	68.55	101.58
M8049	684.49	0.09	0.23	0.04	< 0.02	0.16	0.17	0.03	31.27	< 0.01	0.06	0.34	68.85	101.24
M8049	684.49	0.12	0.20	0.08	< 0.02	0.15	0.17	0.04	31.34	< 0.01	0.07	0.32	69.18	101.67
M8049	684.49	0.16	0.44	0.03	< 0.02	0.19	0.17	0.05	31.13	0.01	0.07	0.31	68.59	101.15
M8049	684.49	0.24	0.56	0.06	< 0.02	2.40	0.16	0.21	31.44	0.01	< 0.03	0.29	66.72	102.08
M8049	684.49	0.17	0.46	0.04	< 0.02	0.84	0.17	0.10	31.27	0.01	0.07	0.32	68.12	101.56
M8049	684.49	0.09	0.18	0.05	< 0.02	0.39	0.17	0.04	31.40	0.01	0.04	0.32	68.96	101.65
M8049	684.49	0.11	0.29	0.04	< 0.02	0.32	0.15	0.04	31.21	< 0.01	0.05	0.29	68.58	101.08
M8049	684.49	0.12	0.26	0.08	< 0.02	0.22	0.18	0.04	31.29	0.01	0.06	0.30	68.90	101.45
M8049	684.49	0.39	1.32	0.19	< 0.02	0.91	0.18	0.11	31.07	0.01	0.06	0.32	66.84	101.40
M8049	684.49	0.11	0.25	0.05	< 0.02	0.26	0.16	0.04	31.26	< 0.01	0.05	0.33	68.77	101.28
M8049	684.49	0.19	0.19	0.06	< 0.02	2.03	0.17	0.22	31.46	0.01	0.04	0.38	67.56	102.31
M8049	684.49	0.10	0.19	0.02	< 0.02	0.42	0.17	0.05	31.31	< 0.01	0.07	0.37	68.76	101.46
M8049	684.49	0.13	0.34	0.05	< 0.02	0.17	0.17	0.06	31.19	0.03	0.04	0.41	68.67	101.26
M8049	684.49	0.09	0.21	0.05	< 0.02	0.29	0.17	0.05	31.23	0.02	0.05	0.40	68.65	101.21
M8049	684.49	0.42	0.98	0.06	< 0.02	0.87	0.16	0.10	30.99	0.01	0.06	0.42	67.48	101.55
M8049	684.49	0.20	0.19	0.07	< 0.02	1.45	0.15	0.18	31.23	0.01	0.05	0.41	67.77	101.71
M8049	757.36	0.13	0.22	0.11	< 0.02	0.27	0.17	0.03	31.13	0.03	0.04	0.34	68.46	100.93
M8049	757.36	0.58	0.37	0.51	< 0.02	0.44	0.16	0.05	30.60	0.02	0.07	0.42	67.94	101.16
M8049	757.36	0.82	0.11	0.04	< 0.02	0.08	0.04	0.05	30.14	0.01	0.07	0.10	70.04	101.50
M8049	757.36	0.80	0.10	0.02	< 0.02	0.04	0.04	0.06	30.01	0.03	0.05	0.10	69.76	101.01
M8049	757.36	0.94	0.23	0.03	< 0.02	0.24	0.05	0.07	29.88	0.02	0.06	0.11	69.54	101.17
M8049	757.36	0.88	0.17	0.02	< 0.02	0.15	0.04	0.07	30.12	< 0.01	0.07	0.11	70.05	101.68
M8049	757.36	0.91	0.11	0.03	< 0.02	0.09	0.06	0.06	29.95	0.01	0.07	0.10	69.99	101.38
M8049	757.36	0.82	0.13	0.03	< 0.02	0.13	0.05	0.07	30.05	0.01	0.05	0.11	69.74	101.19
M8049	757.36	0.46	0.28	0.03	< 0.02	0.20	0.04	0.06	30.60	0.02	0.07	0.10	69.25	101.11
M8049	757.36	0.39	0.11	0.03	< 0.02	0.04	0.03	0.04	30.77	0.02	0.07	0.10	69.77	101.37
M8049	757.36	0.58	0.42	0.02	< 0.02	0.19								

M8049	792.45	0.05	< 0.01	< 0.01	< 0.02	0.11	0.04	0.12	31.08	< 0.01	0.09	0.12	69.41	101.02
M8049	792.45	0.13	0.04	0.05	< 0.02	0.11	0.05	0.13	31.02	< 0.01	0.06	0.09	69.42	101.09
M8049	792.45	0.14	0.05	0.04	< 0.02	0.12	0.04	0.15	30.96	0.02	0.07	0.10	69.42	101.10
M8049	792.45	0.14	0.04	0.05	< 0.02	0.12	0.03	0.14	30.99	< 0.01	0.07	0.10	69.43	101.12
M8049	792.45	0.14	0.04	0.04	< 0.02	0.11	0.03	0.13	30.88	0.02	0.05	0.10	69.21	100.75
M8049	792.45	0.11	0.07	0.04	< 0.02	0.17	0.04	0.15	31.06	0.01	0.06	0.12	69.39	101.22
M8049	792.45	0.14	0.08	0.09	< 0.02	0.16	0.04	0.14	31.05	< 0.01	0.06	0.11	69.34	101.22
M8049	792.45	0.11	0.07	0.07	< 0.02	0.21	0.04	0.13	31.02	< 0.01	0.09	0.12	69.20	101.06
M8049	792.45	0.10	0.06	0.07	< 0.02	0.14	0.05	0.14	31.07	0.02	0.05	0.12	69.32	101.15
M8049	792.45	0.08	0.12	0.09	< 0.02	0.14	0.05	0.13	31.09	0.01	0.06	0.11	69.15	101.03
M8049	792.45	0.11	0.11	0.07	< 0.02	0.25	0.04	0.10	31.27	0.03	0.06	0.10	69.57	101.71
M8049	792.45	0.07	0.08	0.05	< 0.02	0.16	0.03	0.15	31.19	0.02	0.07	0.12	69.53	101.47
M8049	792.45	0.05	0.09	0.05	< 0.02	0.16	0.05	0.15	31.15	0.03	0.07	0.11	69.37	101.28
M8049	792.45	0.05	0.08	0.04	< 0.02	0.23	0.04	0.21	31.15	0.03	0.06	0.12	69.40	101.41
M8049	792.45	0.04	0.07	0.04	< 0.02	0.11	0.05	0.13	31.17	0.02	0.07	0.11	69.42	101.22
M8049	792.45	0.02	0.12	0.04	< 0.02	0.15	0.04	0.14	31.33	0.02	0.08	0.10	69.62	101.67
M8049	792.45	0.12	0.03	0.04	< 0.02	0.13	0.05	0.12	31.09	< 0.01	0.07	0.11	69.52	101.27
M8049	792.45	0.11	0.04	0.03	< 0.02	0.16	0.04	0.14	31.09	0.02	0.06	0.10	69.51	101.29
M8049	792.45	0.06	0.13	0.03	< 0.02	0.14	0.04	0.14	31.21	0.02	0.04	0.10	69.45	101.37
M8049	792.45	0.04	0.10	0.05	< 0.02	0.17	0.04	0.14	31.29	0.02	0.06	0.10	69.55	101.56
M8049	792.45	0.13	0.13	0.12	< 0.02	0.05	0.06	0.12	31.15	0.02	0.05	0.10	69.53	101.47
M8049	792.45	0.25	0.10	0.55	0.03	0.14	0.03	0.15	30.91	0.01	0.06	0.09	68.81	101.13
M8049	792.45	0.13	0.07	0.09	< 0.02	0.12	0.05	0.14	30.99	0.02	0.07	0.09	69.29	101.05
M8049	792.45	0.13	0.08	0.07	< 0.02	0.13	0.04	0.12	31.03	0.02	0.06	0.10	69.36	101.14

Table 4.6 – EPMA analyses of magnetite within sulphide at the Sakatti deposit. Values are calculated weight % oxide with Fe correction applied stoichiometrically.

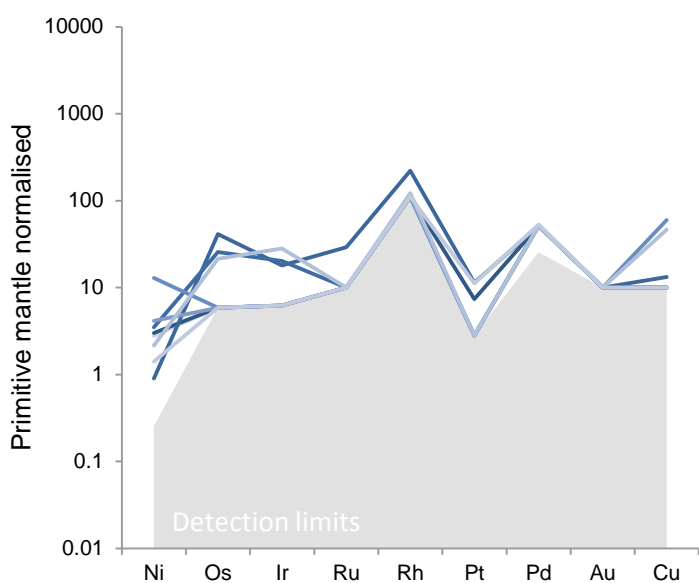
4.3.2.2 LA-ICP-MS



Chalcopyrite

Chalcopyrite has very low PGE contents, mostly at or below detection limits (Fig. 4.13).

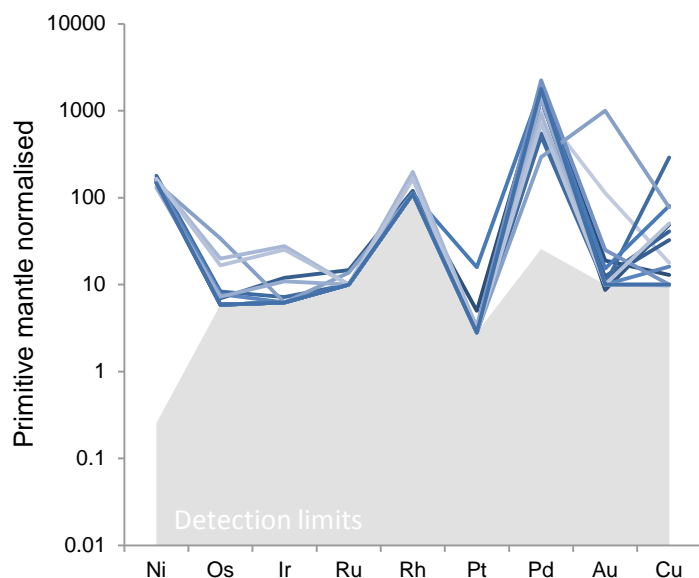
Figure 4.13 – Relative PGE values for chalcopyrite at the Sakatti deposit. Values are primitive mantle normalised (McDonough and Sun, 1995).



Pyrrhotite

Pyrrhotite also has very low PGE contents, mostly at or below detection limits, although there is detectable IPGE and Pt in several samples (Fig. 4.14).

Figure 4.14 - Relative PGE values for pyrrhotite at the Sakatti deposit. Values are primitive mantle normalised (McDonough and Sun, 1995).



Pentlandite

Pentlandite shows very low concentrations of PGE with the exception of Pd (Fig. 4.15). Pentlandite also hosts variable but significant levels of Co, between 0.1 % and 1.7 %.

Figure 4.15- Relative PGE values for pentlandite at the Sakatti deposit. Values are primitive mantle normalised (McDonough and Sun, 1995).

The Pd content of pentlandite can be compared to the whole-rock content of Pd to establish the proportion of Pd that is accommodated in the pentlandite (Table 4.7) using normative mineralogy (Eg. Rollinson, 1993). This requires the proportion of the sample that is made up of pentlandite to be estimated. Rather than rely in polished block observations, which may not be representative, the following assumptions were used.

- All Cu in the sample is present as chalcopyrite
- The proportion of sulphide Ni can be removed using a conversion factor for Mg # to remove silicate Ni
- Sulphide Ni and the remaining S (after chalcopyrite proportion accounted for) are accommodated in pyrrhotite and pentlandite.

The proportion of pentlandite in the sample was estimated by first using the Cu value to remove a stoichiometric equivalent of S based on the formula of chalcopyrite. Then second, using the Mg# to remove the silicate proportion of Ni using the conversion factor of Mg/Ni = 110 (average Mg content of 24.3 wt% and Ni content of 0.22 wt% based on selected whole-rock from unmineralised samples). This step was inconsequential for massive sulphide samples. Lastly the EPMA measured Ni and S content of pentlandite and pyrrhotite were used to estimate the proportions of these two phases as wt% of the whole-rock (Fig. 4.1). These estimates were consistent with observations from core logging.

$$X_{Pn} = \frac{\left(\frac{Ni_{sulph}^{wr}}{S_{residual}^{wr}} - \frac{Ni_{po}^{min}}{S_{po}^{min}} \right)}{\left(\frac{Ni_{pn}^{min}}{S_{pn}^{min}} - \frac{Ni_{po}^{min}}{S_{po}^{min}} \right)}$$

Equation 4.1 - Where: wr = whole-rock values, min = measured mineral chemistry, Ni_{sulph} is the whole-rock Ni content after silicate Ni has been removed and $S_{residual}$ is the whole-rock S content after chalcopyrite has been removed.

Concession	Hole	Depth	% Pn	% of Pd in Pn	% of Co in Pn
M8	44	636.91	4	20	119
M8	44	650.91	3	27	14
M8	44	684.49	6	32	76
M8	44	696.19	11	41	49
M8	44	760.77	0	0	0
M8	44	762.54	13	30	58
M8	49	679.8	0	18	14
M8	49	681.86	1	29	5
M8	49	695.74	1	32	16
M8	49	714.15	0	4	3
M8	49	734.49	1	89	19
M8	49	773.57	12	37	77
M8	49	792.45	9	39	47
M8	49	820	1	44	30

Table 4.7 – Estimation of pentlandite content of the whole-rock measurements and the proportion of the whole-rock Pd and Co that is accommodated in pentlandite. The first sample shows that it accommodates 119% of the Co; this has been kept to show the potential limitations of this method of estimation.

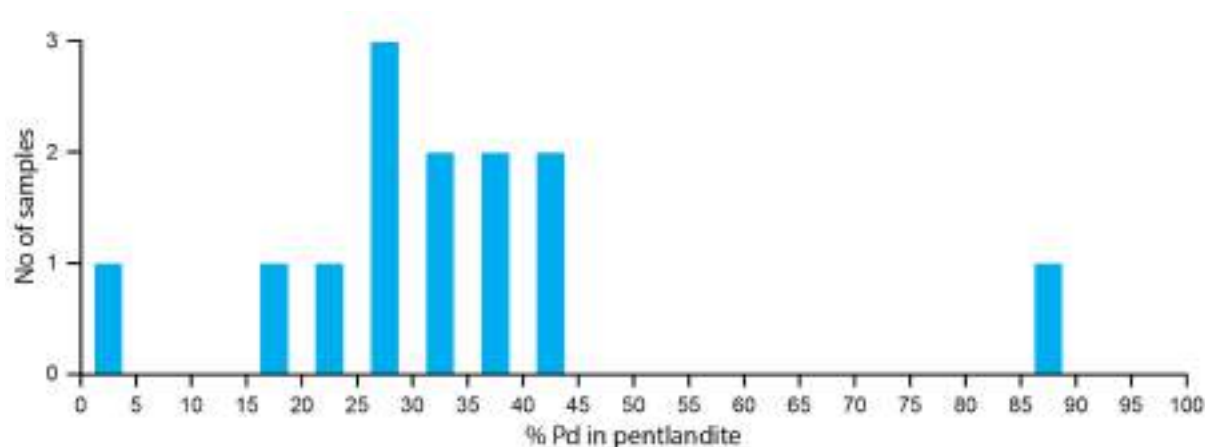
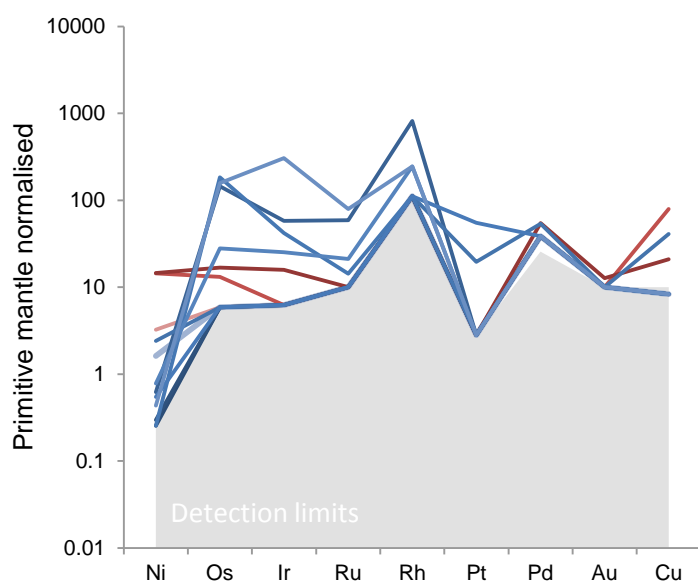


Figure 4.16 – Histogram showing distribution of estimated proportion of whole-rock Pd amounts accommodated in pentlandite using the trace element analysis of pentlandite.

These mass balance estimates indicate that approximately between 15-45 % (mean = 31 %) of the Pd at Sakatti is present within solid solution in the pentlandite (Fig. 4.16).



Pyrite

Pyrite proved to be the phase that contains the most IPGE relative to PPGE (Fig. 4.17). This is particularly evident in the 'clean' pyrite as opposed to the 'stripy' pyrite which was mostly below detection limits for the PGE. The 'clean' pyrite was much easier to analyse by LA-ICP-MS than the stripy pyrite due to the absence of magnetite exsolutions, which made the latter difficult.

Figure 4.17 - Relative PGE values for pyrite at the Sakatti deposit. 'Clean' pyrite is shown in blue and 'stripy' pyrite in red. Values are primitive mantle normalised (McDonough and Sun, 1995).

4.3.2.3 Magnetite

Trace elements in magnetite were analysed separately from the surrounding sulphide, at the Natural History Museum, London (Table 4.14). The elements contained are the lithophiles from the sulphide melt and as such are not comparable with the other mineral plots. They are plotted in order of compatibility (Fig. 4.18) following the method of Dare et al. (2014a).

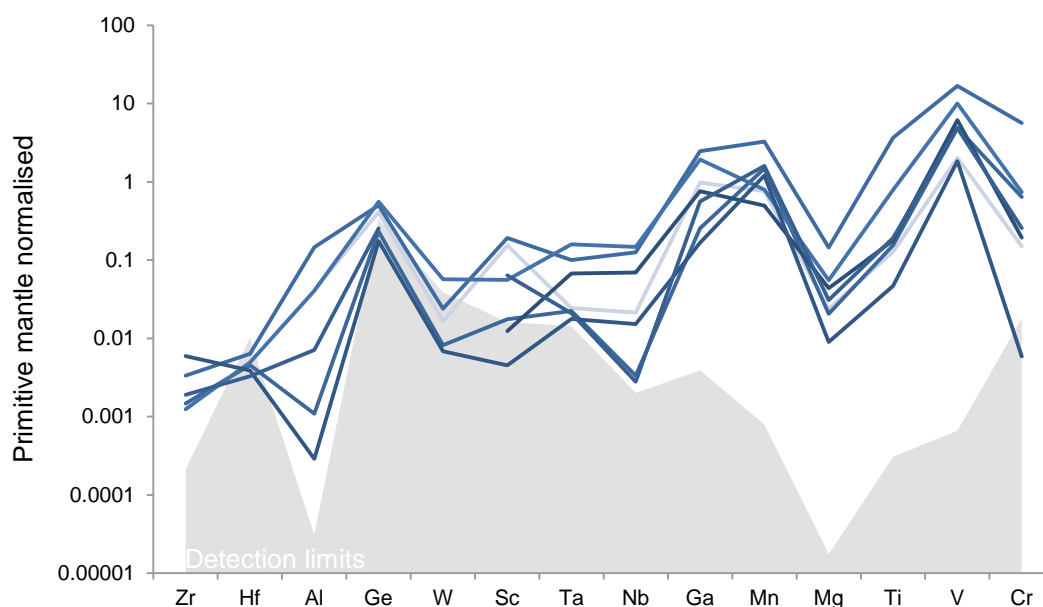


Figure 4.18 - Relative values of lithophile elements within magnetite at the Sakatti deposit. Values are primitive mantle normalised (McDonough and Sun, 1995).

Hole	S	⁵⁷ Fe	⁵⁹ Co	⁶¹ Ni	⁶⁵ Cu	⁶⁶ Zn	⁷⁵ As	⁸² Se	¹⁰¹ Ru*	¹⁰³ Rh*	¹⁰⁶ Pd*	¹⁰⁸ Pd*	¹⁰⁹ Ag	¹¹¹ Cd	¹²¹ Sb	¹²⁵ Te	¹⁸⁵ Re	¹⁸⁹ Os	¹⁹³ Ir	¹⁹⁵ Pt	¹⁹⁷ Au	²⁰⁹ Bi
Memorial FeS	38.5	(%)	(ppm)	(%)	(%)	(ppm)	(ppm)	(ppm)	(ppm)	(ppm)	(ppm)	(ppm)	(ppm)	(ppm)	(ppm)	(ppm)	(ppm)	(ppm)	(ppm)	(ppm)	(ppm)	(ppm)
Memorial FeS	37	59.77	7	<0.05	<0.03	19	<6	<50	36.03	39.29	49.79	49.77	0.19	<0.8	<0.9	<0.9	<0.02	42.84	36.85	45.85	39.99	<0.05
Detection Limits		5	0.05	0.03	10	6	50	0.05	0.1	0.15	0.2	0.1	0.8	0.9	0.9	0.02	0.02	0.02	0.02	0.02	0.01	0.05

Table 4.8 – Quantitative laser-ablation ICP-MS analyses of the Memorial University FeS standard Po724 and the detection limits for all analyses below.

Hole	Depth	Min	No of	S	⁵⁷ Fe	⁵⁹ Co	⁶¹ Ni	⁶⁵ Cu	⁶⁶ Zn	⁷⁵ As	⁸² Se	¹⁰¹ Ru*	¹⁰³ Rh*	¹⁰⁶ Pd*	¹⁰⁸ Pd*	¹⁰⁹ Ag	¹¹¹ Cd	¹²¹ Sb	¹²⁵ Te	¹⁸⁵ Re	¹⁸⁹ Os	¹⁹³ Ir	¹⁹⁵ Pt	¹⁹⁷ Au	²⁰⁹ Bi	
44	636.91	Ccp	2	35.25	26.95	23.83	<0.05	22.35	3330.50	<6	427.50	0.08	<0.1	<0.15	<0.2	21.40	3.23	<0.9	1.31	0.03	<0.02	<0.02	<0.02	0.03	0.08	0.74
44	650.91	Ccp	3	35.10	26.97	13.42	0.15	22.74	3988.50	<6	158.80	0.06	<0.1	<0.15	<0.2	11.27	1.80	<0.9	<0.9	<0.02	<0.02	<0.02	<0.02	<0.01	0.08	0.08
44	684.49	Ccp	3	34.20	27.10	<5	<0.05	25.26	4216.67	<6	103.65	<0.05	<0.1	<0.15	<0.2	11.35	2.23	<0.9	0.92	0.05	<0.02	<0.02	<0.02	<0.01	0.07	0.07
44	760.77	Ccp	3	35.20	32.76	<5	<0.05	27.90	3440.67	<6	169.93	0.06	0.58	<0.15	<0.2	9.85	14.57	0.91	1.40	<0.02	<0.02	<0.02	<0.02	0.02	0.19	0.19
44	762.54	Ccp	3	34.70	28.55	180.21	1.20	26.34	3086.33	<6	104.76	0.07	<0.1	<0.15	<0.2	12.33	2.38	<0.9	1.09	<0.02	<0.02	<0.02	<0.02	<0.01	0.06	0.06
49	679.8	Ccp	4	36.80	28.55	6.71	<0.05	24.83	3065.75	<6	110.66	<0.05	<0.1	0.51	0.52	6.37	1.62	<0.9	1.66	<0.02	<0.02	<0.02	0.14	<0.01	0.27	0.27
49	681.86	Ccp	2	35.40	26.49	11.14	0.13	20.85	1547.75	<6	169.40	0.06	<0.1	<0.15	<0.2	1.36	0.80	<0.9	1.46	<0.02	0.03	<0.02	<0.02	<0.01	0.43	0.43
49	695.74	Ccp	3	34.70	29.09	<5	<0.05	28.23	4374.33	<6	88.71	0.06	<0.1	<0.15	<0.2	3.48	0.85	<0.9	1.22	<0.02	<0.02	0.03	0.07	<0.01	0.12	0.12
49	714.15	Ccp	3	36.50	29.18	<5	<0.05	25.81	773.23	<6	198.37	<0.05	<0.1	<0.15	<0.2	1.79	0.80	<0.9	1.22	<0.02	<0.02	<0.02	<0.02	0.04	0.07	0.07
49	773.57	Ccp	3	35.60	28.06	261.40	0.99	23.21	5062.67	<6	278.50	0.07	<0.1	<0.15	<0.2	8.65	3.56	<0.9	1.25	0.03	<0.02	<0.02	<0.02	<0.01	0.07	0.07
49	792.45	Ccp	2	34.90	26.12	137.74	0.54	26.44	4263.00	<6	229.65	0.09	<0.1	<0.15	<0.2	3.93	3.78	<0.9	1.00	<0.02	<0.02	<0.02	<0.02	<0.01	0.15	0.15
49	820	Ccp	2	35.70	29.30	<5	<0.05	29.71	4122.50	<6	151.60	0.07	<0.1	<0.15	<0.2	7.60	1.93	<0.9	2.14	<0.02	<0.02	<0.02	0.14	<0.01	0.08	0.08
49	869.14	Ccp	3	34.70	28.45	<5	<0.05	25.19	735.10	<6	525.80	0.09	<0.1	0.18	<0.2	0.63	14.21	<0.9	3.59	<0.02	<0.02	<0.02	<0.02	0.06	2.73	2.73

Table 4.9 – Averaged quantitative laser-ablation ICP-MS analyses of chalcopyrite. Data presented is an average of several analysis spots from each sample.

Hole	Depth	Min	No of	S	⁵⁷ Fe	⁵⁹ Co	⁶¹ Ni	⁶⁵ Cu	⁶⁶ Zn	⁷⁵ As	⁸² Se	¹⁰¹ Ru*	¹⁰³ Rh*	¹⁰⁶ Pd*	¹⁰⁸ Pd*	¹⁰⁹ Ag	¹¹¹ Cd	¹²¹ Sb	¹²⁵ Te	¹⁸⁵ Re	¹⁸⁹ Os	¹⁹³ Ir	¹⁹⁵ Pt	¹⁹⁷ Au	²⁰⁹ Bi	
44	636.91	Pn	2	34.90	24.65	15023.50	31.45	0.05	124.30	<6	193.95	<0.05	<0.1	3.93	4.00	38.50	<0.8	<0.9	1.02	<0.02	<0.02	<0.02	<0.02	0.11	0.88	0.88
44	650.91	Pn	3	33.00	23.05	3757.33	32.19	0.04	18.66	<6	191.83	<0.05	<0.1	6.92	6.83	49.68	<0.8	<0.9	1.97	0.15	<0.02	<0.02	0.04	0.02	0.26	0.26
44	684.49	Pn	3	33.40	27.36	9383.33	30.12	0.15	1401.43	<6	111.03	<0.05	<0.1	5.57	5.40	10.01	1.05	<0.9	0.90	0.04	<0.02	<0.02	<0.02	<0.01	0.07	0.07
44	696.19	Pn	3	33.50	29.27	4397.67	32.15	0.10	11.73	<6	126.87	0.07	<0.1	5.00	5.52	6.90	<0.8	<0.9	2.11	<0.02	<0.02	0.04	<0.02	<0.01	0.06	0.06
44	760.77	Pn	3	34.60	34.94	17286.67	29.24	0.12	18.10	<6	369.33	<0.05	<0.1	2.09	2.15	143.97	<0.8	<0.9	10.56	<0.02	<0.02	<0.02	<0.02	<0.01	2.83	2.83
44	762.54	Pn	3	34.23	29.76	7395.67	35.14	0.87	1372.66	<6	118.22	<0.05	<0.1	2.03	1.98	33.01	1.57	<0.9	0.90	<0.02	0.03	<0.02	<0.02	<0.01	0.40	0.40
49	679.8	Pn	3	34.30	24.00	7135.00	29.90	0.24	4223.00	<6	200.33	<0.05	<0.1	7.05	7.03	122.73	2.26	0.97	2.56	<0.02	<0.02	<0.02	0.11	0.02	0.47	0.47
49	681.86	Pn	2	34.00	33.32	2577.50	31.32	0.05	<10.00	<6	304.50	<0.05	<0.1	5.32	5.41	4.20	<0.8	<0.9	0.90	<0.02	0.03	<0.02	<0.02	<0.01	0.36	0.36
49	695.74	Pn	3	32.90	27.34	8762.33	30.47	<0.03	24.48	<6	90.16	<0.05	<0.1	8.61	8.74	17.67	0.80	<0.9	1.33	<0.02	<0.02	<0.02	<0.02	0.03	0.36	0.36
49	714.15	Pn	4	34.60	27.02	1693.70	29.03	0.23	40.54	13.92	927.25	0.07	<0.1	1.13	1.14	64.52	<0.8	2.11	17.87	<0.02	0.12	<0.02	<0.02	1.00	2.94	2.94
49	734.49	Pn	3	33.70	26.87	2342.33	25.58	<0.03	21.66	<6	185.23	<0.05	<0.1	5.35	5.42	9.64	<0.8	<0.9	6.05	<0.02	<0.02	0.04	<0.02	<0.01	0.20	0.20
49	773.57	Pn	3	34.90	27.74	9498.33	31.88	<0.03	584.94	<6	217.13	<0.05	0.18	3.74	3.56	1.79	<0.8	<0.9	0.80	<0.02	0.07	0.09	<0.02	<0.01	0.08	0.08
49	792.45	Pn	3	33.80	27.67	8321.33	32.20	0.15	33.96	<6	252.83	<0.05	0.15	2.78	2.79	1.26	0.83	<0.9	1.25	0.07	0.06	0.08	<0.02	<0.01	0.13	0.13
49	820	Pn	3	33.50	30.21	8149.67	28.83	<0.03	15.58	<6	128.60	<0.05	<0.1	6.88	6.96	2.31	<0.8	<0.9	1.91	<0.02	<0.02	<0.02	<0.02	<0.01	<0.05	<0.05

Table 4.10 – Averaged quantitative laser-ablation ICP-MS analyses of pentlandite. Data presented is an average of several analysis spots from each sample.

Hole	Depth	Min	No of	S	⁵⁷ Fe	⁵⁹ Co	⁶¹ Ni	⁶⁵ Cu	⁶⁶ Zn	⁷⁵ As	⁸² Se	¹⁰¹ Ru*	¹⁰³ Rh*	¹⁰⁶ Pd*	¹⁰⁸ Pd*	¹⁰⁹ Ag	¹¹¹ Cd	¹²¹ Sb	¹²⁵ Te	¹⁸⁵ Re	¹⁸⁹ Os	¹⁹³ Ir	¹⁹⁵ Pt	¹⁹⁷ Au	²⁰⁹ Bi	
44	636.91	Po	3	38.80	46.32	85.33	0.55	<0.03	11.75	<6	148.81	<0.05	<0.1	<0.15	<0.2	1.26	<0.8	<0.9	<0.9	<0.02	<0.02	<0.02	<0.02	<0.01	0.08	0.08
44	684.49	Po	2	39.10	50.51	68.25	0.59	<0.03	10.69	<6	128.30	<0.05	<0.1	0.17	<0.2	<0.1	<0.8	<0.9	0.93	0.03	<0.02	<0.02	0.05	<0.01	0.06	0.06
44	760.77	Po	3	40.40	54.60	91.93	0.18	0.04	11.86	6.94	312.07	0.15	0.20	<0.15	<0.2	2.91	<0.8	<0.9	<0.9	0.06	0.14	0.06	0.08	<0.01	1.28	1.28
44	762.54	Po	2	39.40	51.70	142.53	0.68	<0.03	10.00	<6	156.15	<0.05	<0.1	<0.15	<0.2	1.16	<0.8	<0.9	<0.9	0.07	0.09	0.07	<0.02	<0.01	0.17	0.17
49	695.74	Po	2	39.80	54.63	5.75	0.82	<0.03	20.17	<6	97.84	<0.05	<0.1	<0.15	<0.2	0.56	<0.8	<0.9	<0.9	<0.02	<0.02	<0.02	<0.02	<0.01	<0.05	<0.05
49	773.57	Po	3	41.20	54.07	96.61	0.42	0.14	35.74	<6	200.27	<0.05	0.11	<0.15	<0.2	0.63	<0.8	<0.9	<0.9	0.04	0.07	0.09	<0.02	<0.01	0.07	0.07
49	792.45	Po	3	39.90	48.56	122.07	0.64	<0.03	13.55	6.48	225.50	<0.05	1.26	5.96	5.99	6.19	1.03	<0.9	<0.9	0.06	0.65	0.04	0.32	0.02	0.13	0.13</

Hole	Depth	Min	No of	S	⁵⁷ Fe	⁵⁹ Co	⁶¹ Ni	⁶⁵ Cu	⁶⁶ Zn	⁷⁵ As	⁸² Se	¹⁰¹ Ru*	¹⁰³ Rh*	¹⁰⁶ Pd*	¹⁰⁸ Pd*	¹⁰⁹ Ag	¹¹¹ Cd	¹²¹ Sb	¹²⁵ Te	¹⁸⁵ Re	¹⁸⁹ Os	¹⁹³ Ir	¹⁹⁵ Pt	¹⁹⁷ Au	²⁰⁹ Bi
	(m)		Spots	%	(%)	(ppm)	(%)	(%)	(ppm)	(ppm)	(ppm)	(ppm)	(ppm)	(ppm)	(ppm)	(ppm)	(ppm)	(ppm)	(ppm)	(ppm)	(ppm)	(ppm)	(ppm)	(ppm)	(ppm)
44	636.91	Py	3	52.70	49.95	<6	<0.05	<0.03	13.54	12.53	255.57	<0.05	<0.1	<0.15	<0.2	0.69	<0.8	4.56	1.12	<0.02	<0.02	<0.02	<0.02	<0.01	<0.05
44	650.91	Py	3	47.17	44.00	7.12	0.06	<0.03	14.75	<6	295.03	<0.05	<0.1	<0.15	<0.2	0.24	<0.8	<0.9	<0.9	<0.02	<0.02	<0.02	<0.02	<0.01	<0.05
44	760.77	Py	1	55.20	47.05	11030.00	0.12	<0.03	13.02	23.55	244.50	0.29	0.74	<0.15	<0.2	6.69	<0.8	<0.9	<0.9	0.12	0.49	0.19	<0.02	<0.01	<0.05
49	679.8	Py	3	54.90	53.79	36.23	0.47	0.12	722.65	<6	176.77	<0.05	<0.1	0.21	0.26	5.66	1.38	<0.9	1.28	<0.02	<0.02	<0.02	0.14	<0.01	0.33
49	681.86	Py	1	54.10	48.88	6501.00	<0.05	<0.03	<10	<6	198.70	0.07	<0.1	<0.15	<0.2	<0.1	<0.8	<0.9	<0.9	0.07	0.62	0.13	<0.02	<0.01	0.15
49	695.74	Py	3	52.00	50.24	8763.33	0.11	<0.03	<10	42.34	98.76	<0.05	<0.1	<0.15	<0.2	0.64	<0.8	<0.9	<0.9	0.04	<0.02	<0.02	0.39	<0.01	<0.05
49	714.15	Py	3	49.10	49.63	5352.00	0.15	<0.03	11.29	18.66	73.31	0.11	0.22	<0.15	<0.2	0.07	<0.8	<0.9	<0.9	<0.02	0.10	0.08	<0.02	<0.01	<0.05
49	734.49	Py	3	54.05	51.31	5765.00	0.09	<0.03	12.65	<6	88.22	0.40	0.22	<0.15	<0.2	<0.1	<0.8	<0.9	<0.9	0.03	0.54	0.98	<0.02	<0.01	0.07
49	869.14	Py	2	52.80	47.17	10864.00	0.32	<0.03	<10	84.10	791.35	<0.05	<0.1	<0.15	<0.2	<0.1	<0.8	<0.9	<0.9	<0.02	<0.02	<0.02	<0.02	<0.01	0.18

Table 4.12 – Averaged quantitative laser-ablation ICP-MS analyses of 'clean' pyrite. Data presented is an average of several analysis spots from each sample.

Hole	Depth	Min	No of	S	⁵⁷ Fe	⁵⁹ Co	⁶¹ Ni	⁶⁵ Cu	⁶⁶ Zn	⁷⁵ As	⁸² Se	¹⁰¹ Ru*	¹⁰³ Rh*	¹⁰⁶ Pd*	¹⁰⁸ Pd*	¹⁰⁹ Ag	¹¹¹ Cd	¹²¹ Sb	¹²⁵ Te	¹⁸⁵ Re	¹⁸⁹ Os	¹⁹³ Ir	¹⁹⁵ Pt	¹⁹⁷ Au	²⁰⁹ Bi
	(m)		Spots	%	(%)	(ppm)	(%)	(%)	(ppm)	(ppm)	(ppm)	(ppm)	(ppm)	(ppm)	(ppm)	(ppm)	(ppm)	(ppm)	(ppm)	(ppm)	(ppm)	(ppm)	(ppm)	(ppm)	(ppm)
49	679.8	Stripy Py	2	54.45	53.86	55.88	0.63	<0.03	13.73	<6	200.10	<0.05	<0.1	<0.15	<0.2	5.56	<0.8	<0.9	<0.9	<0.02	<0.02	<0.02	<0.02	<0.01	0.11
49	681.86	Stripy Py	3	54.00	55.16	31.41	2.84	0.24	21.77	<6	363.77	<0.05	<0.1	<0.15	<0.2	5.86	<0.8	<0.9	0.92	<0.02	0.04	<0.02	<0.02	<0.01	0.18

Table 4.13 - Averaged quantitative laser-ablation ICP-MS analyses of 'stripy' pyrite. Data presented is an average of several analysis spots from each sample.

Hole	Depth	Min	No of	⁷ Li	²³ Na	²⁴ Mg	²⁷ Al	²⁸ Si	³¹ P	³⁹ K	⁴³ Ca	⁴⁵ Sc	⁴⁷ Ti	⁵¹ V	⁵³ Cr	⁵⁵ Mn	⁵⁷ Fe	⁵⁹ Co	⁶⁰ Ni	⁶⁵ Cu	⁶⁶ Zn	⁶⁹ Ga	⁷¹ Ga
	(m)		Spots	(ppm)	(ppm)	(ppm)	(ppm)	(ppm)	(ppm)	(ppm)	(ppm)	(ppm)	(ppm)	(ppm)	(ppm)	(ppm)	(ppm)	(ppm)	(ppm)	(ppm)	(ppm)	(ppm)	(ppm)
44	636.91	Mt	20	0.836	54.4	669	1755	2706	28.9	3.54	64.9	3.38	550	278	20.3	587	726240	21.9	560	0.355	15.3	15.7	15.9
44	779.2	Mt	17	<1.44	73.4	1231	1095	3759	<42	28.9	<212	<0.484	768	845	26.2	383	726088	14	600	0.927	4.65	12.1	12.2
44	696.19	Mt	20	<0.402	158	254	12.2	2486	27.9	<2.95	<71.6	<0.136	201	253	0.795	930	727210	12.6	540	0.367	13.3	2.67	2.74
49	792.45	Mt	20	2.13	110	866	300	2298	30.5	64.4	<45.5	1.39	831	669	34.6	1238	726740	17.8	534	0.429	7.11	8.95	8.96
49	773.57	Mt	20	7.29	133	578	45.9	2329	31.1	<2.64	<69.2	0.385	668	673	86.6	1147	726720	20.4	577	0.576	8.01	4.07	4.06
44	684.49	Mt	20	1.45	35.2	3988	5976	3286	27.5	6.89	75.4	4.15	15690	2320	767	2497	719933	21	567	64.8	792	39.1	38.8
49	681.86	Mt	20	2.99	<50.4	1503	1663	3873	<58.6	<10.2	449	1.11	2879	1328	59.6	543	724174	9.65	476	308	75.8	30.5	31.3

Table 4.14 – Averaged quantitative laser-ablation ICP-MS analyses of magnetite. Data presented in an average of several analysis spots from each sample.

Hole	Depth	Min	No of	⁷⁴ Ge	⁷⁵ As	⁸⁸ Sr	⁸⁹ Y	⁹⁰ Zr	⁹³ Nb	⁹⁵ Mo	¹⁰⁷ Ag	¹¹⁸ Sn	¹²¹ Sb	¹⁴⁰ Ce	¹⁷⁸ Hf	¹⁸¹ Ta	¹⁸² W	²⁰⁸ Pb	²⁰⁹ Bi	²³⁸ U
	(m)		Spots	(ppm)	(ppm)	(ppm)	(ppm)	(ppm)	(ppm)	(ppm)	(ppm)	(ppm)	(ppm)	(ppm)	(ppm)	(ppm)	(ppm)	(ppm)	(ppm)	(ppm)
44	636.91	Mt	20	0.537	<0.0958	0.0253	0.125	0.0255	0.171	0.0372	0.0108	0.592	<0.035	0.0241	<0.0119	0.0171	0.0166	0.0755	<0.0219	0.014
44	779.2	Mt	17	<0.61	<0.394	0.178	0.0703	<0.0371	0.557	<0.115	<0.0184	0.636	<0.143	0.0169	<0.0466	0.0473	<0.048	0.206	0.126	<0.00644
44	696.19	Mt	20	0.228	<0.0959	0.00518	0.0123	0.784	0.122	0.0313	<0.0102	1.92	<0.034	0.0118	0.0144	0.0123	<0.0129	0.033	<0.0235	0.00505
49	792.45	Mt	20	0.331	<0.0862	0.0279	0.0209	0.251	0.0224	0.0374	<0.00429	0.66	<0.0341	0.0154	0.0121	0.0148	<0.0113	<0.0257	<0.0231	0.00666
49	773.57	Mt	20	0.302	0.0806	0.0244	0.0255	0.195	0.0267	0.0369	<0.00798	0.912	<0.0399	0.0328	0.017	0.0156	<0.0126	0.0503	<0.0213	0.00673
44	684.49	Mt	20	0.647	0.211	0.118	0.154	0.441	0.998	0.0735	0.203	3.23	<0.0352	0.229	0.0231	0.0703	0.0234	0.853	0.0442	0.183
49	681.86	Mt	20	0.735	<0.279	0.322	0.241	0.141	1.2	<0.0945	0.0322	0.615	<0.154	1.16	<0.0446	0.114	0.0639	0.19	<0.0795	0.189

Table 4.14...cont – Averaged quantitative laser-ablation ICP-MS analyses of magnetite. Data presented in an average of several analysis spots from each sample.

4.3.3 Bulk sulphide chemistry

The distribution of Ni/Cu values within the sulphides of the deposit is not uniform (Fig. 4.19). Massive sulphide shows a shift in Ni/Cu values from relatively Ni-rich deep portions of the body in the north-west to relatively Cu-rich shallower portions in the south-east (Fig. 4.20). Vein sulphide is generally more Cu-rich than massive sulphide. Disseminated sulphide is also more Cu-rich than the massive sulphide, and the disseminated sulphide also shows a Cu tenor shift from low in the north-west to high in the south-east. In the disseminated ore type, Pt and Pd occur roughly in the ratio of 2:1 which is similar to the average ratio (1.8) measured for disseminated sulphide in the Kevitsa ore deposit (Mutanen, 1997).

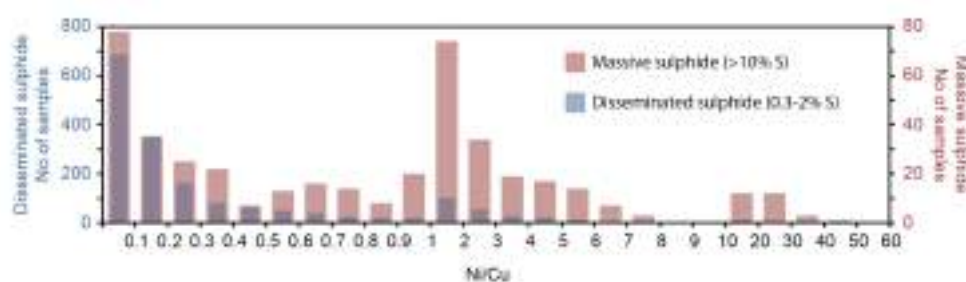


Figure 4.19 – Histogram showing Ni/Cu distribution across the whole Sakatti main body in massive (>10% S) samples and disseminated (0.3-2% S) samples. Note the dominance of Cu in disseminated samples (Ni corrected to remove silicate Ni).

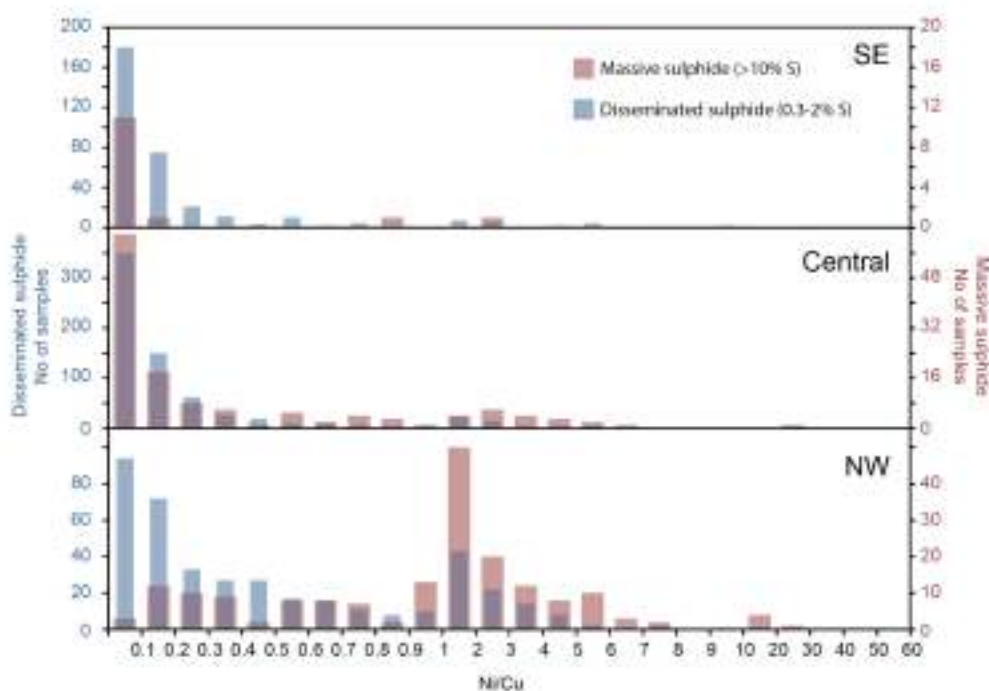


Figure 4.20 – Histogram showing Ni/Cu distribution in massive (>10% S) samples and disseminated (0.3-2% S) samples, separated into the SE, Central and NW parts of the main body.

PGE

The concentrations of IPGE and PPGE show variable primitive mantle-normalised patterns (Figs. 4.21), consistent with sulphide liquid fractionation in the massive sulphide (Eg. Ebel and Naldrett, 1996). High-Cu sulphide is enriched in Pt and Pd and depleted in Os, Ir, and Ru relative to high-Ni sulphide. The disseminated sulphide samples show the same enrichment and depletion pattern as the Cu-rich massive sulphide (Fig. 4.21). Both the Ni/Cu and IPGE/PPGE ratios indicate that this deposit has experienced considerable fractionation of the sulphide liquid.

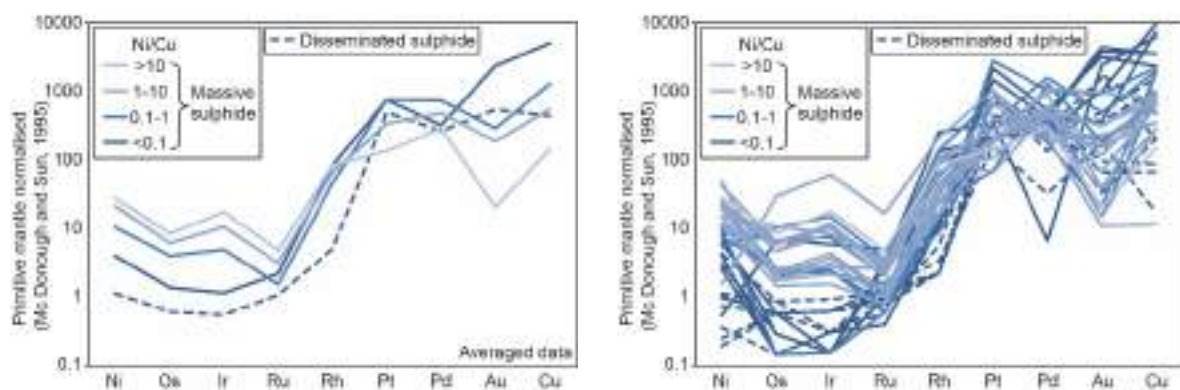


Figure 4.21 – Whole-rock PGE distribution separated according to Ni/Cu ratio. Note that disseminated sulphide is some of the most IPGE depleted, similar to evolved massive.

S/Se

S/Se ratios can be used to assess the origin of S in magmatic deposits in a similar sense to S isotopes (Eckstrand and Hulbert, 1987; Maier et al., 2008; Queffurus and Barnes, 2015). There is a spread of S/Se ratios at the Sakatti deposit. In order to test the validity of the spread of S/Se values samples were chosen for S isotope analysis on the basis of extremes in S/Se values. Mantle values of S/Se domain are 2850-4350 (Eckstrand and Hulbert, 1987). Most samples with S/Se values above mantle values are not mineralised (Fig. 4.22).

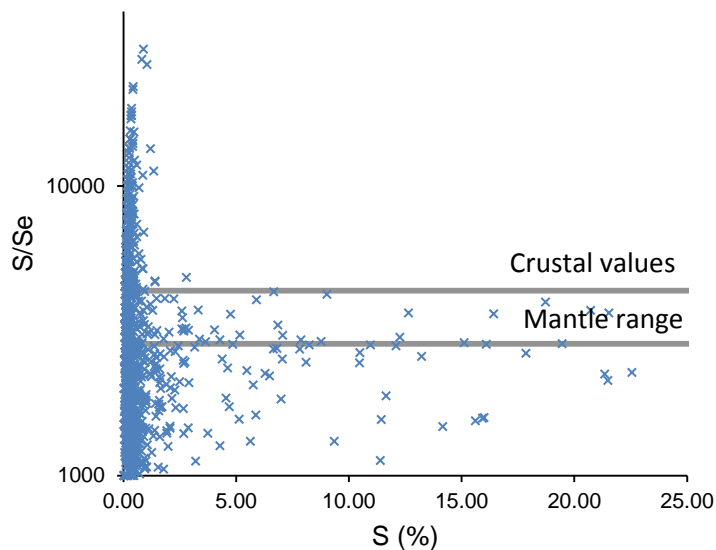


Figure 4.22 – Whole-rock S/Se ratio against S/Se ratio. The majority of mineralised samples (>1% S) are within or below the range of mantle-derived S with very few showing a crustal signature (Eckstrand and Hulbert, 1987).

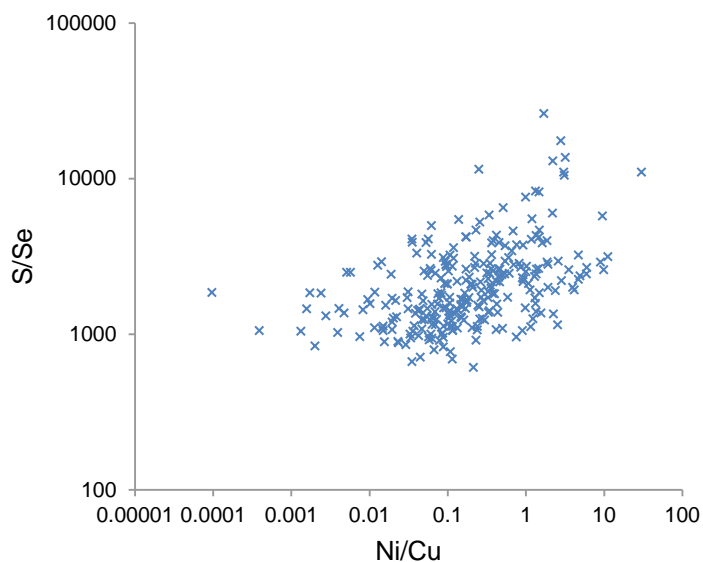


Figure 4.23 – Whole-rock S/Se ratio against Ni_{sulphide}/Cu ratio for mineralised samples only.

It has been shown that S/Se can be fractionated by sulphide crystallisation processes due to incompatibility of Se in primary crystallising MSS (Helmy et al., 2010; Queffurus and Barnes, 2015). This would result in a correlation between S/Se and Ni/Cu as they would both indicate MSS fractionation. There is not a compelling correlation at the Sakatti deposit (Fig. 4.23).

4.3.4 Isotopic studies

4.3.4.1 S isotope analysis

Hole	Depth	Type	Mineral	$\delta^{34}\text{S}$	SD	RSD (%)	
M8	051	855	Anhydrite	Anh	13.6	0.072	0.53
M8	054	1063.7	Anhydrite	Anh	11.2	0.014	0.13
M8	123	941.3	Anhydrite	Anh	14.4	0.022	0.15
M8	054	817.60	Anhydrite	Anh	13.1	0.029	0.22
M8	049	714.25	Dissem	Cpy	4.9	0.024	0.49
M8	044	760.5	Dissem	Cpy	3.7	0.011	0.30
M8	062	1037.00	Dissem	Cpy	3.8	0.015	0.40
M8	049	744.75	Dissem	Cpy	2.2	0.093	4.22
M8	049	869.20	Dissem	Cpy	2.6	0.093	3.64
M8	120	918.85	Dunite-hosted	Cpy	2.5	0.018	0.73
M8	051	870.8	Massive	Py	3.7	0.009	0.24
M8	051	842.2	Massive	Py	1.0	0.014	1.39
M8	051	869.7	Massive	Py	1.1	0.019	1.76
M8	049	800.1	Massive	Py	-1.7	0.019	1.14
M8	049	647.7	Dissem	Cpy	2.5	0.054	2.19
M8	051	862.5	Dissem in Anh	Py	2.8	0.025	0.90
M8	051	870.4	Dissem in Anh	Py	-1.1	0.018	1.69
M8	051	854.7	Dissem in Anh	Py	2.1	0.007	0.34
M8	051	879.3	Massive in Anh	Py	1.0	0.014	1.43
M8	049	731.3	Massive	Py	1.9	0.005	0.26
M8	049	710.9	Dissem	Cpy	3.7	0.011	0.30
M8	052	828	Dissem in Srp vein	Py	1.8	0.005	0.28
M8	052	808	Dissem in Srp vein	Py	1.9	0.072	3.73
M8	052	811.9	Dissem in Srp vein	Po	1.8	0.019	1.06
M8	052	824.1	Dissem	Cpy	2.4	0.022	0.91
M8	052	893	Massive	Py	3.0	0.011	0.37
M8	064	817.05	Massive	Py	1.6	0.012	0.75
M8	064	814.08	Massive	Py	1.8	0.010	0.55
M8	062	890.90	Mafic Volcanic	Po	4.8	0.012	0.25
M8	062	890.90	Mafic Volcanic	Py	3.4	0.022	0.65
M8	083	559.10	Massive	Cpy	3.0	0.010	0.33
M8	049	719.79	Massive	Cpy	3.4	0.014	0.42
M8	090	553.50	Massive	Cpy	3.0	0.010	0.34
M8	049	679.80	Massive	Cpy	2.7	0.012	0.44
M8	078	411.50	Massive	Cpy	3.4	0.023	0.67
M8	085	185.00	Massive	Cpy	2.4	0.024	1.00
M8	079	243.50	Massive	Cpy	2.9	0.014	0.49
M8	079	243.50	Massive	Po	2.5	0.012	0.49
M8	079	243.50	Massive	Pn	2.4	0.015	0.62
M8	049	695.74	Massive	Cpy	2.8	0.005	0.18
M8	049	695.74	Massive	Py	3.2	0.021	0.66
M8	049	695.74	Massive	Po	1.5	0.010	0.68
M8	044	636.93	Massive	Cpy	3.1	0.011	0.35
M8	044	636.93	Massive	Po	3.0	0.015	0.50
M8	044	762.54	Massive	Cpy	3.3	0.016	0.48
M8	044	762.54	Massive	Po	3.6	0.014	0.39
M8	049	767.78	Massive	Cpy	3.0	0.013	0.43
M8	049	767.78	Massive	Py	3.0	0.043	1.42
M8	049	767.78	Massive	Po	3.0	0.007	0.23
M8	049	757.36	Massive	Cpy	2.8	0.013	0.46

Hole	Depth	Type	Mineral	$\delta^{34}\text{S}$	SD	RSD (%)	
M8	049	820.00	Massive	Cpy	1.5	0.041	2.73
M8	049	820.00	Massive	Po	1.1	0.015	1.42
M8	049	681.60	Massive	Py	1.1	0.013	1.16
M8	062	1070.00	Massive	Cpy	3.0	0.023	0.77
M8	049	792.45	Massive	Po	4.1	0.020	0.49
M8	049	773.57	Massive	Cpy	3.6	0.016	0.45
M8	044	739.5	Massive	Py	2.9	0.010	0.35
M8	044	739.5	Massive	Py	2.4	0.007	0.29
M8	076	278.5	NE Massive	Py	2.7	0.012	0.44
M8	044	744	Dissem	Cpy	2.8	0.066	2.36
M8	045	549.6	Massive	Cpy	3.2	0.016	0.50
M8	045	536.4	Dissem	Cpy	3.4	0.014	0.41
M8	045	843.3	Massive	Cpy	2.7	0.018	0.68
M8	045	688	Dissem in Srp vein	Py	-11.4	0.021	0.18
M8	045	527.1	Massive	Cpy	2.5	0.018	0.73
M8	045	692.2	Dissem in Srp vein	Cpy+Py	1.3	0.014	1.10
M8	045	543.15	Massive	Cpy	3.3	0.018	0.55
M8	045	653.6	Dissem	Cpy	3.0	0.014	0.46
M8	045	705.2	Massive	Cpy	2.2	0.021	0.96
M8	044	780	Massive	Cpy	0.5	0.025	5.21
M8	044	590.9	Massive	Cpy	4.2	0.019	0.45
M8	044	725.6	Massive	Py	3.6	0.013	0.36
M8	044	662.8	Massive	Py	4.9	0.008	0.16
M8	044	778.3	Massive	Cpy	-0.3	0.007	2.44
M8	044	739.85	Massive	Cpy	4.1	0.016	0.39
M8	044	638.3	Massive	Cpy	3.2	0.023	0.72
M8	045	531.7	Massive	Cpy	2.2	0.008	0.36
M8	045	684	Dissem in Srp vein	Py	-4.1	0.012	0.29
M8	045	650.55	Massive	Py	2.9	0.013	0.45
M8	044	644.7	Massive	Cpy	0.5	0.006	1.20
M53	007	126.30	Sediments	Po	11.3	0.048	0.42
M63	001	162.00	Sediments	Po	-23.9	0.038	0.16
M53	008	148.20	Sediments	Po	19.4	0.066	0.34
M8	062	901.70	Sediments	Py	5.7	0.013	0.23
M8	075	680.30	Sediments	Py	3.5	0.010	0.29
M7	027	310.70	Sediments	Po	17.0	0.012	0.07
M53	009	253.50	Sediments	Po	16.4	0.024	0.15
M63	002	213.00	Sediments	Po	-13.4	0.028	0.21
M61	005	76	Sediments	Py	20.2	0.017	0.08
M61	003	103.5	Sediments	Cpy	14.4	0.024	0.17
M61	003	59.4	Sediments	Py	14.3	0.016	0.11
M34	002	253	Sediments	Py	-14.1	0.021	0.15
M8	122	729.15	Sediments	Py	-5.3	0.016	0.30
M8	121	608.9	Sediments	Po	-6.2	0.012	0.19
M63	001	216.5	Sediments	Py	-19.0	0.013	0.07
M63	001	202.2	Sediments	Py	-19.3	0.016	0.08
M66	011	172.9	Sediments	Po	10.4	0.082	0.79
M53	007	82.8	Regional	Po	7.6	0.017	0.22
M53	007	83	Regional	Po	7.2	0.013	0.18
M53	007	110.7	Regional	Po	8.1	0.008	0.10

Table 4.15 – S isotope data from the Sakatti deposit (M8) and surrounding sediments. Three analyses from the intrusive M53 regional project are also shown. Data are and Standard Deviations (SD) are in permille deviations from the Vienna Canyon Diablo Troilite (VCDT).

Overview

The Sakatti deposit shows very consistent $\delta^{34}\text{S}$ data drawn from across the deposit between 0–4.5 ‰ (Table 4.15). This is in contrast the $\delta^{34}\text{S}$ data from regional sediments that exhibit a wide variety of $\delta^{34}\text{S}$ values but none within the Sakatti range, which is close to the mantle range (Fig. 4.24). The traditional mantle range is 0 ± 2 ‰ (Ohmoto and Rye, 1979; Thode et al., 1961), however it is now thought that the mantle is slightly more heterogeneous due to ranges in mantle xenoliths of 1.3 ± 3.8 ‰ (Chaussidon et al., 1989; Seal, 2006).

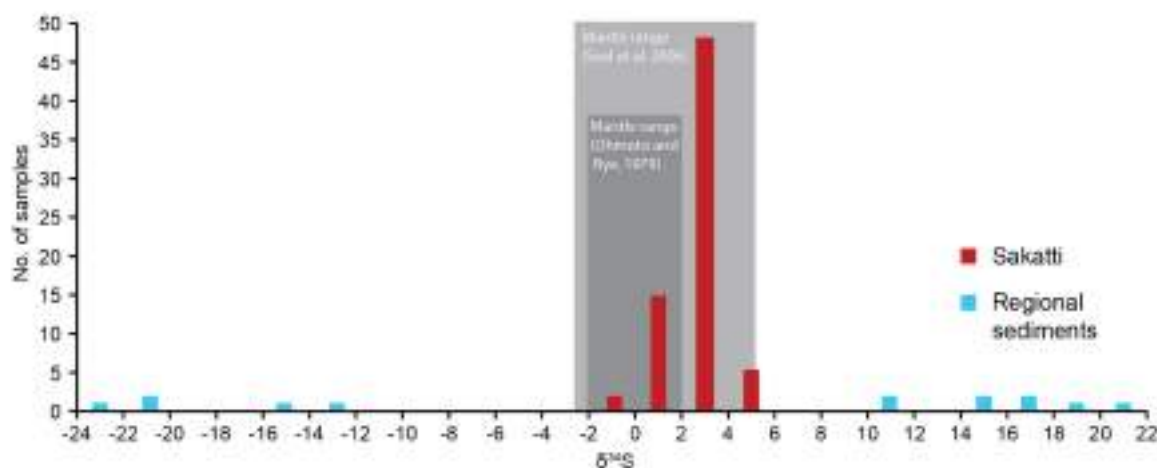


Figure 4.24 – Histogram showing S isotope data from sulphide minerals in the Sakatti deposit and from sediments from surrounding projects.

Category	n	Mean	SD
All Sakatti mineralisation	70	2.6	1.2
<i>Massive mineralisation</i>	53	2.5	1.2
<i>Disseminated mineralisation</i>	15	2.7	1.3
<i>Chalcopyrite</i>	37	2.8	1.0
<i>Pyrrhotite</i>	8	2.5	1.2
<i>Pentlandite</i>	1	2.4	
<i>Pyrite</i>	19	2.3	1.4
<i>Low tenor mineralisation (false ore)</i>	11	1.92	1.5
Sakatti Anhydrite	4	13.1	1.4
Positive regional sediments	8	15.4	3.5
Negative regional sediments	5	-18.0	4.3

Table 4.16 – Table of S isotope analyses split into categories and compared with regional sediments and anhydrite.

Regional

Sulphide bearing footwall sediments have not been encountered at the Sakatti deposit; however they are present in close proximity (Fig. 2.40). In order to compare the S isotope composition of the Matarakoski sediments with the Sakatti deposit, samples were taken from regional prospects within 10 km of the Sakatti deposits.

Sedimentary sulphide is present in each of these regional prospects as interlayered pyrrhotite within the graphitic black schists of the Matarakoski formation. The sulphide chosen for analysis in each case was aligned with the predominant lineation of the metasediment as opposed to cross-cutting veins. This was to ensure the sulphide was most likely to have been sedimentary in origin.

Of the six different prospects analysed there is a stark difference in the S isotope values. The range is over 40‰, and includes some of the lowest $\delta^{34}\text{S}$ recorded in Lower Proterozoic

sediments (Parnell et al., 2010). Two prospects (Mos 34 and Mos 63) had negative S isotope values while the rest (Mos 7, Mos 53, Mos 61 and Mos 66) all had positive S isotope values (Fig. 4.25). None of the sedimentary sulphide was similar to mantle values of $1.3 \pm 3.8 \text{ ‰}$ (Chaussidon et al., 1989; Seal, 2006).

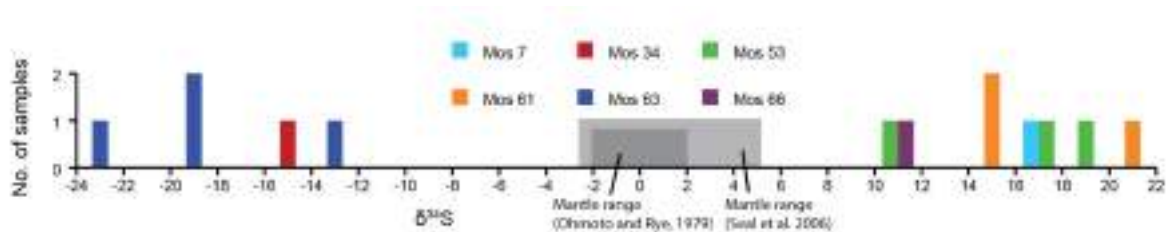


Figure 4.25 – Histogram showing S isotope data showing sediments regional projects surrounding the Sakatti deposit. Two of the six projects have negative $\delta^{34}\text{S}$ values while the remaining four have positive values.

Mos 53 is a Anglo-held prospect located 5 km from the Sakatti deposit. It consists of a pyroxenite sill up to 70 m thick with a graphitic sulphide-bearing meta-sediment basal contact. This regional prospect was chosen as a contrast to Sakatti because there was clear textural evidence of assimilation of the sedimentary footwall.

Four samples were taken from hole 007, one in the footwall at 126.3 m downhole which was 7 m downhole below the basal contact of the intrusion. Of the three within the intrusion, one was in close proximity to the footwall (110.7 m downhole) and two from the centre of the intrusion, one being interstitial sulphide and one from a vein (83.0 m and 82.8 m respectively downhole).

In contrast to the Sakatti deposits all three showed clear sedimentary contamination (Fig. 4.26).

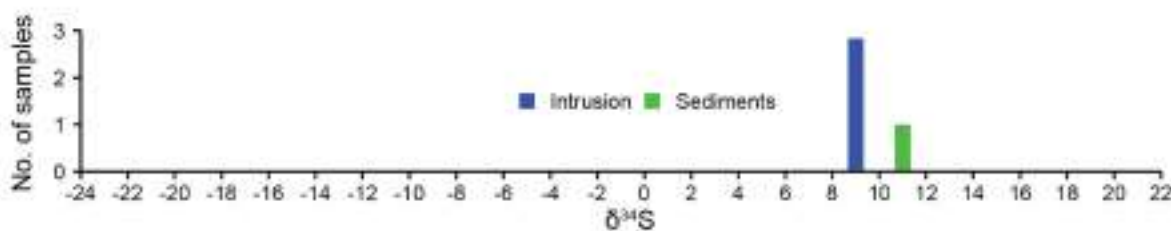


Figure 4.26 – Histogram showing S isotope data from the M53 regional project. Three samples are from the intrusion with clear textural assimilation of the sulphide-bearing graphitic meta-sediment footwall.

Sediments at Sakatti

No sulphide-bearing sediments have been intersected in the footwall of the Sakatti deposit. Some carbonate meta-sediments occur underneath the bounding fault that occurs below the footwall lithology. There are two intersections of sulphide bearing graphitic sediments in the hanging wall of the Sakatti deposit at M8 121 608.9 m and at M8 122 729.15. These are smaller than 1 m intersects and the sulphide present is vein pyrrhotite and pyrite as opposed to the

interlaminated pyrrhotite that was selected in the regional sediments. These gave negative $\delta^{34}\text{S}$ values of -6.2 and -5.3 respectively. Because they are in the hanging wall of the deposit and not texturally related to it, the timing of these sediments in relation to the deposit is questionable. Nonetheless they do suggest that some sediments in close proximity to the Sakatti deposit might be negative as opposed to positive.

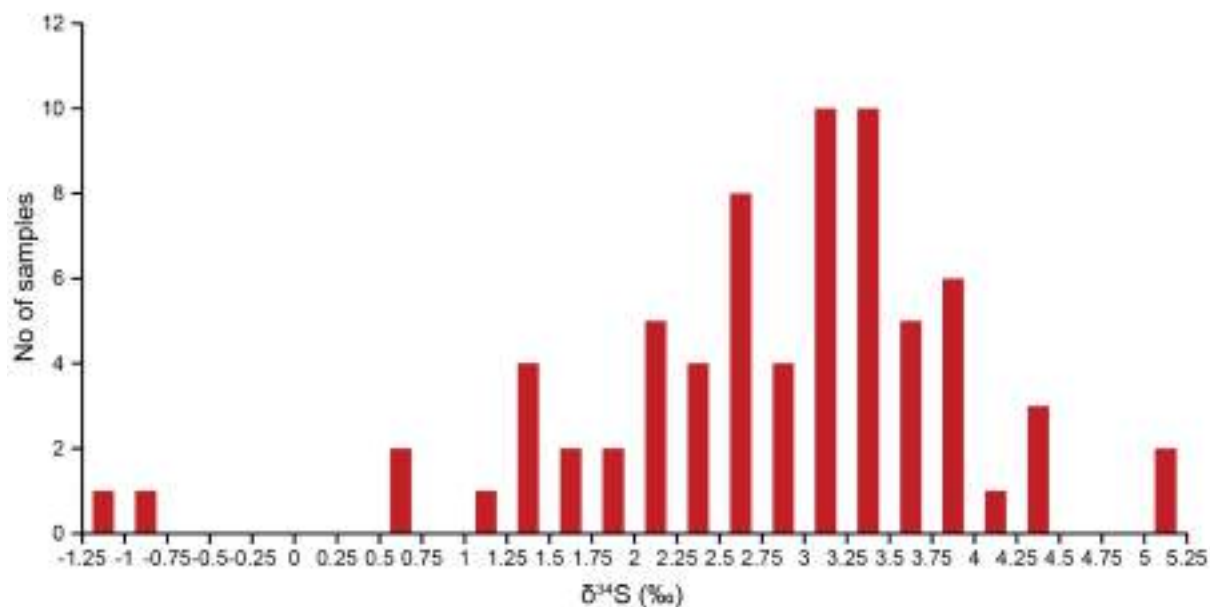


Figure 4.27 – Histogram showing S isotope data showing the analyses of sulphide minerals from the Sakatti deposit.

Sakatti – low $\delta^{34}\text{S}$

Two samples at the Sakatti deposit provided anomalously low $\delta^{34}\text{S}$ and have been excluded from the plots (Fig. 4.24 and 4.27) but are included in the S/Se plots (Fig. 4.32). They are samples M8045 668 m and M8045 684 m which had $\delta^{34}\text{S}$ values of -11.4 and -4.1 respectively and both come from a heavily altered part of the core. The sulphide itself is present as pyrrhotite needles within bottle-green relatively transparent serpentine veins. It is clearly not magmatic in origin and is therefore excluded. However the presence of isotopically negative sulphide within the Sakatti deposit, albeit related to alteration, is again noted.

Sakatti – massive vs. disseminated

There is no isotopic distinction between massive and disseminated ore at the Sakatti deposit with samples from both showing the same relatively consistent range of values. There is a sampling bias in favour of massive sulphide due to the ease of producing a sulphide separate and also the fact there are more readily identifiable distinct types of massive mineralisation, however there is still sufficient data coverage of disseminated to be confident that it has the same values as the massive ore (Fig. 4.28).

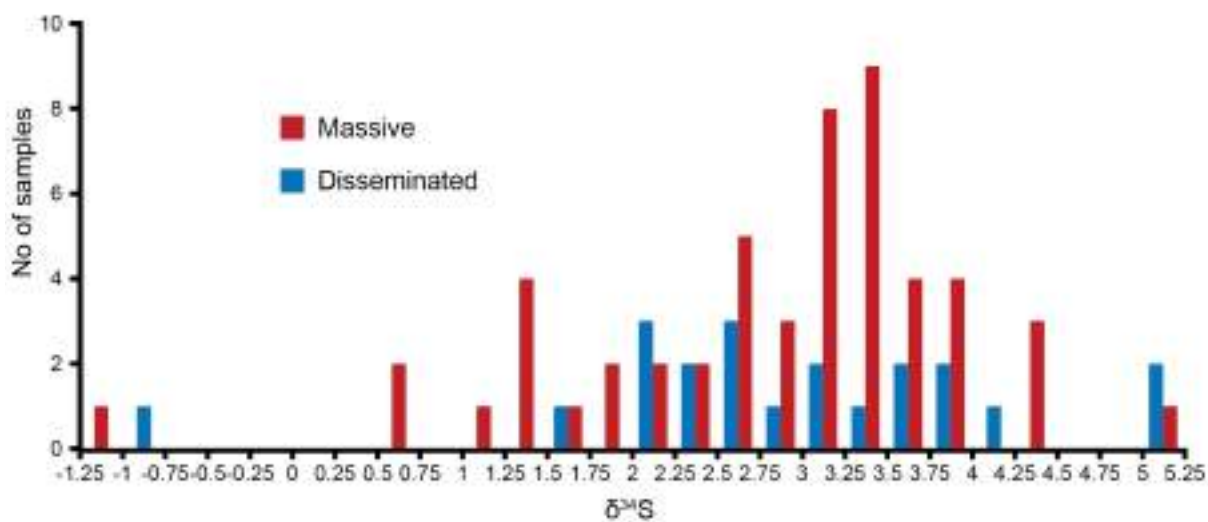


Figure 4.28 – Histogram showing S isotope data from the Sakatti deposit separated into massive and disseminated sulphide.

Sakatti – mineral types

Presenting the $\delta^{34}\text{S}$ data in terms of minerals does not show any particular trend or preference of $\delta^{34}\text{S}$ values to certain minerals. Comparing analyses of separate minerals within one sample can be used, if those minerals are in equilibrium, to ascertain an approximate temperature of formation (Beaudoin and Therrien, 2009). However, the individual samples in which several separate minerals were analysed do not show a consistent pattern in terms of which minerals are isotopically lighter than others, let alone a consistent numerical separation between the minerals (Fig. 4.29). It seems clear that these minerals are not at equilibrium with one another and therefore cannot be used to determine the temperature of formation of the minerals.

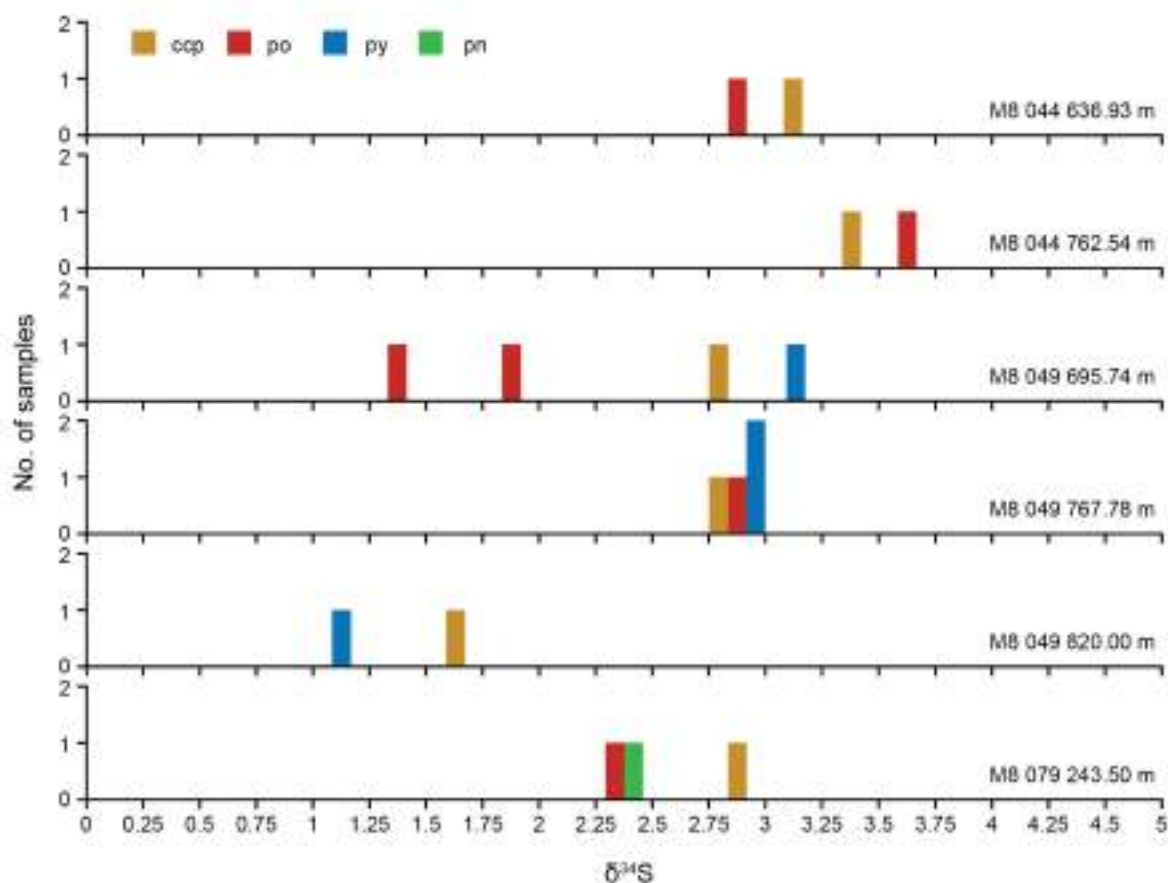


Figure 4.29 – A series of histograms showing $\delta^{34}\text{S}$ values for separate minerals within the same sample at the Sakatti deposit. Note the lack of consistency in the relationships between the separate minerals.

Concession	Hole	Depth	Po-Ccp	Py-Ccp	Py-Po
M8	79	243.5	0.4	-	-
M8	49	695.74	1.2	-0.4	-0.7
M8	44	636.93	0.1	-	-
M8	44	762.54	-0.3	-	-
M8	49	767.78	0	0	0
M8	49	820.00	0.4	-	-

Table 4.17 – The difference in $\delta^{34}\text{S}$ values between pairs of minerals within the same samples. These can be used to estimate the temperature of formation of the deposit, however in this case they are not in equilibrium.

If the sulphide minerals formed together and are at equilibrium then two sets of differences between sulphide minerals can be used to approximate the temperature of formation (Beaudoin and Therrien, 2009). This was attempted for the separated samples at the Sakatti deposit, however it became clear that in the two samples with successful chalcopyrite, pyrite and pyrrhotite separates that in the first (M8049 695.74), the pyrite values were greater than the other minerals, contrary to the expected fractionation and in the second (M8049 767.78), the sample shared the same $\delta^{34}\text{S}$ of 3.0 ‰ (Table 4.17) meaning there was no fractionation (Beaudoin and Therrien, 2009; Kajiwarra and Krouse, 1971; Li and Liu, 2006). It is clear that the minerals are not at equilibrium with one another in these samples and the requirement of pyrite being used is particularly dubious given its uncertain origin (4.4.5).

Sakatti – False ore

'False ore' is a classification of barren sulphide mineralisation at the Kevitsa Ni-Cu-PGE deposit (Mutanen, 1997). Sulphur isotope analysis at Kevitsa showed that while the main ore had $\delta^{34}\text{S}$ values close to mantle values (mean +3.8 ‰, ± 0.2 ‰ range) the false ore had elevated values (mean +8.2 ‰, ± 0.5 ‰ range), and very low grades, due to dilution by sedimentary sulphide (Grinenko et al., 2003; Hanski et al., 1996; Mutanen, 1997). After initial S isotope analysis of the Sakatti deposit some sampling was deliberately targeted at very low Ni and Cu gradecores, which were nonetheless rich in S to determine if there was a similar occurrence at the Sakatti deposit.

This approach of using assay S values highlighted both low grade sulphide intersections, primarily pyrite, but also anhydrite. Frequently pyrite and anhydrite actually occurred together and so this situation is considered separately below.

With the exception of two slightly negative outliers the 'false ore' samples were in the same S isotopic range as the Sakatti 'normal ore' samples suggesting this is not a particularly useful tool as it may be at the Kevitsa deposit. It could be argued that there is a slight preference towards more negative values in the alleged 'false ore' samples (mean +1.92 ‰, SD 1.5 ‰, n=11) when compared with the 'normal ore' (mean +2.8 ‰, SD 0.9 ‰, n = 53) but it is not distinct and could not be stated confidently.

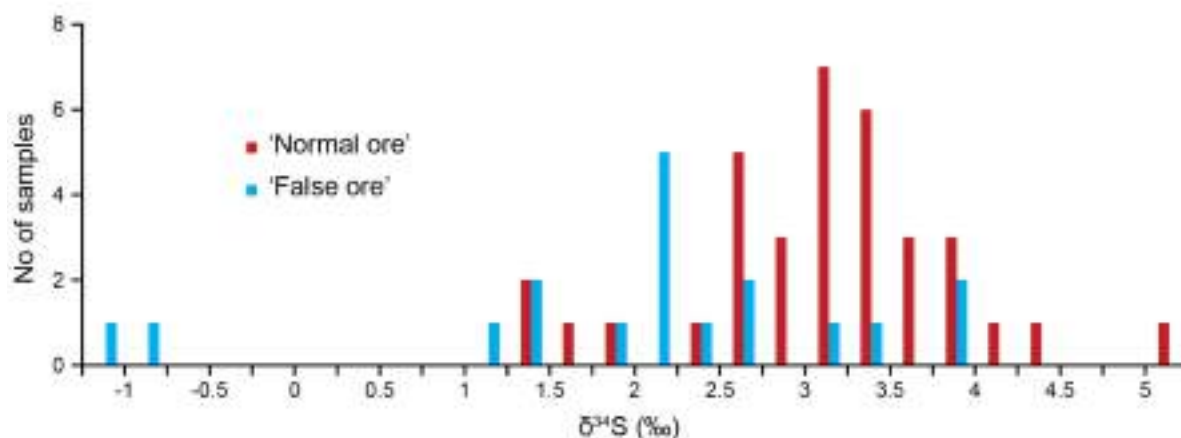


Figure 4.30 – Histogram showing $\delta^{34}\text{S}$ values for samples at the Sakatti deposit, separating those chosen from low tenor intersections as 'false ore'.

Sakatti – Anhydrite

Anhydrite is present as a minor phase in some of the petrological samples analysed. However, there are parts of the Sakatti deposit, particularly at depth where there are extensive intersections of anhydrite. The presence of this anhydrite, contained within the deposit, is interesting as a potential contaminant. As a possible part of the S story it was analysed for $\delta^{34}\text{S}$, and returned positive values of between +11 and +14.5 ‰. This is in contrast to pyrite that is found close textural association with anhydrite, which is within the usual Sakatti range. For example sample M8 051 855 m anhydrite is +13.6 ‰ while M8051 854.7 m is +2.6 ‰.

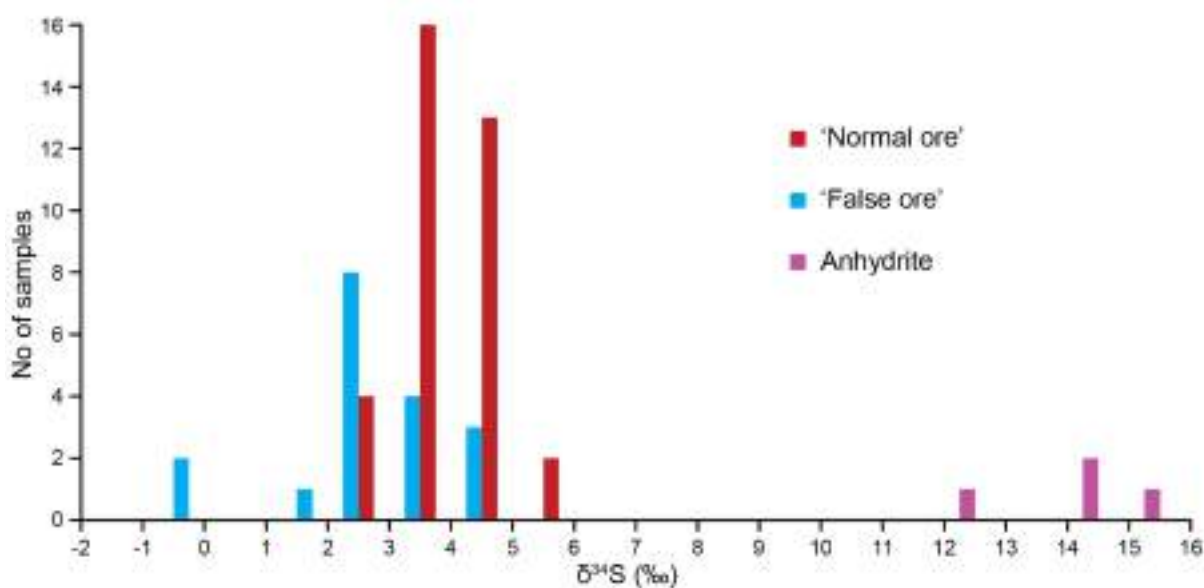


Figure 4.31 – Histogram showing $\delta^{34}\text{S}$ data from the Sakatti deposit in both sulphides and anhydrite. 'False ore' pyrite is shown separately as this is frequently in close proximity to the anhydrite.

Sakatti – S isotopes compared to S/Se values

The ratio of S/Se has been used to establish country rock presence in a similar way to S isotopes, given a well established range for mantle signature (Eg. Smith et al., 2016). There are extensive S and Se data at Sakatti from whole rock measurements and so this was used to inform S isotope sampling as a final attempt to target samples with S isotope signatures that might deviate from the established Sakatti range. Samples with a range of S/Se values, including extremes, were re-sampled for S isotope analysis. This was to increase the chances of finding samples that deviated from the established Sakatti range and to test whether this was an effective proxy for S isotopes.

The majority of samples containing high S values fall within the typical S/Se range of mantle derived S of 2850-4350 (Eckstrand and Hulbert, 1987; cited in Queffurus and Barnes, 2015). However there are samples that fall outside these ranges and these were targeted for sampling.

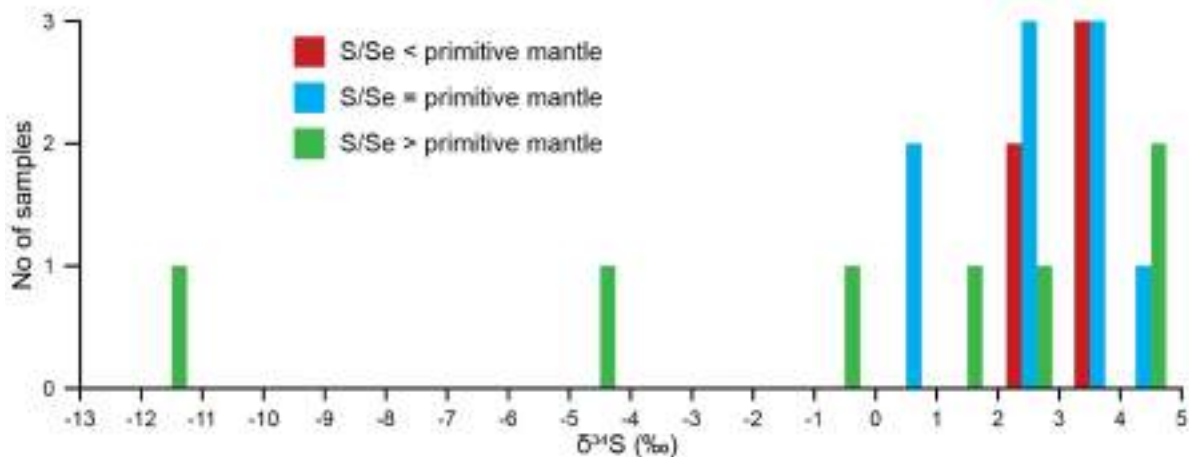


Figure 4.32 – Histogram showing $\delta^{34}\text{S}$ data from the Sakatti deposit, separated into categories based on S/Se ratio (see Fig. 4.16) and their relationship to primitive mantle ranges (Eckstrand and Hulbert, 1987). Two hydrothermal outliers are included, although they have been excluded from previous histograms.

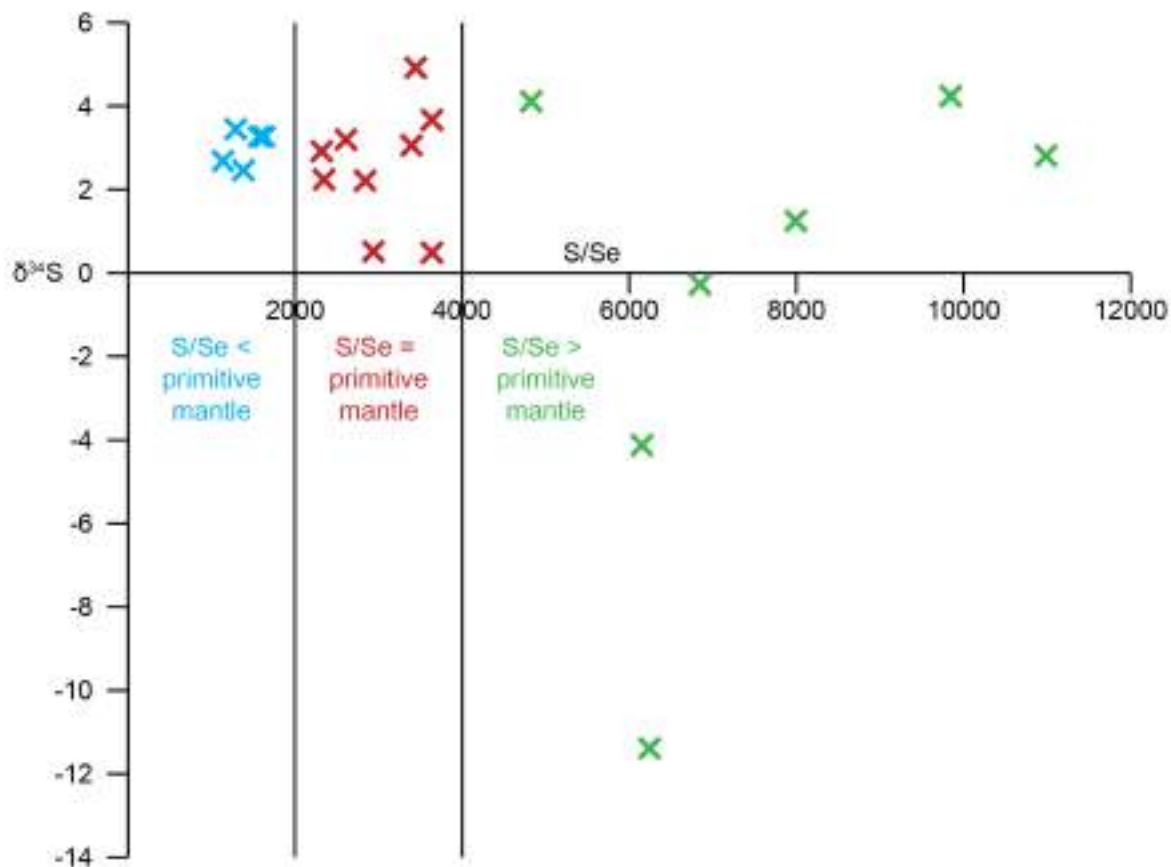


Figure 4.33 – S/Se values against $\delta^{34}\text{S}$, indicating that the hydrothermal outliers do not show a meaningful correlation between S/Se and $\delta^{34}\text{S}$.

There is a small degree of correlation between samples that contain S/Se greater than primitive mantle and negative S isotope samples (Fig. 4.32) but these are strongly affected by the two samples of clear hydrothermal origin (Fig. 4.33). If these samples are removed then there is no correlation between S/Se and $\delta^{34}\text{S}$. S/Se ratio will be affected by hydrothermal and alteration processes (Queffurus and Barnes, 2015; Yamamoto, 1976) and so these data are not providing a useful insight into the magmatic processes that formed the deposit.

Comparison with Kevitsa

The Sakatti data is similar to $\delta^{34}\text{S}$ values for the main ore at Kevitsa (Fig. 4.34) although negative $\delta^{34}\text{S}$ values in the Matarakoski schists have not been recorded there (Grinenko et al., 2003). This study has greatly increased the range of $\delta^{34}\text{S}$ data in the Matarakoski sediments.

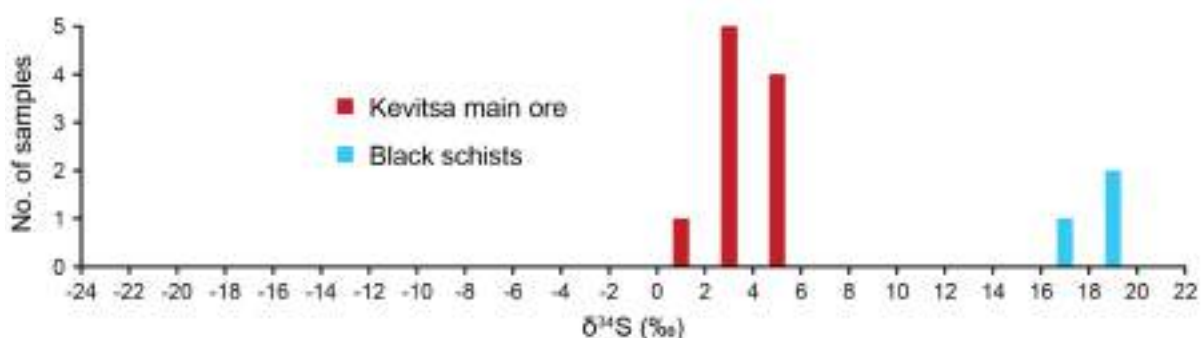


Figure 4.34 – $\delta^{34}\text{S}$ data from the Kevitsa deposit (Grinenko et al., 2003)

4.3.4.2 Ni isotope analysis

Overview

In part because Ni isotope analysis is relatively novel and has not been applied to magmatic Ni deposits before, with two exceptions, the results can only be considered by also considering the previous work which is presented below.

Sudbury

In part because Ni isotope analysis is relatively novel and has not been applied to magmatic Ni deposits before, with two exceptions, the results can only be considered by also considering other studies (Fig. 4.35). This work was undertaken by Louise Gall, Oxford University, and is produced in this thesis with permission.

Magmatic sulphide samples held at the Natural History Museum have been analysed from the Creighton deposit, Sudbury, Canada (Gall, 2011). These indicate that Ni isotopes are fractionated by the crystallisation of MSS and ISS as there is a distinct difference between the heavy pyrrhotite-pentlandite samples, likely to have derived from MSS and the lighter chalcopyrite-rich samples, likely to have derived from ISS (Fig. 4.35).

The unmineralised norite samples from the Creighton deposit have a slight positive anomaly (0.2 ‰), consistent with silicate hosted Ni (Fig. 4.35), while the chalcopyrite-rich samples exhibit a lighter signature (-0.16 ‰ to -0.35 ‰). The disseminated samples between these two are consistent with dilution of the chalcopyrite-rich sulphide by silicate. The pyrrhotite-pentlandite sample has is heavier (0.61 ‰ to 0.76 ‰).

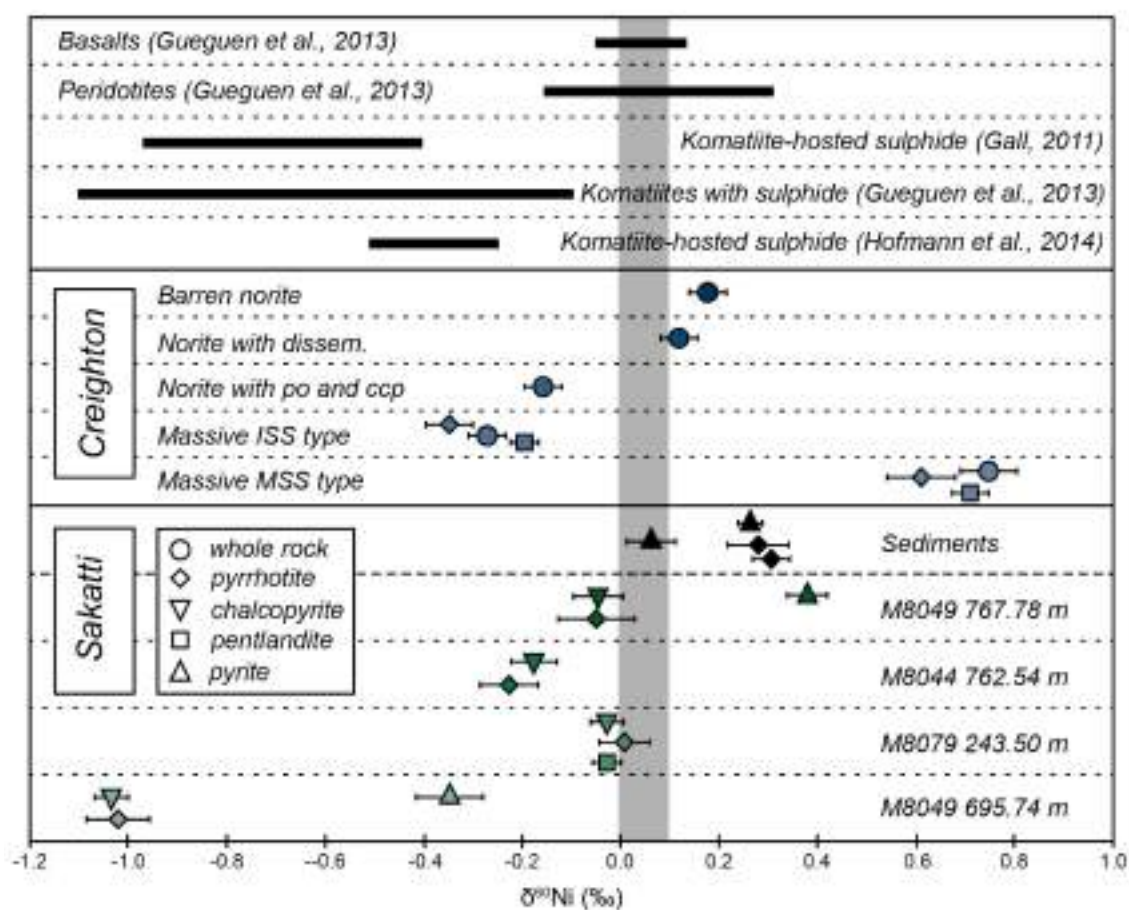


Figure 4.35 – Compilation of Ni isotope data. Grey bar indicates bulk silicate earth values of 0.05 ± 0.05 ‰ (Gueguen et al., 2013). Komatiite-hosted sulphide from Mt Keith, Kambalda and Scotia WA are shown (Gall, 2011). Komatiites with and without sulphide were analysed by Gueguen et al. (2013). Komatiite hosted sulphide from multiple deposits in Zimbabwe is also shown (Hofmann et al., 2014). Ni isotope values for Creighton mine, Sudbury – showing MSS/ISS fractionation and dilution of ISS in disseminated samples – and Sakatti – showing only ISS signatures and positive excursions for pyrite in individual samples (Gall, 2011).

Sakatti

Sedimentary sulphide was analysed both from surrounding concessions to the Sakatti deposit and also from two small hanging wall occurrences of graphitic schist with pyrite veining (Table 4.19). In both cases the $\delta^{60}\text{Ni}$ values are positive (0.06 ‰ to 0.31 ‰). These are typical silicate values, suggesting the sulphide has derived purely from sediments (Gall, 2011). There is variation within the Sakatti samples, but they are generally around zero or negative. Pyrite is the only mineral that exhibits a significantly different value from the surrounding minerals and this is considered separately below. Three of the Sakatti samples give $\delta^{60}\text{Ni}$ values between 0 ‰ and -0.23 ‰. The fourth sample gives $\delta^{60}\text{Ni}$ values of -1.01 ‰ and -1.03 ‰ for pyrrhotite and chalcopyrite respectively.

Concession	Hole	Depth	Style	Mineral
M8	62	901.70	Sediments	Py
M8	75	680.30	Sediments	Py
M53	9	253.50	Sediments	Po
M63	1	162.00	Sediments	Po
M8	49	695.74	Massive	Ccp
M8	49	695.74	Massive	Py
M8	49	695.74	Massive	Po
M8	49	767.78	Massive	Ccp
M8	49	767.78	Massive	Py
M8	49	767.78	Massive	Po
M8	44	762.54	Massive	Ccp
M8	44	762.54	Massive	Po
M8	79	243.50	Massive	Ccp
M8	79	243.50	Massive	Po
M8	79	243.50	Massive	Pn

Table 4.18 – Samples selected for Ni isotope analysis

Pyrite

In the two samples where pyrite is analysed alongside the other phases it can be seen that the pyrite is isotopically heavy compared to other minerals. The petrographic interpretation of this pyrite presented above suggests that the pyrite may be forming as an alteration product of more reduced primary sulphides. In contrast, the minor and trace element (particularly IPGE content) are potentially at odds with this interpretation revealing a distinct fluid non-mobile chemical signature in the pyrite. In the two samples that contain pyrite, the pyrite is 0.4 ‰ and 0.7 ‰ heavier than the other minerals. This significant fractionation suggests that the process responsible for forming the pyrite fractionates Ni isotopes, however it could equally be related to mass balance as late-forming pyrite may inherit the Ni signature of the remaining melt. There is limited understanding of the processes that do fractionate Ni isotopes.

4.4 Discussion

4.4.1 Overview

This discussion is limited to interpreting the sulphide results. Where the interpretation of aspects of the mineralisation requires the use of both sulphide and silicate data, for example the structural interpretation of the mineralisation, then these are included in the separate discussion chapter (6). There are four principal questions that will be addressed regarding the mineralisation.

1. Is there a significant hydrothermal component to the formation of the deposit?
2. What is the cause of the sulphide formation?
3. Why is the deposit Cu-rich?
4. What is the nature of the pyrite mineralisation?

4.4.2 Effect of alteration

The sulphide mineralisation at Sakatti is not particularly altered despite its antiquity. Magmatic textures dominate throughout and the presence of pentlandite flames within pyrrhotite suggests that the sulphide minerals, despite their antiquity, have not been metamorphosed to the extent of reverting to MSS. These flames would be absent in metamorphosed samples due to the slower cooling rates associated with metamorphism resulting in annealing of the sulphides (Collins et al., 2012).

There is no evidence that hydrothermal alteration is an important ore-forming process at the Sakatti deposit rather that the deposit is magmatic in origin and there is only minor remobilisation and chemical changes due to hydrothermal alteration.

4.4.3 Formation of sulphides

The silicate body at Sakatti is a primitive ultramafic cumulate with some indications in trace element chemistry of crustal contamination (3.7.2), which may have been the possible cause of sulphide saturation. However, as highlighted in 3.7.9, the current silicate host is not parental to the sulphides, and therefore the recognised crustal contamination signatures may be unrelated to the event triggering sulphide saturation. Nevertheless, if the interpretation that the parental melt was an earlier stage of magmatism in the same conduit is accepted, then we could expect similar properties in the parental melt itself.

The sulphide does not indicate contamination by S with significantly elevated or depleted $\delta^{34}\text{S}$ values (and elevated S/Se ratios) indicating crustal S. Clearly a mechanism is required to trigger

sulphide saturation, and assimilation of S with mantle or near-mantle $\delta^{34}\text{S}$ and S/Se signatures cannot be ruled out. Relatively high Ag and Te contents along with relatively depleted As content within the deposit (5.3.6) might indicate assimilation of a S source with these characteristics.

4.4.3.1 Sedimentary origin

The S isotope data show that Sakatti falls within the range of mantle isotope data of 1.3 ± 3.8 ‰ (Chaussidon et al., 1989; Seal, 2006).

Mass dependent S isotope fractionation ($\delta^{34}\text{S}$) was not significant in the Archaean, only becoming an important process in the Palaeoproterozoic (Seal, 2006). The age of the Sakatti deposit is, at the time of writing, confidential information. However assuming that it is similar to the Kevitsa deposit, which is 2.05 Ga (Mutanen and Huhma, 2001), then one would expect the S isotopes to be fractionated in sediments that formed shortly before the formation of the deposit, such as the Matarakoski metasediments (Grinenko et al., 2003). However there remains the possibility of contamination by older sediments that were deposited prior to the start of mass dependent S isotope fractionation.

It is reasonably clear that the Sakatti deposit is not the result of piecemeal in-situ assimilation of the surrounding Matarakoski metasediments, as one would expect the deposit sulphides to exhibit $\delta^{34}\text{S}$ that deviates from mantle values. There is an argument that because both extremely positive and negative $\delta^{34}\text{S}$ values have been shown to exist in the Matarakoski metasediments that the Sakatti sulphides could have formed from the assimilation of bulk sediment exhibiting a mean value close to zero.

The consistency of the S isotope values at Sakatti are used as a counter argument to this proposal. If there was in-situ piecemeal assimilation of sedimentary sulphides with a wide range of $\delta^{34}\text{S}$ one would expect to see that reflected in variability in the Sakatti deposit. The samples for S isotope analysis were deliberately selected from a complete geographical spread across the deposit and still remain remarkably homogenous. This homogeneity suggests that the cause of sulphide saturation at the Sakatti deposit has not affected the $\delta^{34}\text{S}$ values, and if it has that there has been thorough and complete mixing of the sulphide, even that which ultimately became disseminated.

The S isotope data indicate that the Matarakoski schists were not involved as a contaminant for the Sakatti deposit, however this does not rule out the involvement of an earlier unknown S-bearing contaminant. Older sediments that the Matarakoski schists could potentially have mantle-like signatures as the $\delta^{34}\text{S}$ values only began to fractionate in the Palaeoproterozoic

(Queffurus and Barnes, 2015). There are no known formations that could fit this role in the Central Lapland Greenstone Belt (Hanski and Huhma, 2005) but this possibility cannot be ruled out.

4.4.3.2 Anhydrite

The occurrence of anhydrite within the Sakatti deposit is enigmatic. It could be viewed two ways. The first is that it is originally sedimentary anhydrite that has been remobilised by the introduction of very hot magma and also possible fluid movements. The second is that it is hydrothermal in origin and has been emplaced into the Sakatti deposit. In this case it could have originated from alteration and oxidation of sulphide in the deposit or from a completely unknown source.

The S isotope data provides the most insight. The anhydrite has elevated S isotope values, while the pyrite that is intergrown with it has the usual Sakatti values. If the sedimentary source proposed were true then one would expect the elevated 'sedimentary' signature of the anhydrite to be reflected in the surrounding sulphide of the Sakatti deposit. It could also be expected that there would be considerable variation in $\delta^{34}\text{S}$ within the deposit depending on the degree of assimilation of the anhydrite. Anhydrite has been shown to act as a crustal S contaminant in several deposits, most notably at the Noril'sk-Talnakh camp, Siberia (Li et al., 2009; Naldrett et al., 1992), however the S isotope data suggest that this is not the case at the Sakatti deposit, leading the assumption that the second proposition is correct.

4.4.3.3 Non-sedimentary

A non-sedimentary input of external S cannot be ruled out at the Sakatti deposit using current evidence. Contamination by potential S source in the Archaean basement is possible, although there is no reason to suppose that large S sources exist within the basement. There is extensive volcanism in the area, including the aphanitic footwall, and it is possible that the Sakatti intrusion has encountered pre-existing sulphide deposits within these.

An input of silica from the Archaean basement is considerably more likely than S, and as increased silica decreases the solubility of S. This is a viable mechanism for S saturation, but would not affect the chemistry of the sulphides produced, consequently this scenario has to be considered when evaluating the silicate host rocks (3.7.2).

4.4.4 Evidence in favour of an evolved sulphide melt

One of the principal questions about the Sakatti deposit that this study is intended to answer is why the Sakatti deposit is so Cu-rich relative to Ni. It is suggested that this is due to loss of Ni as

an early crystallising cumulate leaving the currently explored Sakatti deposit as an evolved Cu-rich residual melt. The evidence for this is discussed below.

4.4.4.1 Ni/Cu ratio

It is important to distinguish the massive and the disseminated mineralisation. The massive mineralisation, being interconnected, is free to move and fractionate while it is forming and exhibits a classic Ni-Cu partitioning based on the formation of MSS cumulates. This is shown well at Sakatti, where the Ni/Cu ratio decreases up dip and particularly steeply when the massive sulphide extends into the aphanitic footwall and hanging wall. The occurrence of higher Pt and Pd grades associated with the most fractionated Cu-rich sulphide is confirmation of this.

The Ni/Cu distribution and also overall Cu-rich nature of the disseminated mineralisation is harder to explain as it has been observed to be not interconnected and appears spatially unrelated to the massive mineralisation. Texturally the disseminated sulphide does not appear to result from percolations of the already fractionated massive sulphide. In spite of these appearances the suggestion that the fractionated disseminated sulphide could derive from the massive sulphide is considered below.

The behaviour of sulphide liquid in olivine cumulate has been examined generally considering the model of compaction segregation, where a dispersed sulphide is driven out of a cumulate pile by compaction to form massive sulphide (Grguric et al., 2006). Experimental studies indicate that sulphide liquid is unable to migrate through semi-solid silicate rocks, however it can migrate below the solidus temperature of the silicate melt (Rose and Brenan, 2001). This means that permeation is only possible through open fractures, free from silicate intercumulus melt but unlikely in an unfractured cumulate pile with intercumulus minerals (Barnes et al., 2008; Godel et al., 2013; Rose and Brenan, 2001). These models suggest that the reverse consideration, where sulphide melt percolates into a cumulate pile from massive sulphide, is not just unlikely but impossible, therefore the possibility that the fractionated disseminated sulphide derives from the massive sulphide can be disregarded.

The interpretation of the Ni/Cu distribution in the disseminated mineralisation is that it is magmatic remobilisation of an already fractionated sulphide related to earlier magmatism, which would be expected in a conduit system. According to this, the disseminated sulphide was entrained by a later melt and deposited along with the cumulate olivines also being transported by that melt.

4.4.4.2 PGE ratio

The Sakatti deposit is depleted in IPGE elements relative to PPGE elements and this correlates well with Ni/Cu ratio (Fig. 4.21). This depletion in IPGE elements is strong evidence in favour of the loss of an earlier evolved sulphide melt, as IPGE elements have been shown to strongly partition into early forming sulphide cumulates (Holwell and McDonald, 2010, and references therein).

4.4.4.3 Magnetite trace elements

There are few studies assessing the trace element content of sulphide derived magnetite in Ni-Cu-PGE deposits (Boutroy et al., 2014; Dare et al., 2014a). Magnetite concentrates the lithophile elements that are present within the sulphide liquid and so provides a good potential indicator of sulphide melt evolution when comparing within the same deposit. Care must be taken when comparing between deposits as the initial lithophile concentrations in the sulphide melt will be heavily dependent on the source silicate magma and the degree of equilibration between them.

The data would be most useful when compared with itself across the deposit. Unfortunately the limited range of sampling in this study has meant that the magnetite analysed does not come from a broad spatial range at the Sakatti deposit.

Two comparisons are presented, the McCreedy East Cu-rich magmatic Ni deposit in the Sudbury complex, Canada (Dare et al., 2014a) and the Talnakh deposit in the Noril'sk-Talnakh Ni-Cu-PGE camp, Siberia (Boutroy et al., 2014). The Mg content varies between these deposits and Sakatti and this is most likely a result of differing Mg content in the host silicate from which the sulphide melt is derived. It can be seen that the V/Cr ratio is <1 in both deposits for the primitive MSS cumulates whereas >1 for evolved MSS and ISS derived sulphide (Figure 1.1). The samples analysed at the Sakatti deposit all have a V/Cr ratio >1 potentially indicating that they are derived only from evolved MSS and ISS rather than primitive MSS cumulates. This is consistent with the other observations above.

Microprobe data of three samples within a single lens of massive sulphide revealed that a decrease in lithophile content in magnetite with decreasing depth of the lens suggesting the sulphide at the top is more evolved than that at the base. This approach could be used on a much broader sample set in order to assess the degree of evolution of the sulphide melt.

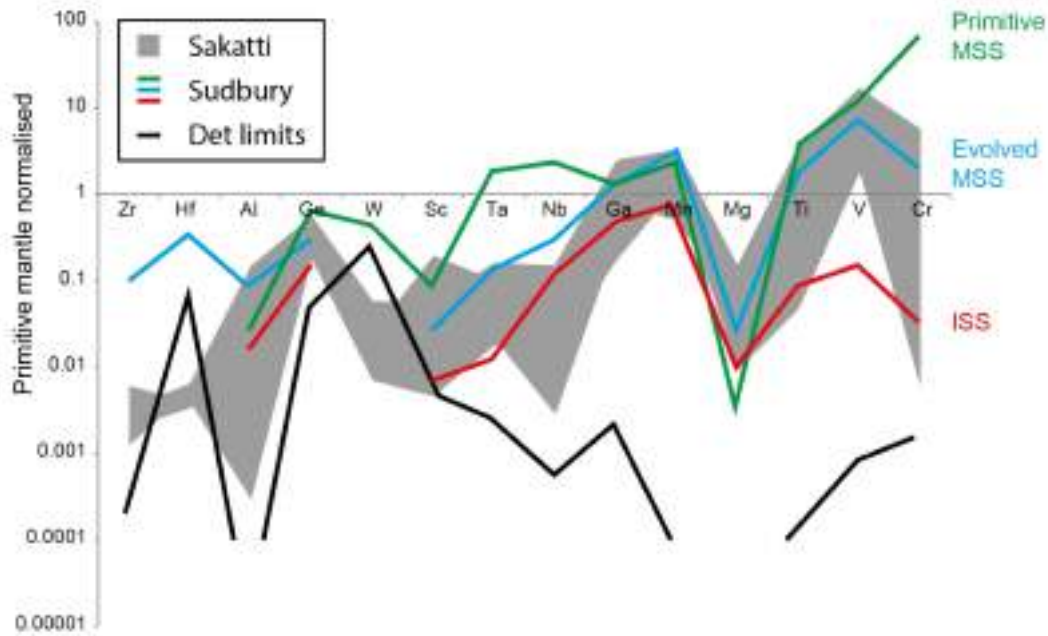


Figure 4.36 – Comparison between Sakatti magnetite trace elements and those at the Creighton and McCreedy East deposits combined, Sudbury, Canada (Boutroy et al., 2014; Dare et al., 2014a). The differing parental lithologies makes a direct comparison difficult but the relative behaviour of elements indicates that the Sakatti system may be an evolved sulphide.

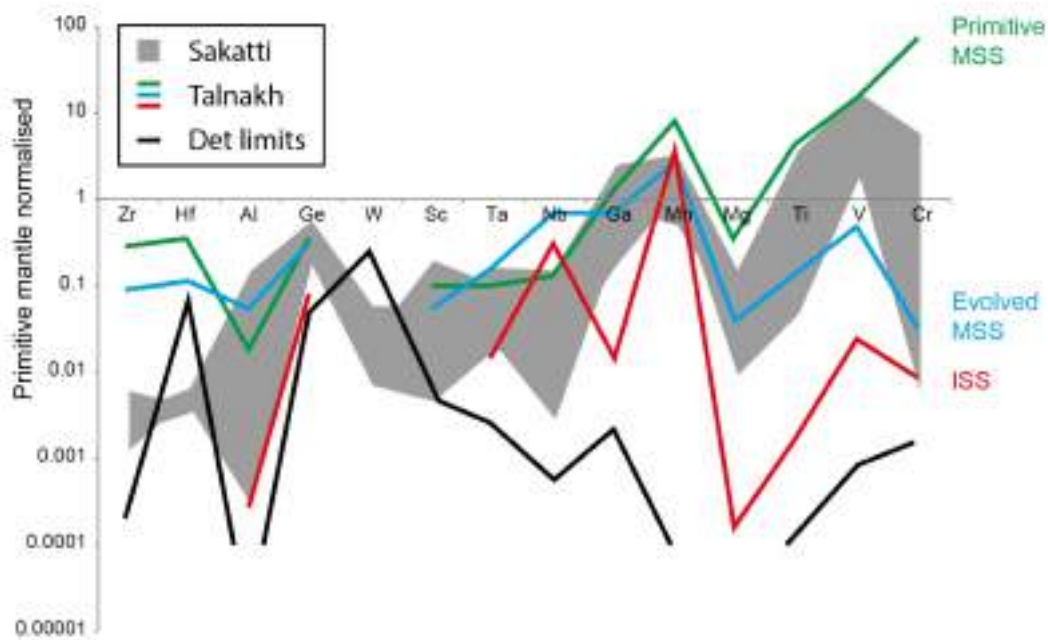


Figure 4.37 - Comparison between Sakatti magnetite trace elements and those at the the Talnakh deposit, Russias (Boutroy et al., 2014). The differing parental lithologies makes a direct comparison difficult but the relative behaviour of elements indicates that the Sakatti system may be an evolved sulphide, especially considering V/Cr ratio.

4.4.4.4 Ni isotopes

An interpretation of the Sudbury data is that this potentially indicates that mass-dependent fractionation is occurring during MSS formation and the heavier Ni isotopes are preferentially being included in the solid MSS and the lighter Ni isotopes are enriched in the residual sulphide liquid that ultimately crystallises to ISS. However the positive unmineralised silicate signature also means that there may be mass-dependent fractionation occurring at the sulphide-silicate separation, with lighter Ni isotopes being preferentially incorporated in the sulphide liquid.

Depending on the interpretation these findings are potentially not consistent with results from a recent study on Cu-Ni-PGE mineralisation at the Duluth Complex (Asp et al., 2015). This study found that unmineralised intrusive silicates had near zero values (-0.07 ‰) while olivine associated with sulphide mineralisation had heavier values (0.22 ‰ to -0.08 ‰) indicating a loss of light Ni to sulphide. Nickel isotope values became progressively lighter with increased sulphide content (0.15 ‰ to -0.97 ‰). The sulphide component was not analysed separately depending on mineralogy and the study concludes that Ni isotope fractionation occurred at the point of sulphide liquid formation (Asp et al., 2015) rather than during sulphide crystallisation as posited above.

The Ni isotopes analysis provides interesting, if not definitive, insight into the formation of pyrite at the Sakatti deposit. This is possible because the change is relative between different minerals within the same sample. It is more problematic to suggest that the Ni isotope data at Sakatti suggests that the sulphide derives from an evolved sulphide liquid that has lost MSS cumulates. This is problematic because it requires comparing the Ni isotope values with other deposits, of which there are few studies available (Asp et al., 2015; Gall, 2011; Gueguen et al., 2013; Hofmann et al., 2014).

There are many differences between both these deposits and Sakatti and the processes that may fractionate Ni isotopes are poorly understood. However, it can be observed that at the Creighton mine the only sample that derives from MSS cumulates has a significantly positive $\delta^{60}\text{Ni}$ while the samples that derive from residual sulphides have a significantly negative $\delta^{60}\text{Ni}$. At the Sakatti deposit all samples (excluding the pyrite) have a negative $\delta^{60}\text{Ni}$. The most negative $\delta^{60}\text{Ni}$ values from the Sakatti deposit of -1.03 ‰ are the most negative Ni isotope signatures that have been reported to date.

4.4.5 Pyrite

Analysis of pyrite at the Sakatti deposit has revealed different characteristics of the pyrite at each stage. Initially in the logging stage the pyrite was assumed to be an in-situ alteration

product of the normal massive sulphide. This was due to the sporadic appearance of the pyrite in amongst normal pyrrhotite-chalcopyrite massive sulphide and some clear textural observations showing that pyrite occurred in potentially fluid altered parts of massive sulphide. Petrographic studies supported this interpretation, with what looked like a progression from pyrrhotite-dominated massive sulphide to pyrite-dominated massive sulphide by the growth of 'clean' pyrite orbicules and the concentration of pentlandite and ultimately Ni-rich pyrite by local redistribution in the matrix between these orbicules. Both of these levels of analysis suggest simple gradual replacement of pyrrhotite-dominated mineralisation with pyrite-dominated mineralisation.

However, bulk sulphide chemistry suggested that wholly pyrite samples have elevated Co grades that exceed the background. EPMA analysis revealed that the 'clean' pyrite is had up to 2 wt% Co contained within it, which means that this cannot simply be an in situ replacement of pyrrhotite-pentlandite mineralogy. The difference in Co content either has to have been present originally or have been added by alteration fluids that may have also resulted in the pyrite formation.

The third complication arises from the LA-ICP-MS data which revealed the 'clean' pyrite to be IPGE/PPGE rich relative to the supposedly original mineralogy. While it is possible to add Co from alteration fluids this is unlikely to be the case with IPGE as they are not considered fluid mobile elements relative to PPGE (Dare et al., 2011; Hanley et al., 2005a; Hsu et al., 1991; Mountain and Wood, 1988; Wood, 1987).

The final piece of evidence is the Ni isotope data that, although relatively new and poorly understood, indicates heavier isotopic Ni values in the pyrite. Nickel isotope fractionation has been suggested to occur between MSS and ISS fractionation but not at low temperature alteration of minerals. This evidence is in agreement with the LA-ICP-MS data indicating that there is a primary magmatic difference between what is now pyrite-dominated mineralisation and simple pyrrhotite-dominated mineralisation at the Sakatti deposit.

It has been observed that pyrite can be enriched in IPGE in massive sulphide deposits; Creighton and McCreedy East at Sudbury, Canada (Dare et al., 2010; Dare et al., 2011), Aguablanca, Spain (Piña et al., 2013), Lac des Illes, Canada (Djon and Barnes, 2012).

Pyrite is not generally considered a mineral that can be produced by simple magmatic processes in Ni-Cu sulphide deposits. Massive sulphide melt cannot produce pyrite directly when it is in equilibrium with a silicate liquid as the S concentrations cannot become high enough due to the buffering effect of the silicate liquid (Naldrett, 2004). For that reason and others IPGE rich

pyrite observed in these deposits is often interpreted to be the result of alteration of pyrrhotite (Dare et al., 2011; Djon and Barnes, 2012; Piña et al., 2013). However, local exsolution of IPGE rich pyrite from MSS has been cited at the McCreedy East deposit (Dare et al., 2011).

In the first instance, the IPGE in pyrite is interpreted as being a remnant from the pyrrhotite and pentlandite that the pyrite replaced, however in the case of McCreedy East it is proposed that the accessory pyrite that forms directly from the MSS and is concentrating IPGE and As (Dare et al., 2011). This stands in contrast to the assertion that it is not possible to crystallise pyrite directly from MSS due to S levels, however it is argued that as it is only small localised nucleation sites this is not a problem.

These explanations are intended for the orbicular pyrite that contains high IPGE and it is clear that there is also simple alteration pyrite at the Sakatti deposit that is not expected to have high IPGE, although this has not been tested.

Pyrite has higher IPGE and Co concentrations than the pyrrhotite at Sakatti and equivalent Co levels to the pentlandite that it is potentially replacing. This is observed both in the LA-ICP-MS data but also in the bulk sulphide chemistry, where pyrite rich intersections have higher IPGE and Co than pyrrhotite-rich ones. Clearly this is problematic if the pyrite is merely an alteration product of the pyrrhotite-rich ore.

However the model of accessory pyrite forming directly from MSS is not satisfactory for the Sakatti because there are multi-metre sections of massive sulphide that are pyrite-dominated and these would have to have resulted from higher S levels than are possible in a massive sulphide liquid in equilibrium with a silicate liquid.

This leaves two possibilities for the pyrite at the Sakatti deposit.

- 1) The pyrite is an alteration product of pyrrhotite and pentlandite that were both initially enriched in IPGE. These pyrrhotite and pentlandite intersections would be the more primitive MSS cumulates than the surrounding sulphide and must have preferentially altered to pyrite when compared with the more evolved MSS and ISS parts of the deposit.
- 2) The pyrite formed directly from primitive MSS cumulates due unusual non-equilibrium behaviour of the early crystallising sulphide liquid at Sakatti.

It is clear from other central conclusions of this chapter that the Sakatti system is not behaving as a sulphide melt in equilibrium with a silicate melt. There is no known experimental work on

the behaviour of crystallising sulphide liquids that produce pyrite and are out of equilibrium with potential host silicates and for that reason it is not possible to speculate much further.

It is not suggested that the pyrite represents the lost primitive MSS cumulates that are suggested to result in the Cu-rich nature of the deposit, instead that they are more evolved MSS cumulates that formed during initial crystallisation of the sulphide following emplacement in the current silicate host.

4.5 Conclusions

The most important findings around the sulphide mineralisation at the Sakatti deposit come from a combination of textural and mineralogical observations, PGE analyses both in minerals and bulk sulphide, S isotope analysis, trace element analysis of magnetite and Ni isotopes.

- Textural and mineralogical observations suggest that the Sakatti deposit is wholly magmatic in origin and that hydrothermal processes do not have a significant role in the formation of the deposit.
- S isotope analysis suggests that the sulphide-bearing Matarakoski schists were not a source of external S that contributed to the formation of the Sakatti deposit.
- The Cu-rich nature of the Sakatti deposit is likely to be due to loss of initial Ni cumulates in an earlier phase of sulphide mineral formation. This is supported by the PGE signature, Ni isotope signature and magnetite trace elements.
- The Cu-rich nature of the disseminated mineralisation suggests that this fractionation preceded the formation of the Sakatti deposit and the sulphide has been magmatically remobilised from an earlier place of crystallisation.

These conclusions feed into a general discussion regarding the origin of the Sakatti deposit (6) combining observations from each of the three strands of investigation.

4.6 Implications for exploration and further work

4.6.1 Implications for exploration

It has often been suggested that as a strategy for exploration for magmatic Ni-Cu sulphides, geologists should look for the coincidence of mafic/ultramafic intrusions and a sulphide bearing crustal rock (Keays and Lightfoot, 2010; Naldrett, 2004). The Central Lapland Greenstone Belt fulfils these criteria, containing the sulphide-bearing Matarakoski schists are punctuated by ultramafic intrusions. However the work presented here shows that the Matarakoski schists are not causal to the Sakatti deposit. This is also similar in the case of the Kevitsa deposit (Grinenko

et al., 2003; Hanski et al., 1996). The $\delta^{34}\text{S}$ analysis on the Mos53 exploration project, which is not currently prospective, shows clear evidence for contamination by Matarakoski sediments, suggesting that in-situ assimilation of the Matarakoski schists might not be sufficient to produce sulphide deposits of economic tonnage. This should affect exploration within the CLGB because the extent of the Matarakoski schists is not relevant and all mafic/ultramafic intrusions have the potential to be prospective.

The interpretation that the Cu-rich nature of the Sakatti deposit results from early fractional crystallisation of sulphide melt also has important exploration implications. As discussed further in chapter 6, the conduit-like nature of the Sakatti intrusion suggests that this earlier phase of fractional crystallisation occurred down-plunge within the same conduit. Bulk sulphide PGE analysis and trace element analysis of magnetite provided the most useful insight into the degree of evolution of the sulphide melt. The application of these techniques sporadically on more recently discovered portions of the deposit would provide indication whether the early Ni cumulate portion has been intersected yet.

4.6.2 Further work

It is recommended that further work on mineralisation at the Sakatti deposits utilises the Ni/Cu ratio to target sporadic bulk sulphide PGE analyses and magnetite trace element analyses. The trace element chemistry of magnetite has the potential to be a powerful exploration tool in numerous settings, and sulphide-derived magnetite is very quick and easy to analyse. The wider application of these techniques would provide the ability to consider the fractionation history of the sulphide mineralisation at Sakatti and this information could be used to assess the likelihood of intersecting additional early Ni cumulate mineralisation at greater depth.

The $\delta^{34}\text{S}$ signature of Sakatti is very uniform and further work on it is not recommended, as this study achieved broad coverage of the deposit. Mass independent S isotope fractionation ($\Delta^{33}\text{S}$ and $\Delta^{36}\text{S}$) at the deposit could be investigated as this may provide insight into any potential Archaean derived sedimentary signature.

Further study could focus on determining the origin of anhydrite in the Sakatti deposit, potentially including Sr isotopic analysis to assess whether it is hydrothermal in origin and fluid inclusion microthermometry to determine the temperature of formation.

5 PGE mineralisation at the Sakatti Deposit

5.1 Introduction

This chapter concerns the mineralogy of the PGE carrying-phases at the Sakatti deposit. Inevitably there is some overlap with chapter 4 concerning the sulphides. The key questions that are confronted in this chapter are:

- i) What is the nature of PGE mineralisation at Sakatti?
- ii) How does that compare to other Ni-Cu-PGE deposits?
- iii) What are the controls on PGE mineralisation and what is its origin?
- iv) Is there a hydrothermal component to the PGE distribution?
- v) Is there a mineralogical control on the Pt:Pd distribution at Sakatti and can the spatial variation in Pt:Pd ratio be explained?

These questions are answered using a traditional petrological approach aided by several different analytical techniques to firstly to locate and image the PGE-bearing phases and then measure their mineral chemistry. High Resolution X-ray Computer Tomography (HRXCT) has been used to great effect in previous studies on Ni-Cu-PGE deposits (Eg. Godel et al., 2010; Godel, 2013; Godel et al., 2014). Three dimensional scanning of the samples gives access to a much larger proportion of the PGE phases than are present in a single 2D cross section.

A Master's project was devised and undertaken by Chris Hunter of Imperial College London and supervised as part of this study. Two samples from Sakatti were HRXCT scanned and then serial sectioned to assess the HRXCT results (Hunter, 2012). This study proved invaluable in validating the HRXCT approach.

5.1.1 PGE mineralogy in Ni-Cu-PGE deposits

Magmatic Ni-Cu-PGE deposits contain a wide variety of PGE minerals (Eg. Cabri, 2002). In general, magmatic Ni-Cu-PGE deposits can be split into two groups based simply on empirical economic considerations into Ni-Cu-dominated deposits, which are sulphide rich and contain accessory PGE and PGE-dominated deposits, which are sulphide poor, high PGE tenor and contain relatively small amounts of Ni-Cu (Naldrett, 2004). Sakatti is in the former category and so the scenario being considered is one where a sulphide melt containing relatively low concentrations of PGE was produced by the magmatic system. Deposits that belong in the sulphide-rich category make the most appropriate comparisons, however much of the

mineralogy and formation processes of the PGE-bearing phases may be shared with the PGE-rich deposits. Of particular relevance to the Sakatti deposit, given the evident dominance of Cu over Ni in the sulphide mineralisation, are Cu-rich magmatic systems (Eg. Cabri and Laflamme, 1976; Czamanske et al., 1992; Dare et al., 2014b; Helmy et al., 2007).

Major PGE minerals found in both deposit types comprise alloys, tellurides, selenides, arsenides, sulpharsenides and sulphides (Cabri, 2002). These discrete PGE minerals typically account for the majority of the PGE in a deposit with the exception of Pd, which commonly occurs in solid solution within pentlandite (Eg. Dare et al., 2010).

There are several interpretations regarding how discrete PGE minerals can form:

Exsolution from crystallised sulphide

PGE are accommodated in the crystalline sulphide (such as ISS) but exsolve as it cools and converts to lower temperature sulphide minerals (Hutchinson and McDonald, 2008).

Directly from highly concentrated residual sulphide melt

PGE become concentrated in a sulphide melt by crystallisation to the point at which they will crystallise directly from the melt to form discrete phases (Dare et al., 2014b; Liu and Brenan, 2015).

Immiscible segregation of a semi-metal melt from sulphide melt

Similar to the previous interpretation but instead of forming as a solid, a separate semi-metal immiscible melt is generated as PGE and semi-metals are concentrated in the residual sulphide melt (Helmy et al., 2007; Holwell and McDonald, 2010).

Hydrothermal remobilisation and emplacement

Hydrothermal remobilisation is cited, especially when PGE phases occur outside of the sulphide mineralisation. Transport by Cl⁻ ions occurs in oxidising conditions (Hanley et al., 2005b; Molnár et al., 2001).

The first two interpretations both rely on concentration of PGE in residual sulphide melt but are difficult to distinguish from one another due to the recrystallisation that occurs when sulphide phases cool. The third interpretation would be evident from a mineralogical bias in the occurrence of the PGE phases and the fourth interpretation would require evidence of hydrothermal activity.

5.1.2 PGE mineralogy at the Kevitsa deposit

The Kevitsa deposit is a magmatic Ni deposit located 15 km to the northeast of the Sakatti deposit, and this deposit also hosts significant PGE mineralisation. Data that are publically available indicate that PGE in the deposit are contained mainly in telluride phases with a partial array of compositions in the moncheite (PtTe_2)-merenskyite (PdTe_2)-melonite (NiTe_2) system. Unlike Sakatti, Kevitsa has a reported PGE arsenide assemblage, comprising sperrylite (PtAs_2), which is present in apparently minor quantities (Gervilla and Kojonen, 2002; Kaukonen, 2009; Mutanen, 1997).

The Kevitsa deposit features both disseminated 'normal ore' (Mutanen, 1997), which is a relatively low PGE tenor sulphide comprising 2-6 by vol% of the host intrusive and also a 'Ni-PGE' ore that, while having similar sulphide/silicate proportions to the 'normal ore', has a much higher PGE and Ni tenor (Mutanen, 1997). It has been tentatively suggested that the 'Ni-PGE' ore could result from assimilation of komatiite hosted Ni-sulphides already present in the country rock prior to intrusion (Yang et al., 2013) although this model is disputed by further PGE analysis as it does not conform with elevated Pd/Ir and Pt/Ir values seen at Kevitsa (Le Vaillant et al., 2016).

5.1.3 Experimental studies

There are numerous experimental studies concerning the partitioning of PGE elements between a) silicate and sulphide melts (Eg. Ballhaus and Ulmer, 1995; Fleet et al., 1993; Mungall and Brenan, 2014) and b) between crystallised sulphides (MSS or ISS) and liquid sulphide (Eg. Li et al., 1996; Liu and Brenan, 2015; Mungall et al., 2005). There have been relatively few studies concerning the partitioning behaviour of PGE elements between sulphide liquid and PGE mineral phases, particularly tellurides (Helmy et al., 2007; 2010; 2013).

It has been shown that crystallisation of MSS will result in continuous enrichment of Pt, Pd, Ag and Au in the residual melt, along with chalcophile semi-metals, but the D values are generally too large for Pt, Pd, As and Te to reach early saturation and form accessory minerals rich in these phases (Liu and Brenan, 2015). The implication of this is that a highly evolved sulphide melt, resulting from extensive sulphide crystallisation, is required for the formation of PGE tellurides. This is consistent with previously published textural observations from the McCreedy East Deposit at Sudbury, Canada (Dare et al., 2014b).

5.2 Sampling

5.2.1 Petrology and mineral chemistry

The same samples that were used for studying the sulphide mineralisation were also used for studying the PGE phases (4.2). These samples were chosen to reflect the diversity of mineralisation styles. Many of them contained PGE phases which were identified using the Scanning Electron Microscope (SEM).

5.2.2 CT Scanning

A separate subset of 10 samples was prepared for HRXCT scanning. These samples were chosen on from core logging as being representative of different mineralisation styles. Six of the samples were chosen using known Pt, Pd and Au grades in order to get samples with high PGE grades to maximise the number of PGE mineral grains that would be observed but also to give varying Pt:Pd ratios.

The method of sampling was carefully adapted to optimise the samples produced for HRXCT. As they are subsamples from drill core, it was necessary to not remove an entire cross section in order to preserve the down-hole continuity of the remaining drill core. However as HRXCT is not a destructive technique even the subsampled portion can be ultimately returned to the original drill core.

Cylinders were drilled from the core using a two centimetre diamond drill bit and water flow in a specially adapted electric power drill. Sections of the core (already halved for assay purposes) up to three centimetres in length were clamped and drilled by hand to produce approximately three centimetre long cylinders that were two centimetres in diameter (Fig. 5.1).

Cylinders are optimal for the process of HRXCT because as they are rotated there is relatively uniform interference from the edges of the sample (Ketcham and Carlson, 2001).



Figure 5.1 – subsampling of NQTK drill core (50.6 mm diameter) with a 20 mm diameter drill to produce cylinders for HRXCT scanning.

Two samples were used as part of a Masters project undertaken by Chris Hunter of Imperial College London (Hunter, 2012). These two samples were serial sectioned to compare HRXCT to SEM imaging, the results of which greatly helped this project (5.3.3).

5.3 Results

5.3.1 Mineralogy

Conventional microscopy and SEM of sulphide samples revealed that PGE were present in discrete mineral phases. Unusually these phases were exclusively Pt,Pd,Ni tellurides, with the one exception being a sub 1 μm grain or potentially sperrylite. This potential occurrence of sperrylite was within the atypical semi-massive style of mineralisation (sample M8 779.20 m) where the sulphide melt shows contamination with silicate melt through much enhanced Ti content in magnetite. It is too small for electron beam analysis so its chemistry cannot be confidently stated. Because of its size and the fact it is within atypical mineralisation this occurrence is not being treated as significant.

While reflected light petrography could be used to identify these minerals, and was successfully used in one case, it was highly limited due to their small size and the similar reflectance of PGE phases. SEM combined with EDS analysis was invaluable in systematically locating and identifying these phases. These were then analysed by EPMA in order to quantitatively establish their major element chemistry.

5.3.2 Chemistry

5.3.2.1 EPMA

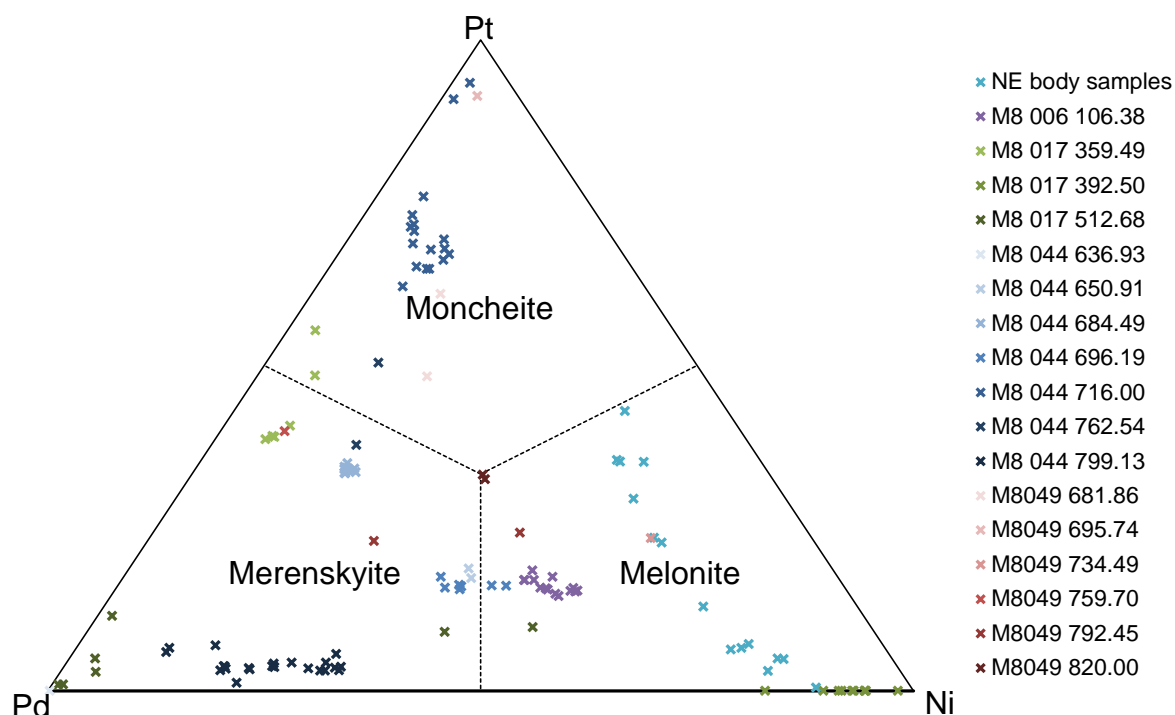


Figure 5.2 – Atomic percentage WDS data showing solid solution of Pt, Pd and Ni in the PGE tellurides at the Sakatti deposit.

The chemistry of these minerals unveils considerable variation between the Pt- Pd- and Ni- end-members of the moncheite-merenskyite-melonite series (Table 5.1, Fig. 5.2). It can be observed that there is systematic variation and trends within individual samples however no samples repeat a trend seen in another. There is no correlation between chemistry and depth, location or characterisation of the samples. There are samples which follow a Pt-Pd trend such as M8 044 636.93 and also those that follow a Pd-Ni trend such as M8 044 799.13 and M8 017 392.50 but the majority of the samples exist between all three end-members. Suggested mechanisms for intra-sample trends are proposed in the discussion section.

Bi is present in all of these minerals, substituting for Te. Some of the phases are in fact michenerite (Pd,Pt)BiTe (Fig. 5.3), these are Pd phases at Sakatti. None of these phases are in the Kotulskite-Soblevskite series, Pd(Te,Bi), and are all stoichiometrically matched with two anions per one cation (Fig. 5.4).

Hole No.	Depth	Grain	S	Fe	Co	Ni	Cu	Se	Pd	Ag	Te	Pt	Bi	Total
006	106.38	1	< 0.06	0.30	< 0.04	8.20	0.13	0.16	9.83	< 0.02	69.83	7.93	3.16	99.54
006	106.38	1	< 0.06	0.05	< 0.04	8.52	< 0.05	0.17	9.10	< 0.02	70.22	8.09	3.23	99.38
006	106.38	1	< 0.06	0.38	< 0.04	8.32	0.26	0.15	9.82	< 0.02	70.04	7.80	3.22	99.99
006	106.38	1	0.06	0.16	< 0.04	7.60	< 0.05	0.14	9.88	< 0.02	68.03	8.18	3.01	97.06
006	106.38	1	< 0.06	0.10	< 0.04	8.42	< 0.05	0.17	9.24	< 0.02	70.33	8.15	3.11	99.52
006	106.38	2	< 0.06	0.27	< 0.04	7.88	< 0.05	0.17	9.85	< 0.02	69.39	8.16	3.55	99.27
006	106.38	2	< 0.06	0.31	< 0.04	7.87	< 0.05	0.16	9.93	< 0.02	69.36	8.30	3.45	99.38
006	106.38	3	< 0.06	1.29	< 0.04	7.20	0.26	0.12	10.22	< 0.02	69.04	8.77	3.57	100.47
006	106.38	3	< 0.06	0.79	< 0.04	7.30	0.61	0.13	10.34	< 0.02	69.15	8.86	3.12	100.30
006	106.38	3	0.11	1.14	< 0.04	7.34	0.83	0.13	9.85	< 0.02	68.28	8.70	3.57	99.95
006	106.38	4	< 0.06	0.22	< 0.04	8.38	0.32	0.13	8.82	< 0.02	70.71	8.03	2.90	99.51
006	106.38	4	< 0.06	0.11	< 0.04	8.27	0.22	0.15	8.91	< 0.02	70.45	8.22	2.95	99.28
006	106.38	5	< 0.06	0.20	< 0.04	7.63	0.17	0.14	9.19	< 0.02	69.91	8.97	3.24	99.45
006	106.38	6	< 0.06	0.45	< 0.04	7.27	0.13	0.13	9.79	< 0.02	68.80	9.57	3.09	99.23
017	512.68	3	< 0.06	0.24	< 0.04	0.10	< 0.05	< 0.03	23.94	0.31	31.81	0.42	43.90	100.72
017	512.68	3	< 0.06	0.19	< 0.04	0.17	< 0.05	< 0.03	23.85	0.22	31.60	0.45	44.31	100.80
017	512.68	3	< 0.06	0.19	< 0.04	0.40	< 0.05	< 0.03	22.40	0.23	31.36	2.22	43.25	100.06
017	512.68	4	< 0.06	0.59	< 0.04	5.45	0.19	< 0.03	11.85	7.50	58.21	3.98	14.18	101.96
017	512.68	4	0.16	0.44	< 0.04	0.49	< 0.05	< 0.03	20.28	6.36	54.67	1.17	14.01	97.58
017	512.68	4	< 0.06	0.33	< 0.04	7.82	0.16	< 0.03	10.84	2.95	62.89	4.97	10.58	100.54
017	512.68	6	< 0.06	< 0.04	< 0.04	0.22	< 0.05	< 0.03	20.46	1.77	27.75	4.97	43.88	99.04
017	359.49	1	< 0.06	0.65	< 0.04	0.43	0.99	0.04	9.98	0.15	53.47	24.51	10.73	100.95
017	359.49	2	< 0.06	0.21	< 0.04	0.78	0.31	0.09	13.53	< 0.02	55.90	17.27	10.47	98.56
017	359.49	3	0.08	0.42	< 0.04	0.87	0.59	0.07	13.43	< 0.02	57.30	17.72	9.06	99.54
017	359.49	4	0.16	0.71	< 0.04	0.90	1.17	0.06	10.98	0.14	57.28	21.73	7.81	100.94
017	359.49	4	0.06	0.27	< 0.04	1.07	0.47	0.08	13.09	0.04	58.47	18.93	7.58	100.06
017	359.49	4	0.56	1.12	< 0.04	0.90	1.30	0.04	13.22	0.07	57.76	17.41	7.74	100.12
017	392.50	1	0.21	1.96	< 0.04	15.86	1.77	0.25	2.18	< 0.02	74.36	< 0.2	6.60	103.19
017	392.50	2	< 0.06	0.59	< 0.04	16.36	0.08	0.25	1.75	< 0.02	77.04	< 0.2	4.32	100.39
017	392.50	2	< 0.06	0.44	< 0.04	16.28	0.17	0.25	1.71	< 0.02	77.20	< 0.2	4.34	100.39
017	392.50	4	< 0.06	0.34	< 0.04	15.43	0.52	0.25	3.25	< 0.02	73.81	< 0.2	7.31	100.91
017	392.50	4	0.07	0.50	< 0.04	13.83	0.54	0.25	5.18	< 0.02	73.33	< 0.2	6.66	100.36
017	392.50	5	0.09	1.59	< 0.04	16.67	0.30	0.22	0.55	< 0.02	81.21	< 0.2	< 0.06	100.63
017	392.50	7	< 0.06	0.78	< 0.04	16.26	0.91	0.26	1.75	< 0.02	77.37	< 0.2	3.84	101.17
017	392.50	8	0.07	0.33	0.05	16.58	< 0.05	0.22	2.71	< 0.02	73.21	< 0.2	7.83	101.00
017	392.50	9	0.06	0.22	< 0.04	15.76	< 0.05	0.21	2.69	< 0.02	72.97	< 0.2	8.02	99.93
044	636.93	8	< 0.06	1.69	< 0.04	< 0.05	0.62	< 0.03	23.74	1.65	29.67	< 0.2	46.25	103.62
044	684.49	1	< 0.06	0.15	< 0.04	2.60	< 0.05	0.07	12.63	0.95	56.36	16.23	11.43	100.42
044	684.49	6	< 0.06	0.28	< 0.04	2.52	< 0.05	0.06	12.70	1.01	56.66	16.54	11.43	101.20
044	684.49	6	< 0.06	0.21	< 0.04	2.53	< 0.05	0.08	12.82	0.98	56.40	16.08	11.58	100.68
044	684.49	6	< 0.06	0.19	< 0.04	2.63	< 0.05	0.06	12.34	0.97	56.53	16.26	11.43	100.41
044	684.49	6	< 0.06	0.16	< 0.04	2.45	0.06	0.08	12.52	1.00	56.64	16.05	11.55	100.51
044	684.49	6	< 0.06	0.21	< 0.04	2.56	< 0.05	0.06	12.57	1.06	56.63	16.16	11.60	100.85
044	684.49	6	0.15	0.51	< 0.04	2.74	0.07	0.07	12.60	1.07	56.31	16.29	11.65	101.46
044	684.49	6	< 0.06	0.24	< 0.04	2.45	< 0.05	0.07	12.42	1.06	56.66	16.65	11.11	100.66
044	684.49	12	0.07	0.23	< 0.04	2.48	0.06	0.07	12.68	0.88	56.65	16.34	11.22	100.68
044	684.49	12	< 0.06	0.17	< 0.04	2.44	< 0.05	0.08	12.58	0.85	56.84	16.39	11.28	100.63
044	684.49	12	< 0.06	0.19	< 0.04	2.55	< 0.05	0.07	12.80	0.89	57.20	16.03	11.67	101.40
044	684.49	12	< 0.06	0.14	< 0.04	2.54	< 0.05	0.07	12.52	0.86	57.17	16.25	11.75	101.30
044	684.49	12	< 0.06	0.13	< 0.04	2.51	0.08	0.08	12.57	0.89	57.12	16.00	11.47	100.85
044	650.91	1	< 0.06	0.45	< 0.04	6.14	< 0.05	0.12	11.73	< 0.02	59.94	8.79	11.35	98.52
044	650.91	1	< 0.06	0.55	< 0.04	5.97	< 0.05	0.11	11.57	< 0.02	59.63	9.52	11.25	98.60
044	762.54	1	< 0.06	1.75	< 0.04	1.74	< 0.05	0.08	8.87	< 0.02	49.28	22.43	15.95	100.10
044	762.54	1	< 0.06	0.99	< 0.04	2.30	< 0.05	0.07	11.31	< 0.02	50.58	17.23	16.80	99.28
044	696.19	1	< 0.06	0.66	< 0.04	6.10	< 0.05	0.14	12.39	< 0.02	63.68	7.95	7.04	97.96
044	696.19	2	< 0.06	0.99	< 0.04	5.68	< 0.05	0.17	12.52	< 0.02	63.04	7.88	7.09	97.37
044	696.19	4	< 0.06	1.19	< 0.04	5.43	< 0.05	0.17	12.30	< 0.02	62.68	8.61	7.05	97.43
044	696.19	5	< 0.06	1.64	< 0.04	6.75	< 0.05	0.16	11.51	< 0.02	63.40	8.42	7.45	99.33
044	696.19	5	0.06	1.62	< 0.04	7.09	< 0.05	0.15	11.15	< 0.02	64.18	8.46	6.47	99.18
044	696.19	6	< 0.06	1.19	< 0.04	6.08	< 0.05	0.10	12.26	< 0.02	63.52	8.16	7.56	98.87
044	696.19	6	< 0.06	1.14	< 0.04	6.02	< 0.05	0.14	12.28	< 0.02	63.66	8.29	7.62	99.15
044	716.00	1	< 0.06	1.44	< 0.04	1.35	< 0.05	0.08	6.87	< 0.02	53.09	28.03	8.88	99.74
044	716.00	2	0.06	1.30	< 0.04	0.72	< 0.05	0.07	4.45	< 0.02	56.10	33.36	3.81	99.87
044	716.00	3	< 0.06	0.31	< 0.04	1.39	< 0.05	0.06	5.31	< 0.02	54.97	30.20	6.28	98.52
044	716.00	5	< 0.06	0.61	< 0.04	0.92	< 0.05	0.07	5.30	< 0.02	54.36	30.78	6.37	98.41
044	716.00	6	< 0.06	0.65	< 0.04	1.62	< 0.05	0.09	6.14	< 0.02	50.48	30.69	9.53	99.20
044	716.00	7	< 0.06	0.98	< 0.04	0.85	< 0.05	0.05	5.19	< 0.02	54.10	31.25	6.33	98.75
044	716.00	8	< 0.06	0.16	< 0.04	0.18	< 0.05	0.08	1.75	< 0.02	54.02	38.22	3.43	97.84
044	716.00	11	< 0.06	1.04	< 0.04	1.46	< 0.05	0.08	4.50	< 0.02	55.98	27.80	6.17	97.03
044	716.00	12	0.07	1.22	< 0.04	1.57	< 0.05	0.06	4.79	< 0.02	54.84	27.46	7.60	97.61
044	716.00	13	< 0.06	0.05	< 0.04	0.72	< 0.05	0.04	5.01	< 0.02	54.26	31.48	7.65	99.21
044	716.00	14	< 0.06	1.83	< 0.04	0.98	< 0.05	0.06	5.31	< 0.02	53.45	28.56	7.46	97.65
044	716.00	15	< 0.06	1.11	< 0.04	0.83	< 0.05	0.07	5.35	< 0.02	53.74	31.18	7.27	99.55
044	716.00	16	< 0.06	1.20	< 0.04	0.26	< 0.05	0.06	1.04	< 0.02	56.70	39.51	0.96	99.73
044	716.00	17	< 0.06	1.10	< 0.04	1.71	< 0.05	0.06	4.84	< 0.02	55.46	29.68	6.78	99.63
044	799.13	1	< 0.06	0.28	< 0.04	2.97	0.40	0.13	22.20	0.03	66.64	1.78	3.70	98.13
044	799.13	2	< 0.06	0.43	< 0.04	4.76	0.19	0.14	18.91	< 0.02	67.60	2.30	3.59	97.92
044	799.13	3	< 0.06	0.32	< 0.04	3.47	< 0.05	0.10	21.73	< 0.02	66.73	1.75	4.02	98.10
044	799.13	4	< 0.06	0.73	0.05	1.70	< 0.05	0.11	23.65	< 0.02	67.25	3.47	1.66	98.62
044	799.13	5	< 0.06	0.74	< 0.04	3.96	< 0.05	0.13	21.22	< 0.02	67.72	1.98	3.65	99.40

044	799.13	6	< 0.06	0.35	< 0.04	4.57	< 0.05	0.13	19.89	< 0.02	67.80	1.84	3.71	98.29
044	799.13	7	< 0.06	0.94	< 0.04	4.84	< 0.05	0.14	19.65	< 0.02	68.01	1.66	3.59	98.83
044	799.13	8	< 0.06	1.14	< 0.04	5.16	< 0.05	0.14	18.89	< 0.02	68.53	1.69	3.62	99.17
044	799.13	9	< 0.06	0.29	< 0.04	4.93	< 0.05	0.15	19.46	< 0.02	68.07	1.66	3.75	98.31
044	799.13	10	< 0.06	0.56	< 0.04	2.92	< 0.05	0.14	22.61	< 0.02	66.44	1.67	3.72	98.06
044	799.13	11	< 0.06	0.36	< 0.04	3.89	< 0.05	0.11	21.07	< 0.02	67.41	2.26	3.31	98.41
044	799.13	12	< 0.06	0.09	< 0.04	4.80	< 0.05	< 0.03	18.21	< 0.02	68.92	2.97	3.86	98.85
044	799.13	13	0.07	0.20	< 0.04	1.71	< 0.05	0.07	15.05	17.08	59.01	2.50	3.65	99.34
044	799.13	14	< 0.06	0.59	< 0.04	3.42	< 0.05	0.09	21.65	< 0.02	67.62	1.86	3.80	99.03
044	799.13	15	< 0.06	0.63	< 0.04	3.40	< 0.05	0.10	22.52	< 0.02	67.52	0.65	4.26	99.08
044	799.13	16	< 0.06	0.76	< 0.04	3.79	< 0.05	0.11	20.62	< 0.02	68.01	2.00	3.77	99.06
044	799.13	17	0.29	1.72	< 0.04	4.36	0.06	0.11	21.17	< 0.02	65.11	2.42	3.54	98.78
044	799.13	18	< 0.06	0.58	< 0.04	5.14	0.06	0.10	18.71	0.04	68.94	1.97	3.40	98.94
044	799.13	19	< 0.06	0.16	< 0.04	4.89	< 0.05	0.11	18.35	< 0.02	68.26	1.83	4.17	97.77
044	799.13	20	< 0.06	0.66	< 0.04	2.79	< 0.05	0.10	21.33	0.06	67.65	1.92	3.81	98.32
044	799.13	21	< 0.06	0.90	< 0.04	2.82	0.18	0.10	21.36	< 0.02	66.89	1.88	4.04	98.17
044	799.13	22	< 0.06	0.54	< 0.04	1.61	< 0.05	0.09	22.74	0.03	68.74	2.98	1.68	98.41
049	681.86	1	< 0.06	0.38	< 0.04	2.70	0.36	0.06	7.96	< 0.02	56.06	22.05	10.04	99.61
049	681.86	2	< 0.06	0.42	< 0.04	1.99	< 0.05	0.04	5.84	< 0.02	55.78	27.13	8.26	99.46
049	695.74	1	< 0.06	1.12	< 0.04	0.51	< 0.05	0.08	1.09	< 0.02	57.47	39.33	1.09	100.69
049	734.49	1	< 0.06	0.40	< 0.04	9.43	< 0.05	0.15	5.49	< 0.02	68.75	12.70	1.39	98.31
049	759.70	1	1.14	6.03	0.09	0.90	0.06	< 0.03	11.57	< 0.02	55.55	16.06	8.43	99.83
049	792.45	1	0.20	1.09	< 0.04	6.51	< 0.05	0.06	9.26	< 0.02	58.68	12.40	12.80	101.00
049	792.45	2	0.16	2.44	< 0.04	3.73	< 0.05	< 0.03	13.13	< 0.02	52.71	10.91	18.29	101.37
049	820.00	1	< 0.06	0.14	< 0.04	5.10	0.18	0.08	8.96	< 0.02	66.97	16.08	1.88	99.39
049	820.00	2	< 0.06	0.14	< 0.04	5.01	0.21	0.09	8.94	< 0.02	67.02	16.44	1.89	99.74
Unknown		1	0.22	0.88	< 0.04	8.12	1.00	0.15	4.89	< 0.02	70.23	15.05	0.55	101.09
Unknown		2	0.27	0.61	< 0.04	15.27	0.06	0.46	4.20	< 0.02	77.29	2.99	0.55	101.70
Unknown		2	0.38	0.74	< 0.04	15.05	0.07	0.46	4.40	< 0.02	76.04	3.05	0.54	100.73
Unknown		3	0.19	1.35	< 0.04	13.35	0.05	0.17	4.82	< 0.02	74.94	4.13	0.49	99.49
Unknown		4	0.30	2.21	0.05	15.30	< 0.05	0.28	3.44	< 0.02	78.87	0.28	0.68	101.41
Unknown		5	0.32	1.94	< 0.04	13.65	1.79	0.22	4.62	< 0.02	78.05	1.71	0.45	102.75
Unknown		6	0.07	0.53	< 0.04	9.02	0.16	0.17	5.10	< 0.02	71.68	12.11	0.56	99.40
Unknown		6	0.57	1.39	< 0.04	9.13	0.73	0.10	4.91	< 0.02	68.49	11.61	0.45	97.38
Unknown		7	< 0.06	0.42	< 0.04	7.31	< 0.05	0.17	4.44	< 0.02	69.04	17.64	0.45	99.47
Unknown		7	0.07	0.38	< 0.04	7.21	0.30	0.13	4.50	< 0.02	69.09	17.70	0.43	99.81
Unknown		1	0.24	1.87	< 0.04	11.11	< 0.05	0.20	5.17	< 0.02	74.36	6.90	0.49	100.34
Unknown		2	0.08	1.10	< 0.04	13.50	< 0.05	0.20	5.27	< 0.02	76.79	3.84	0.42	101.20
Unknown		3	0.11	0.98	< 0.04	7.65	< 0.05	0.19	3.66	< 0.02	69.03	17.46	0.22	99.30
Unknown		3	0.14	1.28	< 0.04	6.64	< 0.05	0.11	3.15	< 0.02	67.62	21.00	0.45	100.39
Unknown		4	0.07	0.77	< 0.04	12.62	1.09	0.22	5.41	< 0.02	76.64	3.52	0.53	100.87

Table 5.1 – WDS Wt% data of PGE telluride chemistry at the Sakatti deposit

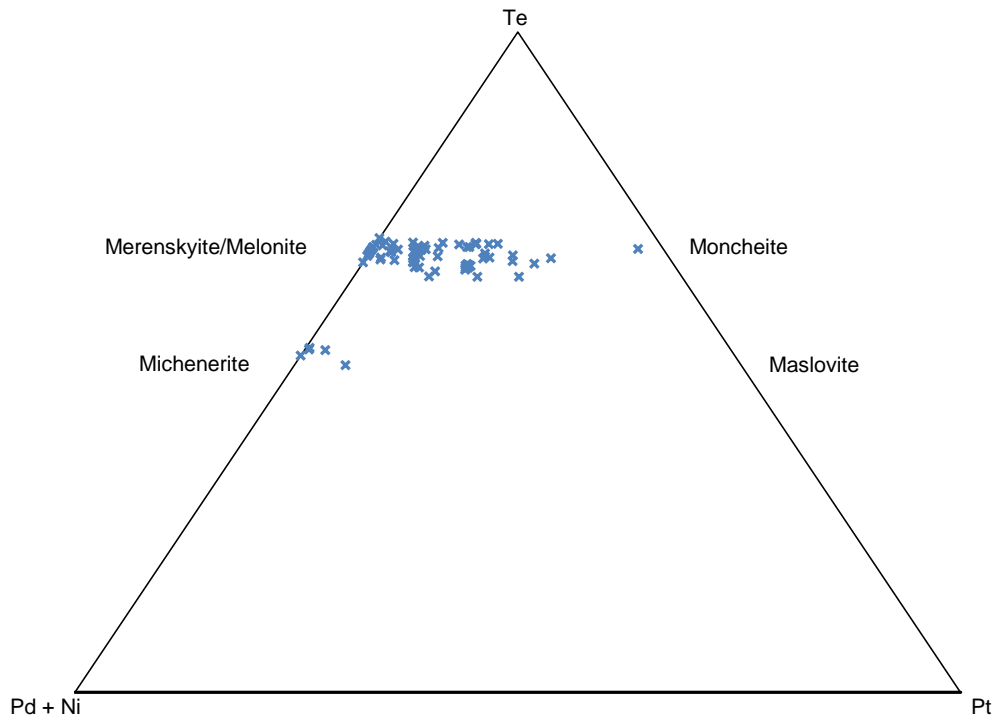


Figure 5.3 – WDS atomic % data showing the dominance of merenskyite-moncheite-melonite $(Pd,Pt,Ni)Te_2$ over michenerite $PdBiTe$

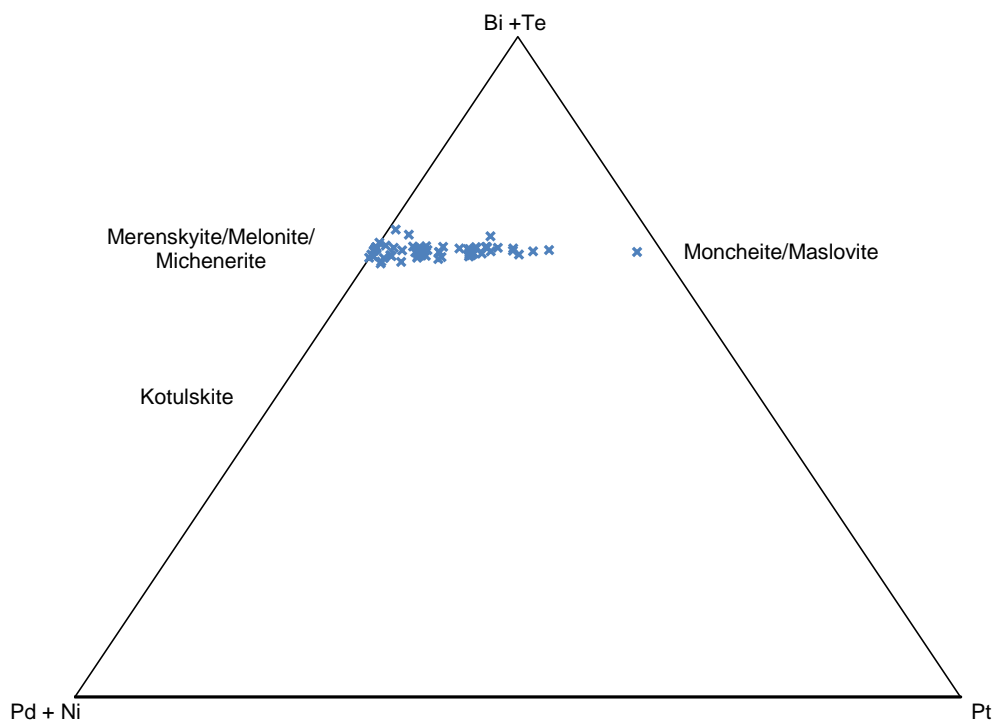


Figure 5.4 – WDS atomic % data showing the PGE telluride occurrences are all $(Pt,Pd,Ni)(Bi,Te)_2$ and not in the kotulskite $Pd(Te,Bi)$ -sobolevskite $Pd(Bi,Te)$ series.

5.3.2.2 LA-ICP-MS

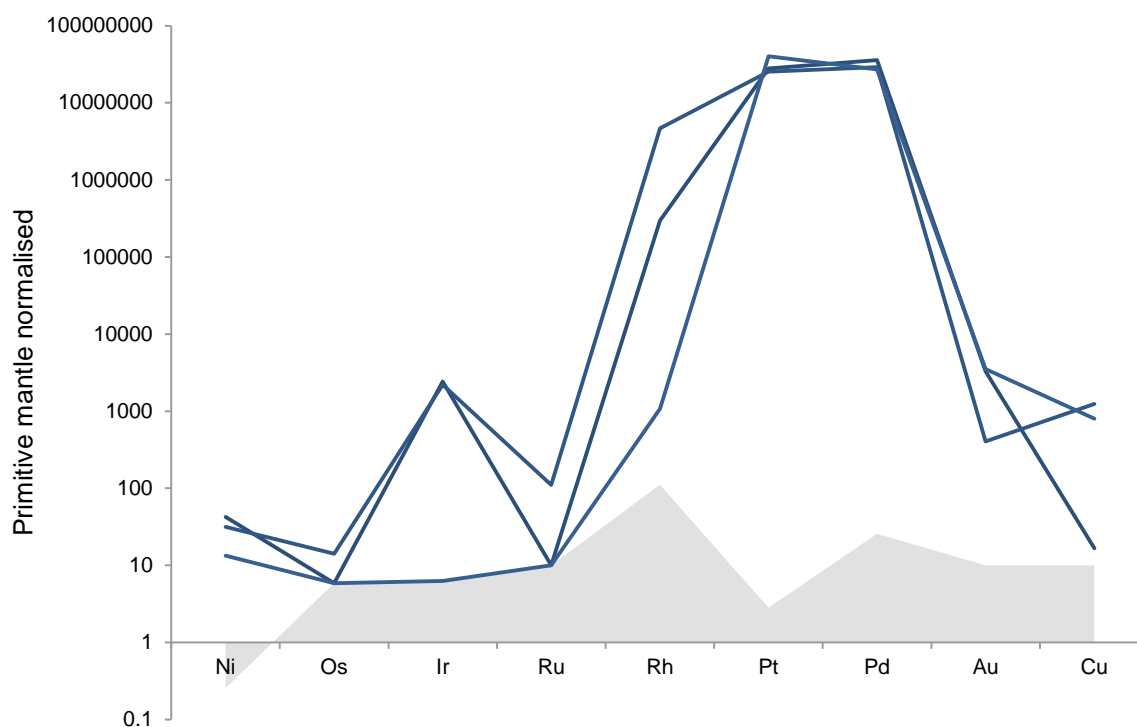


Figure 5.5 – LA-ICP-MS data of PGE telluride minerals at the Sakatti deposit. Detection limits are shown by a dotted line. Normalised to primitive mantle values (McDonough and Sun, 1995).

While the LA-ICP-MS analysis of these phases is not truly quantitative due to their small size, it nonetheless gives representative relative proportions of the PGE within the phases (Table 5.2). It is also useful to consider the distribution of the PGE within these phases (Fig. 5.5) compared with the whole-rock PGE distribution (Figure 4.21). These are largely the same distribution and it is clear that the PGE located within these phases controls PGE distribution in the whole-rock data. It can be seen in both the whole-rock PGE and the telluride PGE that Rh is enriched relative to the IPGE which are largely absent. Ir is also enriched relative to Os and Ru which are near detection limits.

Hole	Depth	Min	Min	Min	⁵⁷ Fe	⁵⁹ Co	⁶¹ Ni	⁶⁵ Cu	⁶⁶ Zn	⁷⁵ As	⁸² Se	¹⁰¹ Ru*	¹⁰³ Rh*	¹⁰⁶ Pd*	¹⁰⁸ Pd*	¹⁰⁹ Ag	¹¹¹ Cd	¹²¹ Sb	¹²⁵ Te	¹⁸⁵ Re	¹⁸⁹ Os	¹⁹³ Ir	¹⁹⁵ Pt	¹⁹⁷ Au	²⁰⁹ Bi
	(m)	PGE	before	after	(%)	(ppm)	(%)	(%)	(ppm)	(ppm)	(ppm)	(ppm)	(ppm)	(ppm)	(ppm)	(ppm)	(ppm)	(ppm)	(ppm)	(ppm)	(ppm)	(ppm)	(ppm)	(ppm)	(ppm)
44	684.49	PGE	Pn	Pn	4.49	1805	8.30	<0.03	14	<6	<50	<0.05	268	139200	133800	832	<0.80	208	499400	<0.02	<0.02	7.77	197700	3.28	44
49	695.74	PGE	Mag	Mag	47.14	75	0.73	<0.03	<5	116	133	<0.05	38.7	13660	13420	<0.1	<0.80	156	455800	<0.02	0.16	26.84	415600	1.42	49
49	820.00	PGE	Cpy	Cpy	3.34	267	6.16	3.71	1066	<6	62	0.55	4225	113300	115500	30	<0.80	19	629400	0.03	0.05	7.04	179900	0.41	49
44	696.19	PGE	Po	Po	46.75	81	3.76	<0.03	31	<6	81	<0.05	906	51240	51030	8.25	<0.80	7.16	215700	0.51	0.14	33.39	37810	0.11	44
44	696.19	PGE	Po	Po	54.63	82	1.78	<0.03	32	<6	143	<0.05	389	29590	29440	35	<0.80	4.40	122100	1.54	<0.02	13.09	22880	0.51	44
44	696.19	PGE	Po	Po	38.87	44	1.94	<0.03	<5	<6	99	<0.05	618	35330	34930	380	<0.80	6.06	155100	8.45	0.24	21.56	30140	0.71	44
44	696.19	PGE	Po	Po	61.16	67	3.13	<0.03	<5	<6	180	<0.05	849	47470	48100	1193	<0.80	7.22	200400	3.52	<0.02	39.14	40080	0.51	44
49	681.86	PGE	Mag	Py	64.12	5676	0.95	0.08	66	<6	89	<0.05	<0.1	24050	19660	1.02	0.93	101	188800	0.03	<0.02	0.10	80720	2.17	49
49	681.86	PGE	Mag	Py	9.39	132	2.61	2.40	46	<6	116	<0.05	0.97	106300	105700	0.14	<0.80	303	677500	0.05	<0.02	0.03	286200	3.52	49
49	792.45	PGE	Pn	Po	34.89	6703	27.99	<0.03	25	<6	364	<0.05	346	21160	21010	3.92	<0.80	131	117800	6.42	<0.02	18.5	27980	0.40	49
44	684.49	PGE	Pn	Pn	4.49	1805	8.30	<0.03	14	<6	<50	<0.05	268	139200	133800	832	<0.80	208	499400	<0.02	<0.02	7.77	197700	3.28	44
49	695.74	PGE	Mag	Mag	47.14	75	0.73	<0.03	<5	116	133	<0.05	38.7	13660	13420	<0.1	<0.80	156	455800	<0.02	0.16	26.84	415600	1.42	49
49	820.00	PGE	Cpy	Cpy	3.34	267	6.16	3.71	1066	<6	62	0.55	4225	113300	115500	30	<0.80	19	629400	0.03	0.05	7.04	179900	0.41	49

Table 5.2 – LA-ICP-MS data of telluride phases. All data are contaminated by sulphide due to the small size of the telluride phases. However the dominance of the PGE in the telluride phases over the sulphide phases means that useful data are still produced.

5.3.3 Morphology

i) Two-dimensional morphology of PGE minerals

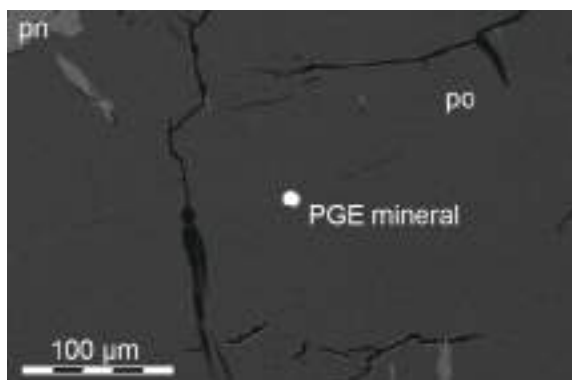


Figure 5.6a – Backscattered electron image showing rounded moncheite grain in pyrrhotite with characteristic pentlandite flames.
M8044 762.54m

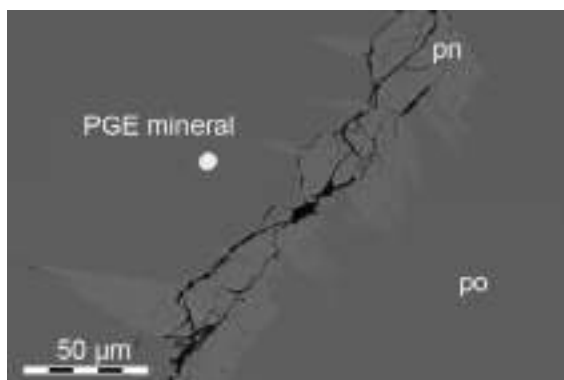


Figure 5.6b – Backscattered electron image showing a round inclusion of merenskyite in pyrrhotite. There is a proximal grain boundary or crack filled with pentlandite, showing characteristic pentlandite flames within the pyrrhotite.
M8049 792.45m

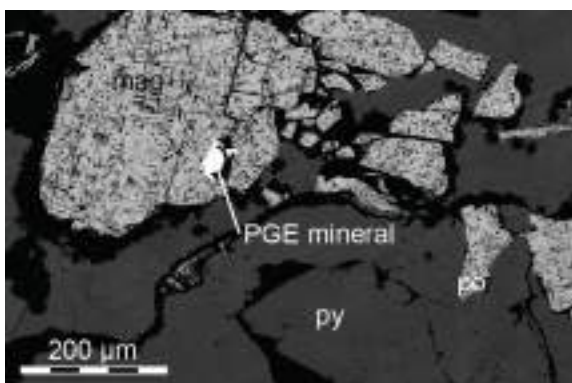


Figure 5.6c – Backscattered electron image showing an irregular inclusion of merenskyite within a grain of pentlandite. The pentlandite is mantled by hematite.
M8044 650.91m

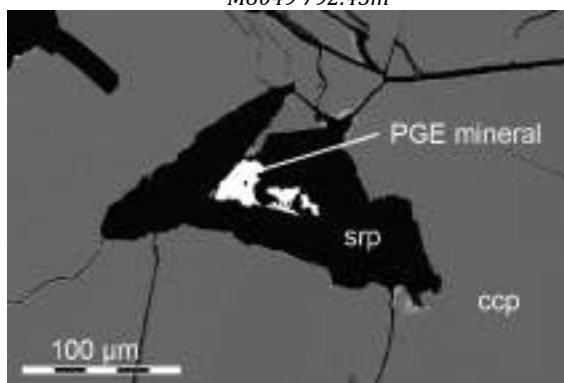


Figure 5.6d – Backscattered electron image showing irregular melonite grain surrounded by serpentine in chalcopyrite.
M8017 106.38m

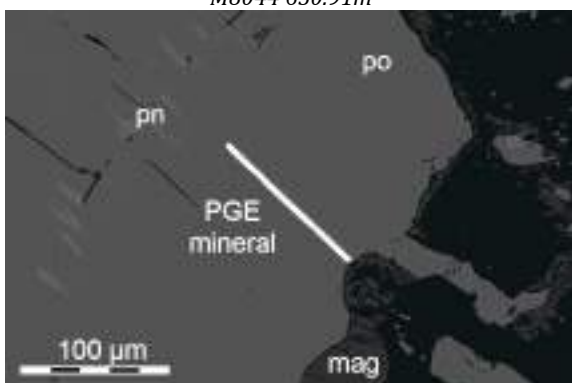


Figure 5.6e – Backscattered electron image showing needle-like moncheite in nickeliferous pyrrhotite at a magnetite-chlorite boundary.
M8044 716.00m

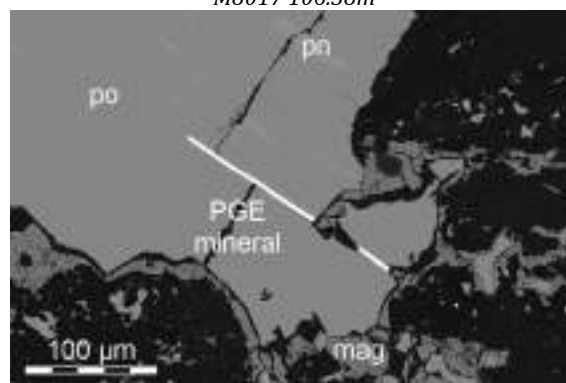


Figure 5.6f – Backscattered electron image showing needle-like moncheite in nickeliferous pyrrhotite, being partially replaced by magnetite and silicate.
M8044 716.00m

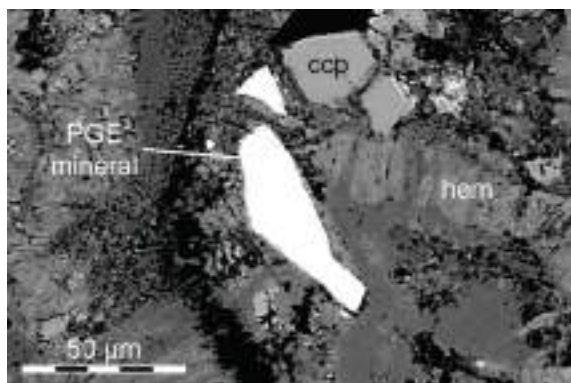


Figure 5.6g – Backscattered electron image showing elongate melonite surrounded by Fe oxide (variably nickeliferous and manganiferous). Associated with a veinlet of serpentine and a grain of chalcopyrite.
M8017 106.38m

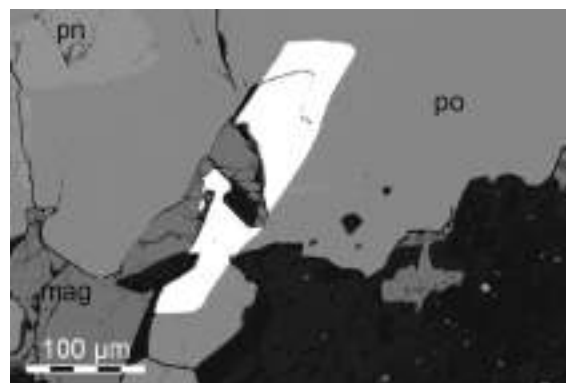


Figure 5.6h – Backscattered electron image showing elongate merenskyite in pyrrhotite being partially replaced by magnetite.
M8044 799.13m

Figure 5.6 – Representative backscattered electron images showing the morphologies of PGE tellurides at Sakatti.

The PGE tellurides exhibit varied morphologies, observed primarily by BSE imaging. In the interest of comparing morphology with chemistry, these can be crudely grouped into: ‘rounded’, where the dimensions of the mineral are roughly equivalent (Fig. 5.6a,b); ‘elongate’, where one dimension is considerably longer than the other (Fig. 5.6g,h); ‘needles’, where one dimension is extremely longer than the other (Fig. 5.6e,f); and ‘irregular’, where the edges of the grain are irregular and undulating, meaning the dimensions are even more subjective (Fig. 5.6c,d). Each of these categories is necessarily subjective, and to some extent represent arbitrary categories in a continuum of shapes, but nonetheless they proved relatively effective at categorising the majority of occurrences.

The largest number of occurrences fell into the ‘rounded’ category, with most of the remaining being either elongate or irregular. Needles are underrepresented in the data, as in order to compare chemistry a successful WDS analysis has to have been acquired from it and the needles were frequently only 1-5 μm wide meaning they were too small for acquiring reliable WDS data. However, it was observed from EDS analysis that the needles were almost invariably Pt-rich or Pt end-member moncheite.

Morphology bears no correlation to chemistry (Fig. 5.7), with the exception of the aforesaid Pt-rich ‘needle’ morphology.

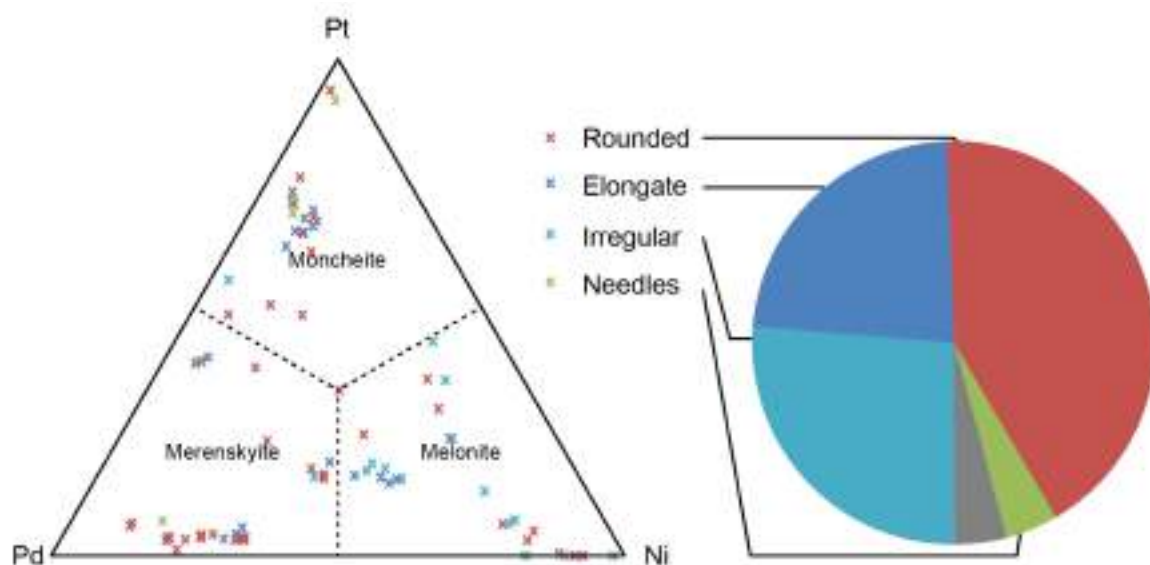


Figure 5.7 – Pt-Pd-Ni atomic% plot as figure 5.2 but coloured to show morphology based groupings of the PGE grains. The proportions of different primary morphologies are shown as a percentage of the PGE grains that were found and have been analysed successfully by microprobe.

ii) Three dimensional morphology

Mineral	Density
Serpentine	2.5-2.6
Chlorite	2.6-3.4
Forsterite	3.2-3.4
Augite	3.2-3.6
Chalcopyrite	4.1-4.3
Barite	4.5
Violarite	4.5-4.8
Chromite	4.5-5.1
Pyrrhotite	4.6
Pentlandite	4.6-5.0
Pyrite	5.0
Magnetite	5.1-5.2
Hematite	5.3
Millerite	5.5
Galena	7.2-7.6
Hessite	7.2-7.9
Melonite	7.3
Kawazulite	7.8
Merenskyite	8.5
Moncheite	10.0
Gold	19.3

Table 5.3 – the approximate density in gcm^{-3} of a variety of commonly occurring minerals in pertinent to samples from Sakatti (Cabri, 2002; Deer et al., 2013)

HRXCT scanning provided a different perspective on the morphology of the PGE minerals above and beyond the usual two dimensional BSE approach. They revealed more complexity to the shapes than the simple BSE approach allowed for. The shapes are less easily categorised than the two dimensional ones and could be broadly covered by the groups of discs or plates, rods, spheres and irregular.

Twelve samples have been successfully scanned producing twelve accurate three dimensional models of each. The three dimensional data differentiate the phases present based on their density. However in order to use these data, it became clear that a reference surface of known mineralogy was required within each sample in order to calibrate the density threshold over which the remaining points were likely to be PGE minerals. The minerals galena and barite have been found in some samples from the deposit and so a grain of known PGE mineral is required to threshold out these minerals, which are less dense than the PGE tellurides (Table 5.3).

There were relatively few occurrences that could be located in both the HRXCT scans and two dimensional BSE images of the same samples. The data validation study, where two HRXCT scanned samples were serial

sectioned, proved most useful for this purpose (Hunter, 2012). The two dimensional ‘needle’ and ‘elongate’ morphologies are revealed as primarily disc or platy three dimensional morphologies (Fig. 5.8a-c), however they could also correlate to long sections of rod shapes. Rod shapes primarily corresponded to ‘rounded’ BSE intersections, which were also shared with spherical shapes (Fig. 5.8d).

Overall, three dimensional appreciation of the PGE mineral morphologies confirmed the wide variety observed in BSE imaging, but it also revealed greater complexity to the shapes that had been characterised solely by BSE imaging.

The technique, however, was limited by a rounding effect created by the small-size of the PGE minerals approaching the resolution of the HRXCT scans ($\sim 1 \mu\text{m}^3$ voxels). This effect was found to conceal more complex shapes and was more likely to represent those shapes as more rounded, or a series of rounded shapes in place of what might be a complex three dimensional structure. Because of this effect it was not suitable to categorise the dimensions into groups as has been done with the two dimensional image data.

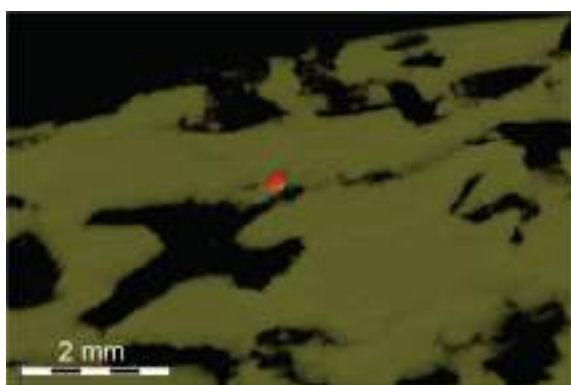


Figure 5.8a – HRXCT image showing a sulphide in disc in yellow and moncheite in red (silicate transparent). Images acquisition and method development undertaken with Chris Hunter (Hunter, 2012).

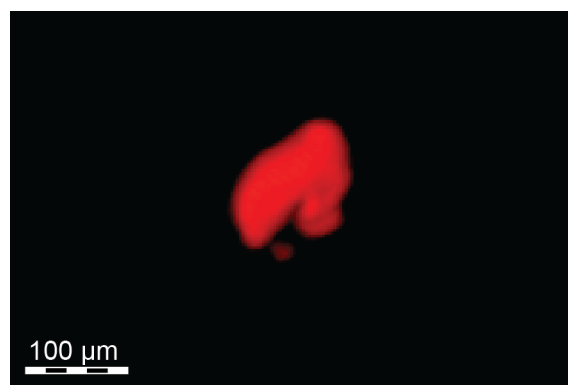


Figure 5.8b – Close up morphology of the PGE grain with no sulphide shown

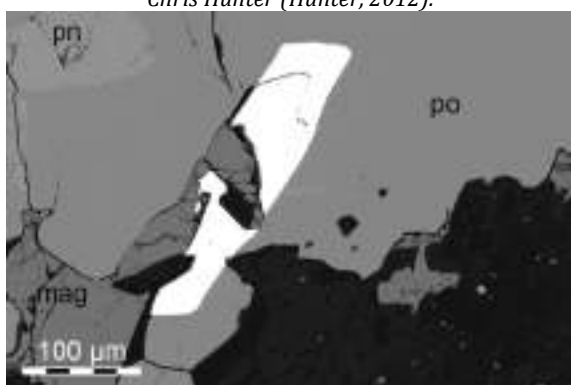


Figure 5.8c – Backscattered electron image of the same PGE grain in figures Figure 5.8a and b. Illustrating that a seemingly elongate grain two dimensions could correspond to a disc in three dimensions.



Figure 5.8d – HRXCT image showing a rod shaped grain that would equate to a round cross section in two dimensions.

5.3.4 Host mineralogy

i) Electron microscopy

Host mineralogy is difficult to define given that the PGE minerals occur primarily at grain boundaries. The most abundant mineral in contact with each PGE mineral occurrence is presented in figure 5.9. It should be noted that PGE minerals were not found completely enclosed in silicate, with the exception of PGE mineral grains that were continuities of grains occurring in sulphide (Eg. Fig. 5.6f).

No correlation between PGE mineral chemistry and host mineralogy was observed. The groupings that can be seen are primarily a result of individual samples having both a particular mineral and also a particular PGE mineral chemistry, but nothing systematic can be observed.

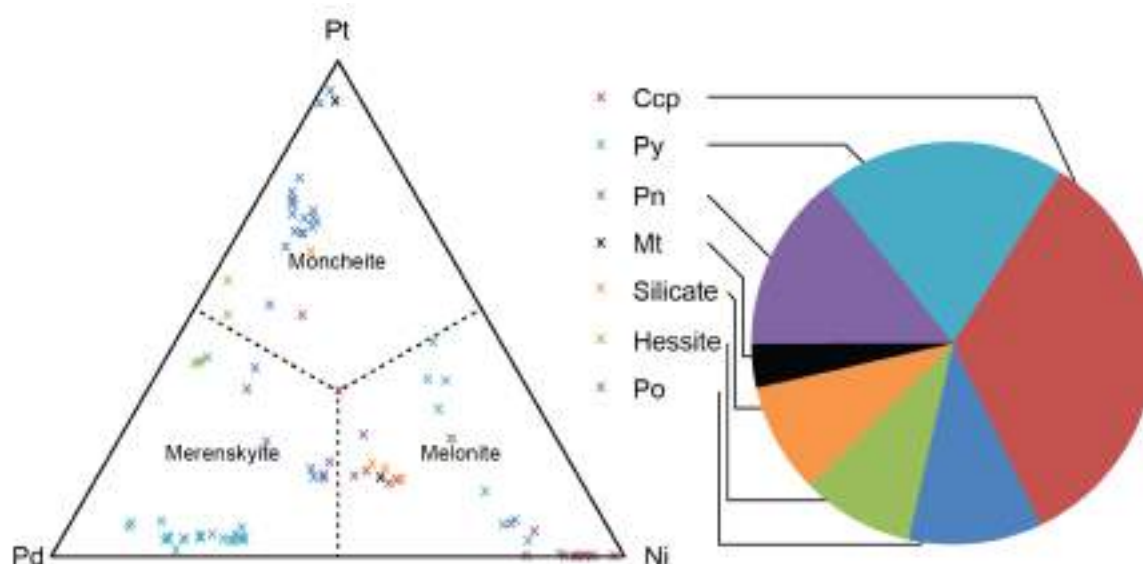


Figure 5.9 - Pt-Pd-Ni atomic% plot as figure **Error! Reference source not found.** but coloured to show the primary host mineral of the PGE grains. There is one data-point per grain. The proportions of different primary host minerals are shown as a percentage of the PGE grains that were found and have been analysed successfully by microprobe.

ii) HRXCT

HRXCT distinguishes minerals based on density. This means that although the tellurides, sulphides and silicates are in general distinguishable from each other it is difficult to separate different sulphides from one another. Pentlandite and pyrite are generally distinguishable from chalcopyrite and pyrrhotite where they are present in large homogeneous masses (Fig. 5.11a,b), however this is not the common form of pentlandite and it frequently occurs as small intergrowths with pyrrhotite. Magnetite was also readily identifiable, providing some texture within massive sulphide. This allowed sulphide at grain boundaries between silicate or

magnetite and sulphide to be identified however sulphide-sulphide grain boundaries were not as easily distinguished (Fig. 5.11a and b).

5.3.5 PGE mineral locations

i) Electron microscopy

PGE mineral locations were categorised depending on whether they appeared to occur along grain boundaries, wholly within a particular mineral or seemingly in 'veins' (or potentially along cracks) within a mineral. The majority of occurrences were at grain boundaries, however, a significant proportion occurred wholly as inclusions within one mineral, usually pyrrhotite or chalcopyrite. There is no correlation between the chemistry of the PGE mineral phase and its location (Fig. 5.10).

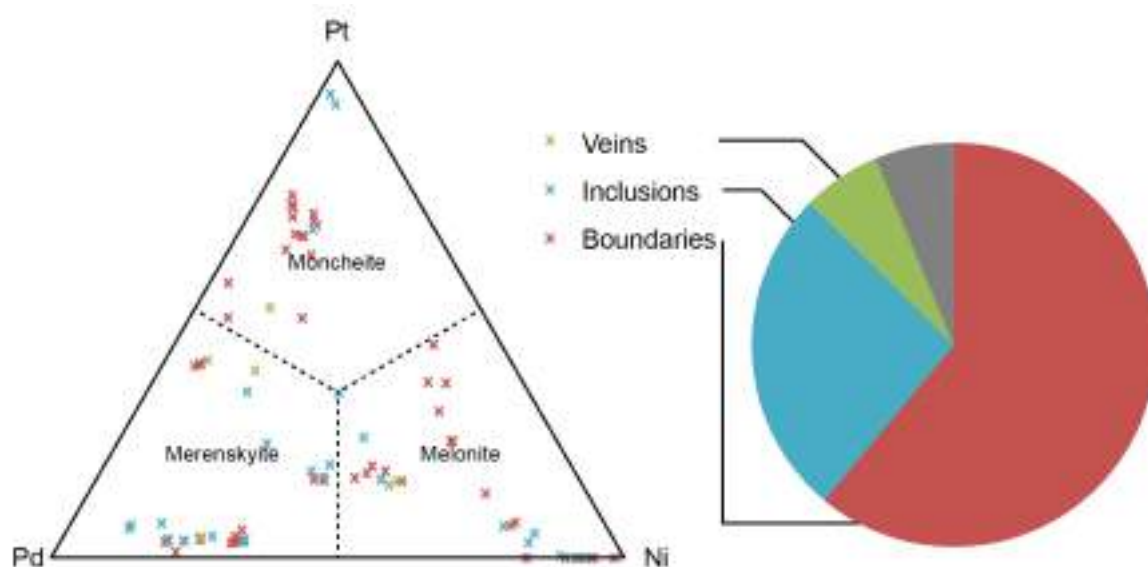


Figure 5.10 - Pt-Pd-Ni atomic% plot as figure **Error! Reference source not found.** but coloured to show the locations of the PGE grains. There is one data-point per grain. The proportions of different locations are shown as a percentage of the PGE grains that were found and have been analysed successfully by microprobe.

ii) HRXCT

HRXCT was well suited to categorising PGE mineral occurrences into either grain boundary occurrences or intra-sulphide inclusions. As stated previously the technique is not well suited to distinguishing sulphide-sulphide grain boundaries due to the similar densities. HRXCT analysis enabled a considerably larger number of PGE to be identified and found that approximately 75% of the PGE occurrences observed were at grain boundaries compared with the rest occurring within sulphide. These findings suggested that simple two-dimensional imaging over-represents the number of PGE minerals that are wholly within sulphide, presumably because the grain boundary is not always visible in the two-dimensional plane imaged (Fig. 5.11).

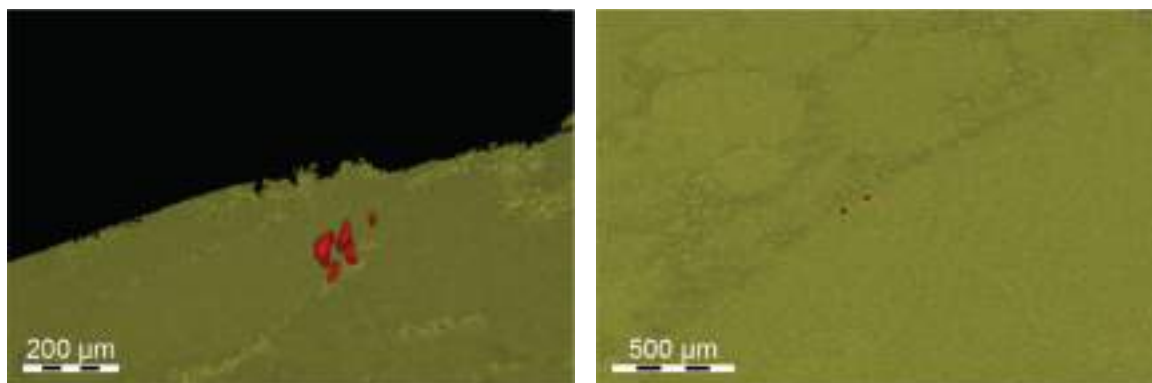


Figure 5.11a,b – HRXCT images of PGE grains along sulphide-sulphide grain boundary – distinguishable by eye but difficult to threshold

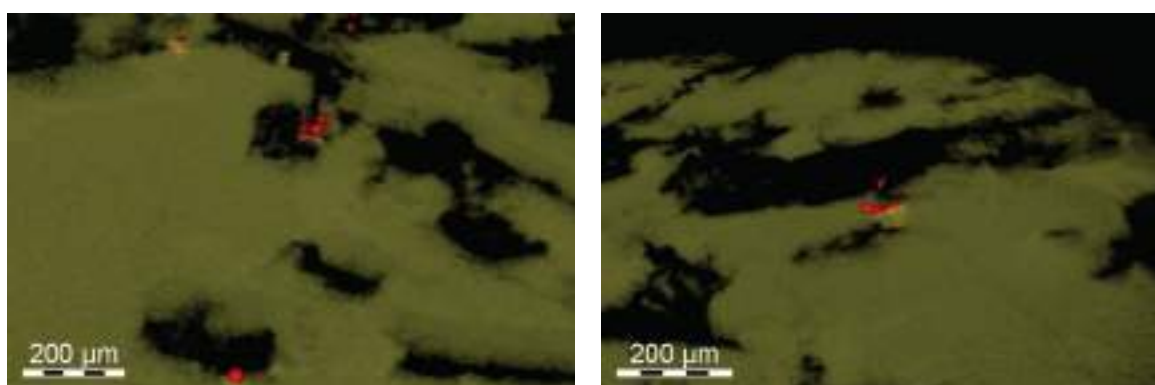


Figure 5.11c,d – HRXCT image of PGE mineral grains on silicate sulphide grain boundaries.

5.3.6 Whole-rock PGE data

i) PGE

Whole-rock PGE data is well constrained for Pt and Pd, as these are routinely assayed, but poorly constrained for the remaining PGE (Rh, Ru, Os, Ir) since whole-rock data is not routinely available. The distribution of PGE within the whole-rock data is pertinent to the behaviour of the sulphide melt and as such is discussed within chapter 4. It should be noted, however, that the whole-rock PGE pattern (Fig. 4.21) is very similar to the PGE telluride PGE distribution (Fig. 5.5). This can be seen as evidence that the bulk of the PGE budget within the sulphide is located within the PGE tellurides. Mass balance calculations estimated that ~99% of the Pt is located within the PGE tellurides and 70% of the Pd (Fig. 4.16).

ii) Semi-metals

All PGE minerals observed in SEM analysis have been shown to be tellurides, however SEM analysis of very small mineral phases can frequently be seen as unrepresentative due to the small number of occurrences observed (in this study 88 separate grains with WDS chemistry).

In the whole-rock data, Pt and Pd correlate well with Te concentrations (Fig. 5.12) compared with no correlation with As concentrations (Fig. 5.13). Arsenic is one of the most common anions in PGE mineralogy and is almost ubiquitous worldwide in magmatic PGE deposits. The whole-rock data confirms the dominance of Te as the primary anion with negligible As in the system. At Sakatti, a simultaneous, but commercially sensitive, bulk rock processing study has confirmed the exclusivity of tellurides as the PGE mineral phases observed in this study.

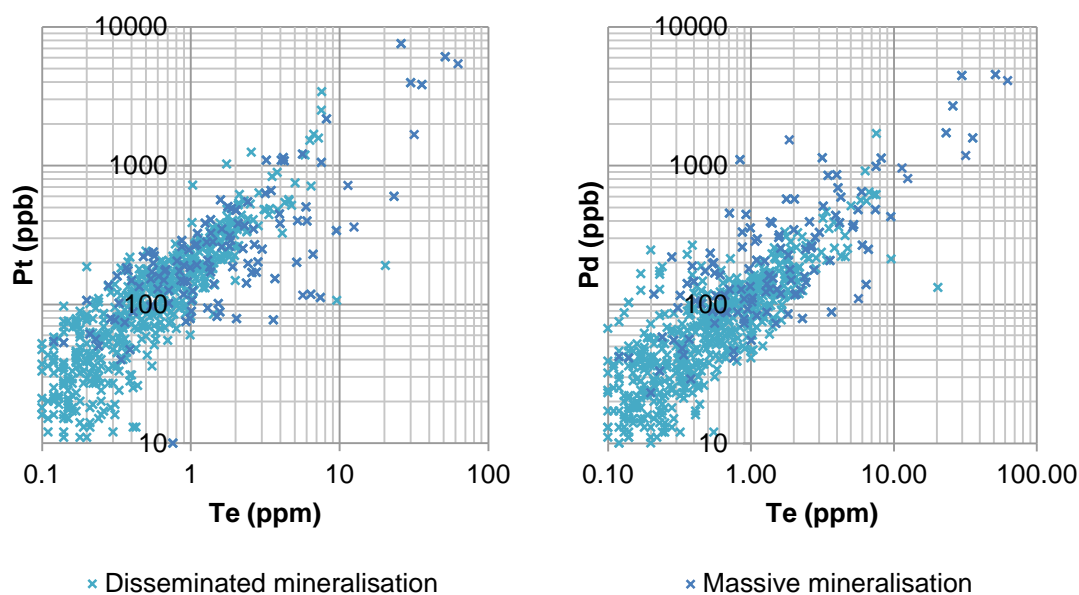


Figure 5.12 – Bulk sulphide Te against Pt and Pd showing that Te correlates with Pt and Pd.

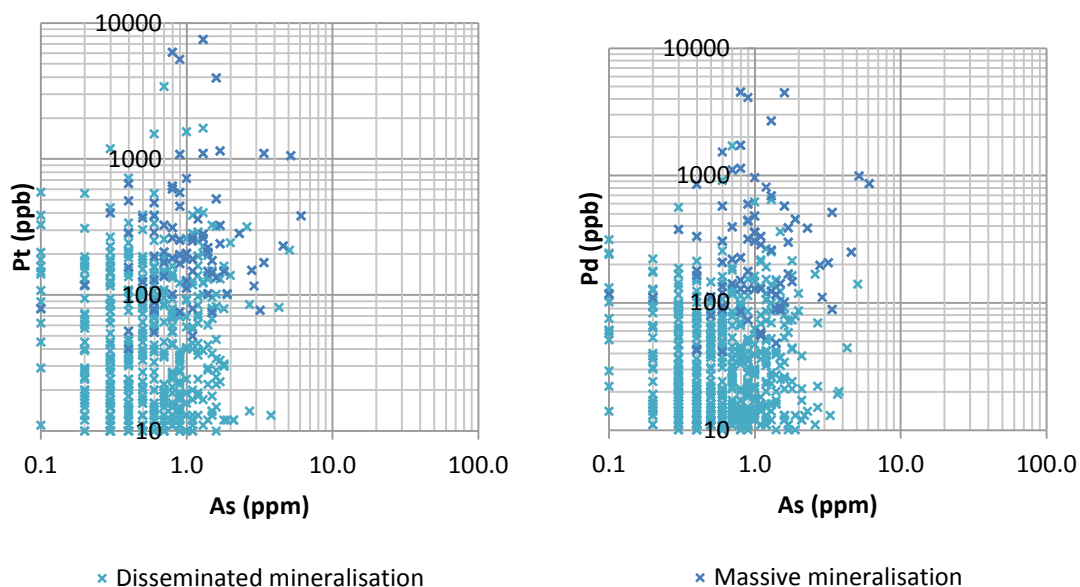


Figure 5.13 – Bulk sulphide As against Pt and Pd showing that As is much less abundant than Te and that it does not correlate with Pt or Pd.

5.4 Discussion

5.4.1 Origin of PGE mineralisation

There can be little doubt from these samples that the PGE mineralisation at Sakatti is directly derived from sulphide mineralisation either by exsolving from the sulphide minerals or crystallising or segregating from sulphide liquid. The PGE minerals are invariably spatially associated and none were found to be enclosed in silicate.

5.4.2 Disseminated vs. massive mineralisation

The samples analysed were largely selected from massive sulphide since discrete observable PGE minerals were only found within massive sulphide samples. This is an inevitable consequence of the sampling method because although as a proportion of total sulphide the disseminated samples are richer in PGE than the massive samples, only a small amount of disseminated sulphide can ever be present in one polished block.

However, HRXCT analysis combined with whole-rock geochemistry and also metallurgical test work and subsequent analysis of the products, undertaken by Outokumpu, provides adequate data to suggest that the disseminated mineralisation has behaved in the same way as the massive-hosted PGE mineralisation. PGE minerals are also exclusively (to date) telluride phases and spatially associated with sulphide (Liipo, 2012).

5.4.3 Comparison with other PGE deposits

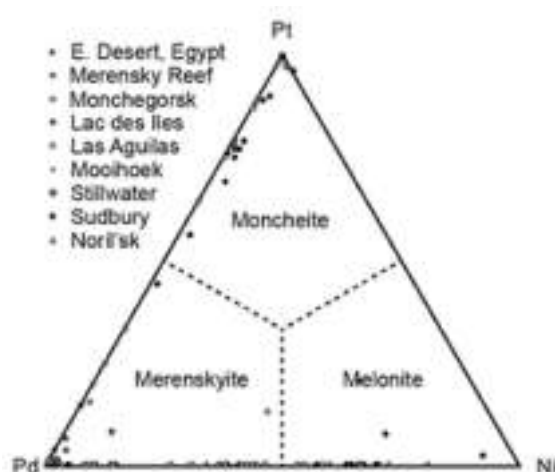


Figure 5.14 – Global moncheite-melonite-merenskyite compositions showing Pt-Pd and Pd-Ni dominance excluding Wellgreen and Kevitsa data (Helmy et al., 2007)

i) Global

Globally, tellurides are a common PGE mineral phase in magmatic Ni-Cu PGE deposits, however the author is not aware of any other deposits where tellurides are the only PGE mineral phase present. The melonite-merenskyite-moncheite series is very common but typically tellurides are only present as either a moncheite-merenskyite solid solution, in PGE-rich sulphides, or merenskyite-melonite, in PGE-poor sulphides

The Wellgreen deposit in Canada as well as the Kevitsa deposit are two deposits that contain PGE tellurides that diverge from the restricted trends of moncheite-merenskyite or merenskyite-melonite seen in most other world-wide deposits of this class (Barkov et al., 2002; Gervilla and Kojonen, 2002).

These two peculiarities of the Sakatti deposit are believed to be interrelated. Having a large range of compositions in the merenskyite-melonite-moncheite series is probably a result of having a telluride-dominated system, in which other common semi-metal ligands such as arsenic are notable by their absence.

Morphologically the PGE grains are similar to most other occurrences of PGE minerals found globally. The seemingly unusual 'needle' (or three dimensional disk) morphology has also been observed in the Pt-end-member mineral moncheite (Cabri, 2002, Plate 1H).

ii) Kevitsa

The Kevitsa deposit, located 15 km from Sakatti, also hosts PGE mineralisation. The PGE mineralisation there also largely occurs as tellurides although, unlike Sakatti, additional PGE phases have been found (Gervilla and Kojonen, 2002; Kaukonen, 2009; Mutanen, 1997). Sperrylite in particular is abundant (14%). Despite a similar telluride mineralogy, a large proportion of the PGE mineralisation occurs within silicates at Kevitsa (57%), quite unlike the situation at Sakatti (Gervilla and Kojonen, 2002).

The chemistry of the moncheite-melonite-merenskyite system (Fig. 5.15) shows data spread away from the typical linear trend of Pt-Pd and Pd-Ni seen elsewhere (Gervilla and Kojonen, 2002) in line to the findings at Sakatti.

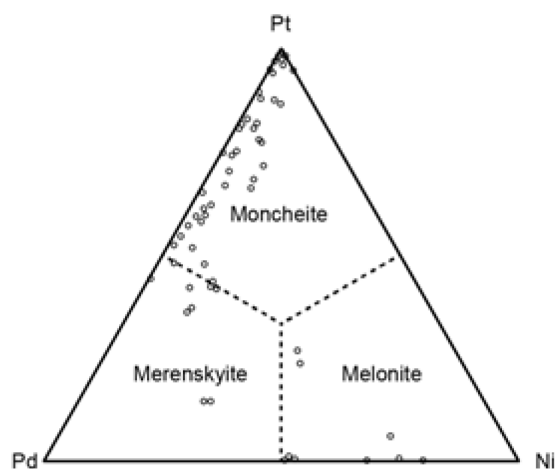


Figure 5.15 - WDS data of PGE tellurides from the Kevitsa deposit (Gervilla and Kojonen, 2002).

A broader spread of data is shown in Kaukonen (2009), however these data comprise normalised EDS analyses, acquired for 10 second live count time on samples that are mostly <2 μm in diameter it must be considered with extreme caution.

Hydrothermal processes have been cited as a redistributor of PGE and As at the Kevitsa deposit, resulting in enriched high Ni-PGE horizons in the upper part of the deposit (Gervilla and Kojonen, 2002). However, such

occurrences have been comprehensively shown to be insignificant (Le Vaillant et al., 2016). This high Ni-PGE ore type is not recorded at Sakatti hence there is no reason to suspect that this process could be present in the Sakatti system.

Sakatti and Kevitsa share similar PGE mineralogies with a dominance of telluride phases and both systems have a wide array of moncheite-merenskyite-melonite compositions. These facts indicate some commonality between the two deposits. The Sakatti system seems to be a more extreme example of a Te-rich system compared to Kevitsa, as shown by the PGE mineralogy which shows the maximum variation within the solid solution series.

The shared dominance of Te as the principle PGE semi-metal host has interesting implications for the genetic history of both deposits. They are morphologically quite different styles of deposit, with different silicate host rocks, however this shared characteristic may well suggest if not a shared genetic history then at least a shared genetic process resulting in the formation of the sulphides.

5.4.4 Controls on PGE mineralogy

5.4.4.1 Hydrothermal

The possibility of hydrothermal effect on the PGE mineralisation has been discussed at Sakatti, particularly as a means of redistributing the Pt:Pd ratio in the mineralisation.

PGE tellurides are particularly insoluble in hydrothermal fluids, and experimentation has shown them to be considerably more insoluble than either native metals or sulphides (Mountain and Wood, 1988). The possibility of tellurium acting as a complexing agent for the transportation of dissolved PGE can therefore be ruled out. Instead, tellurium may be a highly efficient fixer of PGE in the system (Wood, 2002).

Chloride ions are frequently suggested as a transporter ion of PGE, and this has been proposed for the Kevitsa deposit, possibly supported by the abundant Cl-bearing minerals at both Kevitsa (Mutanen, 1997) and Sakatti (3.3.4.6). However, experimental work has shown that chloride is only a viable as a transporter ion for PGE at both highly oxidised and acidic conditions (Wood, 2002). These conditions are not compatible with a stable pyrrhotite-pyrite-pentlandite assemblage which is the case at Sakatti, so this remobilisation mechanism can also be ruled out. In a massive sulphide deposit such as this the bisulphide complex is the most likely ligand for PGE mobility (Simon and Ripley, 2011). Pd is more soluble than Pt in hydrothermal fluids in sulphide-rich environments, which could lead to decoupling of Pt and Pd (Barnes and Liu, 2012).

Since both PGE are relatively insoluble compared to other metals, the hydrothermal remobilisation of Pt and Pd is not thought to be common (Barnes and Liu, 2012). The occurrence of all PGE within telluride minerals does not support the idea of a variable degree of hydrothermal activity redistributing Pt and Pd as one would expect the Pt-rich residual phase to have a different mineralogy to the Pd-rich mobilised phase. Considering the abundance of Te and the unlikely scenario of co-transportation of Te and PGE (Wood, 2002), the possibility of a hydrothermal control should be ruled out. Furthermore the absence of any significant hydrothermal alteration textures, as would be expected in the case of significant hydrothermal fluid flow in the massive sulphide at Sakatti, means that there is no compelling reason to consider it as a process.

5.4.4.2 Magmatic

The formation of PGE minerals in magmatic systems is still not well understood, despite this mechanism being responsible for the majority of PGE mineralisation around the globe. Sakatti is clearly a special case given that the mineralogy is exclusively tellurides. Unlike PGE sulphides, PGE tellurides cannot easily exsolve from a sulphide mineral as they are poorly soluble in monosulphide solid solution (Ballhaus and Ulmer, 1995), thus it follows that another mechanism is required.

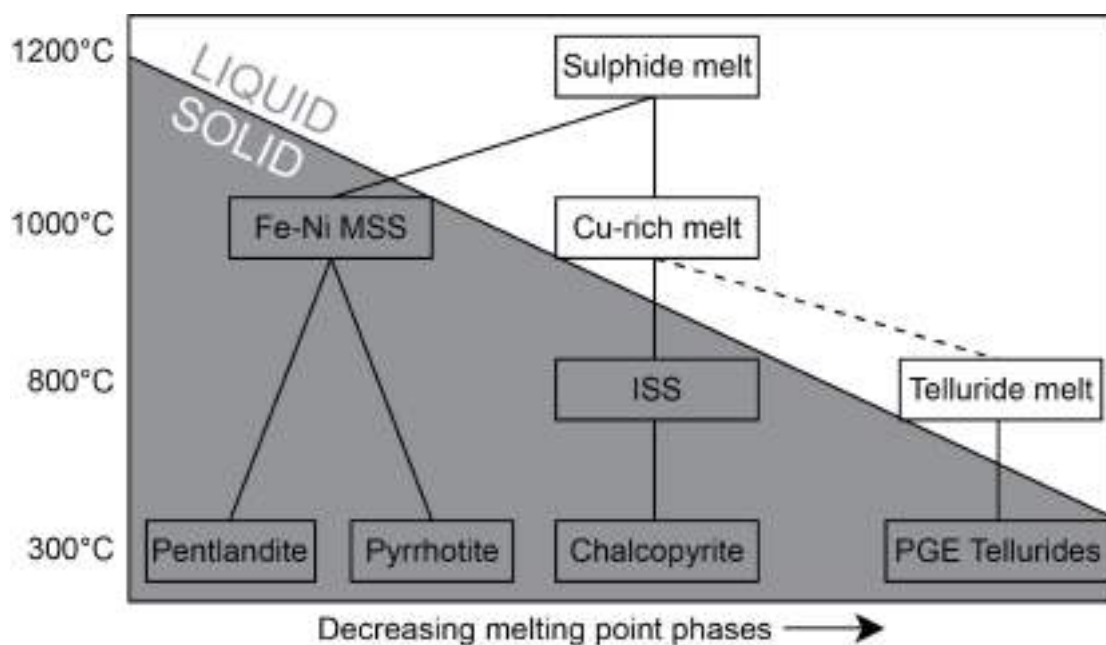


Figure 5.16 – Model for the potential formation of telluride-rich melt after fractional crystallisation of sulphide melt (Helmy et al., 2007).

The behaviour of semi-metals, in particular tellurides, within sulphide liquids is also not well understood. However, recent experimental studies have provided some insights (Helmy et al., 2007; Helmy et al., 2010). The Sakatti deposit may provide a unique view on the behaviour of tellurides because they are the only PGE mineral present and therefore the situation is not complicated by additional semi-metal ligands.

It has been demonstrated that, as opposed to exsolution from solid sulphide, PGE telluride phases can form a separate telluride melt (Fig. 5.16) when saturated within a sulphide liquid (Helmy et al., 2007). Small droplets of telluride melt could be expected to strongly partition the PGE metals from a sulphide liquid in a mechanism similar to the well-known mechanism whereby metals are concentrated in a sulphide melt from a silicate melt (Naldrett and Cabri, 1976). While at present, no partition coefficients have been calculated for telluride-sulphide melt interactions it can be assumed that PGE will strongly partition into a telluride melt due to their presence in telluride phases and relative absence in sulphide phases.

The formation of a telluride melt in these settings is proposed by some (Helmy et al., 2007; Holwell and McDonald, 2010) but rejected by others (Liu and Brenan, 2015). The latter reject the formation of a telluride melt on the grounds that the formation of the melts would not be feasible without the presence of 10s-100s of thousands of ppm of both PGE and Te in the sulphide melts. Instead Liu and Brenan (2015) consider the precipitation of PGE minerals from a sulphide melt as a more realistic model and deduce that in the telluride system, as opposed to the arsenic system, the probability of early formation of these minerals is low and that a very evolved sulphide melt is required in order to form these minerals. This implies it would happen following considerable crystallisation of ISS (Liu and Brenan, 2015), consistent with reported observations (Dare et al., 2014b).

Whether these PGE occurrences derive from small portions of PGE-telluride melt or from PGE minerals precipitating within highly evolved sulphide melt does not affect the model for formation described below, both can still equilibrate with the sulphide liquid and result from residual concentration of PGE and Te in the sulphide melt by crystallisation of sulphides.

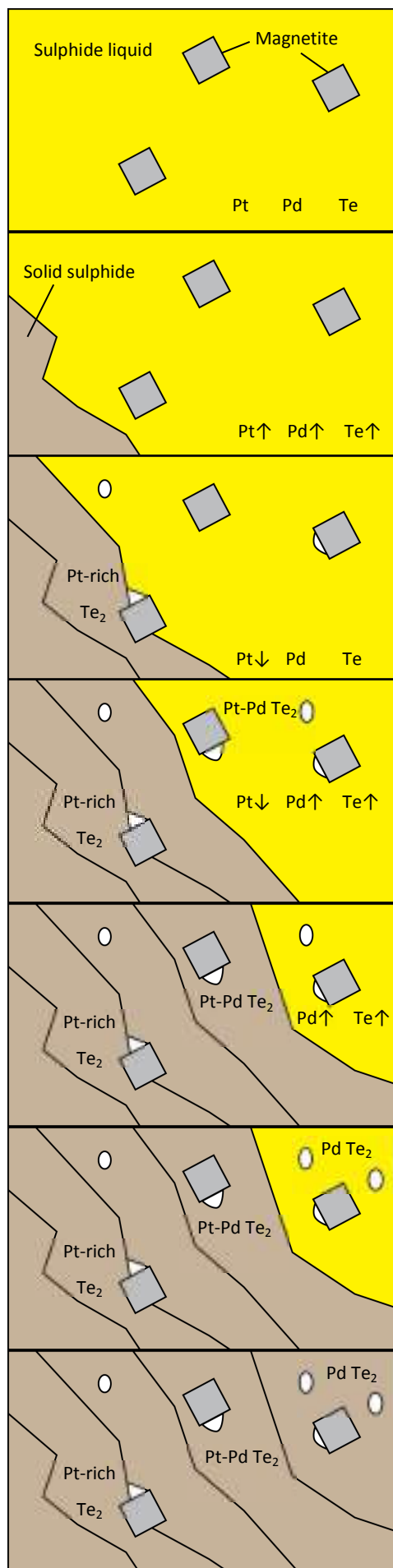


Figure 5.17 – Model for intra-sample variation of PGE telluride chemistry at the Sakatti deposit. A Diagrammatic representation is shown of the crystallisation of an evolved Cu and PGE rich melt that, in the case, is enriched in Te relative to PGE and extremely enriched in Te relative to other common semi-metal ligands for PGE minerals, such as As.

Figure 5.17a – Cu-rich evolved sulphide melt approaching crystallisation, with potential some crystallisation of other phases having occurred, symbolically represented by magnetite.

Figure 5.17b – Crystallisation of sulphide increases concentration of Pt, Pd and Te in the residual sulphide liquid as these elements are not compatible in the crystalline sulphide.

Figure 5.17c – At some point the residual sulphide liquid will become sufficiently enriched in Te and PGE to either segregate a separate Te melt (Helmy, 2007; Holwell and McDonald, 2010) or crystallise PGE Te mineral phases (Liu and Brenan, 2015). As Pt is least compatible in sulphide liquid of solid sulphide this will preferentially transfer into the Te phase and therefore decrease in the residual sulphide liquid. Te will stay in equilibrium with the sulphide liquid.

Figure 5.17d – Continued crystallisation of sulphide will further concentrate Pd and Te in the residual sulphide liquid, resulting in further production of a Te phase. As Pt is depleting in the residual sulphide then the newer tellurides will incorporate further Pd in place of Pt. This is occurring at a late stage of crystallisation so it is likely that some of the earlier telluride phase, rather than continuing to equilibrate with the sulphide liquid will be encased in solid sulphide.

Figure 5.17e – Continued crystallisation of sulphide will further concentrate Pd and Te in the sulphide liquid, Pt having been mostly depleted. Further Pt-Pd telluride compositions are encased in solid sulphide.

Figure 5.17f – PGE tellurides forming from the Pt depleted residual melt will be enriched in Pd due to the depletion of Pd in the residual melt.

Figure 5.17g – There is a small-scale heterogenous distribution of PGE telluride compositions in the resultant crystallised sulphide. In the event that Te is present in substantially larger concentrations than the Pt and Pd then this sequence could continue to include Ni and a wide variety of compositions could occur, such as those at Sakatti. While this model is undoubtedly over simplified, the presence of abundant Te relative to PGE and other semi-metals at Sakatti combined with the proposition that these phases form late-stage in a very evolved crystallising sulphide are likely to give rise to a situation such as this.

i) Small-scale (intra-sample) spatial variations in Pt-Pd ratios

The Sakatti deposit exhibits a wide array of compositions within the melonite-merenskyite-moncheite series which are not commonly observed elsewhere with the exception of two cases. The reason for this array of compositions must therefore be considered. Within samples there are individual trends (Fig. 5.2), which can be explained by preferential depletion of a particular element.

An explanation is proposed below with the caveat that several assumptions need to be made.

Assumption 1) Tellurium is in excess relative to PGE in this system. This is a reasonable assumption because of the dominance of PGE tellurides observed and also the presence of additional telluride minerals, such as hessite and kawazulite.

Assumption 2) Partition coefficients between sulphide melt and telluride melt or telluride mineral phases obey the following order $Pt > Pd >> Ni$. While these partition coefficients have not been shown experimentally it is reasonable to assume that Pt partitions most strongly into tellurides because it is not found in solid solution in remnant sulphides and that Pd partitions more strongly than Ni because the telluride phases strongly concentrate the PGE.

When a sulphide melt containing both Te and Pt and Pd begins to crystallise sulphide, it is inevitable that the Te, Pt and Pd will be concentrated in the residual melt as they are not compatible in the sulphide solid (Helmy et al., 2007). At some point as crystallisation continues there will be a point at which Te is sufficiently concentrated in the sulphide liquid that either an immiscible Te-rich melt will form (Helmy et al., 2007) or discrete PGE mineral phases crystallise (Liu and Brenan, 2015).

At Sakatti there is an abundance of Te, so it is reasonable to assume that this point would occur earlier in the crystallisation of sulphide than at other deposits. However, it is still expected to be during late-stage crystallisation of the sulphide in order to achieve the level of concentrations where Te saturation could occur (Fig. 5.17a,b). The first occurrence of Te-rich melt or a Te mineral phase is likely to concentrate Pt *as this element is least compatible in the sulphide melt and solid* (Fig. 5.17c).

During continued crystallisation, a Te melt or alternatively the precipitating Te mineral phases will continually equilibrate with the sulphide melt. However, as this is occurring during late-stage crystallisation of that sulphide it is reasonable to assume that some of these immiscible Te melt droplets or Te mineral phases will become enclosed within solid sulphide and no longer equilibrate with the melt (Fig. 5.17d). It is through this process that Pt-rich phases could be

preserved and the residual sulphide melt could evolve to more Pd-rich compositions (Fig. 5.17e,f,g). In the event that there is an excess of Te relative to Pt and Pd then the same process can occur with Ni resulting in a variety of compositions on the small scale.

This explanation is dramatically simplified compared to the array of dynamic processes than can be expected to occurring during late-stage crystallisation and enrichment of sulphide. In other deposits where there is an abundance of other semi-metals, particularly As, then it could be expected that Te is only a small part of the story of this late-stage formation of PGE minerals. However at Sakatti where there is an abundance of Te and an absence of other semi-metals then Te is the sole phase it has to incorporate the whole evolution and formation of Pt and Pd minerals and it is this case of affairs that probably gives rise to the array of moncheite-merenskyite-melonite compositions seen here and not elsewhere.

The lack of correlation between morphology and chemistry is seemingly consistent with this concept of the Te phases or melt forming at a late stage in the crystallisation of the sulphide and consequently occupying what space is available rather than growing according to crystallographic preference. Similarly the dominance of grain boundary occurrences is easy to envisage as preferential sites for late mineral growth or melt segregation.

ii) Large-scale (inter-sample) spatial variations in PGE ratios

The above mechanism can be used to explain small scale variation in the Pt:Pd ratios at the Sakatti deposit, however it does not explain variations at the metre scale. Given that the majority of the PGE budget is contained within the same solid solution mineral series it follows that there is not a mineralogical control on the larger scale Pt:Pd ratios within the deposit.

Furthermore disregarding the hydrothermal remobilisation hypothesis means that the Pt:Pd ratio must have been dictated by the Pt:Pd ratio in the host sulphide. It is shown in chapter 3 that Pd is present within pentlandite in solid solution. Telluride segregation or precipitation is controlled by the extent of crystallisation of the sulphide liquid. To this extent it could be argued that there is a potential mineralogical control on the Pt:Pd distribution in the deposit due to the timing and location of preferential pentlandite formation. Pentlandite forms both from MSS and from ISS. It has been shown experimentally that neither Pt nor Pd will partition preferentially into MSS from sulphide liquid, however pentlandite that forms from a more evolved sulphide melt, via ISS, is more likely to be palladian.

A more detailed laser ablation study of sulphides compared to PGE chemistry at the Sakatti deposit might reveal evidence that could point towards a mineralogical, namely pentlandite, control on the Pt:Pd distribution. This is intimately tied up with the evolution and fractional

crystallisation of the sulphide melt itself, which can be considered the overall primary control on PGE distribution at the Sakatti deposit. This concept along with deposit-scale PGE distribution is considered in chapter 3 and chapter 6.

5.5 Conclusions

The only Pt and Pd minerals found at Sakatti are exclusively restricted to (Pt,Pd,Ni) in the moncheite-merenskyite-melonite system and also minor michenerite .

There is almost complete solid solution between these minerals, something which is not found elsewhere with the exception of the Kevitsa deposit in Finland and the Wellgreen deposit in N. Canada.

There is no evidence for a hydrothermal control on PGE distribution at the Sakatti deposit.

Small-scale variation in Pt:Pd ratios in the telluride minerals can be explained by concentration of PGE and Te in the late stage crystallisation of evolved sulphide melt.

The dominance of Te at the Sakatti deposit means that the full range of Pt:Pd chemistry occurs as there are no alternative semi-metal ligands to take up these elements. As such Sakatti provides a unique and interesting insight into the behaviour of this mineral system.

5.6 Further work and implications for exploration

Further work on these mineral phases should focus on using bulk mineral separates to increase the amount of PGE minerals found and analysed. With a larger sample set techniques, such as Ni isotopes discussed in Chapter 4, could be employed. This could be particularly useful in determining the timing and parent sulphide of telluride formation, as Ni isotopes are potentially fractionated by sulphide crystallisation (4.3.4.2).

An extension of the LA-ICP-MS study to include more samples could mean more interesting revelations could be drawn by comparing the PGE contents of the host sulphides and the PGE contents in the tellurides. It could provide validation or disprove the model for Te controlled segregation or crystallisation of PGE phases proposed here.

The information on mode, size and location uncovered in this chapter has important processing implications for recovering PGE from this ore. The chemical homogeneity of the PGE minerals could also have implications on the method of smelting and processing. There are limited exploration implications for these findings, however the genetic implications arising from the dominance of Te and the similarity to the Kevitsa deposit, discussed in chapter 6, yield important exploration implications which have directly arisen from this work.

Experimental work on the behaviour of Te in sulphide melts is recommended. Sakatti provides a unique complementary location to investigate the behaviour of Te in sulphide melts as the other semi-metals, such as As, are absent. This means the Sakatti system could be more easily replicated in experimental systems. It is only with good experimental petrology that the nature of the Te control on PGE mineralisation at Sakatti can be fully understood.

6 Discussion

6.1 Overview of discussion

6.1.1 Summary of silicate discussion

The Olivine Cumulate Unit at the Sakatti deposit is interpreted as a shallow conduit-like intrusion (3.7.1) that is primarily within a plagioclase-rich picrite informally known as the Aphanitic Unit (3.7.6). This unit is composed principally of olivine that is not depleted with respect to Ni and intercumulus minerals that show an ϵ_{Nd} signature indicative of crustal contamination (3.7.2). This same unit also hosts magmatic amphibole suggesting that intercumulus melt was hydrous (3.7.8). The whole-rock geochemistry and mineral chemistry point to several different pulses of magmatic activity reflected in the proportions of olivine to pyroxene and evolution trends within the magmatic minerals (3.7.4). A gabbroic sub-unit represents an evolved melt resulting from fractional crystallisation, which can be associated with intergrown sulphide on account of both being the last liquid phases at the deposit (3.7.7).

6.1.2 Summary of sulphide discussion

The sulphide mineralisation at the Sakatti deposit is hosted primarily within the Olivine Cumulate Unit. The sulphide is magmatic in origin and has been minimally affected by hydrothermal processes (4.4.2). Despite the intrusion being in close proximity to the sulphide-bearing Matarakoski schists, $\delta^{34}\text{S}$ data shows that these are unrelated to the formation of the deposit and anhydrite present in some parts of the deposit texturally seems to post-date mineralisation (4.4.3). This means that the sulphide must have been formed by either a non-sedimentary or Archaean sedimentary S contaminant or by processes that trigger S saturation without the addition of S such as contamination by the addition of silica.

Pyrite present in the deposit, while initially thought to be an alteration product, carries enriched IPGE and Ni isotope characteristics that are difficult to explain by hydrothermal processes. This suggests that these might be the result of the formation of original magmatic MSS cumulates (4.4.4). The low Ni/Cu ratio at the deposit conforms to the low IPGE/PPGE ratios as well as negative Ni isotopes and sulphide-melt-derived magnetite trace element contents. These all suggest that the low Ni/Cu ratio is explained by loss of an earlier phase of sulphide crystallisation as primitive MSS cumulates (4.4.5).

6.1.3 Summary of PGE discussion

PGE mineralisation at the Sakatti deposit originates from the sulphide mineralisation (5.4.1) and is present in both disseminated and massive sulphide (5.4.2). The PGE phases are exclusively tellurides, something which is unusual globally but is similar to telluride dominance at the adjacent Kevitsa deposit (5.4.3). The exclusivity of tellurides suggests hydrothermal processes are not a control on PGE mineralisation. The dominance of telluride phases has led to a wide array of moncheite-merenskyite-melonite compositions, which are not usually seen at one location, and also goes some way towards explaining the Pt:Pd ratio variability at Sakatti (5.4.4).

6.2 Model constraints from the geology

Understanding of the morphology of the Sakatti deposit has progressed alongside this project. This is because the number of drill holes in the deposit has increased from <30 when the project began to >150 currently. This has led to a much greater understanding of the layout and morphology of the deposit largely as a result of the efforts of the Anglo-American Exploration Finland team. This improved morphological understanding is thus not a result of analyses or work undertaken in this study, however it must be discussed and interpreted here as it is fundamental to understanding the deposit.

The main-body Olivine Cumulate Unit, the main unit to host mineralisation, is a broadly tubular structure that plunges from south-east to north-west. It is contained within the Aphanitic Unit footwall and hanging wall but in part cross cuts into the Breccia Unit and Mafic Suite hanging wall above the Aphanitic Unit. The plunge of this tubular body is shallow in the south-east, steeper in the central portion of the deposit and shallower in the deeper north-west. This change of plunge is a key feature of the deposit. It coincides with the breaching of the deposit into the overlying Breccia Unit and could well be the result of an 'unroofing' of the intrusion from the dense, dry Aphanitic Unit into the lower melting point and wetter sediments of the overlying units. This change in plunge is where the largest concentration of mineralisation is and also one of the main occurrences where the mineralisation extends into the footwall.

Traditional considerations of layered cumulate Ni-Cu-PGE systems sought to estimate the volume of silicate melt and the volume of sulphide melt in order to determine the extent of depletion that occurs and to balance the formation of the deposit (Naldrett, 2004). This approach frequently finds that a much larger volume of silicate melt is required than is present (Lightfoot and Naldrett, 1999; Thériault et al., 1997). At the Sakatti deposit the cumulate body is ~400 m thick and yet hosts sulphide accumulations over 25 m. Given that one of the main

conclusions of this study is that the current silicate host is not parental to the sulphide melt it is unsurprising that these estimates of silicate vs. sulphide metal contents do not apply in this setting, however what is clear is that the sulphide deposit would have needed considerably more typical silicate melt to form than is present. This is to be expected, as in a conduit system one could expect the total magma that has passed through to be many orders of magnitude higher than that which remains in place.

In a conduit system, flow dynamics of the magma are a primary control to the deposition of dense sulphide liquid as well as cumulus minerals (Barnes and Lightfoot, 2005; Barnes et al., 2015). The Sakatti intrusion has a conduit-like morphology and it is the change in plunge of this conduit, potentially brought about by a lithological transgression, which has allowed significant volumes of dense sulphide to accumulate, unable to ascend the change in plunge. This model allows for huge amounts of silicate magma to pass through the conduit, potentially depositing sulphide but also potentially resorbing and upgrading the remnant sulphide. Sulphide melt also has the potential to flow gravitational back down towards the change in plunge (Benkó et al., 2015).

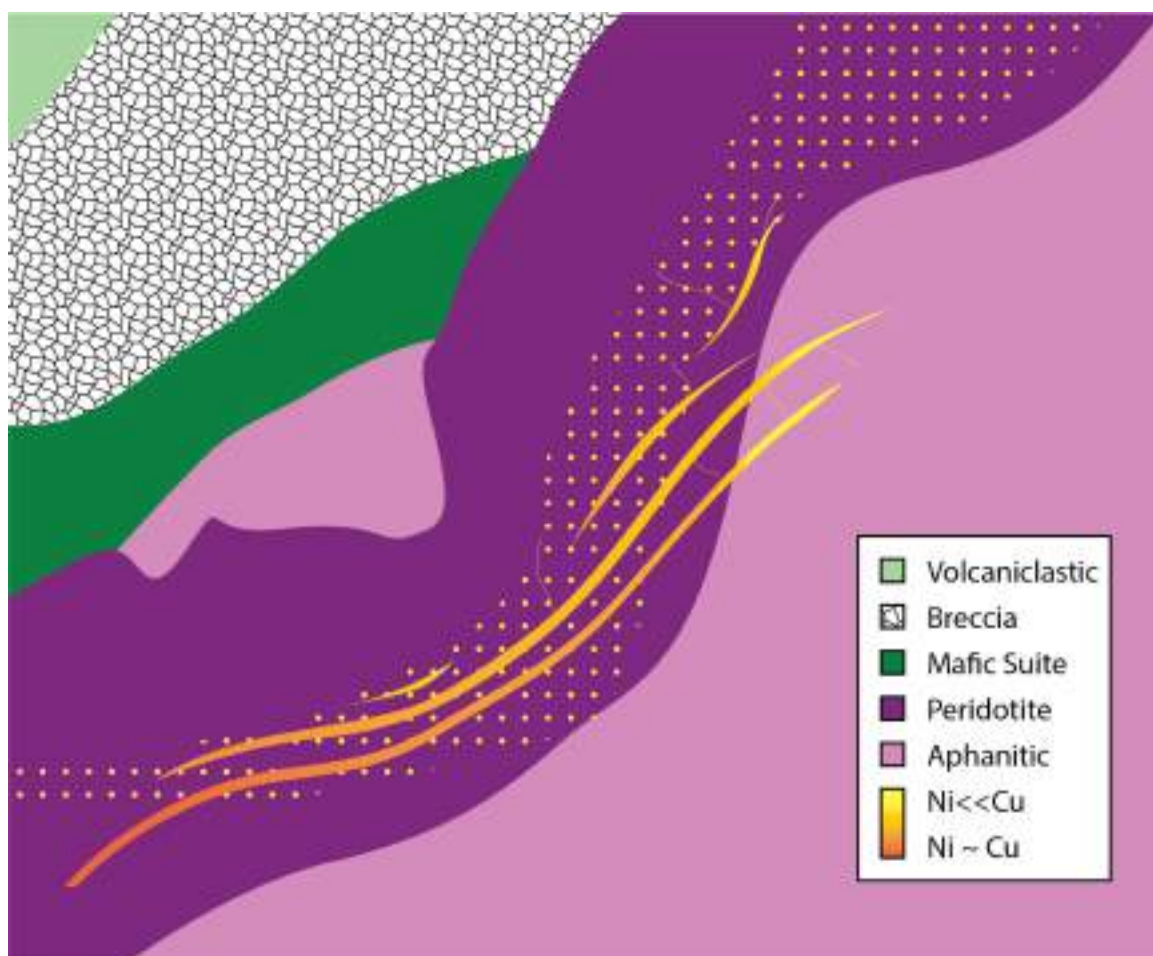


Figure 6.1 – cartoon showing the shape of the deposit and mineralisation

The relationship of the additional cumulate bodies to the main-body cumulate is not clear. It seems likely that the north-east body has been faulted off the main-body whereas the south-west body seems unconnected or potentially another branch of the main-body, stratigraphically higher.

6.2.1 Origins of ultramafic magmatism

There is extensive ultramafic magmatism in the CLGB. There are two stages of komatiitic volcanism, the Onkamo komatiites/picrites and the Savukoski komatiites/picrites as well as several intrusions, particularly at 2.45 Ga, 2.2 Ga and 2.05 Ga (Mutanen and Huhma, 2001; Vuollo and Huhma, 2005). This extensive magmatism is attributed to rifting at the CLGB within the Karelian Craton (Hanski and Huhma, 2005; Weihed et al., 2005).

The Sakatti deposit shares many characteristics with the Kevitsa deposit, which is coeval with the Savukoski komatiites (Hanski et al., 2001a; Mutanen and Huhma, 2001). Both Sakatti and Kevitsa have negative ϵ_{Nd} values while the Savukoski komatiites show uncontaminated ϵ_{Nd} (Hanski et al., 2001a and this study). It could be suggested that these three ultramafic magmatic events are interrelated, however the Savukoski komatiites have travelled to the surface without becoming contaminated with crustal material and they host no ore deposits, while the Kevitsa and the Sakatti intrusions both ascended in a more indirect fashion, becoming contaminated with crustal material, reaching S saturation and having no surviving surface manifestation of extrusive volcanism.

The Aphanitic Unit is not ultramafic by definition due to containing more than 10% plagioclase, however it is very rich in Mg and can be considered as resulting from komatiitic magmatism (Konnunaho et al., 2016). The unit is bounded in turn below by a fault, and then probably the Sodankylä quartzite. Above, the unit is bounded by the Breccia Unit and the Mafic Suite. While it is still not particularly clear where this sits in the regional stratigraphy, the Breccia Unit does feature arkosic quartzite clasts within it and could potentially contain brecciated Sodankylä quartzite.

It is possible that the Aphanitic Unit is part of the same magmatic event as the Olivine Cumulate Unit, preceding it by a short amount of time, or that the Aphanitic Unit was a pre-existing unit that formed from an earlier magmatic event. The Onkamo komatiites are located below the Sodankylä quartzites and occurred around 2.44 Ga (Puchtel et al., 1997). If the Aphanitic Unit is related to an earlier magmatic event this is most likely candidate, however it seems more likely that the Aphanitic Unit is part of the magmatic event resulting in the Sakatti intrusion.

6.2.2 The origin of sulphide mineralisation

The sulphide mineralisation has been shown not to be the result of contamination by the Matarakoski schists (4.4.3), or any other sediments with non-mantle $\delta^{34}\text{S}$ (those that are late Palaeoproterozoic or younger). This does not, however, indicate what has been the cause of sulphide saturation. One of the main conclusions of this study is that the current host cumulate is not the parental melt that formed the sulphide, thus it means that very little can be said about what caused the sulphide to form.

Assuming that the parental melt was similar in composition to the current cumulate host provides two important characteristics, first that it was a primitive ultramafic melt and second that it was at least slightly crustally contaminated. Primitive ultramafic melt presents a problem for S saturation because it needs it have originated from considerable depth in the mantle (Arndt et al., 2005). Because of its deep origin it would have been is very undersaturated with respect to S when it reaches the surface, due to the effect of pressure decrease increasing S solubility (Mavrogenes and O'Neill, 1999).

Three cited methods for achieving S saturation are considered below.

i) Fractional crystallisation

In order for a silicate melt to S saturate it is necessary to crystallise extensive silicate phases (Burrows and Lesher, 2012), the consequence of this is that you end up with a relatively evolved silicate melt, unlike at Sakatti. Furthermore if a melt is not near S saturation then saturation will not occur until there has been a great degree of crystallisation, by which point it is unlikely that any conduit is open enough and massive sulphide will not be able to pool together successfully.

ii) Silica contamination

The current host rock indicates that it has been crustally contaminated to some degree. The extent of crustal contamination is likely to have been low given the primitive nature of the olivine. While increasing silica content decreases the solubility of S, this mechanism has only been applied to relatively near to S saturated melts (Li and Naldrett, 1993; Seat et al., 2009). It would not apply in a conventional ultramafic melt unless it was already near S saturation by some other means.

iii) S addition

Addition of S is the most practical mechanism for bringing a potentially S undersaturated melt to S saturation. However any potential S contaminant remains unconstrained at Sakatti. The intrusion has travelled through thick Archaean basement and the potential for a S source within

it is unknown. Both Sakatti and Kevitsa sulphide bodies have a strong Te control on PGE mineralisation and it would appear that the two deposits potentially share the same S source which may have been enriched in Te.

The problem with each of the interpretations of the models above is that they rely on the parental magma having been similar in composition to the current host cumulate. While it is suggested here that the parental magma is an earlier phase of magmatism in the same conduit system, it could have had considerably different characteristics. Without that information it is only possible to make assumptions based on the current host.

6.2.3 Disequilibrium between silicate and sulphide

As stated above, the host Olivine Cumulate Unit is not a viable source for the metals in the Sakatti sulphide deposit supported by evidence of the olivine chemistry at Sakatti, which is certainly at odds with it being the host rock for a Cu-rich highly evolved deposit (3.7.9). This is evident from the high Ni contents of the olivine and also the Ni depletion at the rims of olivine in the most mineralised parts of the deposit. Therefore it is not possible that the olivine and the sulphide originated from the same parental melt.

This means that the silicate melt and the sulphide melt must have physically interacted, but not had time to fully equilibrate. It is also possible that the olivine was already crystalline, being carried as a cumulus phase prior to collection of the sulphide. That the pyroxene Ni content is variable and correlates between diopside and enstatite suggest that the intercumulus melt was attempting to equilibrate with sulphide to a varying degree. The Ni content in olivine is less variable and does not correlate with either pyroxene suggesting that the olivines had already formed and are only equilibrating at the edges by diffusion (3.4.1.4).

Morphological evidence suggests the geometry of the conduit-like intrusion had a transgressive kink where accumulation of sulphide has occurred and this would also apply to settling of cumulus phases. Cumulus olivine and chromite could well have been carried by the magma flow within a conduit and deposited where a drop in energy occurred prior to change in the angle of the conduit. Olivine could also settle back down the steeper part of the conduit.

It is because of this dynamic flow model that it is not particularly surprising that stratified layers have been identified within the intrusion as it could be better considered as a slumping, crystal mush during formation and the likelihood of neat layers that could be correlated between drill holes is slim.

6.2.4 Cu-rich nature of mineralisation

Sakatti is unusually Cu-rich for a magmatic Ni-Cu deposit. The potential causes for a Cu-rich Ni deposit are (Burrows and Lesher, 2012).

Partial melting

Partial melting of the mantle results in the formation of magmas that form Ni-Cu-PGE deposits. Copper is present within sulphide in the mantle whereas Ni is largely held by olivine (Naldrett and Barnes, 1986). If the mantle source is relatively oxidised this could destabilise sulphide and mean that Cu is liberated at a relatively low degree (15%) of partial melting (Arndt et al., 2008). However the observed silicate mineralogy at Sakatti is not consistent with a low degree of partial melting of the mantle as the lithologies are primitive and ultramafic, which requires a high degree of partial melting (40%).

Fractional crystallisation

Fractional crystallisation of olivine would deplete the melt in Ni meaning that if the remnant silicate melt were S saturated then a Cu-rich sulphide would be formed. This would also result in an evolved silicate melt, for which there is no evidence at Sakatti. Furthermore the crystallisation of substantial amounts of olivine would settle with any forming sulphide mineralisation and so it would likely result in a disseminated deposit only.

Magma/sulphide ratio

Discussion of magma/sulphide ratio (termed R factor) has been avoided in this study because the proportions of the sulphide and especially its parent silicate are completely unknown and estimating them would be inappropriate and probably unhelpful. Given the assumption that this is a conduit system and what is 'downstream' is completely unconstrained, any attempt to use the current proportions of the host, which is also assumed not to be the parent melt, would be potentially misleading. The parent silicate remains to be identified. Where the proportion of parent silicate is vastly greater than the amount of sulphide then a Cu-rich deposit can be formed. However this is not at the expense of Ni, rather high R factors will result in a deposit rich in both, so this again fails to explain the low Ni/Cu ratios seen at the Sakatti deposit.

Fractional crystallisation of MSS

This is the preferred model to account for the Ni/Cu distribution at Sakatti and the evidence for this has been outlined in the sulphide discussion (4.4.5). Crystallisation of MSS from sulphide liquid serves to deplete it in Ni, while as a result the remnant portion becomes Cu, Pt and Pd-

rich. The loss of most primitive MSS cumulates will deplete further forming sulphide in IPGE and Ni. This process can repeat any time that there is sulphide crystallisation and a good example is the very Cu-rich 'vein' type mineralisation that extends into the footwall at Sakatti. The unusual orbicular pyrite is also likely to represent a second phase of MSS cumulate formation during crystallisation of the sulphide, having already been magmatically remobilised at least once.

Hydrothermal/metamorphic/tectonic upgrading

This process is discounted since there is no evidence for significant hydrothermal remobilisation at Sakatti. The presence of pentlandite flames within the pyrrhotite suggests that there has only been minimal metamorphism to the deposit, consistent with little post-formation overprinting to the sulphide mineralisation (4.4.2).

6.2.5 Genetic model

Proposed model

The genetic model proposed here is an attempt to explain the origin of the sulphides and the Cu-rich nature of the Sakatti mineralisation (6.2.3 and 6.2.4). The model is predicated on the need to have crystallisation of sulphide prior to magmatic remobilisation by the current silicate host melt (Fig. 6.2).

The first assertion is that the sulphide deposit initially formed, further down the conduit from the current site occupied by the deposit by an earlier phase of magmatism in the same conduit. This is not temporally constrained allowing for significant, unknown, quantities of magma to flow through the system and result in accumulation of sulphide, pooling because of its density.

This segregated sulphide would need to cool sufficiently to enable crystallisation of MSS cumulates, which occurs at around 1100 °C (Li et al., 1996) assuming no pressure correction. Later magmatism would then bring the current silicate host, potentially already carrying cumulus olivine, into contact with this sulphide and preferentially remobilise the Cu-rich higher portion of the partially or completely crystalline sulphide. This Cu-rich portion is then deposited along with the cumulus olivine at a physical break in slope of the conduit, where it transgresses to a higher, more erodible lithology above the Aphanitic Unit.

Erosion of the Aphanitic Unit footwall results in the micro-intrusive texture documented earlier and also results in contamination of the intercumulus melt, not affecting the already formed olivines. As cumulate olivine is deposited the mineralisation is covered and the upper layers of

cumulate formation did not have any contact with the mineralisation, and therefore do not mobilise it. The massive mineralisation remains mobile after the cumulate-pile silicate solidifies and intrudes both into it and also into the footwall where the plunge of the conduit changes.

Fluid associated with the partially hydrous intercumulus melt auto-serpentinises most of the olivine associated with the deposit. Above the intrusion the Breccia Unit formed as a site of contact metamorphism and metasomatism, potentially resulting in phreatomagmatic brecciation since the breccia protolith was likely to be rich in water.

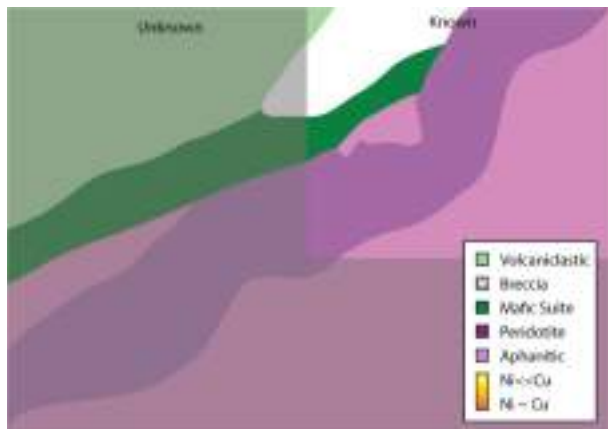


Figure 6.2 – Systematic cartoon of deposit formation Hypothetical scenario based on (Fig. 6.1). The orientation is unknown but it is suggested that the local lithologies are horizontal.

Figure 6.2a – A conduit exists in the place of the current Sakatti deposit. Although dimensions are shown approximal to current dimensions this is not necessarily the case. The Breccia Unit is omitted as it may not have formed prior to the intrusion. Known geology is shown in full colour while speculation is faded.

Magma flow in the conduit is an early precursor of the Olivine Cumulate Unit



Figure 6.2b – An accumulation of sulphide forms down plunge of the site of the current Sakatti project. The parental melt of this sulphide passes through the conduit. The sulphide can accumulate with continual magma flux and potentially be resorbed by S undersaturated magma.



Figure 6.2c – The sulphide accumulation cools sufficiently for fractional crystallisation of MSS to occur. Early MSS cumulates form at the base of the sulphide. The remaining sulphide could also begin to crystallise and any amount of time could elapse provided the conduit did not fully close.



Figure 6.2d – Silicate melt carrying crystalline olivine flows through the conduit. If the sulphide melt had crystallise it is re-melted.

Olivine cumulate begins to accumulate under gravity at a transgressive kink in the conduit. This is the current site of the Sakatti deposit.

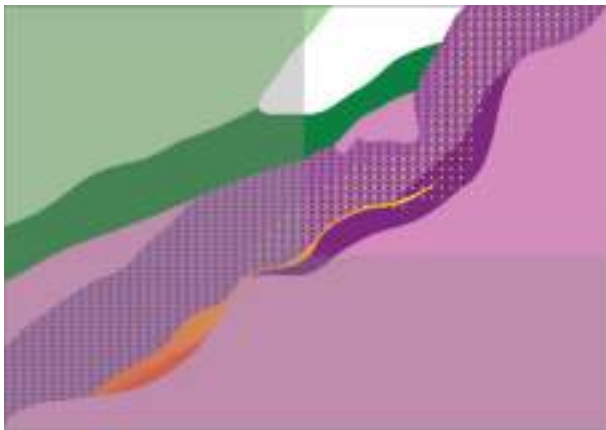


Figure 6.2e – The cumulate carrying crystalline olivine remobilises the Cu-rich fractionated portion of the sulphide deposit. This is carried and deposited along with olivine deposition to form the disseminated mineralisation. Cu-rich massive sulphide is also mobilised by the magma flux.

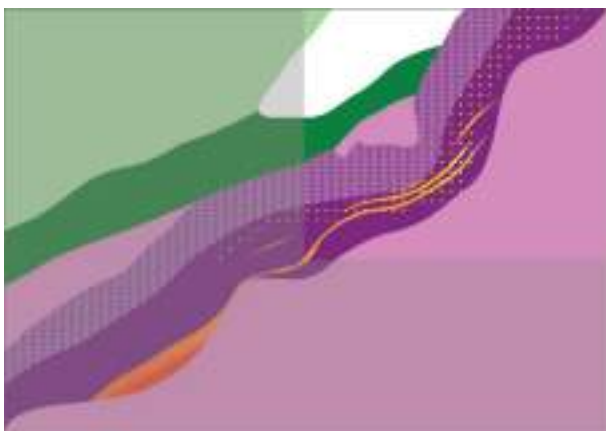


Figure 6.2f – Olivine accumulation continues, trapping the disseminated sulphide and also potentially covering the original sulphide. Unmineralised melt continues to flow over the top of the conduit.

While the silicate melt crystallises around the olivine cumulate pile, the liquid sulphide melt continues to migrate and intrude the sulphide.

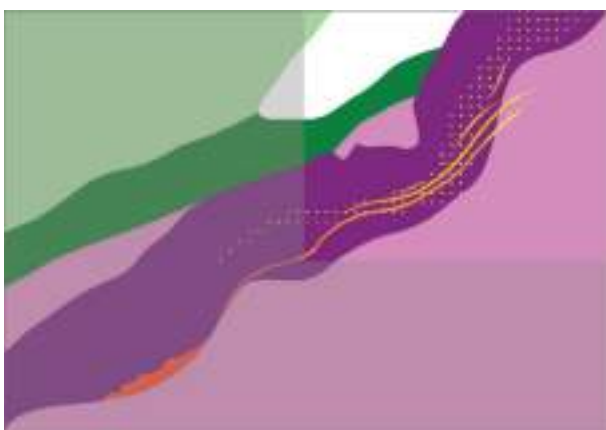


Figure 6.2g – Mobile sulphide melt intrudes the footwall. Ni-rich parts of the deposit crystallise leaving the most evolved Cu-rich sulphide to form the vein-type mineralisation and intrude the footwall. Late stage silicate melt is squeezed from the silicate pile forming dykes of the Pegmatoidal Gabbro Sub-Unit, which mix with mineralisation.

Speculative model

Applying Occam's razor would suggest that the sulphide formation is probably related to similar but slightly earlier magmatism in the same conduit as the deposit. However there are several lines of evidence that tentatively suggest a more speculative interpretation which is included below, however without further supporting evidence it is not endorsed.

- The olivine within the Aphanitic Unit is Ni-depleted and does not show the characteristic decrease in Ni with Mg# suggesting there has been another control to Ni content.
- The Aphanitic Unit has been problematic to define because of its combination of high whole-rock Mg# and also high plagioclase content meaning it is not ultramafic.
- The characteristics that could point towards potential parental host rock of a sulphide deposit are that it would have Ni-depleted minerals and have unusual contamination signatures (6.2.2).
- The stratigraphic location of the Aphanitic Unit is unconstrained with regard to the wider CLGB as it has not been recognised elsewhere. It lies below the Breccia Unit which has been interpreted to have an arkosic quartzite as one of the protoliths (Jillings, 2015). Assuming that the breccia represents the Sodankylä quartzites then the Aphanitic Unit would be placed below that and potentially could be the Onkamo unit of komatiitic magmatism recognised in the CLGB.
- The Onkamo unit has crustally contaminated ϵ_{Nd} signatures (Hanski et al., 2001a).

All these considerations combined could suggest that the Aphanitic Unit could actually be an earlier stage of komatiitic magmatism that may have been parental to a Ni-Cu deposit. The Sakatti intrusion could then be magmatically remobilising this earlier formed deposit. If this were the case it raises the intriguing possibility that there is a prospective komatiitic horizon underlying the CLGB that both the Sakatti deposit and the Kevitsa deposit have remobilised sulphide mineralisation from.

It has to be stated that this model relies on coincidence of two types of potentially deposit forming magmatism occurring in the same place, first Onkamo and then Sakatti. Given how infrequent sulphide and deposit formation is, it is more rational to assume that there has only been the one type of deposit forming magmatism and that it is all related to the Sakatti conduit.

7 Conclusions

7.1 Conclusions

The Sakatti Cu-Ni-PGE deposit is both disseminated and massive sulphide hosted by an olivine cumulate body termed the Olivine Cumulate Unit. This host unit is comprised primarily of Ni-undepleted olivine, which has not formed from the same parent melt as the sulphide. The cumulate body sits within a plagioclase-rich picrite which forms both the footwall and part of the hanging wall and is termed the Aphanitic Unit.

The cumulate body cross cuts hanging wall units and is interpreted as a shallow level conduit-like intrusion in the Aphanitic Unit. This tubular shaped intrusion has a change in angle where the locus of the deposit occurs, potentially due to the intrusion transgressing into higher lithologies. Sulphide has collected in this kink in the conduit body and also intruded into the footwall Aphanitic Unit.

The intrusion as a whole shows a crustally contaminated ϵ_{Nd} signature, in contrast to the primitive olivine chemistry, however the ϵ_{Nd} may be reflecting the isotopic signature of the intercumulus melt. The whole-rock geochemistry and mineral chemistry within the cumulate body indicate several different phases of magmatic activity. A gabbroic sub-unit is present and associated with mineralisation that likely represents final evolved silicate melt from the intercumulus, remobilised through the intrusion in the form of dykes.

The $\delta^{34}S$ signature of the sulphide mineralisation is close to mantle values indicating that the Matarakoski sulphide-bearing schists did not contribute S to the deposit and trigger S saturation. The cause of S saturation is unconstrained but likely to be either contribution of earlier S or silica contamination.

The Cu-rich nature of the deposit relative to Ni correlates with PPGE/IPGE, sulphide-derived magnetite trace elements and Ni isotopes to indicate that it is caused by fractional crystallisation of sulphide melt and loss of early MSS cumulates.

PGE mineralisation at the Sakatti deposit is hosted by telluride phases within sulphide. These are magmatically derived and the unusual dominance of Te suggests a Te-rich As-poor potential contaminant and also potentially a shared genetic history with the Kevitsa deposit.

The model put forward is that intrusion is not the parental melt from which the sulphide mineralisation derived, instead that the sulphide mineralisation formed from earlier, related

magmatism in the same conduit and has been magmatically remobilised by the current silicate host. This earlier stage of sulphide accumulation resulted in at least partial crystallisation of MSS cumulates resulting the remobilised fraction being more evolved and Cu-rich.

7.2 Implications for exploration

The presence of Ni-undepleted olivine hosting a magmatic Cu-Ni sulphide should mean that the exploration strategy of looking for Ni-depleted silicate should be disregarded. The Sakatti deposit indicates that even if a Ni-depleted silicate still exists it could well be spatially so far removed from the deposit that it provides little useful information.

The demonstrated absence of contamination by the Matarakoski schist at Sakatti, and also Kevitsa (Grinenko et al., 2003), means that this unit should not be considered an important ore forming unit. The coincidence of mafic/ultramafic bodies with sulphide bearing sediments is a potential exploration tool, however for the CLGB it should not be considered and all mafic/ultramafic bodies can be treated as potential targets regardless of their proximity to the Matarakoski schists.

The presence of a negative ϵ_{Nd} signature at both Sakatti and Kevitsa, but not in the barren Savukoski komatiites (Hanski and Huhma, 2005), may suggest an exploration tool that indicates prospective ultramafic bodies in the CLGB, however much more analysis is required before this could be stated with confidence. The expense and intricacy of Sm/Nd analysis means that it is not particularly suited to large quantities of analyses as an exploration tool.

The Onkamo komatiites are known to have a negative ϵ_{Nd} signature and are potentially implicated in a highly speculative model presented in this paper. Their occurrence within the CLGB succession could be a potential focus for further research leading to exploration potential.

The model of sulphide fractionation resulting in the Cu-rich nature of the Sakatti deposit has several implications. The mistake of discounting Ni-Cu-PGE systems where the Ni/Cu ratio is low, which almost happened prior to discovery of the Sakatti deposit, should not be repeated. As Sakatti demonstrates a Cu-rich sulphide can still indicate a significant deposit. The implication of a loss of MSS cumulates down-plunge in the same conduit is significant at Sakatti as it implies that a Ni-rich extension of the deposit may exist at greater depth.

Rather than attempting to intersect this potential extension with deep-drilling it is recommended that the techniques that have indicated Ni/Cu fractionation, principally PPGE/IPGE ratios and magnetite trace elements should be applied to a greater spread of the currently delineated deposit. These techniques are both suited to high-throughput analysis.

Once a three dimensional model of fractionation has been established, the potential size of any lost MSS cumulates can be estimated by mass balance and it can be judged whether it warrants further drilling at greater depth.

7.3 Further work

This study has been the first academic investigation into the Sakatti deposit and has used many different techniques. It is therefore inevitable that there is considerable further work to recommend. A priority at the Sakatti deposit should be further analysis to determine the amount of MSS cumulate formation. As the extent of sulphide mineralisation becomes better constrained through the creation of geostatistical models the possibility of estimating the extent of MSS cumulate formation through mass balance calculations becomes available. This approach could be compared to a hypothetical initial sulphide melt (calculated using PPGE/IPGE ratios) to estimate the possibility of further MSS cumulates down-plunge of the deposit.

IPGE/PPGE whole-rock analysis provides a relatively cheap way to assess degree of fractionation and it is recommended that a larger spatial spread of this type of analysis is acquired. Magnetite trace element analysis has the potential to be a quick tool, given the large size of sulphide derived magnetite and it is strongly recommended that a suite of samples with different degrees of sulphide fractionation is examined using this technique.

Nickel isotope analysis has provided an interesting insight into potential MSS-ISS fractionation processes at Sakatti, however there are very few deposits where this technique has been demonstrated. Further Ni isotope analysis is recommended on deposits which are well constrained and samples well characterised. This would provide a framework to test the processes that are governing Ni isotope fractionation, with which this technique could be more usefully applied to new discoveries such as Sakatti.

It is not recommended that further $\delta^{34}\text{S}$ work is carried out at Sakatti unless new styles of mineralisation warrant it, in particular if a 'false ore' style similar to that at Kevitsa is found. However mass independent fractionation of S remains untested, and this could provide insight into a potential Archaean source of contamination.

Further study on the anhydrite at Sakatti, such as fluid inclusions or Sr isotopes could provide a much greater insight into this enigmatic unit. The possibility of a sedimentary origin has to be tested by these techniques. If that is demonstrated then the model for the formation of the deposit will need reforming.

Outside of the deposit itself further investigation into the aphanitic footwall is essential. If this unit could be located in the CLGB stratigraphy it would mean that the wealth of previous study of the CLGB would be more pertinent to the Sakatti deposit. While the deposit remains stratigraphically untethered it is difficult to draw region-wide conclusion on the implications of the deposit.

8 References

- Åhäll, K.-I., and Larson, S. Å., 2000, Growth-related 1.85–1.55 Ga magmatism in the Baltic Shield; a review addressing the tectonic characteristics of Svecofennian, TIB 1-related, and Gothian events: *GFF*, v. 122, no. 2, p. 193-206.
- Alapieti, T., and Lahtinen, J., 1986, Stratigraphy, petrology, and platinum-group element mineralization of the early Proterozoic Penikat layered intrusion, northern Finland: *Economic Geology*, v. 81, no. 5, p. 1126-1136.
- Andersen, J. C. Ø., Thalhhammer, O. A. R., and Schoenberg, R., 2006, Platinum-group element and Re-Os isotope variations of the high-grade Kilvenjarvi platinum-group element deposit, Portimo layered igneous complex, Finland: *Economic Geology*, v. 101, no. 1, p. 159-177.
- Arndt, N. T., Leshner, C. M., and Czamanske, G. K., 2005, Mantle-derived magmas and magmatic Ni-Cu-(PGE) deposits, in Hedenquist, J. W., Thompson, J. F. H., Goldfarb, R. J., and Richards, J. P., eds., *Economic Geology 100th Anniversary Volume 1905-2005*: Littleton, CO, Society of Economic Geologists, p. 5-23.
- Arndt, N. T., Leshner, C. M., and Barnes, S. J., 2008, *Komatiite*, Cambridge, Cambridge University Press, 457 p.:
- Asp, K., Schardt, C., and Spivak-Birndorf, L., 2015, Ni Isotope Signatures of Duluth Complex Cu-Ni-Pge Mineralization: *Goldschmidt abstracts*, no. 132.
- Ballhaus, C., and Ulmer, P., 1995, Platinum-group elements in the Merensky Reef: II. Experimental solubilities of platinum and palladium in Fe_{1-x}S from 950 to 450°C under controlled fS₂ and fH₂: *Geochimica et Cosmochimica Acta*, v. 59, no. 23, p. 4881-4888.
- Barkov, A. Y., Laflamme, J. H. G., Cabri, L. J., and Martin, R. F., 2002, Platinum-group minerals from the Wellgreen Ni-Cu-PGE deposit, Yukon, Canada: *Canadian Mineralogist*, v. 40, p. 651-669.
- Barnes, S.-J., and Lightfoot, P. C., 2005, Formation of magmatic nickel sulfide ore deposits and processes affecting their copper and platinum group element contents, in Hedenquist, J. W., Thompson, J. F. H., Goldfarb, R. J., and Richards, J. P., eds., *Economic Geology 100th Anniversary Volume 1905-2005*: Littleton, CO, Society of Economic Geologists, p. 179-213.
- Barnes, S. J., 1998, Chromite in komatiites, 1. Magmatic controls on crystallization and composition: *Journal of Petrology*, v. 39, no. 10, p. 1689-1720.
- Barnes, S. J., Fiorentini, M. L., Austin, P., Gessner, K., Hough, R. M., and Squelch, A. P., 2008, Three-dimensional morphology of magmatic sulfides sheds light on ore formation and sulfide melt migration: *Geology*, v. 36, no. 8, p. 655-658.
- Barnes, S. J., and Liu, W., 2012, Pt and Pd mobility in hydrothermal fluids: Evidence from komatiites and from thermodynamic modelling: *Ore Geology Reviews*, v. 44, p. 49-58.
- Barnes, S. J., Cruden, A. R., Arndt, N., and Saumur, B. M., 2015, The mineral system approach applied to magmatic Ni-Cu-PGE sulphide deposits: *Ore Geology Reviews*, v. In Press.
- Beaudoin, G., and Therrien, P., 2009, The updated web stable isotope fractionation calculator: *Handbook of Stable Isotope Analytical Techniques*, v. 2, p. 1120-1122.
- Benkó, Z., Mogessie, A., Molnár, F., Severson, M. J., Hauck, S. A., and Raič, S., 2015, Partial Melting Processes and Cu-Ni-PGE Mineralization in the Footwall of the South Kawishiwi Intrusion at the Spruce Road Deposit, Duluth Complex, Minnesota: *Economic Geology*, v. 110, no. 5, p. 1269-1293.
- Bickle, M., 1982, The magnesium contents of komatiitic liquids, in Arndt, N., and EG, N., eds., *Komatiites*: London, Allen and Unwin, p. 479-494.
- Bigeleisen, J., and Mayer, M. G., 1947, Calculation of equilibrium constants for isotopic exchange reactions: *The Journal of Chemical Physics*, v. 15, no. 5, p. 261-267.
- Bogdanov, Y. B., 1987, GREENSTONE BELTS IN THE SOVIET KARELIAN-KOLA: Geological Survey of Finland, Special Paper, no. 4, p. 29.
- Boutroy, E., Dare, S. A. S., Beaudoin, G., Barnes, S.-J., and Lightfoot, P. C., 2014, Magnetite composition in Ni-Cu-PGE deposits worldwide: application to mineral exploration: *Journal of Geochemical Exploration*, v. 145, p. 64-81.
- Brenan, J. M., and Caciagli, N. C., 2000, Fe-Ni exchange between olivine and sulphide liquid: implications for oxygen barometry in sulphide-saturated magmas: *Geochimica et Cosmochimica Acta*, v. 64, no. 2, p. 307-320.

- Brownscombe, W., Ihlenfeld, C., Coppard, J., Hartshorne, C., Klatt, S., Siikaluoma, J., and Herrington, R., 2015, The Sakatti Cu-Ni-PGE sulfide deposit in northern Finland, *in* Maier, W. D., Lahtinen, R., and O'Brien, H. E., eds., *Mineral Deposits of Finland*, Elsevier Amsterdam, p. 211-252.
- Bulle, F., and Layne, G., 2015, Multi-element variations in olivine as geochemical signatures of Ni-Cu sulfide mineralization in mafic magma systems—examples from Voisey's Bay and Pants Lake intrusions, Labrador, Canada: *Mineralium Deposita*, p. 1-21.
- Burrows, D., and Leshner, C., 2012, Copper-rich magmatic Ni-Cu-PGE deposits: Society of Economic Geologists, Special Publication, v. 16, p. 515-552.
- Cabri, L. J., and Laflamme, J. H. G., 1976, The mineralogy of the platinum-group elements from some copper-nickel deposits of the Sudbury area, Ontario: *Economic Geology*, v. 71, no. 7, p. 1159-1195.
- Cabri, L. J., 2002, The platinum-group minerals, *in* Cabri, L. J., ed., *The geology, geochemistry, mineralogy and mineral beneficiation of platinum-group elements*, Canadian Institute Mineral Metallurgy Petroleum, p. 13-129.
- Cameron, V., and Vance, D., 2014, Heavy nickel isotope compositions in rivers and the oceans: *Geochimica Et Cosmochimica Acta*, v. 128, p. 195-211.
- Chaussidon, M., Albarède, F., and Sheppard, S. M., 1989, Sulphur isotope variations in the mantle from ion microprobe analyses of micro-sulphide inclusions: *Earth and Planetary Science Letters*, v. 92, no. 2, p. 144-156.
- Collins, J., Hagemann, S., McCuaig, T., and Frost, K., 2012, Structural Controls on Sulfide Mobilization at the High-Grade Flying Fox Ni-Cu-PGE Sulfide Deposit, Forresteria Greenstone Belt, Western Australia: *Economic Geology*, v. 107, no. 7, p. 1433-1455.
- Cook, D. L., Wadhwa, M., Clayton, R. N., Dauphas, N., Janney, P. E., and Davis, A. M., 2007, Mass-dependent fractionation of nickel isotopes in meteoritic metal: *Meteoritics & Planetary Science*, v. 42, no. 12, p. 2067-2077.
- Cooper, M. J., 2012, Separation of Nd for isotopic analysis by Neptune, Standard Operating Procedure, University of Southampton.
- Czamanske, G. K., Kunilov, V. E., Zientek, M. L., Cabri, L. J., Likhachev, A. P., Calk, L. C., and Oscarson, R. L., 1992, A proton microprobe study of magmatic sulfide ores from the Noril'sk-Talnakh District, Siberia: *The Canadian Mineralogist*, v. 30, no. 2, p. 249-287.
- Daly, J. S., Balagansky, V. V., Timmerman, M. J., and Whitehouse, M. J., 2006, The Lapland-Kola orogen: Palaeoproterozoic collision and accretion of the northern Fennoscandian lithosphere: *Geological Society, London, Memoirs*, v. 32, no. 1, p. 579-598.
- Dare, S. A. S., Barnes, S. J., and Prichard, H. M., 2010, The distribution of platinum group elements (PGE) and other chalcophile elements among sulfides from the Creighton Ni-Cu-PGE sulfide deposit, Sudbury, Canada, and the origin of palladium in pentlandite: *Mineralium Deposita*, v. 45, no. 8, p. 765-793.
- Dare, S. A. S., Barnes, S. J., Beaudoin, G., Meric, J., Boutroy, E., and Potvin-Doucet, C., 2014a, Trace elements in magnetite as petrogenetic indicators: *Mineralium Deposita*, v. 49, no. 7, p. 785-796.
- Dare, S. A. S., Barnes, S. J., Prichard, H. M., and Fisher, P. C., 2014b, Mineralogy and Geochemistry of Cu-Rich Ores from the McCreedy East Ni-Cu-PGE Deposit (Sudbury, Canada): Implications for the Behavior of Platinum Group and Chalcophile Elements at the End of Crystallization of a Sulfide Liquid: *Economic Geology*, v. 109, no. 2, p. 343-366.
- Dare, S. S., Barnes, S.-J., Prichard, H., and Fisher, P., 2011, Chalcophile and platinum-group element (PGE) concentrations in the sulfide minerals from the McCreedy East deposit, Sudbury, Canada, and the origin of PGE in pyrite: *Mineralium Deposita*, v. 46, no. 4, p. 381-407.
- De Hoog, J. C. M., Gall, L., and Cornell, D. H., 2010, Trace-element geochemistry of mantle olivine and application to mantle petrogenesis and geothermobarometry: *Chemical Geology*, v. 270, no. 1-4, p. 196-215.
- Deer, W., Howie, R., and Zussman, J., 1997, *Rock-forming minerals*, Volume 2B, Double-chain silicates: London, The Geological Society, p. 764.
- Deer, W. A., Bowles, J., Howie, R. A., Vaughan, D., and Zussman, J., *Rock-Forming Minerals: Non-Silicates: Oxides, Hydroxides and Sulphides* 2011, Geological Society of London.
- Deer, W. A., Howie, R. A., and Zussman, J., 2013, *An introduction to the rock-forming minerals*, London, The Mineralogical Society, 497 p.:
- Djon, M., and Barnes, S.-J., 2012, Changes in sulfides and platinum-group minerals with the degree of alteration in the Roby, Twilight, and High Grade Zones of the Lac des Iles Complex, Ontario, Canada: *Mineralium Deposita*, v. 47, no. 8, p. 875-896.

- Ebel, D., and Naldrett, A., 1996, Fractional crystallization of sulfide ore liquids at high temperature: *Economic Geology*, v. 91, no. 3, p. 607-621.
- Eckstrand, O., and Hulbert, L., 1987, Selenium and the source of sulphur in magmatic nickel and platinum deposits: *Geol Assoc Canada/Mineral Assoc Canada: Program with Abstracts*, v. 12, p. 40.
- Evins, P. M., and Laajoki, K., 2002, Early Proterozoic nappe formation: an example from Sodankylä, Finland, Northern Baltic Shield: *Geological Magazine*, v. 139, no. 1, p. 73-87.
- Farquhar, J., Wu, N., Canfield, D. E., and Oduro, H., 2010, Connections between sulfur cycle evolution, sulfur isotopes, sediments, and base metal sulfide deposits: *Economic Geology*, v. 105, no. 3, p. 509-533.
- Fettes, D. J., Desmons, J., and Árkai, P., 2007, *Metamorphic rocks: a classification and glossary of terms: recommendations of the International Union of Geological Sciences Subcommittee on the Systematics of Metamorphic Rocks*, Cambridge Univ Pr.
- Fiorentini, M., Beresford, S., Barley, M., Durning, P., Bekker, A., Rosengren, N., Cas, R., and Hronsky, J., 2012, District to camp controls on the genesis of komatiite-hosted nickel sulfide deposits, Agnew-Wiluna greenstone belt, Western Australia: Insights from the multiple sulfur isotopes: *Economic Geology*, v. 107, no. 5, p. 781-796.
- Fleet, M., Chrissyoulis, S., Stone, W., and Weisener, C., 1993, Partitioning of platinum-group elements and Au in the Fe-Ni-Cu-S system: experiments on the fractional crystallization of sulfide melt: *Contributions to Mineralogy and Petrology*, v. 115, no. 1, p. 36-44.
- Fleet, M. E., MacRae, N. D., and Osborne, M. D., 1981, The partition of nickel between olivine, magma and immiscible sulfide liquid: *Chemical Geology*, v. 32, no. 1, p. 119-127.
- Frietsch, R., Tuisku, P., Martinsson, O., and Perdahl, J.-A., 1997, Early proterozoic Cu (Au) and Fe ore deposits associated with regional Na Cl metasomatism in northern Fennoscandia: *Ore Geology Reviews*, v. 12, no. 1, p. 1-34.
- Fujii, T., Moynier, F., Blichert-Toft, J., and Albarede, F., 2014, Density functional theory estimation of isotope fractionation of Fe, Ni, Cu, and Zn among species relevant to geochemical and biological environments: *Geochimica Et Cosmochimica Acta*, v. 140, p. 553-576.
- Gall, L., 2011, Development and application of nickel stable isotopes as a new geochemical tracer: University of Oxford.
- Gall, L., Williams, H., Siebert, C., and Halliday, A., 2012, Determination of mass-dependent variations in nickel isotope compositions using double spiking and MC-ICPMS: *Journal of Analytical Atomic Spectrometry*, v. 27, no. 1, p. 137-145.
- Gall, L., Williams, H. M., Siebert, C., Halliday, A. N., Herrington, R. J., and Hein, J. R., 2013, Nickel isotopic compositions of ferromanganese crusts and the constancy of deep ocean inputs and continental weathering effects over the Cenozoic: *Earth and Planetary Science Letters*, v. 375, p. 148-155.
- German, C. R., Holliday, B. P., and Elderfield, H., 1991, Redox cycling of rare earth elements in the suboxic zone of the Black Sea: *Geochimica et Cosmochimica Acta*, v. 55, no. 12, p. 3553-3558.
- Gervilla, F., and Kojonen, K., 2002, The platinum-group minerals in the upper section of the Keivitsansarvi Ni-Cu-PGE deposit, northern Finland: *Canadian Mineralogist*, v. 40, no. 2, p. 377-394.
- Godel, B., Barnes, S. J., and Maier, W. D., 2010, Platinum ore in three dimensions: Insights from high-resolution X-ray computed tomography: *Geology*, v. 38, no. 12, p. 1127-1130.
- Godel, B., 2013, High-Resolution X-Ray Computed Tomography and Its Application to Ore Deposits: From Data Acquisition to Quantitative Three-Dimensional Measurements with Case Studies from Ni-Cu-PGE Deposits: *Economic Geology*, v. 108, no. 8, p. 2005-2019.
- Godel, B., Rudashevsky, N. S., Nielsen, T. F. D., Barnes, S. J., and Rudashevsky, V. N., 2014, New constraints on the origin of the Skaergaard intrusion Cu-Pd-Au mineralization: Insights from high-resolution X-ray computed tomography: *Lithos*, v. 190-191, p. 27-36.
- Godel, B. M., Barnes, S. J., and Barnes, S.-J., 2013, Deposition mechanisms of magmatic sulphide liquids: Evidence from high-resolution X-ray computed tomography and trace element chemistry of komatiite-hosted disseminated sulphides: *Journal of Petrology*, v. 54, no. 7, p. 18.
- Gramlich, J., Machlan, L., Barnes, I., and Paulsen, P., 1989, Absolute isotopic abundance ratios and atomic weight of a reference sample of nickel: *Journal of research of the National Institute of Standards and Technology*, v. 94, no. 6, p. 347.
- Grguric, B., Rosengren, N., Fletcher, C., and Hronsky, J., 2006, Type 2 deposits: geology, mineralogy and processing of the Mount Keith and Yakabindie Orebodies, Western Australia: *Nickel Deposits of the Yilgarn Craton, Special Publication No.*, v. 13.
- Grinenko, L., Hanski, E., and Grinenko, V., 2003, Formation conditions of the Keivitsa Cu-Ni deposit, northern Finland: evidence from S and C isotopes: *Geochemistry International*, v. 41, no. 2, p. 154-167.

- Gueguen, B., Rouxel, O., Ponzevera, E., Bekker, A., and Fouquet, Y., 2013, Nickel Isotope Variations in Terrestrial Silicate Rocks and Geological Reference Materials Measured by MC-ICP-MS: *Geostandards and Geoanalytical Research*, v. 37, no. 3, p. 297-317.
- Halkoaho, T., Liimatainen, J., Papunen, H., and Välimaa, J., 2000, Exceptionally Cr-rich basalts in the komatiitic volcanic association of the Archaean Kuhmo greenstone belt, eastern Finland: *Mineralogy and Petrology*, v. 70, no. 1-2, p. 105-120.
- Hanley, J., Mungall, J., Pettke, T., Spooner, E., and Bray, C., 2005a, Ore metal redistribution by hydrocarbon-brine and hydrocarbon-halide melt phases, North Range footwall of the Sudbury Igneous Complex, Ontario, Canada: *Mineralium Deposita*, v. 40, no. 3, p. 237-256.
- Hanley, J. J., Mungall, J. E., Pettke, T., Spooner, E. T. C., and Bray, C. J., 2005b, Ore metal redistribution by hydrocarbon-brine and hydrocarbon-halide melt phases, North Range footwall of the Sudbury Igneous Complex, Ontario, Canada: *Mineralium Deposita*, v. 40, no. 3, p. 237-256.
- Hanski, E., 1987, Differentiated albite diabases - gabbro wehrlite association: Geological Survey of Finland - Report of Investigation, v. 76.
- Hanski, E., Huhma, H., Rastas, P., and Kamenetsky, V. S., 2001a, The Palaeoproterozoic Komatiite-Picrite association of Finnish Lapland: *Journal of Petrology*, v. 42, no. 5, p. 855-876.
- Hanski, E., Walker, R. J., Huhma, H., and Suominen, I., 2001b, The Os and Nd isotopic systematics of c. 2.44 Ga Akanvaara and Koitelainen mafic layered intrusions in northern Finland: *Precambrian Research*, v. 109, no. 1-2, p. 73-102.
- Hanski, E., and Huhma, H., 2005, Central Lapland greenstone belt, in Lehtinen, M., Nurmi, P. A., and Rämö, O. T., eds., *The Precambrian Geology of Finland*, Elsevier, p. 139-193.
- Hanski, E. J., Grinenko, L. N., and Mutanen, T., 1996, Sulfur isotopes in the Keivitsa Cu-Ni-bearing intrusion and its country rocks, northern Finland: evidence for crustal sulfur contamination., IGCP Project 336 Symposium in Rovaniemi, Finland, 21-23 August 1996, Program and abstracts., Publications of the Geology Department, University of Turku.
- Harmer, R. E., and Sharpe, M. R., 1985, Field relations and strontium isotope systematics of the marginal rocks of the eastern Bushveld Complex: *Economic Geology*, v. 80, no. 4, p. 813-837.
- Helmy, H. M., Ballhaus, C., Berndt, J., Bockrath, C., and Wohlgemuth-Ueberwasser, C., 2007, Formation of Pt, Pd and Ni tellurides: experiments in sulfide-telluride systems: *Contributions to Mineralogy and Petrology*, v. 153, no. 5, p. 577-591.
- Helmy, H. M., Ballhaus, C., Wohlgemuth-Ueberwasser, C., Fonseca, R. O. C., and Laurenz, V., 2010, Partitioning of Se, As, Sb, Te and Bi between monosulfide solid solution and sulfide melt - Application to magmatic sulfide deposits: *Geochimica Et Cosmochimica Acta*, v. 74, no. 21, p. 6174-6179.
- Helmy, H. M., Ballhaus, C., Fonseca, R. O. C., and Nagel, T. J., 2013, Fractionation of platinum, palladium, nickel, and copper in sulfide-arsenide systems at magmatic temperature: *Contributions to Mineralogy and Petrology*, v. 166, no. 6, p. 1725-1737.
- Hoefs, J., 2008, *Stable isotope geochemistry*, Springer Science & Business Media.
- Hofmann, A., Bekker, A., Dirks, P., Gueguen, B., Rumble, D., and Rouxel, O. J., 2014, Comparing orthomagmatic and hydrothermal mineralization models for komatiite-hosted nickel deposits in Zimbabwe using multiple-sulfur, iron, and nickel isotope data: *Mineralium Deposita*, v. 49, no. 1, p. 75-100.
- Hölttä, P., Väisänen, M., Väänänen, J., and Manninen, T., 2007, Paleoproterozoic metamorphism and deformation in Central Lapland, Finland: *Gold in the Central Lapland Greenstone Belt: Geological Survey of Finland Special Paper*, v. 44, p. 7-56.
- Holwell, D., and McDonald, I., 2007, Distribution of platinum-group elements in the Platreef at Overysel, northern Bushveld Complex: a combined PGM and LA-ICP-MS study: *Contributions to Mineralogy and Petrology*, v. 154, no. 2, p. 171-190.
- Holwell, D. A., and McDonald, I., 2010, A review of the behaviour of platinum group elements within natural magmatic sulfide ore systems: *Platinum Metals Review*, v. 54, no. 1, p. 26-36.
- Hsu, L., Lechler, P. J., and Nelson, J. H., 1991, Hydrothermal solubility of palladium in chloride solutions from 300 degrees to 700 degrees C; preliminary experimental results: *Economic Geology*, v. 86, no. 2, p. 422-427.
- Hunter, C., 2012, Understanding the controls on the spatial distribution of Platinum Group Elements (PGE) in orthomagmatic sulphides: insights from tomographic reconstruction, reflected light and electron microscopy [MSci Masters Thesis]: Imperial College.
- Hutchinson, D., and McDonald, I., 2008, Laser ablation ICP-MS study of platinum-group elements in sulphides from the Platreef at Turfspruit, northern limb of the Bushveld Complex, South Africa: *Mineralium Deposita*, v. 43, no. 6, p. 695-711.

- Iljina, M., and Hanski, E., 2005, Chapter 3 Layered mafic intrusions of the Tornio--Näränkäväära belt, *in* M. Lehtinen, P. A. N., and Rämö, O. T., eds., *Developments in Precambrian Geology, Volume Volume 14*, Elsevier, p. 101-137.
- Jillings, K. E. L., 2015, Origin of the hanging wall breccias at the Sakatti Ni-Cu-PGE deposit, Finland [MSci thesis]: Imperial College London.
- Kajiwara, Y., and Krouse, H., 1971, Sulfur isotope partitioning in metallic sulfide systems: Canadian Journal of Earth Sciences, v. 8, no. 11, p. 1397-1408.
- Karinen, T., 2010, The Koillismaa intrusion, northeastern Finland: evidence for PGE reef forming processes in the layered series, Geological Survey of Finland.
- Kaukonen, R. J., The melonite-merenskyite-möncheite-michenerite system in the Kevitsa polymetallic ore deposit, northern Finland., *in* Proceedings Golden Jubilee celebrations of the Geological Society of India, Bhubaneswar, India, 1st-4th December 2009, Geological Society of India.
- Keays, R., and Lightfoot, P., 2010, Crustal sulfur is required to form magmatic Ni-Cu sulfide deposits: evidence from chalcophile element signatures of Siberian and Deccan Trap basalts: Mineralium Deposita, v. 45, no. 3, p. 241-257.
- Kerr, A., and Leitch, A. M., 2005, Self-destructive sulfide segregation systems and the formation of high-grade magmatic ore deposits: Economic Geology, v. 100, no. 2, p. 311-332.
- Ketcham, R. A., and Carlson, W. D., 2001, Acquisition, optimization and interpretation of X-ray computed tomographic imagery: applications to the geosciences: Computers & Geosciences, v. 27, no. 4, p. 381-400.
- Konnunaho, J., Hanski, E., Wing, B., Bekker, A., Lukkari, S., and Halkoaho, T., 2016, The Hietaharju PGE-enriched komatiite-hosted sulfide deposit in the Archean Suomussalmi greenstone belt, eastern Finland: Ore Geology Reviews, v. 72, p. 641-658.
- Korja, A., Lahtinen, R., and Nironen, M., 2006, The Svecofennian orogen: a collage of microcontinents and island arcs: Geological Society, London, Memoirs, v. 32, no. 1, p. 561-578.
- Lahtinen, R., Korja, A., and Nironen, M., 2005, Paleoproterozoic tectonic evolution, *in* Lehtinen, M., Nurmi, P. A., and Rämö, O. T., eds., *The Precambrian Geology of Finland*, Elsevier, p. 481-531.
- Lahtinen, R., Korja, A., Nironen, M., and Heikkinen, P., 2009, Palaeoproterozoic accretionary processes in Fennoscandia: Geological Society, London, Special Publications, v. 318, no. 1, p. 237-256.
- Latypov, R., Hanski, E., Lavrenchuk, A., Huhma, H., and Havela, T., 2011, A 'three-increase model' for the origin of the marginal reversal of the Koitelainen layered intrusion, Finland: Journal of Petrology, v. 52, no. 4, p. 733-764.
- Lauri, L., Andersen, T., Räsänen, J., and Juopperi, H., 2012, Temporal and Hf isotope geochemical evolution of southern Finnish Lapland from 2.77 Ga to 1.76 Ga: Bulletin of the Geological Society of Finland, v. 84, p. 121-140.
- Le Maitre, R. W., Streckeisen, A., Zanettin, B., Le Bas, M., Bonin, B., and Bateman, P., 2002, *Igneous rocks: a classification and glossary of terms: recommendations of the International Union of Geological Sciences Subcommittee on the Systematics of Igneous Rocks*, Cambridge, Cambridge University Press.
- Le Vaillant, M., Barnes, S. J., Fiorentini, M. L., Santaguida, F., and Törmänen, T., 2016, Effects of hydrous alteration on the distribution of base metals and platinum group elements within the Kevitsa magmatic nickel sulphide deposit: Ore Geology Reviews, v. 72, Part 1, p. 128-148.
- Lehtonen, M., Airo, M.-L., Eilu, P., Hanski, E., Kortelainen, V., Lanne, E., Manninen, T., Rastas, P., Räsänen, J., and Virransalo, P., 1998, The stratigraphy, petrology and geochemistry of the Kittilä greenstone area, northern Finland (English summary): Geological Survey of Finland - Report of Investigation, v. 140, p. 144.
- Leshner, C., and Keays, R., 2002, Komatiite-associated Ni-Cu-PGE deposits: geology, mineralogy, geochemistry and genesis, *in* Cabri, L. J., ed., *The geology, geochemistry, mineralogy and mineral beneficiation of platinum-group elements*, Canadian Institute Mineral Metallurgy Petroleum, p. 579-619.
- Li, C., and Naldrett, A. J., 1993, Sulfide capacity of magma; a quantitative model and its application to the formation of sulfide ores at Sudbury, Ontario: Economic Geology, v. 88, no. 5, p. 1253-1260.
- Li, C., Barnes, S. J., Makovicky, E., Rose-Hansen, J., and Makovicky, M., 1996, Partitioning of nickel, copper, iridium, rhenium, platinum, and palladium between monosulfide solid solution and sulfide liquid: Effects of composition and temperature: Geochimica et Cosmochimica Acta, v. 60, no. 7, p. 1231-1238.
- Li, C., Maier, W. D., and De Waal, S., 2001a, Magmatic Ni-Cu versus PGE deposits: Contrasting genetic controls and exploration implications: South African Journal of Geology, v. 104, no. 4, p. 309-318.

- Li, C., Maier, W. D., and de Waal, S. A., 2001b, The role of magma mixing in the genesis of PGE mineralization in the Bushveld complex: thermodynamic calculations and new interpretations: *Economic Geology*, v. 96, no. 3, p. 653-662.
- Li, C., and Ripley, E., 2005, Empirical equations to predict the sulfur content of mafic magmas at sulfide saturation and applications to magmatic sulfide deposits: *Mineralium Deposita*, v. 40, no. 2, p. 218-230.
- Li, C., Ripley, E. M., and Naldrett, A. J., 2009, A new genetic model for the giant Ni-Cu-PGE sulfide deposits associated with the Siberian Flood Basalts: *Economic Geology*, v. 104, no. 2, p. 291-301.
- Li, Y., and Liu, J., 2006, Calculation of sulfur isotope fractionation in sulfides: *Geochimica et Cosmochimica Acta*, v. 70, no. 7, p. 1789-1795.
- Lightfoot, P., and Naldrett, A., 1999, Geological and geochemical relationships in the Voisey's Bay intrusion, Nain plutonic suite, Labrador, Canada: *Geological Association of Canada Short Course Notes*, v. 13, p. 1-30.
- Liipo, J., 2012, Mineralogical Characterization of Massive Pyrite and Low Grade Chalcopyrite Ores: Outotec Research Centre.
- Lindsley, D. H., Frost, B. R., Frost, C. D., and Scoates, J. S., 2010, Petrology, geochemistry, and structure of the Chugwater anorthosite, Laramie anorthosite complex, southeastern Wyoming: *The Canadian Mineralogist*, v. 48, no. 4, p. 887-923.
- Liu, Y. N., and Brenan, J., 2015, Partitioning of platinum-group elements (PGE) and chalcogens (Se, Te, As, Sb, Bi) between monosulfide-solid solution (MSS), intermediate solid solution (ISS) and sulfide liquid at controlled fO(2)-fS(2) conditions: *Geochimica Et Cosmochimica Acta*, v. 159, p. 139-161.
- Longerich, H. P., Jackson, S. E., and Günther, D., 1996, Inter-laboratory note. Laser ablation inductively coupled plasma mass spectrometric transient signal data acquisition and analyte concentration calculation: *Journal of Analytical Atomic Spectrometry*, v. 11, no. 9, p. 899-904.
- Luukkonen, E. J., 1992, Late Archaean and early Proterozoic structural evolution in the Kuhmo-Suomussalmi terrain, eastern Finland, Turun yliopisto.
- Maclean, W. H., 1969, Liquidus phase relations in the FeS-FeO-Fe₃O₄-SiO₂ systems and their application in geology: *Economic Geology*, v. 64, p. 19.
- Maier, W. D., Barnes, S. J., Chinyepi, G., Barton, J. M., Jr., Eglington, B., and Setshedi, I., 2008, The composition of magmatic Ni-Cu-(PGE) sulfide deposits in the Tati and Selebi-Phikwe belts of eastern Botswana: *Mineralium Deposita*, v. 43, no. 1, p. 37-60.
- Mäkimattila, O., 2015, Petrological and Geochemical Characteristics of the Ponostama Ultramafic Intrusion, Sodankylä, Northern Finland.
- Makkonen, H. V., and Huhma, H., 2007, Sm-Nd data for mafic-ultramafic intrusions in the Svecofenni-an (1.88 Ga) Kotalahti Nickel Belt, Finland—implications for crustal contamination at the Archaean/Proterozoic boundary: *Bulletin of the Geological Society of Finland*, v. 79, p. 175-201.
- Manninen, T., and Huhma, H., 2001, A new U-Pb zircon age from the Salla schist belt, northern Finland., *in* Vaasjoki, M., ed., *Radiometric age determinations from Finnish Lapland and their bearing on the timing of Precambrian volcano-sedimentary sequences*: Espoo, Geological Survey of Finland, special paper 33, p. 201-208.
- Mathez, E. A., 1976, Sulfur solubility and magmatic sulfides in submarine basalt glass: *Journal of Geophysical Research*, v. 81, no. 23, p. 4269-4276.
- Mavrogenes, J. A., and O'Neill, H. S. C., 1999, The relative effects of pressure, temperature and oxygen fugacity on the solubility of sulfide in mafic magmas: *Geochimica et Cosmochimica Acta*, v. 63, no. 7-8, p. 1173-1180.
- McDonald, I., Development of sulphide standards for the in-situ analysis of platinum-group elements by laser ablation inductively coupled plasma-mass spectrometry (LA-ICP-MS), *in* *Proceedings 10th International Platinum Symposium, Ext Abstracts2005*, p. 468-471.
- McDonough, W. F., and Sun, S.-S., 1995, The composition of the Earth: *Chemical geology*, v. 120, no. 3, p. 223-253.
- Molnár, F., Watkinson, D. H., and Jones, P. C., 2001, Multiple Hydrothermal Processes in Footwall Units of the North Range, Sudbury Igneous Complex, Canada, and Implications for the Genesis of Vein-Type Cu-Ni-PGE Deposits: *Economic Geology*, v. 96, no. 7, p. 1645-1670.
- Mountain, B. W., and Wood, S. A., 1988, Chemical controls on the solubility, transport and deposition of platinum and palladium in hydrothermal solutions; a thermodynamic approach: *Economic Geology*, v. 83, no. 3, p. 492-510.
- Moynier, F., Blichert-Toft, J., Telouk, P., Luck, J.-M., and Albarède, F., 2007, Comparative stable isotope geochemistry of Ni, Cu, Zn, and Fe in chondrites and iron meteorites: *Geochimica et Cosmochimica Acta*, v. 71, no. 17, p. 4365-4379.

- Mungall, J., Andrews, D., Cabri, L., Sylvester, P., and Tubrett, M., 2005, Partitioning of Cu, Ni, Au, and platinum-group elements between monosulfide solid solution and sulfide melt under controlled oxygen and sulfur fugacities: *Geochimica et Cosmochimica Acta*, v. 69, no. 17, p. 4349-4360.
- Mungall, J. E., and Su, S., 2005, Interfacial tension between magmatic sulfide and silicate liquids: constraints on kinetics of sulfide liquation and sulfide migration through silicate rocks: *Earth and Planetary Science Letters*, v. 234, no. 1, p. 135-149.
- Mungall, J. E., and Brenan, J. M., 2014, Partitioning of platinum-group elements and Au between sulfide liquid and basalt and the origins of mantle-crust fractionation of the chalcophile elements: *Geochimica et Cosmochimica Acta*, v. 125, p. 265-289.
- Mutanen, T., 1997, Geology and ore petrology of the Akanvaara and Koitelainen mafic layered intrusions and the Keivitsa-Satovaara layered complex, northern Finland, Espoo, Geological Survey of Finland, Bulletin, v. 395, 233 p.:
- Mutanen, T., and Huhma, H., 2001, U-Pb geochronology of the Koitelainen, Akanvaara and Keivitsa layered intrusions and related rocks, in Vaasjoki, M., ed., Radiometric age determinations from Finnish Lapland and their bearing on the timing of Precambrian volcano-sedimentary sequences: Espoo, Geological Survey of Finland, special paper 33, p. 229-246.
- Mutanen, T., and Huhma, H., 2003, The 3.5 Ga Siurua trondhjemite gneiss in the Archaean Pudasjarvi granulite belt, northern Finland, Espoo, Geological Survey of Finland, Bulletin, v. 75, 17 p.:
- Mutanen, T., 2005, The Akanvaara intrusion and the Keivitsa-Satovaara complex with stops at Kaikkivaltiaanlehto and Rantavaara intrusions - fieldtrip guidebook, 10th Platinum Symposium: Oulu, Finland, Geological Survey of Finland.
- Naldrett, A., and Cabri, L., 1976, Ultramafic and related mafic rocks; their classification and genesis with special reference to the concentration of nickel sulfides and platinum-group elements: *Economic Geology*, v. 71, no. 7, p. 1131-1158.
- Naldrett, A., and Barnes, S.-J., 1986, The behaviour of platinum group elements during fractional crystallization and partial melting with special reference to the composition of magmatic sulfide ores: *Fortschr Mineral*, v. 64, no. 2.
- Naldrett, A. J., Lightfoot, P., Fedorenko, V., Doherty, W., and Gorbachev, N., 1992, Geology and geochemistry of intrusions and flood basalts of the Noril'sk region, USSR, with implications for the origin of the Ni-Cu ores: *Economic Geology*, v. 87, no. 4, p. 975-1004.
- Naldrett, A. J., 2004, *Magmatic Sulfide Deposits: Geology, Geochemistry and Exploration*, Heidelberg, Springer-Verlag, 728 p.:
- Nironen, M., 2005, Proterozoic orogenic granitoid rocks, in Lehtinen, M., Nurmi, P. A., and Rämö, O. T., eds., *The Precambrian Geology of Finland*, Elsevier, p. 443-479.
- Nisbet, E., Cheadle, M., Arndt, N., and Bickle, M., 1993, Constraining the potential temperature of the Archaean mantle: a review of the evidence from komatiites: *Lithos*, v. 30, no. 3, p. 291-307.
- Ohmoto, H., and Rye, R., 1979, Isotopes of sulfur and carbon, in Barnes, H. L., ed., *Geochemistry of hydrothermal ore deposits*: New York, John Wiley & Sons Inc, p. 509-567.
- Papunen, H., Halkoaho, T., Tulenheimo, T., and Liimatainen, J., 1998, Excursion to the Kuhmo greenstone belt: SPECIAL PAPER-GEOLOGICAL SURVEY OF FINLAND, p. 91-106.
- Parnell, J., Boyce, A. J., Mark, D., Bowden, S., and Spinks, S., 2010, Early oxygenation of the terrestrial environment during the Mesoproterozoic: *Nature*, v. 468, no. 7321, p. 290-293.
- Pearce, T., 1989, Getting the most from your data: Applications of Pearce element ratio analysis: Theory and application of Pearce element ratios to geochemical data analysis. Geological Association of Canada, Short course notes, v. 8, p. 99-130.
- Peltonen, P., Huhma, H., Santaguida, F., and Beresford, S., 2014, U-Pb zircon and Sm-Nd isotopic constraints for the timing and origin of magmatic Ni-Cu-PGE deposits in northern Fennoscandia, SEG 2014 Conference: Keystone, Colorado, USA.
- Piirainen, T., 1988, The geology of the Archaean greenstone-granitoid terrain in Kuhmo, eastern Finland: Archean geology of the Fennoscandian Shield. *Geol Surv Finl, Spec Pap*, v. 4, p. 39-51.
- Piña, R., Gervilla, F., Barnes, S.-J., Ortega, L., and Lunar, R., 2013, Platinum-group elements-bearing pyrite from the Aguablanca Ni-Cu sulphide deposit (SW Spain): a LA-ICP-MS study: *European Journal of Mineralogy*, v. 25, no. 2, p. 241-252.
- Porter, S. J., Selby, D., and Cameron, V., 2014, Characterising the nickel isotopic composition of organic-rich marine sediments: *Chemical Geology*, v. 387, p. 12-21.
- Prichard, H. M., Fisher, P. C., McDonald, I., Knight, R. D., Sharp, D. R., and Williams, J. P., 2013, The distribution of PGE and the role of arsenic as a collector of PGE in the Spotted Quoll nickel ore deposit in the Forrestania Greenstone Belt, Western Australia: *Economic Geology*, v. 108, no. 8, p. 1903-1921.

- Puchtel, I. S., Haase, K. M., Hofmann, A. W., Chauvel, C., Kulikov, V. S., Garbe-Schönberg, C. D., and Nemchin, A. A., 1997, Petrology and geochemistry of crustally contaminated komatiitic basalts from the Vetreny Belt, southeastern Baltic Shield: Evidence for an early Proterozoic mantle plume beneath rifted Archean continental lithosphere: *Geochimica et Cosmochimica Acta*, v. 61, no. 6, p. 1205-1222.
- Queffurus, M., and Barnes, S.-J., 2015, A review of sulfur to selenium ratios in magmatic nickel-copper and platinum-group element deposits: *Ore Geology Reviews*, v. 69, p. 301-324.
- Rajamani, V., and Naldrett, A., 1978, Partitioning of Fe, Co, Ni, and Cu between sulfide liquid and basaltic melts and the composition of Ni-Cu sulfide deposits: *Economic Geology*, v. 73, no. 1, p. 82-93.
- Rämö, O. T., Halla, J., Nironen, M., Lauri, L. S., Kurhila, M. I., Käpyaho, A., Sorjonen-Ward, P., and Äikäs, O., 2005, Eurogranites 2005 - Proterozoic and Archean granites and related rocks of the Finnish Precambrian, Eurogranites 2005 Field Conference, Publications of the Department of Geology A1, p. 130.
- Räsänen, J., and Huhma, H., 2001, U-Pb datings in the Sodankylä schist area, central Finnish Lapland, *in* Vaasjoki, M., ed., Radiometric age determinations from Finnish Lapland and their bearing on the timing of Precambrian volcano-sedimentary sequences: Espoo, Geological Survey of Finland, special paper 33, p. 153-188.
- Rastas, P., Huhma, H., Hanski, E., Lehtonen, M. I., Härkönen, I., Kortelainen, V., Mänttari, I., and Paakkola, J., 2001, U-Pb isotopic studies on the Kittilä greenstone area, central Lapland, Finland., *in* Vaasjoki, M., ed., Radiometric age determinations from Finnish Lapland and their bearing on the timing of Precambrian volcano-sedimentary sequences: Espoo, Geological Survey of Finland, special paper 33, p. 95-142.
- Ratie, G., Jouvin, D., Garnier, J., Rouxel, O., Miska, S., Guimaraes, E., Vieira, L. C., Sivry, Y., Zelano, I., Montarges-Pelletier, E., Thil, F., and Quantin, C., 2015, Nickel isotope fractionation during tropical weathering of ultramafic rocks: *Chemical Geology*, v. 402, p. 68-76.
- Ripley, E. M., and Li, C., 2003, Sulfur isotope exchange and metal enrichment in the formation of magmatic Cu-Ni-(PGE) deposits: *Economic Geology*, v. 98, no. 3, p. 635-641.
- Roeder, P., and Emslie, R., 1970, Olivine-liquid equilibrium: *Contributions to mineralogy and petrology*, v. 29, no. 4, p. 275-289.
- Rollinson, H. R., 1993, Using geochemical data: evaluation, presentation, interpretation, London, Longman, 352 p.:
- Rose, L. A., and Brenan, J. M., 2001, Wetting properties of Fe-Ni-Co-Cu-OS melts against olivine: Implications for sulfide melt mobility: *Economic Geology*, v. 96, no. 1, p. 145-157.
- Saverikko, M., 1987, The Lapland greenstone belt: Stratigraphic and depositional features in northern Finland: *Bulletin of the Geological Society of Finland*, v. 59, p. 129-154.
- Seal, R. R., 2006, Sulfur isotope geochemistry of sulfide minerals: *Reviews in mineralogy and geochemistry*, v. 61, no. 1, p. 633-677.
- Seat, Z., Beresford, S. W., Grguric, B. A., Gee, M. M., and Grassineau, N. V., 2009, Reevaluation of the role of external sulfur addition in the genesis of Ni-Cu-PGE deposits: Evidence from the Nebo-Babel Ni-Cu-PGE deposit, West Musgrave, Western Australia: *Economic Geology*, v. 104, no. 4, p. 521-538.
- Simon, A. C., and Ripley, E. M., 2011, The role of magmatic sulfur in the formation of ore deposits: *Reviews in Mineralogy and Geochemistry*, v. 73, no. 1, p. 513-578.
- Slabunov, A. I., Lobach-Zhuchenko, S. B., Bibikova, E. V., Sorjonen-Ward, P., Balangansky, V. V., Volodichev, O. I., Shchipansky, A. A., Svetov, S. A., Chekulaev, V. P., Arestova, N. A., and Stepanov, V. S., 2006, The Archaean nucleus of the Fennoscandian (Baltic) Shield: *Geological Society, London, Memoirs*, v. 32, no. 1, p. 627-644.
- Smith, J. W., Holwell, D. A., McDonald, I., and Boyce, A. J., 2016, The application of S isotopes and S/Se ratios in determining ore-forming processes of magmatic Ni-Cu-PGE sulfide deposits: A cautionary case study from the northern Bushveld Complex: *Ore Geology Reviews*, v. 73, p. 148-174.
- Sorjonen-Ward, P., and Luukkonen, E. J., 2005, Archean rocks, *in* Lehtinen, M., Nurmi, P. A., and Rämö, O. T., eds., *The Precambrian Geology of Finland*, Elsevier, p. 19-99.
- Suvanto, K., 2014, Geology of the Pikku-Vaiskonselkä differentiated sill in the Kevitsa area, northern Finland [MSc: University of Oulu, 54 p.
- Tanaka, T., Togashi, S., Kamioka, H., Amakawa, H., Kagami, H., Hamamoto, T., Yuhara, M., Orihashi, Y., Yoneda, S., Shimizu, H., Kunimaru, T., Takahashi, K., Yanagi, T., Nakano, T., Fujimaki, H., Shinjo, R., Asahara, Y., Tanimizu, M., and Dragusanu, C., 2000, JNdi-1: a neodymium isotopic reference in consistency with LaJolla neodymium: *Chemical Geology*, v. 168, no. 3-4, p. 279-281.

- Thériault, R. D., Barnes, S.-J., and Severson, M. J., 1997, The influence of country-rock assimilation and silicate to sulfide ratios (R factor) on the genesis of the Dunka Road Cu-Ni-platinum-group element deposit, Duluth Complex, Minnesota: *Canadian Journal of Earth Sciences*, v. 34, no. 4, p. 375-389.
- Thode, H., Monster, J., and Dunford, H., 1961, Sulphur isotope geochemistry: *Geochimica et Cosmochimica Acta*, v. 25, no. 3, p. 159-174.
- Urey, H. C., 1947, The thermodynamic properties of isotopic substances: *Journal of the Chemical Society (Resumed)*, p. 562-581.
- Vaasjoki, M., and Sipila, P., 2001, U-Pb isotopic determinations on baddeleyite and zircon from the Halti-Ridnitsohka intrusion in Finnish Lapland: a further constraint on Caledonide evolution: *SPECIAL PAPER-GEOLOGICAL SURVEY OF FINLAND*, p. 247-254.
- Veblen, D. R., 1981, Amphiboles, Michigan, Mineralogical Society of America, *Reviews in Mineralogy*.
- Ventura, G. T., Gall, L., Siebert, C., Prytulak, J., Szatmari, P., Hurlimann, M., and Halliday, A. N., 2015, The stable isotope composition of vanadium, nickel, and molybdenum in crude oils: *Applied Geochemistry*, v. 59, p. 104-117.
- Vuollo, J., and Huhma, H., 2005, Paleoproterozoic mafic dikes in NE Finland, *in* Lehtinen, M., Nurmi, P. A., and Rämö, O. T., eds., *The Precambrian Geology of Finland*, Elsevier, p. 195-236.
- Wager, L., 1968, Rhythmic and cryptic layering in mafic and ultramafic plutons: *Basalts*, v. 2, p. 573-622.
- Wasylenki, L. E., Howe, H. D., Spivak-Birndorf, L. J., and Bish, D. L., 2015, Ni isotope fractionation during sorption to ferrihydrite: Implications for Ni in banded iron formations: *Chemical Geology*, v. 400, p. 56-64.
- Waters, D. J., 2004, Amphiboles, *Practical Aspects of Mineral Thermobarometry*, Volume 2015: Oxford University.
- Weihed, P., Arndt, N., Billstrom, K., Duchesne, J., Eilu, P., Martinsson, O., Papunen, H., and Lahtinen, R., 2005, Precambrian geodynamics and ore formation: the Fennoscandian shield: *Ore Geology Reviews*, v. 27, no. 1-4, p. 273-322.
- Williams, D. A., Kerr, R. C., Leshner, C. M., and Barnes, S. J., 2001, Analytical/numerical modeling of komatiite lava emplacement and thermal erosion at Perseverance, Western Australia: *Journal of volcanology and geothermal research*, v. 110, no. 1, p. 27-55.
- Wood, S., 2002, The aqueous geochemistry of the platinum-group elements with applications to ore deposits, *in* Cabri, L. J., ed., *Geology, Geochemistry, Mineralogy and Mineral beneficiation of Platinum Group Elements*, Canadian Institute Mineral Metallurgy Petroleum, p. 211-249.
- Wood, S. A., 1987, Thermodynamic calculations of the volatility of the platinum group elements (PGE): the PGE content of fluids at magmatic temperatures: *Geochimica et Cosmochimica Acta*, v. 51, no. 11, p. 3041-3050.
- Yamamoto, M., 1976, Relationship between Se/S and sulfur isotope ratios of hydrothermal sulfide minerals: *Mineralium Deposita*, v. 11, no. 2, p. 197-209.
- Yang, S.-H., Maier, W., Hanski, E., Lappalainen, M., Santaguida, F., and Määttä, S., 2013, Origin of ultra-nickeliferous olivine in the Kevitsa Ni-Cu-PGE-mineralized intrusion, northern Finland: *Contributions to Mineralogy and Petrology*, v. 166, no. 1, p. 81-95.

9 Appendix

9.1 Analytical parameters

9.1.1 SEM and EPMA

In this study, petrological investigation was undertaken using a conventional reflected light microscope and camera. The samples were then carbon coated and initially analysed with a Zeiss EVO 15LS Scanning Electron Microscope (SEM) with Energy Dispersive Spectroscopy (EDS). Samples were manually, systematically scanned for general petrogenetic characteristics using Back-Scattered Electron (BSE) imaging. The Zeiss EVO 15LS was operated using Oxford Instruments INCA EDS software with a beam current of 3nA and an accelerating voltage of 20keV. This was undertaken at the Natural History Museum, London (NHM).

Follow up investigation was then made using a Cameca SX100 Wavelength Dispersive Spectroscopy (WDS) electron microprobe in order to derive quantitative mineral chemistry data from the PGE minerals and surrounding mineral chemistry. The microprobe typically required a grain to have a minimum dimension of at least 8-10 μm . A beam current of 20nA and an accelerating voltage of 20keV. Different element lists were used for different analysis types and a variety of standards (Table 1.1) were used to calibrate for each element. PGE minerals analysis were undertaken manually one at a time due to their small size.

Element	Standard mineral	Std code	Crystal
Na	Jadite	JAD3 STD048	LTAP
Mg	Forsterite	FOR STD277	LTAP
Al	Corundum	COR4 STD028	LTAP
Si	Fayalite	FAY STD278	LTAP
K	Orthoclase	ORT3 STD067	LPET
Ca	Wollastonite	WOL4 STD097	PET
Ti	Rutile	RUT STD082	LPET
Cr	Chromite	CRO2 STDIC	LPET
Mn	Manganite	MNT STDIC	LLIF
Co	Synthetic Co	PCO STD121	LLIF
Ni	Synthetic NiO	NIO2 STDIC	LLIF

Table 9.1 – Standards used to calibrate EMPA analysis

9.1.2 Silicate LA-ICP-MS

Laser ablation ICP-MS for silicates and oxides was undertaken at the Natural History Museum London using a New Wave Research 193 UV laser system and an Agilent 7700 ICP-MS. Analyses were undertaken on the same sites as WDS analysis and data was normalised to the site's WDS data for Si in the case of olivine, pyroxene and amphibole and Fe for magnetite and chromite.

The standards NIST 612 and GSD-1g were used for silicate minerals and GSE-1g, GSD-1g and BC28 for oxide minerals. Analyses were corrected for instrument drift and the ablation response of each element, relative to the normalising element, were measured using these standards (Longerich et al., 1996).

Laser ablation system	
Instrument	ESI NWR193
Laser type	ArF excimer
Wavelength	193 nm
Pulse duration	20 ns
Repetition rate	10 Hz (5 Hz for magnetite)
Analysis type	Spot
Spot diameter	35 or 50 μm
Fluence	3.5 J/cm ²
Carrier gas (He)	350 ml/min
Primary reference material	NIST 612 (GSE-1g for magnetite)
Secondary reference material(s)	GSD-1g (and BC28 for magnetite)

Table 9.2 – Operating parameters for LA-ICP-MS of silicates

Mass spectrometer	
Instrument	Agilent 7700 ICP-Q-MS
Plasma gas flow (Ar)	1.1 l/min
Analysis duration	60s
Blank duration	30s

Table 9.3 – Operating parameters for LA-ICP-MS of silicates

Spots of 35 or 50 μm were used and gas blanks of 30 seconds were acquired for each spot followed by 60 second of ablation. Samples were pre-ablated to remove the carbon coating. A fluence of 3.5 J/cm² was used and the laser was pulsed at 10 Hz for silicate minerals and 5 Hz for magnetite. Data was reduced using an internally developed VBA-based data handling.

Separate element lists were analysed for each mineral (olivine, pyroxene, amphibole, magnetite, chromite). In the case of olivine and pyroxene duplicate analyses were run with a method containing only Rare Earth Elements (REE) in order to decrease detection limits. Detection limits are calculated using the methodology of Longerich et al. (1996) and vary for each individual spot analysis and are given alongside the tabulated data within the electronic appendix.

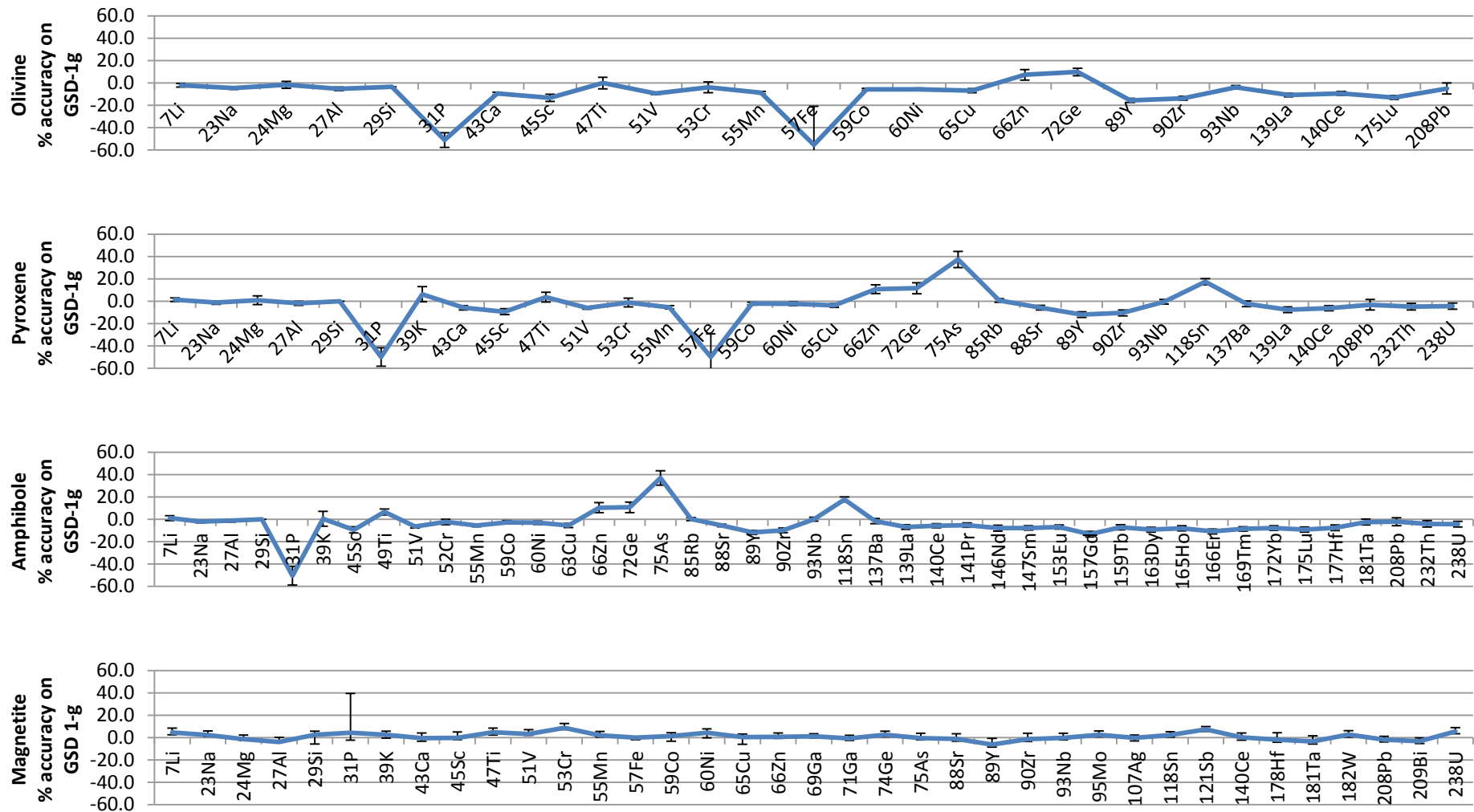


Figure 9.1 - Plots showing the accuracy of analyses on GSD secondary standard as a percentage deviation from reported values. Error bars indicate RSD of the secondary standard measurements.

Olivine	7Li	23Na	24Mg	27Al	29Si	31P	43Ca	45Sc	47Ti	51V	53Cr	55Mn	57Fe	59Co	60Ni	65Cu	66Zn	72Ge	89Y
Det limits	0.034	1.758	0.073	0.123	38.303	2.375	26.736	0.052	0.116	0.013	0.258	0.083	1.107	0.007	0.051	0.040	0.091	0.144	0.001
	90Zr	93Nb	139La	140Ce	175Lu	208Pb													
	0.003	0.003	0.001	0.001	0.001	0.028													
Pyroxene	7Li	23Na	24Mg	27Al	29Si	31P	39K	43Ca	45Sc	47Ti	51V	53Cr	55Mn	57Fe	59Co	60Ni	65Cu	66Zn	72Ge
Det limits	0.046	2.623	0.114	0.177	59.120	3.688	1.839	42.250	0.079	0.367	0.018	0.388	0.128	1.909	0.011	0.073	0.055	0.134	0.212
	75As	85Rb	88Sr	89Y	90Zr	93Nb	118Sn	137Ba	139La	140Ce	208Pb	232Th	238U						
	0.199	0.019	0.004	0.002	0.004	0.002	0.361	0.017	0.002	0.002	0.036	0.002	0.003						
Amphibole	7Li	23Na	27Al	29Si	31P	39K	45Sc	49Ti	51V	52Cr	55Mn	59Co	60Ni	63Cu	66Zn	72Ge	75As	85Rb	88Sr
Det limits	0.036	2.036	0.780	65.528	3.066	1.607	0.068	0.236	0.015	0.383	0.116	0.010	0.070	0.047	0.121	0.184	0.193	0.015	0.003
	89Y	90Zr	93Nb	118Sn	137Ba	139La	140Ce	141Pr	146Nd	147Sm	153Eu	157Gd	159Tb	163Dy	165Ho	166Er	169Tm	172Yb	175Lu
	0.002	0.003	0.003	0.325	0.015	0.002	0.001	0.001	0.009	0.010	0.003	0.009	0.001	0.006	0.001	0.004	0.001	0.006	0.002
	177Hf	181Ta	208Pb	232Th	238U														
	0.008	0.002	0.036	0.003	0.002														
Magnetite	7Li	23Na	24Mg	27Al	29Si	31P	39K	43Ca	45Sc	47Ti	51V	53Cr	55Mn	57Fe	59Co	60Ni	65Cu	66Zn	69Ga
Det limits	0.305	9.869	0.128	0.350	#####	14.708	4.202	97.680	0.156	0.439	0.032	1.303	0.308	8.815	0.014	0.086	0.161	0.382	0.042
	71Ga	74Ge	75As	88Sr	89Y	90Zr	93Nb	95Mo	107Ag	118Sn	121Sb	140Ce	178Hf	181Ta	182W	208Pb	209Bi	238U	
	0.047	0.231	0.164	0.008	0.007	0.014	0.006	0.053	0.016	0.237	0.048	0.004	0.018	0.005	0.019	0.058	0.029	0.004	

Table 9.4 – Average detection limits for GSD-1g analyses for olivine, pyroxene, amphibole and magnetite. Actual detection limits are given in the electronic appendix.

9.1.3 Whole Rock geochemistry

Whole rock geochemistry was undertaken by ACME commercial laboratories. Elements were analysed by a combination of ICP-MS and ICP-AES using Li borate fusions, aqua regia, 4 acid digests and fire assay.

Digestion	Analysis	Method	Elements
Li borate fusion	ICP-AES	Sample fused with Li-meta/tetraborate flux then digested in dilute nitric acid.	SiO ₂ , Al ₂ O ₃ , Fe ₂ O ₃ , CaO, MgO, Na ₂ O, K ₂ O, MnO, TiO ₂ , P ₂ O ₅ , Cr ₂ O ₃ , LOI, C, S, Sc
	ICP-MS	Same as above	Ba, Ga, Hf, Nb, Rb, Sn, Sr, Ta, Th, U, W, V, Y, Zr, La, Ce, Pr, Nd, Sm, Eu, Gd, Tb, Dy, Ho, Er, Tm, Yb, Lu
Aqua Regia	ICP-MS	A 30g sample digested in modified aqua regia in a hot bath. Solution is made to volume with dilute HCl	Au, Ag, As, B, Be, Cd, Co, Cr, Cs, Cu, Ge, Hg, In, Li, Mn, Mo, Ni, Pb, Pd, Pt, Re, Sb, Se, Te, Tl, Zn
4 acid	ICP-AES	Total determination by the ore-grade assay method using a 4-acid digestion on a 0.5 g sample	Ni
Fire assay fusion	ICP-MS	Overlimit samples reanalysed for Pb collection fire assay on a 30 g sample	Au, Pd, Pt

Table 9.5 - Summary table of analytical methods for whole rock geochemistry, undertaken by ACME labs.

9.1.4 Sulphide LA-ICP-MS

Laser-ablation-ICP-MS was undertaken at Cardiff University using a New Wave Research UP213 UV laser system and a Thermo X series ICP-MS. Details of the LA-ICP-MS methodology are given in (Holwell and McDonald, 2007; Prichard et al., 2013). This work was undertaken separately from silicate LAICPMS due to the lack of suitable sulphide standards at the NHM.

A set of synthetic sulphide standards was used to quantify the analyses, the preparation of which is detailed in (McDonald, 2005). The Memorial University FeS standard Po724 was also analysed (Table 4.9).

Laser ablation system	
Instrument	ESI NWR UP213
Laser type	Nd-YAG
Wavelength	213 nm
Pulse duration	20 ns
Repetition rate	10 Hz
Analysis type	Line
Speed	6 $\mu\text{m/s}$
Beam diameter	40 μm
Fluence	3 J/cm^2
Carrier gas (He)	300 ml/min
Primary reference material	In-house Cardiff University standard
Secondary reference material(s)	Memorial Po724

Table 9.6 – Operating parameters for LA-ICP-MS of sulphides

Mass spectrometer	
Instrument	Thermo X series
Plasma gas flow (Ar)	1 l/min
Analysis duration	80-400 s
Blank duration	25 s

Table 9.7 – Operating parameters for LA-ICP-MS of sulphides

Isotopes, ^{33}S , ^{57}Fe , ^{59}Co , ^{61}Ni , ^{65}Cu , ^{68}Zn were measured to determine the mineralogy of sulphides. The semi metals, ^{75}As , ^{82}Se , ^{111}Cd , ^{121}Sb , ^{125}Te , ^{209}Bi were measured to establish whether precious metals are present in solid solution within sulphides or as micro-inclusions of semi-metal phases. The precious metals ^{99}Ru , ^{101}Ru , ^{103}Rh , ^{106}Pd , ^{108}Pd , ^{109}Ag , ^{185}Re , ^{189}Os , ^{193}Ir , ^{195}Pt , ^{197}Au were measured to establish their concentrations in solid solution in sulphide phases.

Analyses were undertaken using a line produced by tracking the sample, at $6 \mu\text{ms}^{-1}$, relative to the laser. A gas blank standard was measured for 25 s before ablation and acquisition lasted between 80 and 400 s. The beam diameter was 40 μm at a frequency of 10 Hz. Isotope dwell times ranged from 2 to 4 ms for major elements, 10 ms for semimetals and 20 ms for precious

metals (Prichard et al., 2013). Electron Microprobe analyses for each mineral within each sample were used to obtain S values as an internal standard.

Isotope used	Units	Detection Limits
57Fe	%	0.50
59Co	ppm	5.5
61Ni	%	0.05
65Cu	%	0.03
66Zn	ppm	10
75As	ppm	6
82Se	ppm	50
101Ru*	ppm	0.05
103Rh*	ppm	0.10
106Pd*	ppm	0.15
108Pd*	ppm	0.20
109Ag	ppm	0.10
111Cd	ppm	0.80
121Sb	ppm	0.90
125Te	ppm	0.90
185Re	ppm	0.02
189Os	ppm	0.02
193Ir	ppm	0.02
195Pt	ppm	0.02
197Au	ppm	0.01
209Bi	ppm	0.05

Table 9.8 – Detection limits for sulphide LA-ICP-MS

9.1.5 Sm/Nd analysis

9.1.5.1 Separation

Mineral separation was done by hand at the NHM. The samples were crushed within polythene bags using a press and a hammer. These were then sieved and the 250-500 μm fraction used for the separates. The magnetic fraction was removed. This usually removed 90-95% of the rock due pervasive magnetite produced during serpentinisation. Minerals were then picked from the remains by hand using a binocular microscope and a hair. Clinopyroxene in the samples is identifiable as a green transparent phase, which has fractured along straight cleavage surfaces. Orthopyroxene is similar but a yellow-brown colour and less likely to exhibit straight edges. Plagioclase is readily identifiable in one sample as the only colourless phase present. A sub-sample of sub 63 μm magnetic fraction was also run from one of the samples.

Olivine had largely been removed from the samples in the magnetic fraction. This is due to magnetite being present, without exception, in olivine crystals as a product of serpentinisation.

9.1.5.2 Testing the separation

The accuracy of mineral separation was initially tested using X-Ray Diffraction (XRD) but while this verified the separation it was found to be too costly in terms of sample consumption.

As an alternative a selection of separates from each sample was mounted on photographic film and then analysed in a Scanning Electron Microscope (SEM). A LEO 1455VP SEM based at the NHM was used in variable pressure mode. EDS analysis in this mode was sufficient to verify the identity of the minerals in the separates, when compared with previous analysis of thin sections.

However it was noted that mounting on photographic film contaminated the separates with silver and so these separates were not included in the chemical preparations, but were used as a reference for further picking.

9.1.5.3 Analysis

Subsamples were dissolved to completion using a combination of concentrated HF, concentration HNO₃ and concentrated HCl using the procedure in

Vials were checked for complete dissolution at each stage. Procedural blanks were included, following the same procedure but without sample.

Stage	Description	Hot plate temperature (°C)	Time
1	3 ml conc HNO ₃		
2	1ml conc HF		
3	Ultrasonic bath		10 minutes
4	Sealed on hotplate	130	2 nights
5	Dry down	130	~6 hours
6	0.5 ml conc HNO ₃	130	~2 minutes
7	Dry down	130	~20 minutes
8	0.5 ml conc HNO ₃	130	~2 minutes
9	Dry down	130	~30 minutes
10	4 ml 6 M HCL	130	

Table 9.9 - Dissolution procedure used for Nd analysis

In order to separate Nd Small funnel columns (3.7 cm long x 2.5 mm wide) were loaded with approximately 1ml of AG50-X8 200-400 mesh resin. These were cleaned with 2 ml 2M HCl and 2 ml MQ H₂O to clean the column.

Step	Volume	Acid
Condition	2 ml	1.75M HCl
Load sample	100 µl	1.75M HCl
Wash in	100 µl	1.75M HCl
Elute Fe	1.5 ml	1.75M HCl
Elute Ba	3 ml	2M HNO ₃
Collect Nd	1.5 ml	6M HNO ₃
Clean	Funnel	6M HCl
Clean	Funnel	MQ H ₂ O

Table 9.10 - Cation exchange column procedure for Nd analysis AG50-X8 200-400 mesh resin step (Cooper, 2012).

The collected fraction was then dried down in preparation for the second column and then dissolved in 0.3 ml 0.2M HCl. Small diameter LN Spec columns

Step	Volume	Acid
Condition	0.5 ml	0.2M HCl
Condition	1 ml	0.2M HCl
Load sample	300 μ l	0.2M HCl
Wash in	3 x 100 μ l	0.2M HCl
Elute Ba	2 ml	0.2M HCl
Collect Nd	4 ml	0.2M HCl
Elute	1 ml	0.4M HCl
Collect Sm	2 ml	0.4M HCl
Clean	2 x Funnel	6M HCl
Clean	Funnel	MQ H ₂ O

Table 9.11 – Cation exchange column procedure for Nd analysis LN Spec step (Cooper, 2012).

This was all undertaken at the University of Southampton by the author with supervision.

Element ratios were measured using a Thermo X-series 2 quadrupole ICP-MS on the sub-samples of the same solutions prior to Nd separation. $^{143}\text{Nd}/^{144}\text{Nd}$ was measured using a Thermo Neptune multicollector ICP-MS also at the University of Southampton.

The JNdi-1 reference material (Tanaka et al., 2000) was measured at $^{143}\text{Nd}/^{144}\text{Nd} = 0.512120 \pm 0.000012$ (2SD, n=9) during the analytical session. Results were corrected to JNdi $^{143}\text{Nd}/^{144}\text{Nd} = 0.512115$.

9.1.6 S isotope analysis

Sulphides were handpicked from crushed samples. The analyses were undertaken at the Scottish Universities Environmental Research Centre (SUERC) over the course of two weeks.

Sulphur dioxide was liberated from sulphides by combustion under vacuum with Cu_2O at 1050°C (Robinson and Kusakabe, 1975) and from sulphates with the addition of Cu at 1125°C (Coleman and Moore, 1978). Liberated SO_2 gas was purified in a glass extraction line prior to analysis using a VG SIRA II gas mass spectrometer.

A total of 96 separate sulphide samples were analysed and ten duplicates. Four sulphate samples were analysed.

Data are reported as $\delta^{34}\text{S}$ recording variations from the Vienna Canyon Diablo troilite (VCDT) standard in per mil (‰). Sulphide standards used were the SUERC standard CP-1, and international standards NBS-123 and IAEA-S-3. These have $\delta^{34}\text{S}$ values of -4.56 ‰, 17.1 ‰ and -31.5 ‰ respectively.

Standard	IAEA S3	CP1	NBS123
Mineral	Ag ₂ S	Chalcopyrite	Sphalerite
Reported value	-31.5	-4.3	16.9
n	9	9	9
Relative % error			
Average	0.76	1.89	-0.4
SD	1.10	4.18	0.8
Absolute ‰$\delta^{34}\text{S}$ error			
Average	-0.2	-0.1	-0.1
SD	-0.3	-0.2	0.1

Table 9.12 – Standards analysed during S isotope measurements and error as deviations from recorded values.

The sulphate standard used was international standard NBS-127, which gave the $\delta^{34}\text{S}$ value of 21.17 ‰.

9.1.7 Ni isotope analysis

Samples were selected and separated into different minerals by the author and then supplied to Dr Louise Gall. These separates were the same used for S isotope analysis (4.2) and were selected from across the deposit to attempt to cover the extent of sulphide fractionation. Pyrite, pyrrhotite, chalcopyrite and pentlandite separates were produced, from the same sample were possible.

Ion exchange separation was undertaken by Dr Louise Gall at Oxford University and samples were analysed by Multi-Collector-Inductively-Coupled-Plasma-Mass-Spectrometry (MC-ICP-MS) on a Nu instruments Nu Plasma-HR at the Department of Earth Sciences, University of Oxford. Samples were measured using a double spike of ^{61}Ni and ^{62}Ni and bracketed by NIST SRM986 standard analyses (Gall et al., 2012).

Parameters	Setting
RF power	1300 W
Acceleration voltage	5.85 kV
Sampler cone (Nu Instruments)	Ni, B-type, 1 mm Ø
Skimmer cone (Nu Instruments)	Ni, WA-type, 0.7 mm Ø
Ar gas flow rates (l min ⁻¹):	
Coolant	13
Auxiliary	0.8–1.0
Nebuliser	1.0–1.2
Uptake rate (mL min ⁻¹)	50–75
Sample uptake time	60 s
Background measurement time	20 s
Cycle integration time	10 s
No. cycles per analysis	40
Washout time	300 s

Table 9.13 - Typical instrument parameters used during Ni isotope ratio analysis on the Nu Plasma-HR (Gall et al., 2012)

Values are expressed in $\delta^{60}\text{Ni}$ in per mille (‰) deviations from NIST (SRM 986) pure Ni metal (Gall et al., 2012).

$$\delta^{60}\text{Ni} = \left[\frac{({}^{60}\text{Ni}/{}^{58}\text{Ni})_{\text{sample}}}{({}^{60}\text{Ni}/{}^{58}\text{Ni})_{\text{SRM986}}} - 1 \right] \times 1000$$

Equation 9.1- Definition of the $\delta^{60}\text{Ni}$ notation

9.1.8 High Resolution X-Ray Computed Tomography (HRXCT)

i) Scanning

The cylinders of ore were scanned using 200-215 kV, a 200 μA electron source and between 2-3 mm Cu filters. This was found to be sufficient to penetrate 2 cm of sulphide. Scans took approximately an hour and produced 3600 images of the revolving sample.

ii) Data reduction and presentation

An optimum system for viewing and presenting the CT data has been established. This involves separating silicates and carbonates from the sulphides by density and removing the silicates. A PGE threshold is established and the PGE minerals are coloured red. The visible sulphides are restricted to a 10 μm thick disc and this is moved up the sample recording the position of each PGE mineral relative to the sulphide disc. However uncertainty remains about the thresholding of the PGE, principally whether the threshold is accurately separating PGE minerals from all other minerals.

iii) Data validation

A serial sectioning project (Hunter, 2012) showed that the CT scans were very reliable at reproducing the PGE mineral distribution particularly after applying a threshold using a known PGE mineral grain. The location of the polished surfaces were chosen using the CT scans themselves so that they are likely to include suspected PGE minerals or can be polished down to encounter them.

9.1.9 Analytical References

- Cooper, M. J., 2012, Separation of Nd for isotopic analysis by Neptune, Standard Operating Procedure, University of Southampton.
- Gall, L., Williams, H., Siebert, C., and Halliday, A., 2012, Determination of mass-dependent variations in nickel isotope compositions using double spiking and MC-ICPMS: *Journal of Analytical Atomic Spectrometry*, v. 27, no. 1, p. 137-145.
- Holwell, D., and McDonald, I., 2007, Distribution of platinum-group elements in the Platreef at Overysel, northern Bushveld Complex: a combined PGM and LA-ICP-MS study: *Contributions to Mineralogy and Petrology*, v. 154, no. 2, p. 171-190.
- Hunter, C., 2012, Understanding the controls on the spatial distribution of Platinum Group Elements (PGE) in orthomagmatic sulphides: insights from tomographic reconstruction, reflected light and electron microscopy [MSci Masters Thesis]: Imperial College.
- Longerich, H. P., Jackson, S. E., and Günther, D., 1996, Inter-laboratory note. Laser ablation inductively coupled plasma mass spectrometric transient signal data acquisition and analyte concentration calculation: *Journal of Analytical Atomic Spectrometry*, v. 11, no. 9, p. 899-904.
- McDonald, I., Development of sulphide standards for the in-situ analysis of platinum-group elements by laser ablation inductively coupled plasma-mass spectrometry (LA-ICP-MS), *in Proceedings 10th International Platinum Symposium, Ext Abstracts2005*, p. 468-471.
- Prichard, H. M., Fisher, P. C., McDonald, I., Knight, R. D., Sharp, D. R., and Williams, J. P., 2013, The distribution of PGE and the role of arsenic as a collector of PGE in the Spotted Quoll nickel ore deposit in the Forrestania Greenstone Belt, Western Australia: *Economic Geology*, v. 108, no. 8, p. 1903-1921.
- Tanaka, T., Togashi, S., Kamioka, H., Amakawa, H., Kagami, H., Hamamoto, T., Yuhara, M., Orihashi, Y., Yoneda, S., Shimizu, H., Kunimaru, T., Takahashi, K., Yanagi, T., Nakano, T., Fujimaki, H., Shinjo, R., Asahara, Y., Tanimizu, M., and Dragusanu, C., 2000, JNdi-1: a neodymium isotopic reference in consistency with LaJolla neodymium: *Chemical Geology*, v. 168, no. 3-4, p. 279-281.

9.2 Glossary of mineral abbreviations

Following recommendations by the IUGS Subcommission on the Systematics of Metamorphic Rocks by J. Siivola and R. Schmid.

Mineral	Abbreviation	Formula
Amphibole	am	-
Anhydrite	anh	CaSO ₄
Augite	aug	(Na,Ca)(Mg,Fe ²⁺ ,Al,Fe ³⁺ ,Ti)(Si,Al) ₂ O ₆
Calcite	cal	CaCO ₃
Chalcopyrite	ccp	CuFeS ₂
Chlorapatite	-	Ca ₅ (PO) ₃ Cl
Chlorite	chl	-
Chromite	chr	Fe ²⁺ Cr ³⁺ ₂ O ₄
Clinopyroxene	cpx	-
Cubanite	cub	CuFe ₂ S ₃
Diopside	di	CaMgSi ₂ O ₆
Dolomite	dol	CaMg(CO ₃) ₂
Enstatite	en	MgSiO ₃
Edenite	ed	NaCa ₂ Mg ₅ (AlSi ₇ O ₂₂)(OH) ₂
Fayalite	fa	Fe ₂ SiO ₄
Forsterite	fo	Mg ₂ SiO ₄
Hematite	hem	Fe ₂ O ₃
Hessite	-	Ag ₂ Te
Hornblende	hbl	Ca ₂ (Fe,Mg) ₄ Al(AlSi ₇ O ₂₂)(OH) ₂
Ilmenite	ilm	Fe ²⁺ TiO ₃
Kaersutite	krs	NaCa ₂ Mg ₃ AlTi(Al ₂ Si ₆ O ₂₂)O ₂
Kotulskite	-	Pd(Te,Bi)
Magnesite	mgs	MgCO ₃
Magnetite	mag	Fe ²⁺ Fe ³⁺ ₂ O ₄
Maslovite	-	PtBiTe
Melonite	-	NiTe ₂
Merenskyite	-	PdTe ₂
Michenerite	-	PdBiTe
Millerite	-	NiS
Moncheite	-	PtTe ₂
Muscovite	ms	KAl ₂ (AlSi ₃ O ₁₀)(OH) ₂
Olivine	ol	(Mg,Fe) ₂ SiO ₄
Orthopyroxene	opx	-
Pargasite	prg	NaCa ₂ Mg ₄ Al(Al ₂ Si ₆ O ₂₂)O ₂
Pentlandite	pn	(Fe,Ni) ₉ S ₈
Phlogopite	phl	KMg ₃ (AlSi ₃ O ₁₀)(OH) ₂
Plagioclase	pl	Na(AlSi ₃ O ₈) to Ca(Al ₂ Si ₂ O ₈)
Prehnite	prh	Ca ₂ Al ₂ Si ₃ O ₁₀ (OH) ₂
Pumpellyite	pmp	Ca ₂ MgAl ₂ (Si ₂ O ₇)(SiO ₄)(OH) ₂ .H ₂ O
Pyrite	py	FeS ₂
Pyroxene	px	-
Pyrrhotite	po	Fe ₇ S ₈
Quartz	qtz	SiO ₂

Scapolite	scp	$\text{Na}_4\text{Al}_3\text{Si}_9\text{O}_{24}\text{Cl}$ to $\text{Ca}_4\text{Al}_6\text{Si}_6\text{O}_{24}\text{CO}_3$
Serpentine	srp	$\text{Mg}_2\text{Si}_2\text{O}_5(\text{OH})_4$
Talc	tlc	$\text{Mg}_3(\text{Si}_4\text{O}_{10})(\text{OH})_2$
Tremolite	tr	$\text{Ca}_2\text{Mg}_5(\text{Si}_8\text{O}_{22})(\text{OH})_2$
Tschermakite	ts	$\text{Ca}_2\text{Mg}_3\text{Al}_2(\text{Al}_2\text{Si}_6\text{O}_{22})(\text{OH})_2$
Violarite	-	$\text{Fe}^{2+}\text{Ni}^{3+}_2\text{S}_4$

9.3 LA-ICP-MS Data

See attached excel file

9.4 EPMA Data

See attached excel file